

Superior Weapons Systems Through Castings (SWC)

Final Report



Award Number: W15QKN-10-2-0001

Period of Performance: April 1, 2010 – September 30, 2012

Organization: Advanced Technology International dba SCRA Applied R&D

20121203014

Contents

<i>Abstract.....</i>	<i>3</i>
<i>Introduction</i>	<i>3</i>
1. <i>Visual Inspection of Casting Surfaces: Principal Investigator Dr. Frank Peters, Iowa State University.....</i>	<i>7</i>
2. <i>Development of High Strength PH13-8Mo Alloys: Principal Investigator Dr. Robert C. Voigt, Penn State University.....</i>	<i>23</i>
3. <i>Verification of New Radiographic Testing (RT) Standard through Mechanical Testing: Principal Investigator Dr. John Griffin, University of Alabama at Birmingham.....</i>	<i>53</i>
4. <i>Effect of Surface Indications on Mechanical Properties in Steel Castings: Principal Investigator Dr. John Griffin, University of Alabama at Birmingham.....</i>	<i>65</i>
5. <i>Industry Capabilities for Preparedness and Sustainment/Process Capability Improvements for Cast Metals Industry: Principal Investigator Jerrod A. Weaver, Non-Ferrous Founders' Society.....</i>	<i>113</i>
6. <i>Advanced Aluminum Metal Matrix Composites for Sand and Investment Casting Applications: Principal Investigator Kenneth Kremer, M Cubed Technologies, Inc.</i>	<i>121</i>
7. <i>High Performance Nano-Composite Materials: Principal Investigators Stephen P. Udvardy, North American Die Casting Association; Jacob Nuechterlein, Colorado School of Mines; Makhlof M. Makhlof, Worcester Polytechnic Institute.....</i>	<i>133</i>
8. <i>High Strength, High Toughness, Cast Aluminum Alloy: Principal Investigators Robin D. Foley, University of Alabama at Birmingham.....</i>	<i>149</i>
9. <i>Developing an Improved Combination of Strength and Permeability for Investment Shells used with Foam Patterns: Principal Investigators Dr. Von L. Richards, Missouri University of Science and Technology</i>	<i>185</i>
10. <i>Steel Founders' Society of America (SFSA) Final Report: Principal Investigator Malcolm Blair, SFSA.....</i>	<i>217</i>
11. <i>American Foundry Society (AFS) Final Report: Principal Investigator Thomas Prucha, AFS.....</i>	<i>221</i>
12. <i>North American Die Casting Association (NADCA) Final Report: Principal Investigator Steve Udvardy, NADCA.....</i>	<i>223</i>

Abstract

Military operations demand rapid responses to maximize warfighter performance and readiness. The Army is making significant changes to its acquisition decisions and maintenance operations in order to reduce the weight and extend the service life of ground combat systems.

The American Metalcasting Consortium's (AMC) Superior Weapons Systems through Castings (SWC) enhances the Army's ability to procure higher performance, lighter weight parts for both legacy and new weapons systems. The SWC program has developed new processes and materials that ensure the rapid availability of high-quality light-weight parts for assembling prototypes, as well as spare and replacement parts for fielded units. The program has also boosted the number of domestic suppliers capable of developing critical defense components.

Casting processes and materials developed under this program have many advantages over other manufacturing processes.

- "Net Shape:" The part that comes out of the mold is often ready to be used, with little or no additional processing. This reduction in finishing can eliminate more than two-thirds of the production costs for some parts.
- Controlled solidification: The Department of Defense's (DoD) foundry suppliers tailor the structural makeup of a part, as well as its resulting properties, by controlling the speed at which the part cools after it is cast. This ensures that the part has the highest integrity, allowing it to be used longer in a weapons system
- Improved design techniques: Parts can be designed more efficiently so that they require less time to produce and have a lower weight and cost with the same or better functionality.

The SWC program has successfully:

- developed materials that reduce weight and/or are more suitable for extreme service conditions;
- enhanced the processes and geometries of certain critical cast parts;
- improved the casting industry's predictive tools;
- redesigned existing components to capture the advantages of castings.

The SWC effort integrated the U.S.'s top academic metalcasting researchers with industry experts and dozens of small-business foundry shops across the U.S. to solve the Army's need for lightweight, high-performance replacement parts. The SWC Team worked closely with the Army and Benet Labs to obtain insight into their spare part challenges. This unique partnership of government, industry, and academia ensured that results were rapidly integrated into industry.

Introduction

Metalcastings are critical to the capability of the DoD's weapon systems. However supply chain constraints have made it difficult to obtain high-quality, lightweight, cost-effective metalcastings for weapon systems within reasonable lead times. These difficulties are a result of numerous constraints affecting the reliability of the supply chain, including the

demise of many original equipment manufacturers/suppliers, the undetectable presence of castings in technical data packages (TDP), obsolescence of technical data and/or specifications, retired expertise, lost or discarded tooling, and the movement of metalcasting capability overseas. In addition, opportunities to use the unparalleled advantages of metalcastings to solve repeating legacy weapon system problems or for new weapons systems designs are lost.

The American Metalcasting Consortium's (AMC) strategic direction is to ensure a rapid and reliable metalcasting supply chain for high quality and lightweight parts in both new and legacy weapons systems. AMC's SWC program utilized distributed technology management among industry and research resources to develop, leverage, deliver, and apply innovative technologies and processes in support of Benet's procurement and utilization of cast components in weapon systems. The AMC SWC team consisted of:

- The nation's top academic metalcasting researchers
 - Colorado School of Mines
 - Iowa State University
 - Missouri University of Science and Technology
 - M Cubed
 - Penn State University
 - University of Alabama – Birmingham
 - Worcester Polytechnic Institute
- The CAST-IT team of metalcasting industry experts with over 150 years of metalcasting industry experience
- The four leading metalcasting industry associations (and their members)
 - American Foundry Society
 - Non-Ferrous Founders' Society
 - North American Die Casting Association
 - Steel Founders Society of America
- ATI, a leader in building and managing custom-tailored R&D manufacturing programs

AMC's industry associations, representing over 2,000 foundries, ensured the rapid transition of the program results into industry. SWC's goal is to enhance the reliability and performance of cast parts, while reducing costs and lead times associated with the procurement process. In addition, this program ensures a dependable US metalcasting manufacturing base for the procurement of cast components to improve the performance of the warfighter.

AMC is the only metalcasting consortium consisting of the dominant industry associations, their membership, and the premier metalcasting research universities in the United States.

SWC was proposed as a three year manufacturing R&D effort. Year 3 was included in the original SWC proposal and part of the GFY2011 Senate Appropriations bill. However the actual GFY2011 budget passed by Congress did not include the appropriated funds for SWC Year 3.

The projects under the two-year SWC program effort included the following:

- Visual Inspection of Castings, Iowa State University - This project provided a methodology to improve the visual inspection process for the metalcasting industry.
- Development of High Strength PH13-8Mo Alloys, Penn State University - This research effort developed processing and composition guidelines to develop a cast version of PH13-8Mo precipitation hardened stainless steel, making possible direct substitution for titanium casting alloys in military applications without a weight penalty.
- High Performance Nano-Composite Materials, Colorado School of Mines, Worcester Polytechnic Institute, North American Die Casting Association - This effort developed castable high performance nano-composite materials that can be used for lightweight weapon system components.
- High Strength, High Toughness, Cast Aluminum Alloy, University of Alabama - Birmingham - The objective of this research was to optimize the chemistry of an existing high strength aluminum alloys to make them suitable for mortar base applications, and develop a mechanical property database for designers.
- Developing an Improved Combination of Strength and Permeability for Investment Shells used with Foam Patterns - This effort optimized the performance of ceramic mold shell materials for expendable foam patterns for producing limited run large scale (over 300 lbs.) parts of complex shape and lighter weight.
- Technology Diffusion into Industry and Government: AFS, NADCA, and SFSA worked to link their SWC-sponsored researchers and with industry and Army/DoD groups in order to implement and maximize the impact of the emerging metalcasting technologies.

The projects only performed in Year 1 of the SWC program effort included the following:

- Verification of New Radiographic Testing (RT) Standard through Mechanical Testing, University of Alabama - Birmingham - This project produced, radiographed, and tested cast steel tensile specimens and verified the indication fraction/stiffness/yield stress relationship.
- Industry Capabilities Assessment for Preparedness and Sustainment, Non-Ferrous Founders Society - This effort determined current and future industry capabilities to support DoD procurement requirements and developed a resource that proactively identified and addressed supply chain gaps for cast parts, with an emphasis on land systems.
- Process Capability Improvements for the Cast Metals Industry, Non-Ferrous Founders Society - This project developed training materials and documented procedures to assist the metalcasting industry with conducting internal process capability studies in order to ensure critical product criteria (e.g. tensile, hardness, linear dimensions, etc.) are repeatable and consistent with customer specifications.

- Engineering Support for New Casting Design / Improvement of Old Casting Designs, CAST-IT Team – This project leveraged AMC's CAST-IT team to advance four primary focus areas for Benet:
 1. Material development optimized for service conditions
 2. New casting processes for enhanced materials and geometries
 3. Predictive tools for improved castings
 4. Design new/redesign of existing components to capture the advantages of castings

The projects only performed in Year 2 of the SWC program effort included the following:

- Effect of Surface Indications on Mechanical Properties in Steel Castings, University of Alabama – Birmingham – Developed design information on the relationship between linear and non-linear indications on tensile properties on four steels (ASTM A27 Grade 70-40, ASTM A148 Grade 105-85, ASTM A148 Grade 165-150, and Eglin steel).
- Advanced Aluminum Metal Matrix Composites for Sand and Investment Casting Applications, Non-Ferrous Founders Society - Developed casting methods to produce the Al/SiC-55p metal matrix composites (MMCs) in complex shape at attractive cost for military applications

1. Visual Inspection of Casting Surfaces: Principal Investigator Dr. Frank Peters, Iowa State University

Visual inspection of casting surfaces is a very subjective process that is prone to measurement errors. To improve this process, several investigations were undertaken at metalcasting companies as well as in the laboratory. The field studies showed that operators were not following a consistent search pattern nor were they covering the entire casting surface. Studies in the laboratory showed that this can be corrected by utilizing rastering (i.e., side to side, top to bottom) training. Overlays of a suggested search pattern onto the casting proved to be distracting and not beneficial. The use of comparator plates during the inspection process improves an operator's ability to make correct acceptable/unacceptable decisions regarding a surface. However, reproducibility still remains to be an issue. The cognitive style of the operator is an important factor and can be tested using a very simple test made available to industry. A white light scanning technology that is affordable enough to be routinely utilized on the shop floor was investigated. While it cannot replace the human operator, it would be a very valuable training and 'calibration' tool for inspectors. In addition, a software program to help collect, manage, and analyze data from component surfaces was created.

Objective

The visual inspection of cast products is a very subjective process that has a significant impact on the manufacturing systems and product delivery of most metalcasting facilities. The process is often plagued by large measurement errors. Peters (with Daricilar) studied the measurement error of in-process inspection of castings at three companies and found errors over 50%.¹

Poor visual inspection decisions can result in excessive rework, unnecessary scrap, unacceptable parts reaching the customer, and delivery delays. If unacceptable areas of a casting are not identified during an inspection process, the part will later need to be addressed again, causing longer than necessary lead times. Or, if the unacceptable area is never identified, the customer will receive the unacceptable product, which will likely result even longer delays to receive the desired product. To counteract this problem, inspectors will often mark areas to be rectified that are indeed acceptable. This practice results in added time and cost to produce the casting.

The objectives of this project were to develop methods for improving the inspection process. Since automated inspection of the entire casting is not likely in the near or medium term, the casting industry will still rely on the human operators. Therefore, training and inspection aids that will improve the performance of an operator in making correct inspection decisions will be developed. Ultimately, this will benefit the casting producer with the increased ability to ship acceptable parts with less rework effort and less production delays. The casting consumer will benefit by receiving parts as specified within shorter lead times.

In related work, a software program that can manage surface information for 3D components will be enhanced and made available to industry. With this software, the user can record information regarding the component surface, such as areas that need to be upgraded or are a source of scrap. The software will manage the entry, storage, and

retrieval of this information. With this information, manufacturing engineers will be able to make informed decisions about their processes.

Introduction and Approach

The visual evaluation of casting surfaces is conducted several times during the production of metalcastings. The most obvious persons conducting these visual evaluations are the inspectors which markup unacceptable areas for remediation or justification to be scrapped. However, evaluations are also done by operators while they are processing the castings, by management, by sales, and ultimately by the customer. Previous work has shown that there is significant measurement error, both repeatability and reproducibility.¹ Undetected surface defects will result in additional rework cycles or worse, returns from the customer. Marking acceptable anomalies as defects will result in excessive processing. Operators must be provided with appropriate training and inspection aids to help reduce the measurement error.

Review Of Previous Work and Factors That Effect Visual Inspection

Current literature provides information on the factors that affect visual inspection performance which will be reviewed below for the application to metalcasting tasks.

Environmental Factors

Temperature is an obvious but often overlooked factor in visual inspection environments. Temperature and humidity together affect our ability to achieve optimal thermal exchange with our environment, too hot and our body will focus on cooling, too cold and it must focus on the conservation of heat. Both of these actions affect a human's ability to achieve optimal cognitive performance. It has been found that cooling sensations (e.g. from a fan) activate the brain and excite the nervous system controlling thermoregulation, and that this activation of the sympathetic nervous system elevates mental alertness thus increasing general attention capabilities.² Interestingly, a slight (<1 degree) increase in body temperature can be an indication of heightened awareness and performance.³ This increased body temperature may be a result of the extra alertness of the operator; a higher environment temperature is not needed to achieve this result. Extremes in a work environment cause issues in the perception of moderate exertion and cooling can increase an inspector's long term capabilities. Ideally, it is suggested to utilize work stations that have localized cooling sources (e.g. a fan or personal cooling unit) to keep an environment near 70°F with a relative humidity between 60 and 70%.⁴

Operator Factors

Many individual factors have been shown to be of particular importance in the area of visual inspection. Some of these factors are obvious and include visual acuity, color vision, and depth perceptions. As an eye becomes less accurate so will its ability to accurately interpret defects. Experience on the job can be a very positive individual factor; in fact, inspectors who are experienced in performing a specific visual inspections task can concentrate longer and perform with a higher degree of accuracy than those with less experience.⁵ Most of these benefits, however, were found in search tasks that have a controlled amount of variation, unlike typical casting surface inspection tasks.

General intellectual aptitude is another known factor in determining the capabilities of a visual inspector.⁶ As one would expect, higher intellectual aptitude correlated positively with higher levels of visual inspection success. This appears to be due to an increased ability to adapt strategies and utilize memory techniques that aid in the visual inspection process. The cognitive inspection style of individuals also appears to be a factor in visual inspection capability. Specifically, the Matching Familiar Figures Test (MFFT) has been shown to have potential in determining individual potential in performing visual inspection tasks.⁷⁻⁸ The use of this test will be discussed below.

Task Factors

The task itself can greatly affect an operator's ability to perform a visual inspection. Depending on the kind of visual inspection being performed the posture and physical strain can impact visual inspection capabilities. Several authors have shown that select visual inspection jobs suffer from decline in visual inspection performance as a result of physical strain.^{4,9,10} Studies like this have shown that as time on task increases, participants tended to lean forward, change postures more frequently, report more discomfort, and take more time performing visual inspection. However, this increased time does not lead to increased accuracy, rather, error rates go up. Issues related to postural discomfort, physical fatigue and biomechanical strain resulting in visual inspection decrements can largely be quantified using known evaluation methods. These factors could be significant given the typical components being inspected and work areas of metalcasting inspection operations.

Another task factor that has been shown to impact the performance capability of visual inspectors is the level of documentation provided for on the job comparisons. It is much easier to perform a relative judgment than it is to make an absolute one. Providing aids, such as comparator plates, that allow visual inspectors to compare a possible flaw to a known category of flaw can be very beneficial. Several studies have shown that the visual inspectors that are given an effective comparison aid consistently outperformed those that were forced to make absolute judgments alone.^{6,11} Hence, simply giving the visual inspector a visual reference aid to refer to can greatly increase their basic capabilities.

Field Studies

Field studies were conducted at both steel and iron foundries producing castings from 1 to 10,000 pounds from shell, investment, chemically bonded sand and green sand. The goal of these field studies was to identify factors influencing visual inspection that could be an opportunity for improvement. An eye tracker was developed so studies of the search strategies being utilized during the inspection process, Figure 1-1. This tool allows analysis of the search pattern as well as determining the percent of the casting surface that is being inspected. It is mounted on a face shield and goggles to provide the eye protection often used in the shop floor environment. The eye tracker has three cameras, two recording the world view in front of the operator, and the other records the



Figure 1-1 The eye tracker used to determine where inspector was looking.

location of the pupil within the eye. Two cameras on the world view are necessary to collect data on operators that are inspecting larger castings. The video feeds from the two world view cameras are 'stitched' together. After this, the world view and the pupil view are compiled together which results in a video of the world view with crosshairs to show where the user was looking at any given time. This compiled video can be analyzed, frame by frame, to determine the operator's search patterns.

To understand the results of the eye tracker, the useful field of view (UFOV) needs to be defined. UFOV is the area where humans can see the most detail at in their vision due to the greater concentrations of rods at that particular location. For the purpose of this study a reasonable value of 6 degrees is assumed. Assuming that the parts were 22" from the operator's eye, the useful field was calculated to be 2.25 inches wide. It should be noted that the UFOV used in this study was generous and assumed the best case scenario for viewable area (this was done to avoid biasing results in favor of experimental solutions). This was used to determine the percent of casting surface which was being inspected. Figure 1-2 shows an example casting with the search path line and the useful field of view overlayed on the part.

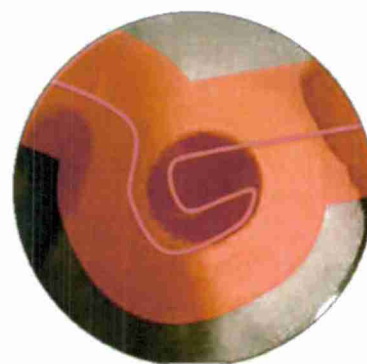


Figure 1-2 Example of a casting with the search pattern and the UFOV highlighted.

Laboratory Studies

Based on what was learned during the field studies, laboratory experiments were designed to investigate key factors. These experiments allowed the research team to isolate certain factors that could improve the inspection process, and study their effect. Specifically, three experiments were conducted on the ISU campus.

The field study results clearly showed that operators were not using a consistent search pattern, nor were they getting adequate coverage of the casting surface. These issues would lead to the poor measurement error that had been observed in industry. Based on this, experiments were run on methods that we could use to help train operators. This directly supported one of the main deliverables of the project, training tools.

The first experiment studied the use of visual overlays on the casting surface to help guide the inspector to inspect the entire casting surface. The second experiment investigated video methods to help train operators to develop a systematic search pattern. The third experiment specifically investigated the ability of human operators to discriminate between acceptable and unacceptable surfaces. This experiment also looked at the effectiveness of comparator plates for improving accuracy.

Results and Key Findings

The findings from the industry research steering committee meetings, visits, and field studies were used to help shape the approach to develop meaningful results.

Selecting Operators for Inspection Tasks

Schwabish and Drury⁷ designed an experiment to evaluate the influence of the reflective-impulsive cognitive style on visual inspection. They utilized the Matching Familiar Figures Test (MFFT) which asks the participant to choose from six figures the one that is the same as the one on top of the screen. The time until the correct match is made and how many errors are made before getting the correct match are the dependent variables that are recorded. Figure 1-3 has some examples that are used in the MFFT.

According to the accuracy and response time of subjects taking the MFFT, subjects were classified into four different cognitive styles: fast-accurates (spend shorter times, make fewer errors), reflectives (spend longer times, make fewer errors), impulsives (spend shorter times, make more errors), and slow-inaccurates (spend longer times, make more errors). Their results indicated that there was a grouping phenomenon based on the accuracy dimension. The accurate group (i.e., reflective and fast-accurate) was faster than the inaccurate group (i.e., impulsive and slow-inaccurate) and made fewer size-judgment errors. Research in this field indicates that those classified as 'fast accurates' will have the greatest inspection capability followed by 'reflectives', 'impulsives', and lastly those classified as 'slow inaccurate'.



Figure 1-3 Two examples from the Matching Familiar Figures Test (MFFT)

Given the success of Schwabish and Drury in using MFFT for evaluating the potential of individuals to be aircraft inspectors, it appears that MFFT could also be effective in the metalcasting industry to evaluate the effectiveness of the MFFT test for casting operations. To accomplish this, a computer based MFFT program was developed. Three groups of



Figure 1-4 Example screen of the visual inspection task with the 'defect' circled

people were evaluated using MFFT for the current work. They include undergraduate engineering students, members of the United Association of Plumbers and Pipefitters Union undergoing initial welding certification, and workers in the metalcasting field that have visual inspection as part of their work tasks. The

metalcasting personnel were from four different companies. The groups will be referred to as the student, pipefitter, and casting groups. All of the participants were given the MFFT as well as a computerized visual inspection task. An example of the visual inspection task can be seen in Figure 1-4. In this task, the time and accuracy is recorded.

The MFFT data set included 58 students, 16 pipefitters, and 33 casting personnel. Since the population groups were not equal, the analysis randomly selected an equal number (twelve) from all three groups. This was repeated five times, and the average values are reported in Table 1-1. For the time to complete the tasks, the person was determined to be 'fast' or 'slow' based on whether they completed the tasks in less than or more than the median time for the group of thirty six subjects. Similarly, they were labeled 'accurate' or 'inaccurate' based on their score relative the median score for accuracy. Of the students, 22% were labeled as fast accurate while 17% of the pipefitters and 9% of the casting personnel achieved this classification. For the slow inaccurate category, the students and pipefitters each had 3% in this category while 39% of the casting personnel fell in this category based on their MFFT performance. While the sampling to create equal populations eliminates the bias of having unequal population sizes, these three groups of people are still not representative of the general population. Regardless, the results do provide insight on the potential of these populations to do the cognitive tasks needed for visual inspection and the need for training to make them more effective.

Table 1-1 Results of MFFT when twelve people were randomly chosen from each population. Data presented is the average of five trials.

Population Group	Percentage of Population Group in Each Classification			
	Fast Accurate	Reflective (Slow Accurate)	Impulsive (Fast Inaccurate)	Slow Inaccurate
Students	22	31	43	3
Pipefitters	17	47	33	3
Metalcasting	9	25	28	39

When the cognitive style was considered with respect to the visual search task shown in Figure 1-4, the Fast Accurate group had the best performance, in terms of speed and accuracy. There was a statistically significant difference in the speed of the task between the Fast Accurate and both the Reflective and Impulsive groups. Interestingly, the Fast Accurate did not have significantly different time compared with the Slow Inaccurate subjects. This is attributed to the Slow Inaccurates speeding up to just get done with the task. This conclusion is supported by the fact that in terms of accuracy of the decision-making, the Fast Accurates were superior to the other three groups.

Field Study Results

Field studies were conducted at foundries producing castings of a range of sizes in iron and steel. For data collected on castings up to approximately 15 inches, the eye tracker revealed that on average, 59% of the casting surface was not being viewed sufficiently enough for the inspector to make meaningful decisions. Furthermore, the search patterns used were quite random; 71% of the time the search pattern was not consistent with the one used for the immediately preceding casting of the same geometry.

Figure 1-5 shows the results from a field study at a foundry producing large castings (greater than 1000 pounds). The initial results from the eye tracker showed a random search pattern used to inspect the castings, which led to only 84% coverage of the casting surface.



Figure 1-5 Larger steel casting (about 5' high) with the (left) initial search pattern and (right) search pattern after rastering training.

After some short rastering training, where the operators were instructed to use a consistent left to right search pattern, the eye tracking results were again collected. This time, 96% of the casting surface was adequately covered, as shown on the right side of Figure 1-5.

Laboratory Experiment on the Use of Overlays

Since there is a need to encourage more thorough and consistent search patterns, a laboratory experiment was designed to investigate the effectiveness of projecting an overlay on the casting surface.

Three conditions were tested related to the training and inspection aids provided to the subjects. The first group was only given instructions on what surface indications that they were to look for, but was not instructed on how to inspect the castings (basic training group). The second group received the basic training as well as using a left to right search strategy called rastering (raster group), and they were instructed to raster the entire time. The third group was provided the same training as the raster group but was also provided green static lines projected onto the part with a projector (overlay group). There were 24 participants in this study.

Specifically, the raster training included instructions to first follow lines on a sheet of paper as if they were reading (left to right top to bottom). They were encouraged to continue this process and increase their speed through multiple runs. The participants were encouraged to raster on an image which had points of interest the participants were to point out. Once this had been completed the participants repeated this procedure with an actual casting.

Once training had been completed, the participants were asked to inspect 90 parts from 5 differing casting types ranging from 2 to 55 pounds. The laboratory experiment was set up to as closely resemble a casting visual inspection process as possible. They would inspect the part for surface anomalies. Each anomaly that met the criteria was to be circled using a piece of chalk. Then the part was placed back onto the conveyance system and the process repeated for each part.

The variables being measured in this experiment are the performance measures related to signal detection (d' , hit rate, and false alarm rate). Hits are the correct identification of a

surface area as unacceptable. Conversely, a false alarm is when a participant designates an area to contain an unacceptable indication when it was actually acceptable. The surface acceptance criterion was set to ASTM A802 SCRATA plate standard at the B4 and C1 level. This was done independently by three individuals familiar with the standard. For each part, the number of hits and false alarms were determined for each subject.

An important metric to consider with signal detection theory is d' . This is a measure of how good a subject is at the inspection task. It is the ratio of how many hits to how many misses the participant had. Sensitivity d' is the ratio of the ordinate of the SN (signal plus noise) at the criterion to the ordinate of the random variation of the N (Random variation plus noise) distribution at the criterion.¹¹

The analysis of variance showed that there was a significant difference in the d' values for the subjects with different training conditions. A plot of the d' score by training condition with box plots can be seen below in Figure 1-6. In order to determine which training condition was significant from one another a Tukey-Kramer HSD test was done. This showed that the raster training group is superior to the basic training group. However there is no statistically significant difference between the overlay group and either other group.

For the false alarm rates, there was a significant difference between the training. A plot of the false alarm rate by training condition with box plots can be seen below in Figure 1-7. The basic training group was significantly different from both the overlay and the raster training group. The lack of search pattern training resulted in more false alarms.

The analysis of variance showed that there was not a significant difference in hit rates among the different training groups. The raster training group was superior to the basic training group with regards to overall signal detection (d'). However, despite the fact the overlay group received raster training they were not superior to the basic overlay group.

Due to previous literature it would be expected that the overlay group would have the same level of performance (d') as the raster training group if not increased performance.¹²⁻

13

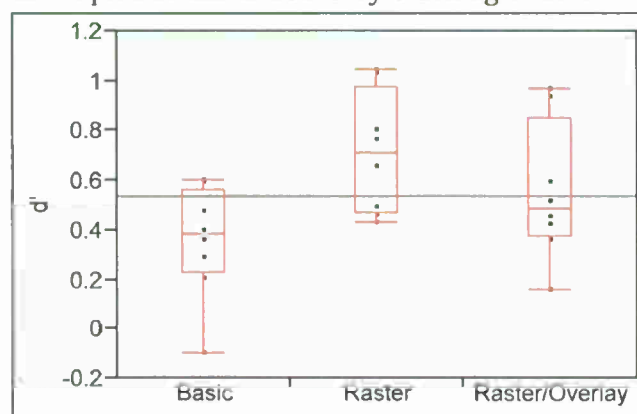


Figure 1-6 Box plot showing effect of training on d' values.

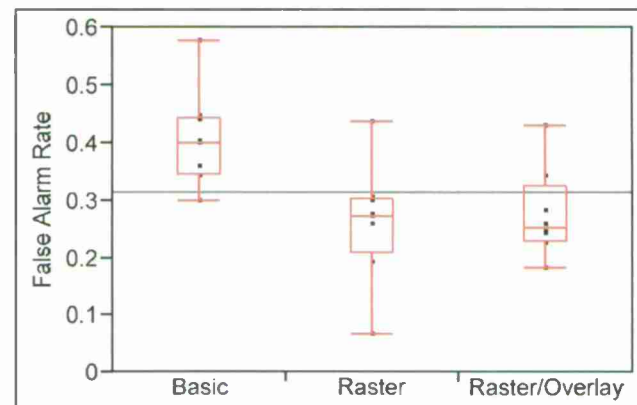


Figure 1-7 Box plot shows effect of training on false alarm rate

The likely reason for the overlay group not performing superior to the others is that the overlay lines are proving to be distracting. That is they are very salient and are causing the inspectors' eyes to be drawn to those areas and not to the surface areas to be inspected. This is a common effect with humans.¹⁵⁻¹⁹

The likely reason inspectors in previous literature responded well to a visual overlay is that they were presented in a different media. Most were inspecting on a computer screen where the lines were static and did not move. In this experiment the static overlay lines would move relative to the casting if they were holding the part in their hands during the inspection the lines could fluctuate and move. Hence alignment issues may have effected an individual's ability to effectively adapt to edge prediction (a factor in the development of systematic search pattern training), this would lead to slow downs and eventual skipping of raster lines. Another factor to consider was that the participants would have to utilize more mental effort to confirm line existence, thus slowing the process. This time loss had to be compensated by reducing peripheral inspection activities.

The data from the eye tracker confirms what was observed with the signal detection scores. The raster training group had the highest percentage of the part viewed and were able to make the best decision about what an indication was, leading to the higher d' values. The overlay group had the second highest d' values, however, the distraction that the lines provided likely caused their performance to drop. Finally, the basic training group had the lowest training percentage of the part viewed. This again confirms the d' values, the participants would view only a certain percentage of the part before making a decision which would generally be a bad one.

Additionally, it was found that both groups with rastering training adopted a more optimal (rastering) search pattern as opposed to the basic training group whose search patterns were more random. The systematic search pattern would have likely helped with both rastering groups, if not for the distracting effect of the overlay.

Laboratory Study on Rastering Training Methods

While the overlays proved to be distracting, the results did show a benefit of rastering training to support the subjects' systematic coverage of the casting surfaces. A second experiment was conducted that focused on rastering training. Subjects were asked to follow a blue dot on a computer screen that traversed either Left-Right, Left-Right or Left-Right-Left. The training screen starts with grid lines, but then changes to an actual casting photograph with the blue dot traversing across it, see Figure 1-8. The goal was to encourage the subject to have a systematic search pattern across



Figure 1-8 Screen shot of the rastering training video showing the blue dot traversing a casting photograph. The subject was asked to follow the dot to support a systematic search pattern.

the whole casting, and not reach the edge of the casting and follow it, as had been seen in our previous studies.

After the video training, the subjects were asked to inspect about 100 castings and look for surface areas which were not acceptable, and then mark those areas. The marks they made were compared to the 'standard' markings of acceptable/unacceptable surfaces. This research shows that the video rastering training increased the percentage of unacceptable areas which were correctly identified, or an increased 'hit rate'. The training also caused more areas which were acceptable to be marked as unacceptable, or increased 'false alarm' rate. This is logical in that since we are getting the subjects to systematically look at more of the surface, this results in more 'hits' but also more 'false alarms'. Subjects are 'seeing' more surface, but have the same difficulty in discriminating between acceptable/unacceptable surfaces. The video training will be packaged onto a website for use by industry.

Study on the Effect of Comparator Plates Over Time

The purpose of this experiment was to test the ability of subjects to discriminate between acceptable and unacceptable surfaces. The participants were asked to make a binary decision, acceptable or unacceptable, for twenty five casting surface samples. The casting surface replicas were made to avoid the distraction of handling castings and searching the whole casting for areas of interest. Using rubber mold making and epoxy model materials, actual casting surfaces were replicated in hard grey colored epoxy samples that were four inch squares. These samples had the texture, color and finish very similar to ferrous casting surfaces.

There were forty participants in the first session, of these, thirty-two returned after a month for the second session. At the time, the participants were not aware that they would be invited back for the second session.

Three comparator plates with surface anomalies similar in type to what the test surfaces contained were utilized in this experiment. The participants were instructed to consider the comparator plate surfaces to be the threshold between acceptable and unacceptable. During each session, the participants conducted the experiment twice, once with and once without the comparator plate. In the first session, it was randomly chosen whether they had the comparator plates for the first or second trial. For the second session, the first inspection task was without the plates to test their recall on what was acceptable or not.

The hit rate was calculated as the percentage of correct rejections over total number of defects, and the false alarm rate was calculated as the percentage of false rejections over total number of acceptable samples. Unlike the previous two laboratory trials discussed, each plate only had a single binary acceptable/unacceptable decision. (Since actual castings were used in the other experiments, there could be an infinite number of possible indication areas to trigger a 'hit').

Before each test, training and a practice trial was provided. In the training, the standard for acceptance was illustrated by three comparator plates, followed by a practice trial with 5 casting samples.

The results for hit and false alarm are presented in Table 1-2. A series of two samples tests were performed to examine whether a significant effect existed with the presence of

comparator plate. The hit rate was significantly improved when comparator plate presented in the second session. This shows that the presence of the comparator plates improves inspection performance when considered over longer time periods since the last training.

Table 1-2 Hit and False Alarm Rates

	Hit Rate	False Alarm Rate
1 st Session – With Comparator Plates	0.64	0.25
1 st Session – Without Comparator Plates	0.66	0.29
2 nd Session – With Comparator Plates	0.78	0.30
2 nd Session – Without Comparator Plates	0.67	0.26

Reproducibility of Visual Inspection Investigation

The previous experiment on the use of comparator plates was also used to extract information on reproducibility, or the agreement between inspectors. As described above, each of forty participants made a binary acceptable/unacceptable decision for each of twenty five samples. The range of agreement among subjects for the samples was 58 to 100%. The average agreement was 80% and the median value was 78%. Note that this was a very easy inspection task compared with the typical casting surface inspection; the specimen was a square sample with essentially one area of interest centered on it. Despite this, the subjects could only agree among themselves 80% of the time.

Anomaly Mapping Software

Another aspect of the project was to enhance Anomaly Mapping Software. This software provides the user with a way to collect, manage, and analyze 3D surface information collected from any object. Its initial intended purpose was to track the in process surface anomalies on the casting surface such that the information can be used proactively to make process control decisions. There was a prototype version developed previously and with this effort it was rewritten to be on a more stable platform. The new version uses SQL to

manage the data. This software allows the user to setup data collection for a casting by first importing the casting geometry via an STL file.

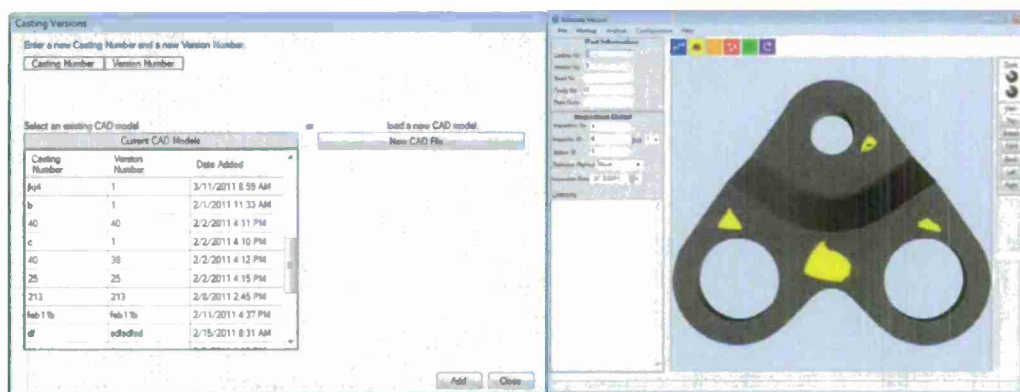


Figure 1-9 Two sample screen shots from the Anomaly Mapping Software: data collection setup, actual data collection, and output.

With this loaded, the user can select the appropriate casting view (usually the six standard views, but others are possible). On each view, the user uses the mouse to select the type of surface indication to be recorded and the location on the casting view. This data is stored and managed, to allow the user to access the data. Output that is currently supported by the software includes frequency plots, histograms, and simple correlations. As with any

database, the user can interrogate the data based on any of the other input data such as the date produced, inspector, production operator, or gating changes. Some sample screen shots of the data input, file management, and data output is shown in Figure 1-9.

After the software was written under this effort, it was rolled out to industry. They recommended several changes including how the database is managed to avoid firewall issues as well as some data analysis tools that they identified as important. These changes were incorporated into the current version. This will continue to be provided to industry. An industry workshop is planned for December 2012 to help introduce the software.

White Light Scanning



Figure 1-10 Affordable white light scanning system from 3D3 systems.

3D3 Solutions that markets a white light scanner for \$9,999. At this price, it becomes reasonable to use it as a 'shop floor' evaluation system. The system is shown in Figure 1-10 and an iron casting with a sample patch scan is shown in Figure 1-11.

Several options are possible for such a system. While 100% inspection of the entire casting surface would not be practical, there are some very valuable uses for this technology. First, it could be used to establish new ways of communicating surface requirements between the designer/buyer and the producer/seller. Current methods include photographs or replicas of a small surface that are hard to interpret and extrapolate. Second, the device could be used as a very valuable training tool. As identified in the current work, the subjective decision making is still subject to much measurement error. This tool could be used to help take the subjectivity out of the decision making and therefore to help 'calibrate' the human inspector.

Figure 1-12 shows an example scan of the SCRATA C1 comparator plate compared to a photograph of the same plate.



Figure 1-11 Photograph of a casting and the white light scan of the portion of the surface.

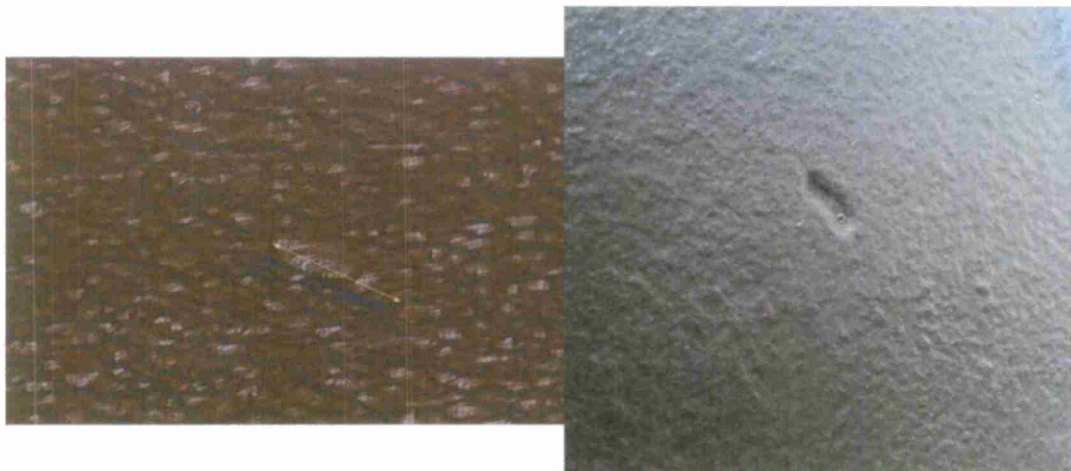


Figure 1-12 An example white light scan of a surface compared with a photograph of the surface.

Transition

The results of this work were provided to industry in a variety of methods, some of which are continuing after the conclusion of this project.

Field Studies

The field studies were conducted at six metalcasting plants. Not only was this valuable to the research team to understand the conditions and requirements of the system, but it also helped raise awareness at these locations of the difficulties with the current visual inspection processes and the need to improve. Additional outreach visits will be conducted by the research team to aluminum foundries to help communicate the results of this work.

Anomaly Mapping Software

A beta version of the mapping software was developed and rolled out to industry. Based on their feedback, improvements and changes were made in the functionality of the software as well as how it handled the database so that it would be more readily used within the constraints of the firewalls in place. The final product is now complete and will continue to be made available to industry, with a plan of continuing to update the software. Specifically in this regard, an industrial workshop is planned for December 2012 to highlight its capabilities to industry.

Website

A website has been created and will be hosted by the Steel Founders' Society of America with links from the American Foundry Society website. This site will contain the MFFT so that companies can use this to identify the cognitive style of their employees. This could be used as a selection tool for identifying future inspectors. The tool will also be helpful for companies to identify training needs for their current inspectors to improve their ability to inspect parts. There will be a supervisor password which will limit access to the test by potential test takers.

The web site also hosts the video training which was shown to improve a subject's ability to raster. One of the underlying causes of the poor repeatability of visual measurement can be attributed to the fact that inspectors are not adequately viewing the entire casting

surface, as identified via the eye tracker during the field studies. The video training requires the operators to follow the cursor in an orderly left to right rastering pattern which has been shown to encourage such behavior when inspecting castings.

Presentations

All off the work results have been presented to industry at various SFSA Technical & Operations Conferences, SFSA Carbon & Low Alloy Research Reviews, and AFS Metalcasting Congresses.

Conclusions and Recommendations

Visual inspection by human operators is a very difficult task. Within a minute, the inspector is interrogating tens of square feet of casting surface and making decisions on if any areas are unacceptable and need to be remedied or even to scrap the part. This is a substantial amount of information for the human to process.

There are several factors that can be modified to help the operators complete their tasks including reasonable temperature, humidity, lighting and noise levels. These issues should be the first to be remedied. Visual inspection can result in fatigue due to the mental load as well as the muscles used to move the eyes and head. Job rotation is recommended to help partially alleviate this situation.

The MFFT has been shown to be useful in determining the cognitive style of a potential operator, and is available to industry to use in making hiring decisions. Since the metalcasting population has a large percentage of people in the slow-inaccurate category, the tool can also be used to identify these individuals for targeted training. This will be hosted on a website at the Steel Founders' Society of America for industry to use.

A key to improving inspection of casting surfaces is to encourage the inspectors to visualize the entire casting surface. One step towards that is to have reasonable expectations on the amount of inspections that need to be completed for a given time period. The field studies showed that the inspectors were not utilizing a consistent search pattern; this too will lead to lack of coverage and reduced inspection performance. Rastering training was shown to improve this situation. Rastering training tools which would be simple to implement are available on the project website to be hosted by the Steel Founders' Society of America. Not only should the rastering training be done as the initial training, it would be useful for retraining operators to help to re-encourage the use of consistent search patterns.

Providing comparator plates to the operators was also shown to improve their ability to make decisions regarding acceptable and unacceptable surfaces. These are inexpensive to produce via art casting supplies, and therefore should be used by each inspector.

Human visual inspection will be needed for the foreseeable future. However, white light scanning is available at a reasonable price point that can be used to improve the human visual inspection process. First, this technology can be used to help communicate the specific casting surface needs between customer and producer. Likewise, this can be used to communicate the requirements within an organization. The existing standards that rely on comparator plates or pictures are extremely difficult to interpret. A standard should be developed based on the non-contact scanning technologies that give a quantitative

assessment of the surface. Such a standard could have limits for maximum deviations or limit certain geometries that negatively affect casting performance.

Team

Frank Peters, Richard Stone, Iowa State University

References

1. Daricilar, G., and F. Peters, "Assessment of Measurement Error for Visual Surface Inspections," *International Journal of Metalcasting*, vol 5, no 3, pp. 7-15, (Summer 2011).
2. Tham K.W. and Willem H. "Room air temperature affects occupants' physiology, perceptions and mental alertness," *Building and Environment*, vol 45, pp. 40-44 (2010).
3. Wright K., J. Hull. and C. Czeisler, "Relationship between alertness, performance, and body temperature in humans,) *American Journal of Physiology*, vol 283, pp. 1370-1377, (2002).
4. Drury, C. G. and J. Watson, J. "Good Practices in Visual Inspection," Final Report for the FAA/Office of Aviation Medicine, (2002).
5. Ericsson, K., and A. Lehmann, "Expert and Exceptional Performance: Evidence of Maximal Adaption to Task Constraints," *Annual Review of Psychology*, vol 47, (1998).
6. Harris, D.H. and F.B. Chaney. *Human Factors in Quality Assurance*, Wiley, New York, (1969).
7. Schwabish, S. D. and C.G. Drury, "The influence of the reflective-impulsive cognitive style on visual inspection," *Human Factors*, vol 26, no 6, pp. 641-647, (1984).
8. Gallwey, T. J., "Selection tests for visual inspection on a multiple fault type task," *Ergonomics*, vol 25, pp. 1077-1092, (1982).
9. Bhatnager, V., C.G. Drury and S.G. Schiro, "Posture, postural discomfort, and performance," *Human Factors*, vol 27, no 2, pp. 189-200, (1985).
10. Drury, C. G. and V. Paquet, "Posture and performance", In N. Delleman, C. Haslegrave and D. Chaffin (eds), *Working Postures and Movements - Tools for Evaluation and Engineering*, New York, Taylor & Francis, (2002).
11. Stone, R. T., "Augmented multisensory interface design: Performance enhancement capabilities and training potential," PhD dissertation. Amherst, N.Y.: State University of New York at Buffalo, (2008).
12. Nickles III, G. M., B.J. Melloy and A.K. Gramopadhye, "A comparison of three levels of training designed to promote systematic search behavior in visual inspection," *International Journal of Industrial Ergonomics*, vol 32, pp. 331-339, (2003).
13. Nalanagula, D., J.S. Greenstein and A.K. Gramopadhye, "Evaluation of the effect of feedforward training displays of search strategy on visual search performance," *International Journal of Industrial Ergonomics*, vol 36, pp. 289-300, (2006).

14. Parkhurst, D., K. Law, and E. Niebur, "Modeling the role of salience in the allocation of overt visual attention," *Vision Research*, vol 42, pp. 107–123, (2002).
15. Vincent, B.T., T. Troscianko and I.D. Gilchrist, "Investigating a space-variant weighted salience account of visual selection," *Vision Research*, vol 47, pp. 1809–1820, (2007).
16. Mannan, S. K., K.H. Ruddock, and D.S. Wooding, "Automatic control of saccadic eye movements made in visual inspection of briefly presented 2-D images," *Spatial Vision*, vol 9, pp. 363– 386, (1995).
17. Mannan, S. K., K.H. Ruddock, and D.S. Wooding, "The relationship between the locations of spatial features and those of fixation made during the visual examination of briefly presented images," *Spatial Vision*, vol 10, pp. 165–188, (1996).
18. Parkhurst, D., and E. Niebur, "Scene context selected by active vision," *Spatial Vision*, vol 16, pp.125– 15, (2003).
19. Rayner, K., "Eye movements and attention in reading, scene perception, and visual search," *The Quarterly Journal of Experimental Psychology*, vol 62, no 8, pp. 1457-1472, (2009).

2. *Development of High Strength PH13-8Mo Alloys: Principal Investigator Dr. Robert C. Voigt, Penn State University*

Research on the development of a high strength, corrosion resistant cast stainless steel based on the wrought alloy PH13-8Mo and on high strength, low alloy steels with lower carbon contents are presented in an effort to improve strength-to-weight ratios of advanced cast steels in weapons systems. Cast PH13-8Mo can achieve high yield strength levels of 190 ksi with a 125% improvement over the widely used CB7Cu grades of material (17-4PH and 15-5PH). In addition, the mechanical properties of conventional and silicon-alloyed high strength low alloy cast steels have been compared to that of cast ES-1 steel (Eglin Steel). Good combinations of strength and low temperature toughness have been achieved for cast ES-1 steels at yield strength levels of 180-190 ksi. These initial trials have led to expanded Army and Air Force study of the performance of ES-1 steels a part of an ongoing ManTech DMS&T focus on cast steel for armor and protection applications.

Objective

The objective of this research was to develop high strength cast steel alloys that can be substituted for titanium castings with no weight penalty. The effort focused on the development of high strength corrosion resistant alloys based on wrought alloy PH13-8Mo and low alloy cast steels with both high strength and good low temperature toughness and include the development of alloy and processing guidelines for casting producers.

Introduction

High strength cast steels, whether high alloy or low alloy steels, are typically used and specified at yield strengths of less than 140 ksi. Higher strength levels are achievable with existing alloys and processing methods, but the corresponding drop in toughness and ductility is of great concern.

Past Penn State studies of corrosion resistant casting alloys focused on improving the strength of the workhorse Cb7Cu corrosion resistant grades of material through effective composition control and improved '+' processing techniques that include hot isostatic pressing (HIP) prior to heat treatment for both homogenization and reductions in micro-porosity [1,2]. It has been demonstrated that Cb7Cu+ composition and processing strategies can reliably be used to achieve yield strength levels of 160 ksi with appropriate heat treatments. Further study of experimental Fe-Cr-Ni-Ti-Mo alloys, based on next generation high strength wrought precipitation hardened stainless steels, have demonstrated that yield strengths of greater than 180 ksi can be achieved. However, more study is needed to fully understand composition and processing techniques for this new alloy system. Another commonly used wrought precipitation hardening stainless steel alloy PH13-8Mo (Fe-Cr-Ni-Mo-Al) can also be expected to achieve higher strength levels than Cb7Cu (17-4PH or 15-5PH) alloys. Initial studies in the late 1980's by an aerospace consortium demonstrated that vacuum-melted PH13-8Mo cast alloys can achieve yield strength levels of 195 ksi [3]. Follow-up studies by Hochanadel et. al. [4-6] characterized the structure/property/processing relationships for this alloy system. These past studies suggest that cast PH13-8Mo+ alloys can be developed with improved performance.

Great potential exists both for defense and commercial applications if affordable ultrahigh strength low alloy (UHSLA) cast steels can be developed with ultrahigh strength and improved impact toughness. The term "ultrahigh strength" steel is typically used to describe wrought steels with yield strengths of 200 ksi (1380MPa) and above. Traditionally high strength steels such as 4340 can achieve these ultrahigh strength levels, but their toughness is low. By lowering carbon contents, adding microalloying elements such as vanadium, and coupling these changes with proper heat treatments, alloys with improved impact properties and fatigue resistance have been developed for wrought alloys. Most of the research and development that has been carried out on UHSLA steels has been completed on wrought steel alloys that rely on thermomechanical processing and premium melting practices to develop desired microstructure and mechanical properties.

Parallel studies on the development of high strength, low alloy cast steels have demonstrated that yield strength levels of 190 ksi can be achieved with excellent low temperature impact toughness for Fe-C-Si-W type cast steels, commonly referred to as Eglin Steel [2]. These lower carbon content steels (<0.3% C) can achieve both high strength and toughness when HIP processed, austenitized at high temperatures and tempered at lower tempering temperatures. It is suggested that small metastable intra-lath carbide phases are responsible for the strength and toughness combinations in these alloys. The role of tungsten and the other alloying elements on the development of properties at low tempering temperatures, if any, has not been carefully studied. However, based on physical metallurgy principles, it is reasonable to expect that other commonly specified cast steels such as 4330, 4130, or 8630 may also achieve exceptional properties when given similar heat treatments.

After solidification, the initial heat treatment step for most high strength steel castings is typically homogenization (normalizing), which is thought to reduce the segregation of alloying elements that exist in the casting after solidification. Homogenization helps to more evenly distribute the alloying elements throughout the microstructure [7]. Higher homogenization temperatures have led to significant improvements in the impact toughness of investment cast silicon modified 4340 steel alloy without affecting the yield strength [2]. These improvements in impact toughness have led to questions regarding micro segregation reduction during homogenization. Other recent studies have reported similar improvements in toughness for other high strength steels due to homogenization [8, 9]. However, the literature is mixed on whether or not higher homogenization temperatures above 1700°F (927°C), are required to improve the impact toughness and possibly even the yield strength of high strength low alloy cast steels. An early study by Eddy and Marcotte [10] concluded that heat treatments employing high temperature homogenization treatments (1650 - 2100°F) (899 - 1149°C) were not effective in materially improving the impact and hardenability properties of high strength low alloy cast steel for thin walled sections. Leger has reported that HSLA cast steels in France are typically homogenized between 1920 and 1980 F (1050 - 1080°C) for the development of the necessary property specifications [9]. Presumably these high homogenization temperatures are needed to more fully solutionize the V and Nb microalloying additions that allow the development of higher strength and toughness in these alloys.

High temperature hot isostatic processing (HIP) of the ultrahigh strength cast alloys is also expected to improve mechanical performance. During HIP, castings are heated to a high temperature (typically in the homogenization temperature range) while they are also exposed to high pressure. HIPing has the ability to remove both micro and macroporosity, helping to improve the impact toughness of ultrahigh strength cast steels [11]. At the same time, during this long time, high temperature treatment, HIP can be expected to also reduce microsegregation. This dual benefit of HIPing suggests that it can replace a homogenization step in the steel casting heat treatment process. Cast UHSLA steels that have been HIPed prior to conventional quench and temper heat treatments have been reported to have properties similar to that of forged alloys [12]. As the HIP technology becomes more economical for metal casters, it is becoming more and more widely used. It is currently being used widely for the production of high integrity non-ferrous investment castings for the defense industry and by ferrous investment casters [13].

A thorough analysis of the effect of homogenization or HIPing on reducing microsegregation in ultrahigh strength low alloy steels has not yet been carried out. Questions remain about how much of the solidification microsegregation can be expected to be removed during high temperature homogenization or HIPing cycles and the resultant improvements in properties that are possible.

Results of on-going studies of both high alloy and low alloy high strength cast steels are reported. An air induction melted cast precipitation hardening stainless steel based on PH13-8Mo has been cast and subjected to various heat treatments. The purpose of this study is to evaluate the strength levels that can be achieved in '+ processed' material. Both microstructure and mechanical properties have been characterized. Also, a series of commercially produced 8630 and 4330 type alloys, with and without silicon additions, have been given '+ processing' heat treatment cycles previously developed for cast Eglin Steels. The results of this initial mechanical property testing are reported. Also a mathematical diffusion model that can be used by foundries to make estimates of the homogenization hold times and temperatures needed to effectively reduce microsegregation of alloying elements in steel castings during homogenization or HIPing thermal cycles has been developed and validated.

Procedures

An initial heat of a cast PH13-8Mo alloy was air induction melted and cast into keel blocks and step block castings with section sizes ranging from 1-4 inches. The heat composition is shown in Table 2-1.

Table 2-1 Composition of cast PH13-8Mo

C	Mn	P	S	Si	Ni	Cr	Mo	V	Nb	Fe
0.12	0.16	0.017	ND	0.25	7.83	12.79	2.28	0.04	0.03	bal

A series of heat treatments were performed to evaluate the influence of HIP processing, homogenization treatment, solutionizing temperature, and aging temperature on the mechanical properties of PH13-8Mo. The heat treatment conditions were selected based on previous studies of cast Cb7Cu+ materials. The heat treatment conditions evaluated in this designed experiment were as follows:

HIP Conditions	1950°F (1066°C), 4 hrs at 15 ksi
Selected:	2125°F (1163°C), 4 hrs at 15 ksi no HIP
Homogenizing Cycles	1950°F (1066°C), 4 hrs, air cool
Selected:	2125°F (1163°C), 4 hrs, air cool no homogenization
Solutionizing Cycles	1900°F (1038°C), 30 min, ice water quench
Selected:	1700°F (927°C), 30 min, ice water quench
Aging Cycles Selected:	1000°F (538°C), 4 hrs, water quench 950°F (510°C), 4 hrs, water quench

The tensile properties and the room temperature impact toughness were measured and the microstructure after heat treatment was characterized. SEM fracture surface characterization and SEM-EDS characterization of fracture surface inclusion was carried out on selected samples.

Commercial heats of common low alloy steels and silicon-alloyed low alloy steels, with a nominal carbon content of 0.3% were produced by SFSA member foundries were also evaluated. The composition of the alloys, and that of a cast Eglin Steel previously studied [2], are shown in Table 2-2.

Table 2-2 Composition of cast low alloys evaluated

Heat	%C	%Mn	%P	%S	%Si	%Ni	%Cr	%Mo	Other
#1 (8630)	0.24	0.80	0.015	0.006	0.41	0.68	0.47	0.26	
#2 (8630+Si)	0.28	0.74	0.009	0.004	1.39	0.59	0.56	0.22	
#3 (4330+Si)	0.27	0.78	0.010	0.004	1.38	1.86	0.86	0.27	
#4 (8630+Si)	0.27	0.82	0.014	0.014	1.20	0.56	0.62	0.22	
#5 (4330+Si)	0.29	0.80	0.015	0.016	1.23	1.88	0.77	0.29	
#6 (8630+Si)	0.31	0.82	0.012	0.007	1.29	0.53	0.52	0.22	
#7 (8630)	0.29	0.82	0.012	0.006	0.45	0.55	0.46	0.22	
#8 (Eglin Steel)	0.27	0.78	0.010	0.002	0.98	1.00	2.59	0.40	0.11 V, 0.98 W

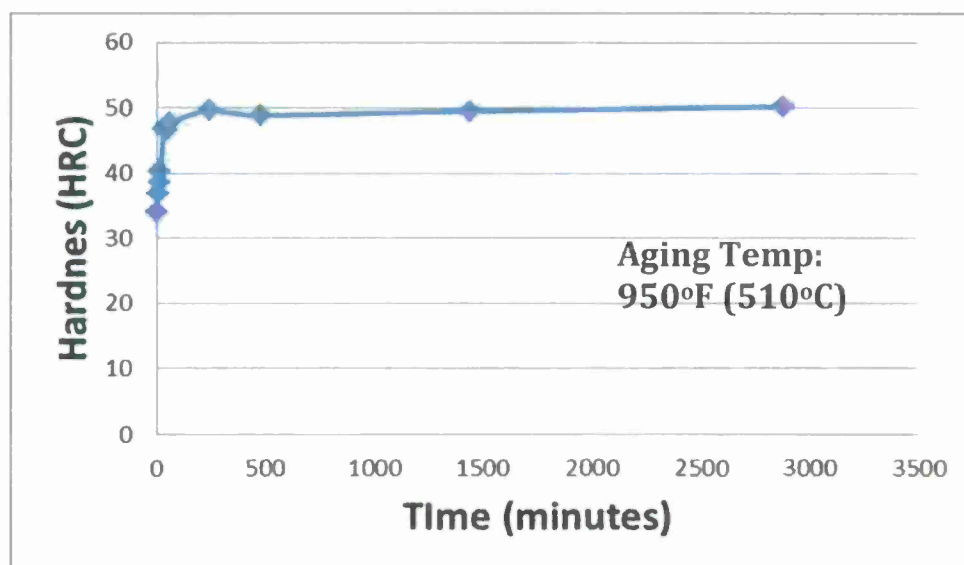
After casting, the same standard heat treatment procedure was carried out for all alloys. All materials were hot isostatic processed and heat treated using heat treatment cycles used in previous studies of cast Eglin Steel [2] as follows:

HIP Condition:	2125°F (1163°C), 4 hrs at 15 ksi
Homogenizing Cycle:	2000°F (1093°C), 2 hrs, air cool
Austenitize:	1900°F (1038°C), 1 hr, water quench
Temper:	375°F (191°C), 4 hrs, water quench

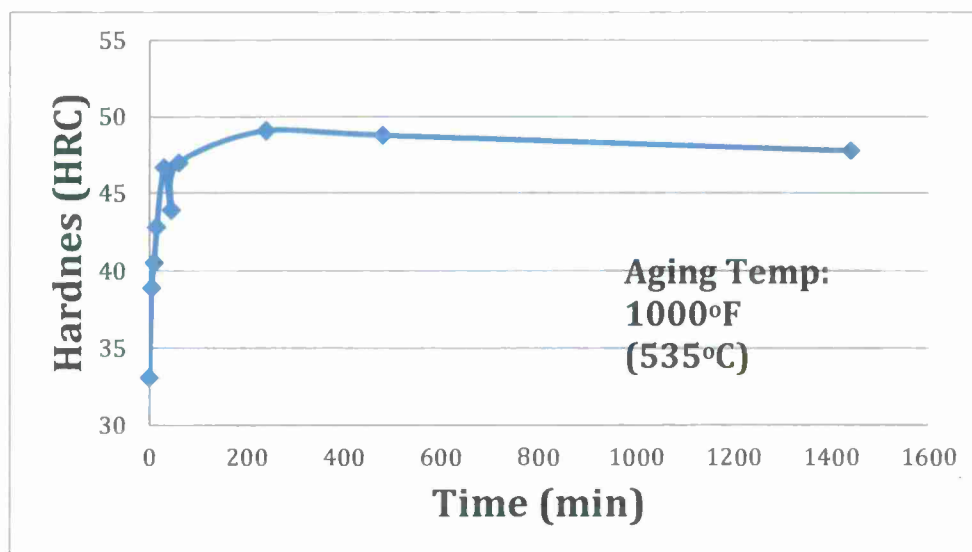
After heat treatment, room temperature tensile properties and -40°F Charpy impact toughness were measured and the microstructures were characterized.

Results/Key Findings

The results of initial aging studies on PH13-8Mo are shown in Figure 2-1. Peak hardness is achieved after 4 hours of aging at both aging temperatures of 950°F (510°C) or 1000°F (538°C).



a) aged at 950°F (510°C)



b) aged at 1000°F (538°C)

Figure 2-1(a-b) Influence of aging time on the hardness of cast PH13-8Mo steel.
a) aged at 950°F (510°C), b) aged at 1000°F (538°C)

The results of tensile and room temperature impact testing for all samples after various heat treatments are shown in Table 2-3. Yield strength levels above 200 ksi were achieved for all heat treatments. Some slight trends in mechanical properties as a function of heat treatment variables were observed. Prior HIP or homogenizing heat treatment resulted in slight improvements in ductility and impact toughness with no changes in hardness or strength. The lower HIP temperature used, 1950°F (1066°C), was sufficient to improve the toughness and ductility of the material. Impact toughness was only slightly higher and ductility was unchanged at higher HIP temperatures. The addition of a homogenization cycle after HIPing resulted in no improvements in properties and could possibly be

eliminated for thinner section size castings (as those evaluated in this study). Variations in aging temperatures of 950-1000°F (510-538°C) had no significant influence on the resultant strength or toughness of PH13-8Mo. It can be expected that higher aging temperatures will result in alloys with lower strength, but improved toughness and ductility.

Table 2-3 Tensile properties and room temperature impact toughness for cast PH13-8Mo after various heat treatments.

HIP	Homogenize	Solution Treatment	Aging	UTS (ksi)	0.2% YS (ksi)	EL (%)	CVN _{RT} (ft-lbs)	HARDNESS (HRC)
HIP 2125°F	N/A	1700°F	1000°F	214	201	7	11	50
HIP 1950°F	N/A	1700°F	1000°F	220	203	10	9	52
N/A	N/A	1700°F	1000°F	219	203	7	4	53
HIP 2125°F	N/A	1700°F	950°F	223	204	6	7	50
HIP 1950°F	N/A	1700°F	950°F	223	202	9	5	52
N/A	N/A	1700°F	950°F	222	200	5	3	53
HIP 2125°F	1950°F	1700°F	950°F	226	204	11	7	52
HIP 1950°F	1950°F	1700°F	950°F	224	202	10	6	48
N/A	1950°F	1700°F	950°F	225	204	10	5	51
HIP 2125°F	2125°F	1700°F	950°F	224	202	9	9	52
HIP 1950°F	2125°F	1700°F	950°F	226	206	3	5	52
N/A	2125°F	1700°F	950°F	219	206	2	4	52
HIP 2125°F	N/A	1900°F	950°F	228	204	8	5	52
HIP 1950°F	N/A	1900°F	950°F	227	202	8	3	52
N/A	N/A	1900°F	950°F	225	200	6	4	52

Figure 2-2 shows the resultant microstructure of selected PH13-8Mo materials in the as-cast and HIPed conditions at low and high magnification. High temperature HIPing treatment can lead to the near elimination of delta ferrite both in the as-cast structure. The morphology of the delta ferrite after HIPing at low temperatures (1950°F) became more globular but did not fully disappear. At the higher HIP temperature (2125°F), the delta ferrite was completely eliminated.



a) 100X, Etched, As Cast



b) 500X, Etched, As Cast



c) 1950°F HIP, 100X



d) 1950°F HIP, 500X



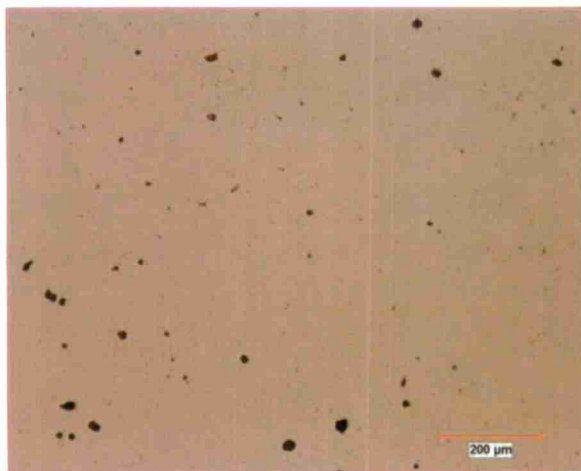
e) 2125°F HIP, 100X



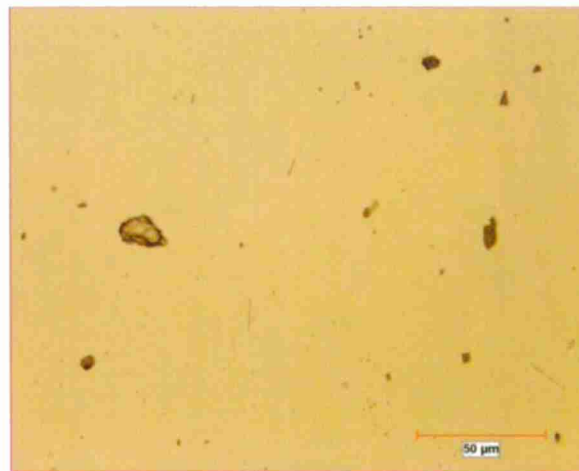
f) 2125°F HIP, 500X

Figure 2-2(a)-(f): As cast vs. HIP microstructure of PH13-8Mo at various magnifications (etched, Fry's Reagent).

Figure 2-3 shows the resultant microstructure of selected PH13-8Mo materials at low and high magnification in the un-etched condition. High levels of inclusions were noted in all samples. An analysis of the resultant fracture surfaces clearly showed that these large 5-25 micron inclusions limited the toughness and ductility of the material. SEM-EDS analysis of the inclusions imaged on micrographs indicates that most of the inclusions were aluminum nitride inclusions, Figure 2-4. Improved air-melting practices can be expected to produce PH13-8Mo alloys with lower, acceptable levels of micro and macro-inclusions.



(a) 2125°F HIP/ 1700°F Sol./1000°F Age, 100X



(b) 2125°F HIP/ 1700°F Sol./1000°F Age, 500X

Figure 2-3(a)-(b) Representative PH13-8Mo microstructures in the unetched condition.



(a) 2125°F HIP/ 1700°F Sol./1000°F Age



(b) 2125°F HIP/ 1700°F Sol./1000°F Age

Figure 2-4(a)-(b): SEM images of cast PH13-8Mo inclusions.

The low ductility and room temperature impact toughness values reported in this study can be expected to be strongly influenced by the high inclusion levels in this heat of material. During tensile testing it was also observed that early fracture at inclusions invalidated the tensile test results from several of the test bars.

The mechanical properties of the various low alloy steels can be compared to that of a cast Eglin Steel (ES-1) given an identical heat treat treatment in Table 2-4. All 4330+, 8630+ and 8630 alloys were either arc melted or induction melted commercial grades of material. However the Eglin Steel material was induction melted, vacuum degassed and ingot cast. All steels had similar tensile and yield strength values. Although the ductility and low temperature toughness of the commercially produced materials did not approach that of

the Eglin Steel, the overall combination of strength and toughness in these materials is very good.

Table 2-4 Tensile and impact properties of cast low alloy steels and a cast Eglin steel (identical heat treatments)

HEAT	UTS (ksi)	0.2% YS (ksi)	EL (%)	CVN ₄₀ (ft-lbs)	HARDNESS (HRC)
#1 8630	228	183	11.5	17	49
#2 8630+Si	238	181	9.5	13	53
#3 4330+Si	241	188	11.5	15	51
#4 8630+Si	259	195	9.5	16	55
#5 4330+Si	267	200	10.5	20	54
#6 8630+Si	260	200	9.5	14	52
#7 8630	247	195	8.5	15	55
Eglin Steel	253	193	15.0	40	49

The specific reasons for the differences observed in the toughness and ductility of the cast Eglin steel compared to the 8360 and 4330 grades of material given identical heat treatments cannot be fully explained without further study. Both the improved cleanliness level of the Eglin steel and its composition designed to respond to low temperature can be expected to have a strong influence on low temperature toughness. The lower levels of tramp and residual elements in the premium melted Eglin Steel alone can certainly be expected to be a major contributor to the improved low temperature toughness of the Eglin Steel compared to the other commercial grade materials [3]. Premium, low residual heats of 8630, 4130, and 4330 type alloys can be expected to have even better low temperature toughness values that may even approach that of Eglin Steel with + processing techniques and appropriate low temperature tempering treatments.

Segregation Mitigation in Steel Castings

Normal segregation of alloying elements during casting solidification can be expected to also degrade the low temperature toughness. A larger amount of thermal activation is required to move substitutional atoms such as W, Mo, Cr, Mo from one lattice site to another when compared to the movement of smaller interstitial atoms such as C. However, limited movement or diffusion of substitutional atoms can be expected during high temperature homogenization, potentially reducing the microsegregation of alloying elements occurring between the dendrite cores and the interdendritic regions resulting from initial solidification. Classical diffusion modeling can be used to estimate the amount of temperature and time required for adequate diffusion of these alloying elements during heat treatment. The initial solidification cooling rate of a casting is also expected to play an important role in the development of the initial segregation profiles in the casting during solidification processing. Heavy section castings solidify at low cooling rates resulting in both coarser dendrite arm spacing and more alloy segregation between the dendrite cores and the interdendritic regions. Thus the required diffusion distances for segregation mitigation are greatly increased in heavy section castings requiring more extensive homogenization or HIP cycles.

Diffusion modeling was used to estimate the extent of micro-segregation reduction (% reduction) of Cr, Mo, Ni, Mn, and W at various secondary dendrite arm spacings (DAS) ranging from 20 to 120 μm for homogenization/HIP temperatures ranging from 1500F - 2200F (816C - 1204C), and homogenization/HIP times ranging from 2 to 6 hours. Appendix 2-A summarizes the development of the diffusion models used to investigate segregation mitigation in steel castings. A summary of the results for different steel casting dendrite arm spacings (DAS) can be seen in Tables 2-5 through 2-9. The initial concentrations of alloying elements in the dendritic and inter-dendritic regions were chosen to be ± 0.5 wt % from given alloy nominal concentrations.

Table 2-5 Summary of tungsten segregation reduction after homogenization at various times, temperatures, and dendrite arm spacings.

Time (min.)	Percent Reduction in W Segregation							
	$(x_0^D = 0.5\text{wt}\%; x_0^{ID} = 1.5\text{wt}\%; x_0 = 1.0\text{wt}\%)$							
	20 μm DAS							
	1500°F	1600°F	1700°F	1800°F	1900°F	2000°F	2100°F	2200°F
	816°C	871°C	927°C	982°C	1038°C	1093°C	1149°C	1204°C
120	< 1%	< 1%	2%	7%	19%	42%	75%	96%
240	< 1%	1%	4%	13%	34%	67%	94%	100%
360	< 1%	2%	6%	19%	46%	81%	98%	100%
Time (min.)	80 μm DAS							
	1500°F	1600°F	1700°F	1800°F	1900°F	2000°F	2100°F	2200°F
	816°C	871°C	927°C	982°C	1038°C	1093°C	1149°C	1204°C
	1500°F	1600°F	1700°F	1800°F	1900°F	2000°F	2100°F	2200°F
120	< 1%	< 1%	< 1%	< 1%	1%	3%	8%	18%
240	< 1%	< 1%	< 1%	< 1%	3%	7%	16%	33%
360	< 1%	< 1%	< 1%	2%	4%	10%	23%	45%
Time (min.)	200 μm DAS							
	1500°F	1600°F	1700°F	1800°F	1900°F	2000°F	2100°F	2200°F
	816°C	871°C	927°C	982°C	1038°C	1093°C	1149°C	1204°C
	1500°F	1600°F	1700°F	1800°F	1900°F	2000°F	2100°F	2200°F
120	< 1%	< 1%	< 1%	< 1%	< 1%	1%	2%	3%
240	< 1%	< 1%	< 1%	< 1%	< 1%	1%	3%	6%
360	< 1%	< 1%	< 1%	< 1%	1%	2%	4%	9%

Table 2-6 Summary of chromium segregation reduction after homogenization at various times, temperatures, and dendrite arm spacings.

Time (min.)	Percent Reduction in Cr Segregation							
	$(x_0^D = 2.09\text{wt}\%; x_0^{ID} = 3.09\text{wt}\%; x_0 = 2.59\text{wt}\%)$							
	20 μm DAS							
	1500°F	1600°F	1700°F	1800°F	1900°F	2000°F	2100°F	2200°F
	816°C	871°C	927°C	982°C	1038°C	1093°C	1149°C	1204°C
120	1%	4%	11%	29%	61%	90%	100%	100%
240	2%	7%	21%	50%	85%	99%	100%	100%
360	3%	10%	30%	65%	94%	100%	100%	100%
Time (min.)	80 μm DAS							
	1500°F	1600°F	1700°F	1800°F	1900°F	2000°F	2100°F	2200°F
	816°C	871°C	927°C	982°C	1038°C	1093°C	1149°C	1204°C
	1500°F	1600°F	1700°F	1800°F	1900°F	2000°F	2100°F	2200°F

	816°C	871°C	927°C	982°C	1038°C	1093°C	1149°C	1204°C
120	< 1%	< 1%	1%	2%	6%	13%	28%	51%
240	< 1%	< 1%	1%	4%	11%	25%	49%	76%
360	< 1%	1%	2%	6%	16%	35%	63%	88%
Time (min.)	200 μ m DAS							
	1500°F	1600°F	1700°F	1800°F	1900°F	2000°F	2100°F	2200°F
	816°C	871°C	927°C	982°C	1038°C	1093°C	1149°C	1204°C
120	< 1%	< 1%	< 1%	< 1%	1%	2%	5%	11%
240	< 1%	< 1%	< 1%	1%	2%	4%	10%	21%
360	< 1%	< 1%	< 1%	1%	3%	7%	15%	29%

Table 2-7 Summary of molybdenum segregation reduction after homogenization at various times, temperatures, and dendrite arm spacings.

Time (min.)	Percent Reduction in Mo Segregation							
	$(x_0^D = 0.00\text{wt\%}; x_0^{ID} = 1.00\text{wt\%}; x_0 = 0.50\text{wt\%})$							
	20 μ m DAS							
	1500°F	1600°F	1700°F	1800°F	1900°F	2000°F	2100°F	2200°F
	816°C	871°C	927°C	982°C	1038°C	1093°C	1149°C	1204°C
120	1%	3%	8%	23%	51%	83%	99%	100%
240	1%	5%	16%	40%	76%	97%	100%	100%
360	2%	8%	23%	54%	88%	100%	100%	100%
Time (min.)	80 μ m DAS							
	1500°F	1600°F	1700°F	1800°F	1900°F	2000°F	2100°F	2200°F
	816°C	871°C	927°C	982°C	1038°C	1093°C	1149°C	1204°C
120	< 1%	< 1%	1%	2%	4%	10%	23%	43%
240	< 1%	< 1%	1%	3%	9%	20%	40%	68%
360	< 1%	< 1%	2%	5%	13%	28%	54%	82%
Time (min.)	200 μ m DAS							
	1500°F	1600°F	1700°F	1800°F	1900°F	2000°F	2100°F	2200°F
	816°C	871°C	927°C	982°C	1038°C	1093°C	1149°C	1204°C
120	< 1%	< 1%	< 1%	< 1%	1%	2%	4%	9%
240	< 1%	< 1%	< 1%	1%	1%	4%	8%	17%
360	< 1%	< 1%	< 1%	1%	2%	5%	12%	24%

Table 2-8 Summary of nickel segregation reduction after homogenization at various times, temperatures, and dendrite arm spacings.

Time (min.)	Percent Reduction in Ni Segregation							
	$(x_0^D = 0.5\text{wt\%}; x_0^{ID} = 1.5\text{wt\%}; x_0 = 1.0\text{wt\%})$							
	20 μ m DAS							
	1500°F	1600°F	1700°F	1800°F	1900°F	2000°F	2100°F	2200°F
	816°C	871°C	927°C	982°C	1038°C	1093°C	1149°C	1204°C
120	< 1%	1%	3%	11%	31%	65%	94%	100%
240	< 1%	2%	7%	21%	52%	87%	100%	100%
360	1%	3%	10%	30%	67%	96%	100%	100%
Time (min.)	80 μ m DAS							

	1500°F	1600°F	1700°F	1800°F	1900°F	2000°F	2100°F	2200°F
	816°C	871°C	927°C	982°C	1038°C	1093°C	1149°C	1204°C
120	< 1%	< 1%	< 1%	< 1%	2%	6%	16%	34%
240	< 1%	< 1%	< 1%	1%	5%	12%	29%	56%
360	< 1%	< 1%	1%	2%	7%	18%	40%	71%
Time (min.)	200 μ m DAS							
	1500°F	1600°F	1700°F	1800°F	1900°F	2000°F	2100°F	2200°F
	816°C	871°C	927°C	982°C	1038°C	1093°C	1149°C	1204°C
120	< 1%	< 1%	< 1%	< 1%	< 1%	1%	3%	6%
240	< 1%	< 1%	< 1%	< 1%	1%	2%	5%	12%
360	< 1%	< 1%	< 1%	< 1%	1%	3%	8%	18%

Table 2-9 Summary of manganese segregation reduction after homogenization at various times, temperatures, and dendrite arm spacings.

Time (min.)	Percent Reduction in Mn Segregation							
	$(x_0^D = 0.28\text{wt\%}; x_0^{ID} = 1.28\text{wt\%}; x_0 = 0.78\text{wt\%})$							
	20 μ m DAS							
	1500°F	1600°F	1700°F	1800°F	1900°F	2000°F	2100°F	2200°F
	816°C	871°C	927°C	982°C	1038°C	1093°C	1149°C	1204°C
120	< 1%	1%	5%	13%	33%	63%	90%	99%
240	1%	3%	9%	25%	55%	86%	99%	100%
360	1%	4%	14%	35%	70%	95%	100%	100%
Time (min.)	80 μ m DAS							
	1500°F	1600°F	1700°F	1800°F	1900°F	2000°F	2100°F	2200°F
	816°C	871°C	927°C	982°C	1038°C	1093°C	1149°C	1204°C
120	< 1%	< 1%	< 1%	1%	2%	6%	13%	27%
240	< 1%	< 1%	1%	2%	5%	12%	25%	47%
360	< 1%	< 1%	1%	3%	7%	17%	35%	61%
Time (min.)	200 μ m DAS							
	1500°F	1600°F	1700°F	1800°F	1900°F	2000°F	2100°F	2200°F
	816°C	871°C	927°C	982°C	1038°C	1093°C	1149°C	1204°C
120	< 1%	< 1%	< 1%	< 1%	< 1%	1%	2%	5%
240	< 1%	< 1%	< 1%	< 1%	1%	2%	5%	10%
360	< 1%	< 1%	< 1%	< 1%	1%	3%	7%	14%

From these tables, it is evident that as casting section size increases and casting cooling rates slow (large DAS), it becomes increasingly more difficult to reduce micro-segregation through heat treatment. This is expected. A typical homogenization treatment for an ultrahigh strength low alloy steel casting is often 60-120 minutes. Out of the five alloying elements studied, tungsten segregation is the most difficult to reduce. At very small DAS of 20 μ m, it would still take 4 hours at 2100°F (1149°C) to achieve a 90%+ reduction in microsegregation for tungsten. For thicker sections, DAS of 80 μ m, it would take 6 hours at 2200°F (1204°C) to achieve just a 45% reduction in W micro-segregation. Even for castings with a smaller section size and faster cooling rate (i.e. DAS of 20-40 μ m), homogenization treatments of 2000°F (1093°C) or above for at least 4 hours are necessary to achieve a 90%+ reduction in alloying element micro-segregation. These estimates also support

Flemings [9] suggestion that very little diffusion of substitutional elements will occur over DAS greater than 200 μm even at heat treatment temperatures exceeding 2200°F (1204°C) for 4 to 6 hours.

To achieve the premium strength and toughness combinations required in UHSLA cast steels, high temperature, long time homogenization heat treatments and/or HIPing at high temperatures is required. This analysis suggests that a high temperature hot isostatic processing treatment could potentially replace a homogenization treatment for UHSLA cast steels as a result of the estimation of microsegregation reduction as a result of the HIP treatment. The Abrahams et al. study on Cr and W alloyed UHSLA cast steels showed evidence of superior impact toughness and yield strength for cast steels when a high temperature HIP treatment was coupled with a high temperature homogenization and austenization step in the heat treatment process [2]. HIP could potentially combine the benefits of removing micro and macroporosity with reducing microsegregation eliminating the homogenization step in the heat treatment process resulting in sound, homogenized castings with improved impact and tensile properties.

A small experimental heat of a silicon modified 4340 cast steel was, heat treated under various conditions to get an indication of the influence of relationship between segregation mitigation and mechanical properties for a high strength cast steel. The composition of the 4340+ heat is given in Table 2-10.

The thermal cycles used during heat treatment were used to determine the corresponding segregation mitigation for the various heat treatments. Figure 2-10 shows the effects of homogenization temperature on the room temperature toughness of a 4340+ cast steel alloy. As the homogenization temperature was increased from 1675°F (913°C) to 1950°F (1066°C), the Charpy impact energy increased while the yield strength and ductility remained relatively unchanged. The full list of mechanical property data can be found in Table 2-11.

Table 2-10 Composition of 4340+ test materials.

4340+ (Investment Cast) (wt%)									
element	C	Cr	Ni	V	Mo	Mn	Si	P	S
	0.450	0.831	1.834	0.100	0.397	0.757	1.628	0.008	0.010

Table 2-11 Heat treatments for 4340+ cast steel.

Homogenization	1675°F (913°C) / 1.0 hr 1800°F (982°C) / 1.0 hr 1950°F (1066°C) / 1.0 hr
Air Cool	Air Cool to Room Temperature
Austenization	1600°F (871°C) / 1.0 hr
Quenching	Water Quench at 74°F
Double Tempering	600°F (316°C), 4 hours Water Quench at 74°F 600°F (316°C), 4 hours Water Quench at 74°F

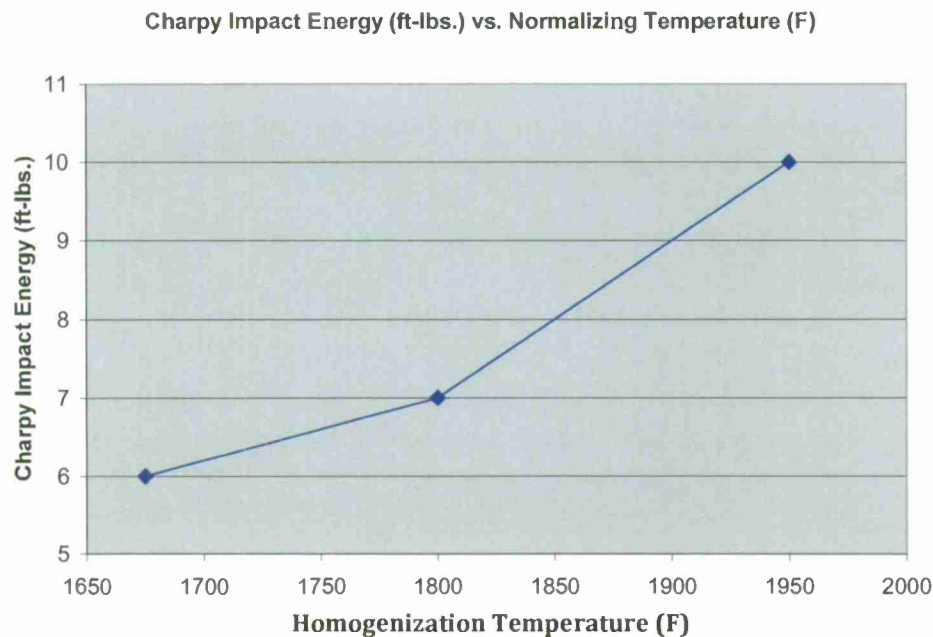


Figure 2-5 The effect of homogenization temperature on the room temperature Charpy impact toughness of the investment cast 4340+ alloy, given individual quench & temper final heat treatments.

Table 2-12 Mechanical Property Data for Investment Cast 4340+ alloy.

Homo. Temp. (°F)	UTS (ksi)	0.2% YS (ksi)	Elong (%)	Energy (ft-lbs)	Hardness (Rc)
1950	297.6	250.3	4	10	50
1800	299.1	251.5	4	7	52
1675	298.9	251.9	5	6	53

Using the diffusion model, the extent of microsegregation reduction (% reduction) was estimated for Cr, Ni, and Mo at small DAS (20, 40 μm) likely for small investment casting section size studied (0.5 in.) at the various homogenization temperatures. The microsegregation reductions are based on the heat treatments outlined in Table 2-11. A summary of the segregation reduction estimates for both DAS can be seen in Table 2-13. The initial concentrations of alloying elements in the dendritic and inter-dendritic regions were chosen to be ± 0.5 wt % from given alloy nominal concentrations.

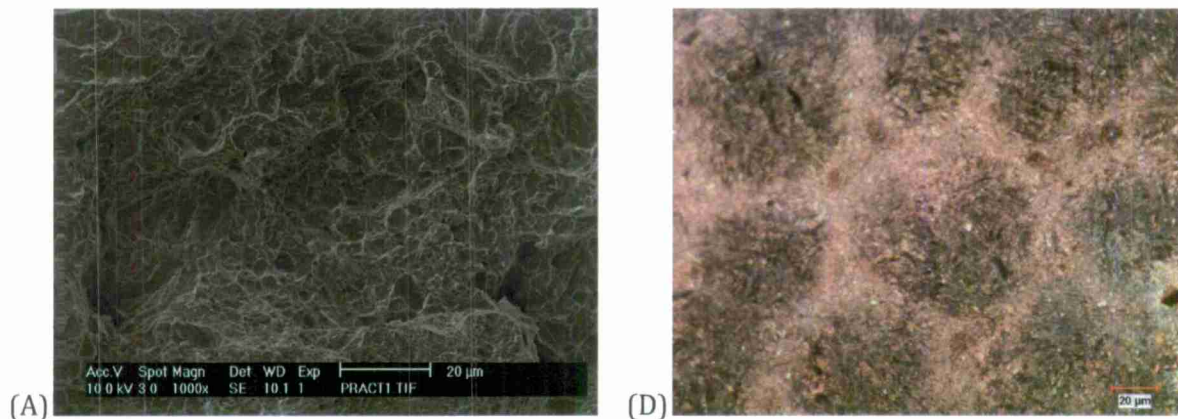
Table 2-13 Estimates of percent reduction in segregation for Cr, Ni, and Mo throughout the heat treatment cycle in Table 2-11 for the investment cast 4340+.

Homogenization Temp. (°F)	Percent Reduction in Segregation								
	Cr: ($x_0^D = 0.33\text{wt}\%$; $x_0^{ID} = 1.33\text{wt}\%$; $x_0 = 0.83\text{wt}\%$)								
	Ni: ($x_0^D = 1.35\text{wt}\%$; $x_0^{ID} = 2.35\text{wt}\%$; $x_0 = 1.85\text{wt}\%$)								
	Mo: ($x_0^D = 0.0\text{wt}\%$; $x_0^{ID} = 1.0\text{wt}\%$; $x_0 = 0.5\text{wt}\%$)								
	20 μm DAS								
	Homogenized			Homo. + Austenitize			Full Heat Treatment		
	Cr	Ni	Mo	Cr	Ni	Mo	Cr	Ni	Mo
1675°F	4%	1%	3%	6%	2%	4%	6%	2%	4%

1800°F	16%	6%	12%	17%	6%	13%	17%	6%	13%
1950°F	53%	23%	43%	53%	23%	44%	53%	23%	44%
Homogenization Temp. (°F)	40 µm DAS								
	Homogenized			Homo. + Austenitize			Full Heat Treatment		
	Cr	Ni	Mo	Cr	Ni	Mo	Cr	Ni	Mo
1675°F	1%	<1%	1%	2%	<1%	1%	2%	<1%	1%
1800°F	4%	1%	3%	5%	2%	4%	5%	2%	4%
1950°F	17%	8%	13%	17%	8%	14%	17%	8%	14%

As shown in Table 2-13, for a DAS of 20 µm, significant differences in microsegregation reduction exist between the three homogenization temperatures for Cr, Ni, and Mo. For Cr, the model estimates that 53% of the microsegregation is removed after homogenization at 1950°F (1066°C) for 1 hour while the percent reductions are estimated to be just 16% and 4% when homogenization is at 1800°F (982°C) and 1675°F (913°C) respectively. For thin section castings with a small DAS, it is likely that higher homogenization temperatures can have significant impact on microsegregation reduction (Table 2-13) and thus impact toughness (Table 2-12). Even at 1950°F (1066°C) for a DAS of 20 µm, the maximum reductions in microsegregation after homogenization are at or below 50% for Cr, Ni, and Mo. In terms of diffusion and percent reduction of substitutional alloying elements, the renewed interest in higher homogenization temperatures for the next generation of ultrahigh strength cast steels makes sense.

The fractographs and etched micrographs of the 4340+ materials are shown below in Figure 2-6. As shown higher homogenization temperatures led to more dimpled rupture and less quasi-cleavage fracture of the cast alloy. Evidence of alloy segregation on the polished and etched microstructures is still evident after high temperature homogenization. But less segregation is clearly observed after high temperature homogenization.



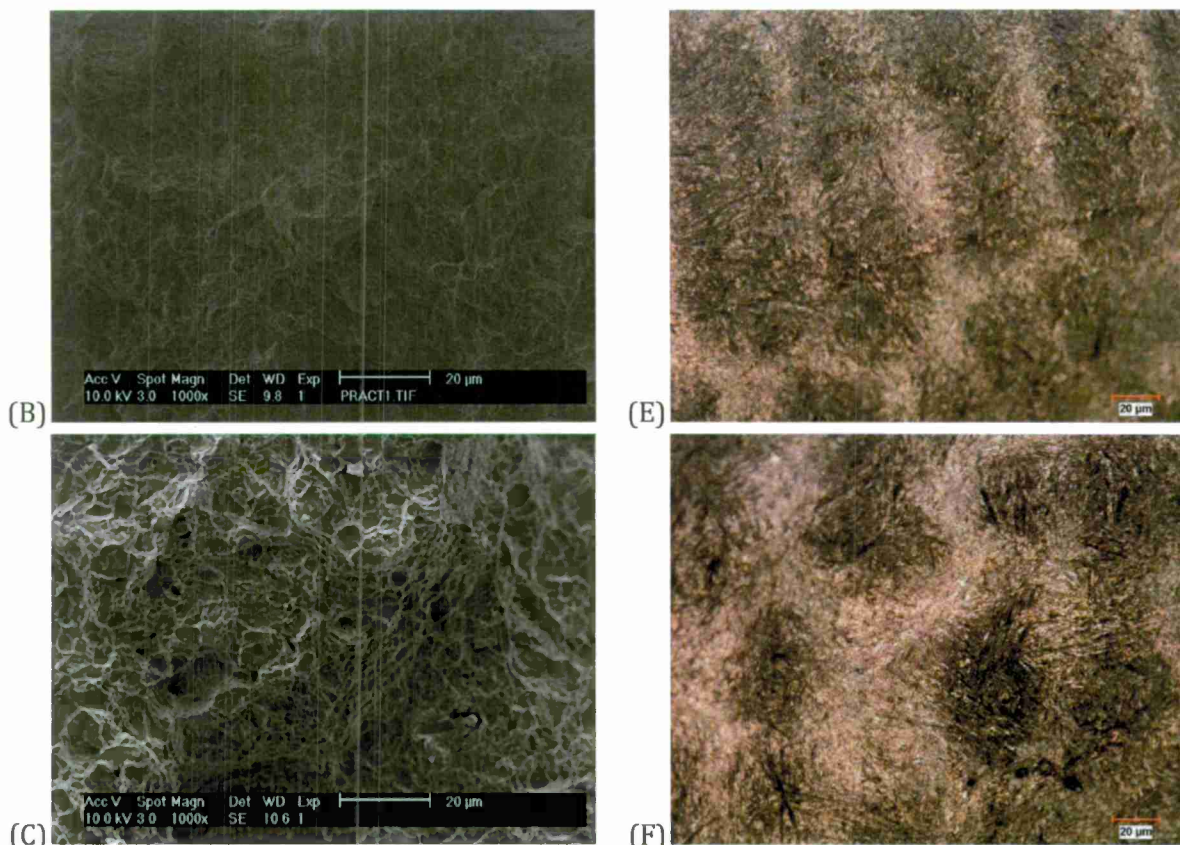


Figure 2-6 Fracture surface images from the SEM for the investment cast 4340+ alloy homogenized at (A) 1675F(913°C), (B) 1800F(982°C), and (C) 1950F(1066°C). Micrographs in the etched condition for the investment cast 4340+ alloy homogenized at (D) 1675F(913°C), (E) 1800F(982°C), and (F) 1950F(1066°C).

Transition

Throughout the program, industry and government research partners have participated directly in the research effort. In addition, research results have been presented at industry and government forums, including SFSA Technical & Operating Conferences and SFSA Research Review Committee Meetings. Of particular note, in Spring 2012 an Eglin Steel Workshop was jointly sponsored by Penn State University and the Army Research Lab at which more than 30 researchers from all branches of DoD and industry were in attendance. Many of the workshop participants are now directly involved in an ongoing ManTech DMS&T effort focused on cast steel for armor and protection applications (Kyu Cho, Army Research Lab, Principal Investigator).

Conclusions and Recommendations

Initial study of cast PH13-8Mo has shown that these alloys, when processed with HIPing or high temperature homogenization prior to conventional heat treatment, can achieve yield strength levels approaching 200 ksi. This is a significant improvement compared to the higher strength levels than the widely used CB7Cu grades of material (160 ksi yield strength) and HIP processed CB7Cu+ (170 ksi yield strength). Additional work is needed to further understand composition/microstructure/property/processing relationships for

this new alloy system and to further understand melt processing and pouring practices for this high aluminum content alloy so that casting quality can be assured.

Cast Eglin Steel and other widely used and silicon-modified conventional grades of cast low alloy steels have been observed to have an excellent combination of strength and low temperature toughness. HIP processing of these lower carbon content steels ($<0.30\%C$) tempered at low temperatures results in a superior low temperature impact toughness at high strength levels. These combination of properties compare favorably to the more widely specified $0.4\%C$ low alloy steels that are commonly heat treated at tempering temperatures greater than $1000^{\circ}F$ ($538^{\circ}C$). The improved performance of the premium melted, tungsten alloyed Eglin Steel also suggests that further improvements in the low temperature toughness of premium processed 8630, 4130 and 4330 type cast steels is possible.

A successful model has been developed to provide estimates of percent reduction of microsegregation of alloying elements between the dendritic and inter-dendritic sections of steel castings at different temperatures and times. Casting section size and cooling rate directly influence the amount of segregation reduction possible during HIP or homogenization of steel castings. The segregation reduction is proportional to the DAS of cast steels.

Model estimates show that little, if any diffusion of substitution alloying elements will occur during the homogenization of steel castings with $DAS \geq 200 \mu m$ regardless of the homogenization temperature. The model presented demonstrates the importance of higher homogenization temperatures in particular for UHSLA steel castings containing significant amounts of substitutional alloying elements. Segregation modeling has shown that it is only above $2000^{\circ}F$ ($1093^{\circ}C$) that a significant amount of microsegregation reduction of substitutional alloying elements can be achieved. High temperature ($>2000^{\circ}F$ ($1093^{\circ}C$)) HIP cycles as well as high temperature homogenization cycles have been shown to improve the impact toughness and ductility of UHSLA cast steels.

Diffusion modeling suggests that high temperature HIP cycle should also significantly reduce the microsegregation of substitutional alloying elements and can replace the homogenization step in the heat treatment of UHSLA cast steels. HIP processing provides both micro and macro porosity reduction and microsegregation reduction benefits. The initial HIP or homogenization step during the heat treatment of cast steels is critical to reducing microsegregation. Very little, if any reduction in segregation occurs during subsequent austenization and tempering steps in a conventional heat treatment.

Team

Robert C. Voigt, Penn State University

Bibliography

[1] Abrahams, R. A. and R. C. Voigt, "Physical Metallurgy and Processing of Cb7Cu", Proceedings, 2008 SFSA T&O Conference, Chicago IL, 19 pages [2008].

- [2] Abrahams, R., P. Lynch and R. Voigt, "Processing and Composition of High Strength Cast Steels", Proceedings, 2009 SFSA Technical & Operating Conference, Chicago IL, 29 pages [2009].
- [3] "Steel Casting, Vacuum Melted, Vacuum Cast, Investment, Corrosion Resistant 13Cr - 8.0Ni - 2.2Mo - 1.1Al", SAE Aerospace Material Specification AMS 5412 [Jul 1990, reaffirmed Sep 2007].
- [4] Cieslak, M. J., C. R. Hills, P. F. Hlava and S. A. David, "An investigation of the High-Temperature and Solidification Microstructures of PH 13-8 Mo Stainless Steel", Metallurgical Transactions A: Vol. 21A, pp.2465-2475 [Sept 1990].
- [5] Hochanadel, P. W., C. V. Robino, G. R. Edwards and M. J. Cieslak, "Heat Treatment of Investment Cast PH 13-8 Mo Stainless Steel: Part I. Mechanical Properties and Microstructure", Metallurgical and Materials Transactions A: Vol. 25A, pp. 789-798 [Apr 1994].
- [6] Robino, C. V., P. W. Hochanadel, G. R. Edwards and M. J. Cieslak, "Heat Treatment of Investment Cast PH 13-8 Mo Stainless Steel: Part II. Isothermal Aging Kinetics", Metallurgical and Materials Transactions A: Vol. 25A, pp. 697-704 [Apr 1994].
- [7] Fredriksson, H. and Akerlind, U., "Heat Treatment and Plastic Forming," *Materials Processing During Casting*, John Wiley & Sons, Ltd., England, 2006, pp. 227-251.
- [8] Lebeau, C., "Production and Control of HSLA Steel Castings," *AFS Transactions*, Volume 92, Paper 84-47P, 1984, pp. 645-654.
- [9] Leger, M.T., "Characterization of HSLA Cast Steel 12 MDV6-M Influence of Wall Thickness and Heat Treatment," *Proceedings of 1st International Steel Foundry Conference, sponsored by SFSA*, Chicago, IL, Nov. 11-13, 1985, pp. 145-162.
- [10] Eddy, C.T. and Marcotte, R.J., "Determination of the Effect of Homogenization on the Hardenability and Impact Strength of Cast Steels," *Final Report on Research Project No. 11*, Steel Founders' Society of America, 1947.
- [11] Atkinson, H.V. and Davies, S., "Fundamental Aspects of Hot Isostatic Pressing: An Overview," *Metallurgical and Materials Transactions*, December 2000, Volume 31A, 12, pp. 2981-3000.
- [12] Fredriksson, H. and Akerlind, U., "Heat Treatment and Plastic Forming," *Materials Processing During Casting*, John Wiley & Sons, Ltd., England, 2006, pp. 227-251.
- [13] Barre', C., "HIP Increasingly Used for Upgrading of Castings as Process Becomes More Economical," *International News Magazine of the Investment Casting institute*, August 1998, pp. 14-15, Dallas, TX.
- [14] Flemings, M.G., *Solidification Processing*, McGraw-Hill, USA. 1974.
- [15] Askeland, D.R., *The Science and Engineering of Materials*, Brooks/Cole Engineering Division, Monterey, CA: 1984.
- [16] Campbell, J., *The New Metallurgy of Cast Metal Castings*, Butterworth-Heinemann, Jordan Hill, Oxford: Second Edition, 2003.
- [17] Reill, W., Hoffman, H., Röhl, K., "Interdiffusion in amorphous FeB multilayer thin films," *Journal of Materials Science Letters* 4, 1985, pp. 359-362.

- [18] Röhl, K., Reill, W., "A Study of Interdiffusion in Multilayer Cu/Ni Thin Films by Auger Electron Depth Profiling", *Thin Solid Films*, Vol 89, 1982, pp. 221-224.
- [19] Fredriksson, H., Åkerlind, U., *Materials Processing During Casting*, John Wiley & Sons Ltd, West Sussex, England: 2006.
- [20] Krishtal, M.A., and Mokrova, A.M., "Mobility of Atoms of Alloyed Elements in Austenite", *Metallovedenie i Termicheskaya Obrabotka Metallov*, No. 5, May 1966, pp. 2-5.
- [21] Nohara, K., and Hirano, K., *Journal of Japanese Industrial Metals*, Vol. 40, 1976, pg. 1053.
- [22] Parke, H., *Trans. ASM*, Vol. 31 (4), 1943, pg. 877.
- [23] Alberly, P.J., and Haworth, C.W. "Interdiffusion of Cr, Mo, and W in Iron", *Journal of Metal Science*, Vol. 8, 1974, pp. 407-412.
- [24] Růžičková, J., Million, B., Kučera, J., *Kovové Materials*, Vol. 19, 1981, pg. 3.
- [24] Gruzin, P.L., *In Coll: Problems of Metal Science and Physics of Metals*, No. 4, 1955.
- [26] Krishtal, M.A., *Fiz. Metal. I Metalloved.*, Vol. 14, No. 2, 1966.
- [27] Umanskii, Y.A., Finkel'shtein, B.N., Blanter, M.E., *Physical Metal Science*, Metallurgizdat, 1955.
- [28] Kupalov, I., and Zemskii, S.V., "Diffusion of Tungsten in Austenite In High-Speed Steels", *Metallovedenie i Termicheskaya Obrabotka Metallov*, No. 2, Feb. 1968, pp. 10-12.
- [29] Nohara, K., and Hirano, K., *Trans. Iron Steel Inst. Jpn. (Suppl.)*, Vol. 11, 1971, pg. 1267.
- [30] Hoshino, A., and Araki, T., *Trans. Nat. Res. Inst. Metals*, Vol. 13, 1971, pg. 99.
- [31] Wells, C., and Mehl, R., *Metals Technology*, Jan. 1941.
- [32] Bowen, A., and Leak, G., *Metall. Trans.*, Vol. 1, 1970, pg. 1695.
- [33] Grigorev, G., and Pavlinov, L. *Fiz. Met. Metalloved.*, Vol. 25, 1968, pg. 377.
- [34] Smith, A., "The Diffusion of Chromium in Type 316 Stainless Steel", *Journal of Metal Science*, Vol. 9, 1975, pp. 375-378.
- [35] MacEwan, J., and Yaffe, L. *Can. J. Chem.*, Vol. 37, 1959, pg. 1629.
- [36] Adda and Philibert, J., *La Diffusion dans les Solides Vol. II*, Presses Université de France, Paris, 1966, pg. 893.
- [37] Badia, M., Vignes, A., *Acta Metall.*, Vol. 17, 1969, pg. 177.
- [38] Hirano, K., Agarwala, R.P., Averbach, B.L., and Cohen, E., *J. Appl. Phys.*, Vol. 33, 1962, pg. 3049.
- [39] Wells, C., and Mehl, R. - *Metals Technology*, Feb. 1941.
- [40] Borg, R.J., and Lai, D., *Acta Met.*, Vol. 11, 1963, pg. 861.
- [41] Lippard, H., *et al*, "Microsegregation Behavior during Solidification and Homogenization of AerMet100 Steel" *Metallurgical and Materials Transaction B*, Vol. 29B, Feb. 1998 pp. 205-210.

APPENDIX 2-A Diffusion Model Development

Much of the casting segregation modeling that is still ongoing today is an extension of the pioneering work by Flemings and co-workers in the 1960s [14]. The literature cites many models for estimating diffusion during homogenization, all of which are based upon Fick's Laws. Fick's Second Law describes dynamic or non-steady state diffusion and is the basis for many diffusion models. In three dimensions, Fick's second law can be stated as:

$$(1) \quad \frac{\partial c}{\partial t} = D \left(\frac{\partial^2 c}{\partial^2 x^2} + \frac{\partial^2 c}{\partial^2 y^2} + \frac{\partial^2 c}{\partial^2 z^2} \right) \quad \text{Eq.A1}$$

where c is concentration, and D is the diffusion coefficient.

Solutions of this expression depend on the specific boundary conditions. Askeland [15] suggests one solution to Fick's Second Law which permits the calculation of the concentration profile for one diffusing species into another. The equation allows simple calculation of the concentration profile for one element diffusing into another in a direction normal to the diffusion plane. This solution is dependent upon the diffusion coefficient (D) remaining constant regardless of concentration [15] can be expressed as:

$$(1) \quad \frac{c_x - c_m}{c_1 - c_m} = \text{erf} \left(\frac{x}{2\sqrt{Dt}} \right) \quad \text{Eq.A2}$$

where c_1 is the concentration of atom A in material 1, c_m is the average concentration of element A in materials 1 and 2, and c_x is the concentration of element A in material 2 at a distance x from the original interface after time t . D is the diffusion coefficient of element A in material 2 at a specific temperature [15].

A simplified and useful solution to Fick's Diffusion Equation is given by:

$$(1) \quad x \approx \sqrt{Dt} \quad \text{Eq.A3}$$

where again, x is the diffusion distance, t is the time and D is the diffusion coefficient of the element of interest in austenite. The effect of temperature on the diffusion coefficient can be expressed by the Arrhenius equation:

$$(1) \quad D = D_0 * \exp \left(\frac{-Q}{RT} \right) \quad \text{Eq.A4}$$

where Q is the activation energy (usually kJ/mole), R is the universal gas constant, T is the absolute temperature (K) and D_0 is the diffusivity coefficient.

Smaller activation energies increase the diffusion coefficient (D) because less thermal energy is required to overcome the energy barrier for atom movement. Based on Eq.A4, it becomes apparent that as the heat treatment temperature increases, the diffusion constant and flux of atoms increases as well. At higher temperatures, the thermal energy supplied to the diffusing atoms permits the atoms to overcome the activation energy barrier and more easily move to new lattice sites [15].

For simple diffusion in single-phase alloys, Flemings [14] describes a simple and elegant model of the micro-segregation present in the dendrites. He defines a useful parameter called the index of residual micro-segregation, δ , as:

$$(1) \quad \delta = \frac{C_M - C_m}{C_M^0 - C_m^0} \quad \text{Eq.A5}$$

where C_M = the maximum solute concentration of the element in inter-dendritic spaces at time t and C_m = the minimum solute concentration of element in the center of the dendrite arm at time t . concentration element in the center of the dendrite arm (both at time zero) [14].

After any thermal cycle resulting in diffusion, δ will have some intermediate value between zero (0%) and one (100%) [16]. If homogenization is sufficient to completely remove solidification segregation, then $\delta = 0$.

Assuming a sinusoidal distribution of the concentration of the element across the dendrite, Flemings [14] describes the appropriate solution for the index of residual micro-segregation as:

$$(1) \quad \delta = \exp(-\pi^2 D t / l_0^2) \quad \text{Eq.A6}$$

where D is the diffusivity constant, t is time and l_0 is half of the secondary dendrite arm spacing.

This equation is very useful for approximating the times and temperatures required to homogenize a given cast structure [16]. Flemings demonstrates that carbon is completely homogenized by the time low-alloy steel reaches 900°C (1652 °F) for any typical casting dendrite arm spacing. However, significantly longer times and higher temperatures are expected to be necessary to mitigate the segregation of other alloying elements. Flemings reports that steel homogenization treatments for steels 1100°C (2012°F) can be expected to achieve only the homogenization of carbon.

For the common substitutional elements of concern in steel (Ni, Mn, Cr, Mo), little homogenization has been reported to occur below 1100°C (2012 °F) [9]. Flemings theorizes that at secondary dendrite arm spacings (DAS) $\geq 200 \mu\text{m}$, practically no homogenization can be achieved ($\delta \geq 0.9$) even at homogenization temperatures greater than 1300°C (2372°F) for one hour. However, the diffusion models used by Flemings and co-workers use simple diffusion boundary conditions that do not fully capture the segregation profiles in actual castings.

Reill et al. [17] describe a more detailed method to model the concentration profiles during the inter-diffusion in amorphous thin films. This paper details a unique technique, compared to other complex diffusion methods previously described, because it allows for a periodically modulated composition distribution instead of a single concentration step [17, 18]. Possibly even more useful is the similarity between thin solid film boundary conditions and the as-cast dendritic structure. By assuming one thin film to be the dendrite structure and the second thin film to be the neighboring inter-dendritic material, the same initial boundary conditions applied by Reill et al. can be satisfied when considering casting segregation.

In multilayer thin films, with a composition changing periodically in a direction normal to the film plane, the diffusion equation can be solved by a Fourier series expansion [17].

Assuming a constant diffusion coefficient, D , the concentration profile of element (a) is given by:

$$(1) \quad C_a(z, t) = \alpha + \sum_m \beta_m \exp[-(\pi/H)^2 m^2 Dt] * \sin(m\pi z/H) \quad \text{Eq.A7}$$

where H is the layer thickness, $2H$ is the length of periodicity, t is the diffusion time, and z is the coordinate normal to the film plane.

The Fourier coefficients α and β_m describe the initial concentration profile at time $t = 0$ prior to diffusion. During inter-diffusion, the exponential functions with $m > 1$ decay very fast with time. Assuming an initially square wave concentration distribution at $t = 0$, the contribution of the terms with $m > 1$ becomes very small for typical diffusion times where $(\pi/H)^2 Dt \geq 0.3$ [17]. Therefore, for most practical cases only the first term of the series expansion from Eq.A7 is important. In a dendritic structure, the inter-diffusion from heat treatments eventually leads to a sinusoidal concentration distribution given by the first term in the series expansion of equation A7. However, the solution of this diffusion expression requires a periodical concentration distribution at $t = 0$ prior to diffusion. The amplitude of this resultant sinusoidal distribution, ΔC_a , can be expressed by:

$$(1) \quad \Delta C_a = \beta_1 * \exp[-(\pi/H)^2 Dt] \quad \text{Eq.A8}$$

Fredriksson and Åkerlind [19] provide a similar expression to that of Eq.A7, which can be used to model dendritic segregation. They state that while the initial concentration distribution is much more complicated than a simple sine wave segregation assumption, it is possible to use either a rectangular or a sine wave approximation. This is because after a short diffusion time, only the fundamental tone of the concentration remains, independent of the initial shape, as explained by Fredriksson's solution to Fick's Second Law for Homogenization [19]. Therefore, prior to homogenization, the alloy concentration (x) as a function of an arbitrary distance y can be written as:

$$(1) \quad x = x_0 + \left(\frac{x_0^M - x_0^m}{2} \right) * \sin\left(\frac{2\pi y}{\lambda_{prim}} \right) \quad \text{Eq.A9}$$

where, x_0 is the average concentration throughout the material. The wavelength (λ) of the sine wave for the first Fourier component (considered the fundamental tone) is equal to the secondary dendrite spacing. x_0^M is the maximum concentration, which from the discussion on segregation, is found in the inter-dendritic material. x_0^m is then the minimum concentration, found in the center of the dendrite core.

This initial concentration then has an amplitude before heat treatment given by:

$$(1) \quad \text{Amplitude} = \left(\frac{x_0^M - x_0^m}{2} \right) \quad \text{Eq.A10}$$

Solving the partial differential in Eq.A1 and combining it with Eq.A9, it is possible to determine the concentration profile for the fundamental wave after homogenization. This final solution can be expressed as [19]:

$$(1) \quad x = x_0 + \left(\frac{x_0^M - x_0^m}{2} \right) * \exp \left(-\frac{4\pi D}{\lambda_{prim}^2} \right) \sin \left(\frac{2\pi y}{\lambda_{prim}} \right) \quad \text{Eq.A11}$$

where again, x_0 is the average concentration throughout the material. x_0^M is the maximum concentration, and x_0^m is then the minimum concentration. λ_{prim} is considered here to be the secondary dendrite arm spacing (DAS).

This solution describes what happens to each alloy component independently of the others. It also shows that an arbitrary sine-shaped concentration profile will keep its sine shape while its amplitude decreases with time, as suggested by Fredriksson [19].

This solution can be verified by differentiating equation Eq.11 twice with respect to y and once with respect to time [14]. Comparing Eq. A11 to Eq. A7 it becomes apparent that $\alpha = x_0$ and $\beta_m = \left(\frac{x_0^M - x_0^m}{2} \right)$ for the case of initial concentration over a dendritic structure. Because of this direct agreement between equations Eq. A7 and Eq.A11, it stands to reason that with the selection of correct diffusivity coefficients (D_0), it is possible to accurately model the concentration profile of segregated alloying elements during heat treatment.

Estimation of Diffusivity Coefficients (D_0) and Activation Energies (Q)

The accuracy of segregation diffusion modeling depends strongly on estimates of the diffusion coefficient (D_0) and the activation energy (Q) for each alloying element in steel. Study of the literature indicates that large differences exist in the diffusion parameter estimates for diffusivity coefficients and activation energies for the various alloying elements in iron. Tables 2-A1 through 2-A6 summarize the results of a literature search for diffusivity coefficients (D_0) and activation energies (Q) of common alloying elements within an austenitic (γ) iron matrix.

Table 2-A1 Diffusion data for molybdenum in austenitic (γ) iron and iron based alloys.

D_0 (cm ² /sec)	Q (kJ/mole)	Material	Reference
0.043	255.224	Fe	[20]
25.1	323.7	Fe	[21]
0.0684	246.85	Fe	[22]
0.0358	239.8	Fe	[23]
20.4	313.8	Fe-Cr-Mn-Ti-Mo	[20]

Table 2-A2 Diffusion data for tungsten in austenitic (γ) iron and austenitic iron based alloys.

D_0 (cm ² /sec)	Q (kJ/mole)	Material	Reference
0.13	267.4	Fe	[24]
0.509	272	Fe	[25]
4400	376.56	Fe	[26]
460	338.9	Fe	[27]
--	261.5	Fe	[28]
0.6	267.357	R9K10 Tool Steel	[29]
13	313.8	U8 Tool Steel	[25]
49	310	R9 Tool Steel	[30]

Table 2-A3 Diffusion data for manganese in austenitic (γ) iron and austenitic iron based alloys.

D_0 (cm ² /sec)	Q (kJ/mole)	Material	Reference
0.038	246.85	Fe	[20]
0.16	261.7	Fe	[29],[30]
0.019	240.8	Fe	[29]
0.486	277.8	Fe	[31]
0.23	271.96	Fe+Cr	[20]

Table 2-A4 Diffusion data for chromium in austenitic (γ) iron and in austenitic iron based alloys.

D_0 (cm ² /sec)	Q (kJ/mole)	Material	Reference
0.0624	252.3	Fe	[23]
10.8	291.8	Fe	[32],[33]
0.063	243	Stainless Steel	[34]

Table 2-A5 Diffusion data for nickel in austenitic (γ) iron and in austenitic iron based alloys.

D_0 (cm ² /sec)	Q (kJ/mole)	Material	Reference
6.92	324.9	Fe	[35]
4.1	267.76	Fe	[36]
3.0	314	Fe	[37],[38]
0.344	282.42	Fe	[39]
0.77	280.5	Fe	[40]

The differences in diffusivity coefficients and activation energies appear to be quite large under initial mutual examination. These discrepancies may be due to both techniques used for parameter estimation (diffusion couples [37], electroplating [24], thin films [37] and dried solutions [32]) and differences in data quality and data analysis methods. Choosing the best diffusivity coefficient and activation energy values for the steel casting segregation modeling is extremely important because D , the diffusion constant, above is dependent on both D_0 and Q estimates. To get a better idea of the impact that diffusivity coefficients and activation energy estimates reported in the literature have on the diffusivity of these alloying elements in steel, the diffusion constant (D) was plotted for each element over homogenization temperature range of interest for the various alloying elements, Figures 2-A1 through 2-A5.

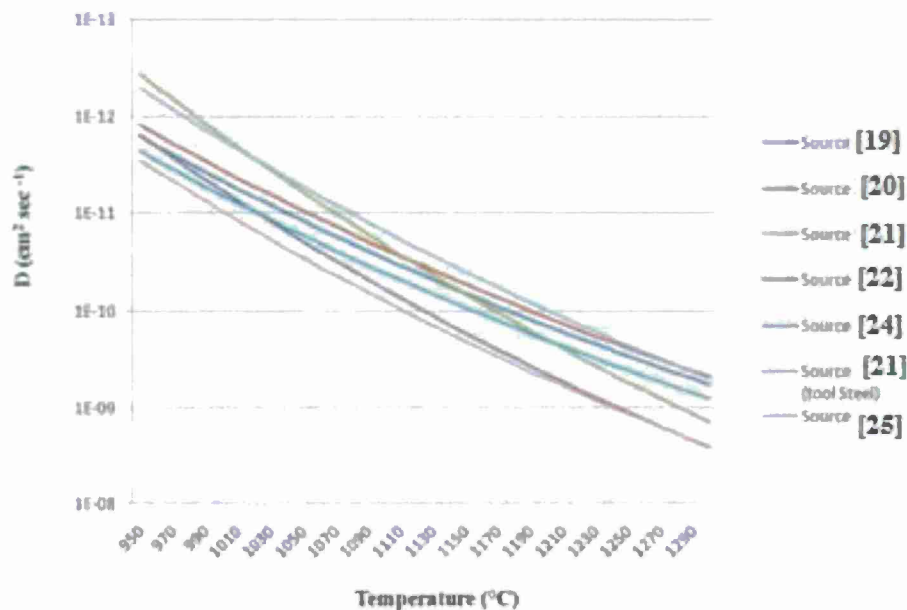


Figure 2-A1 Comparison of the temperature dependence of the diffusion constant (D) for different estimates of diffusivity coefficients (D0) and activation energy (Q) for tungsten diffusion in FCC iron.

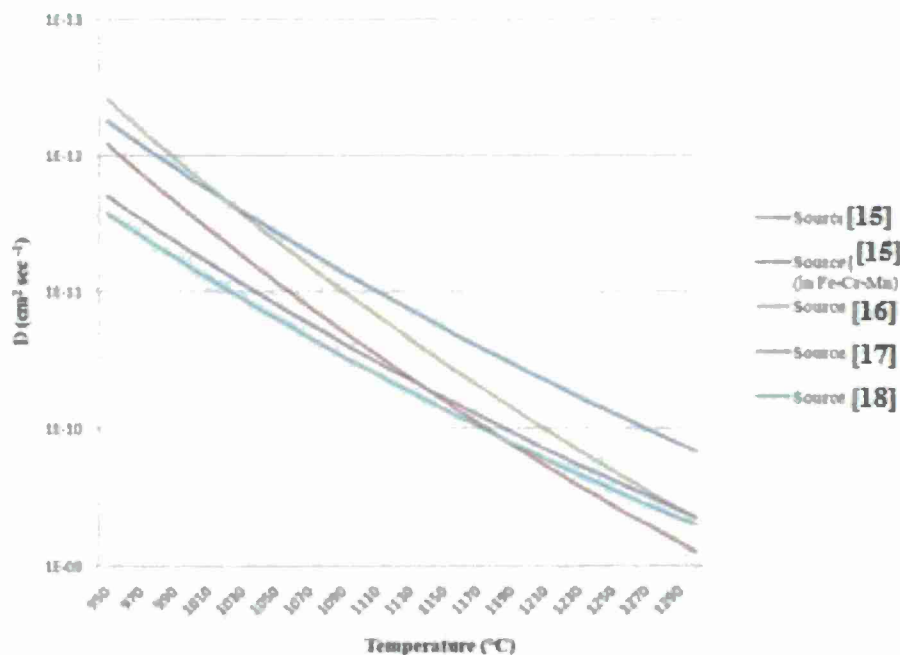


Figure 2-A2 Comparison of the temperature dependence of the diffusivity constant (D) for different estimates of diffusivity coefficients (D0) and activation energy (Q) for molybdenum diffusion in FCC iron.

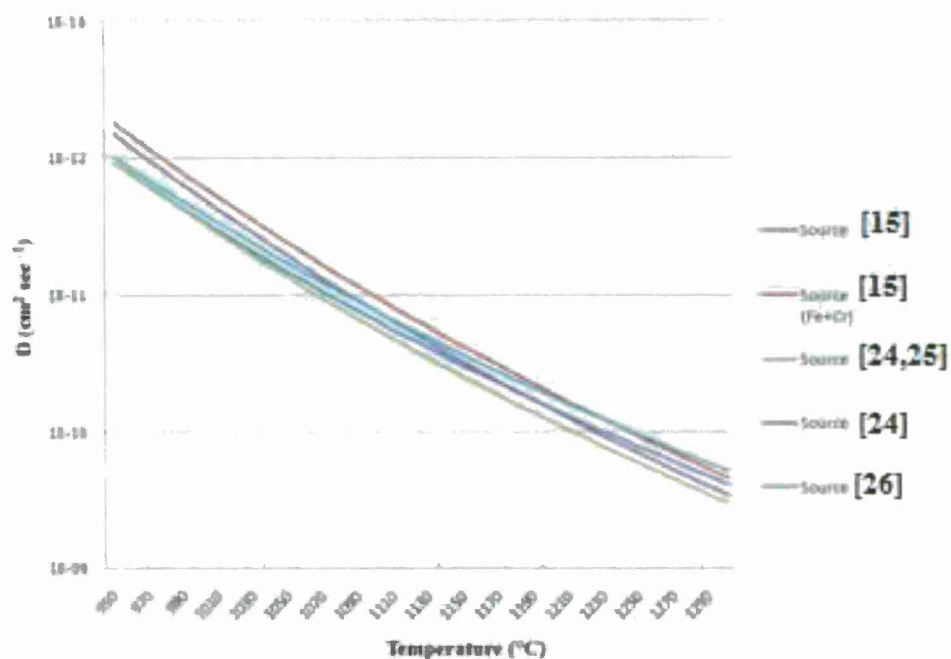


Figure 2-A3 Comparison of the temperature dependence of the diffusivity constant (D) for different estimates of diffusivity coefficients (D_0) and activation energy (Q) for manganese diffusion in FCC iron.

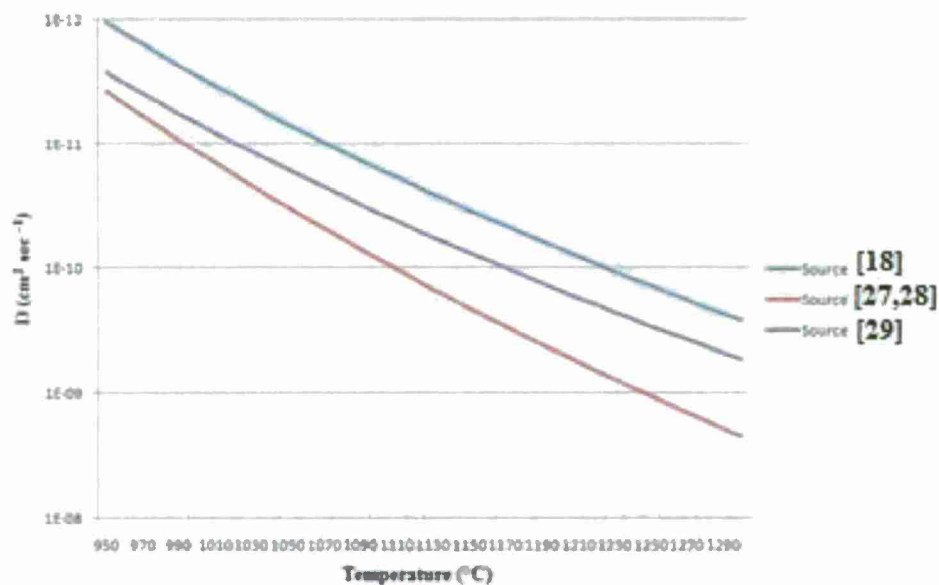


Figure 2-A4 Comparison of the temperature dependence of the diffusivity constant (D) for different estimates of diffusivity coefficients (D_0) and activation energy (Q) for chromium in FCC iron.

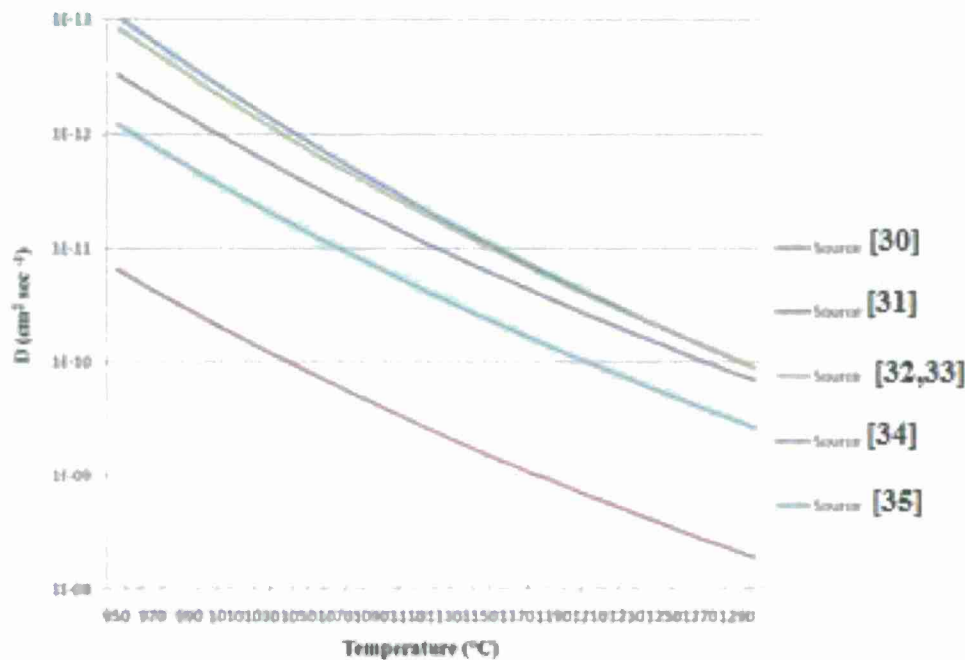


Figure 2-A5 Comparison of the temperature dependence of the diffusivity constant (D) for different estimates of diffusivity coefficients (D₀) and activation energy (Q) for nickel in FCC iron.

Even though D₀ and Q values reported in the literature varied greatly from study to study, the variation in the resultant diffusivity constant (D) estimates in the range of interest was much smaller. For this segregation analysis, best values for the diffusivity coefficient and activation energy for each of the elements were chosen by selecting the most representative plot from each of the figures. Table 2-A6 below shows the diffusivity coefficients and activation energies that were selected for use in the diffusion models estimate reductions in microsegregation during heat treatment in this study.

Table 2-A6 Diffusivity coefficients (D₀) and activation energies (Q) chosen to be used in the diffusion model to estimate the diffusivity constant (D).

Element (in γ-Fe)	D ₀ (cm ² /sec)	Q (kJ/mole)	Reference
Mo	0.0684	246.85	[22]
W	0.13	267.4	[24]
Mn	0.038	246.85	[20]
Ni	0.063	243	[34]
Cr	0.77	280.5	[40]

Model Implementation

Using Microsoft Excel, a simple model to estimate the reduction in microsegregation throughout a steel heat treatment cycle was constructed. The diffusion coefficient (Eq. 4) can be expressed as:

$$D = D_0 * \exp\left(\frac{-Q}{kT}\right) \quad \text{Eq.A4}$$

where:

D_0 = diffusivity constant (cm^2/sec)

Q = activation energy per particle (eV)

T = temperature (K)

k = Boltzmann constant $8.614\text{E-}5$ (eVK^{-1}) [used in place of R for pure particles]

Individual values for the diffusivity constant (D_0) and activation energy (Q) for the elements W, Cr, Mo, Ni, and Mn were evaluated. The model could be adapted in the future to include additional alloying elements. The temperature (T) and time (t) for common heat treatment cycles and cycles for high strength steel castings could readily be input.

The second part of the Excel model consisted of coding the profile for the fundamental wave after heat treatment. The model (Eq.A12) is a combination of Eq. (A7) & (A11):

$$C_a(z, t) = \alpha + \sum_m \beta_m \exp[-(\pi/H)^2 m^2 D t] * \sin(m\pi z/H) \quad \text{Eq.A7}$$

$$x = x_0 + \left(\frac{x_0^M - x_0^m}{2} \right) * \exp\left(-\frac{4\pi D}{\lambda_{prim}^2}\right) \sin\left(\frac{2\pi y}{\lambda_{prim}}\right) \quad \text{Eq.A11}$$

$$x = \left(\frac{x_0^D + x_0^{ID}}{2} \right) + \left(\frac{x_0^{ID} - x_0^D}{2} \right) * \exp\left[-\left(\frac{\pi}{(\lambda_{prim}/2)}\right)^2 * D * t * 60\right] * \sin\left(\frac{\pi y}{(\lambda_{prim}/2)}\right) \quad \text{Eq.A12}$$

where:

x_0^D = initial concentration of alloying element in the dendrite

x_0^{ID} = initial concentration of alloying element in the inter-dendritic region

λ_{prim} = secondary dendrite arm spacing (microns)

D = the diffusivity constant from Eq. A 7 at the temperature (T) in Eq. A7

t = the time (in minutes) spent at the temperature (T) in Eq. A7

y = the location (arbitrary distance) at which the concentration is determined (microns)

For the modeling results described in this paper, the initial concentrations of alloying elements in the dendritic and inter-dendritic regions were chosen to be +/- 0.5 wt % from given alloy nominal concentrations in most cases. It was made based on the typical range of interdendritic segregation expected for low alloy steels in the literature. This initial segregation assumption can be relaxed for future experimentation. The expected micro segregation profile in castings depends not only on the partition ratio of the specific alloying element, but also on the solidification cooling rate which controls the secondary dendrite arm spacing (DAS). Representative DAS values were used in this analysis ranging from $80\mu\text{m}$ to $200\mu\text{m}$ representative of the DAS expected for thin section and heavy section steel castings respectively [41].

The model was developed to estimate overall diffusion effects from multiple steps in a heat treatment cycle (e.g. HIP + homogenization + austenization + tempering). This multi stage model can be expressed as:

$$Z = \sum_{i=1}^n D_i t_i \quad \text{Eq.A13}$$

Implemented into Eq. (A12), overall diffusion distance, z from multiple heat treatment (diffusion) cycles can be expressed as:

$$Z = (D_1 * t_1 + D_2 * t_2 + \dots + D_n * t_n) \quad \text{Eq.A13}$$

3. Verification of New Radiographic Testing (RT) Standard through Mechanical Testing: Principal Investigator Dr. John Griffin, University of Alabama at Birmingham

Steel castings are currently radiographically graded by comparing the radiographic appearance of selected areas of interest to reference radiographs. Commonly used steel casting radiographic standards include ASTM E446, E186, and E280. These standards have reference radiographs graded from 1 to 5 with 1 having no indications and 5 having numerous indications. The standards have three graded categories (shrink porosity, gas porosity, and slag/sand) with shrink porosity having four subcategories.

While these standards have been used for decades and are well known by designers, they have a number of deficiencies. These deficiencies include non-linearity in the graded images (a grade 3 image may not be significantly worse than grade 2), significant variation in inspector interpretation (reproducibility between inspectors is low), and proration of the reference image to larger or smaller areas of interest in the part. The biggest deficiency however is the lack of any relationship to the performance of the part. Current standards are workmanship standards.

A new standard of radiographic acceptance criteria for steel castings has been proposed by Steel Founders' Society of America and The University of Iowa. This standard uses the sum of radiographic indication lengths along a specified direction of interest divided by a specified feature length in that direction to calculate a maximum indication fraction. The indication is assumed to extend thru thickness so the design yield strength or stiffness is reduced proportional to the maximum indication fraction i.e. a maximum indication fraction of 30% reduces the design yield strength by 30%. This proposed standard eliminates the need for proration and interpretation of the film. The indication shape or type is also not needed. The standard allows designers to specify acceptance criteria useful in predicting part performance in service.

The objective of this project was to produce, radiograph, and test cast steel tensile specimens and verify that the maximum indication fraction/stiffness/yield stress relationship is safe and conservative. The cast steels tested will cover a range of yield strengths from 35 to 165 ksi and the tensile specimens will contain a variety of maximum indication fractions.

Four cast steel grades were selected by the SFSA steering committee for evaluation. These grades included three carbon and low alloy steels (70/40, 110/80, and 165/135) and one high alloy steel (CF8). The three C&LA steels provide a wide range of yield strengths of 40 to 135 ksi. The 110/80 and 165/135 steels are actually the same chemistry but with different heat treatments. The high alloy CF8 was added to provide a steel with tensile properties similar to 70/40 but with a different microstructure and modulus. A 36"l x 8"w x 1"t test plate was designed to provide material to produce the number of necessary test specimens. The plate was underfed to produce centerline shrink porosity.

Three SFSA member steel foundries agreed to produce all four alloy grades at the require strength level. Some flexibility in timing was needed to wait for the alloy grade to be specified in a commercial order since the amount of molten metal needed to cast the test plate is too small for a special order. This caused some delay in the delivery of test plates to UAB. Once the castings were received, 3/16 inches of steel were removed from the cope

and drag to produce a 5/8 inch thick plate from the centerline as shown in Figure 3-1. The machined plates were marked to designate the strength level and the location and orientation of the tensile blanks along the plate length. The blanks were oriented so that any centerline shrinkage was restricted to the gauge section. The tensile blanks were sawcut from each plate producing approximately 34 tensile blanks per strength level. The number of tensile blanks per alloy varied because some of the blanks from under the riser contained significant shrinkage from the riser pipe. These blanks were discarded. The remaining blanks were then machined to final dimensions as per ASTM A370/E8 sheet type standard specimen (Figure 3-2).

The tensile specimens were baked at 300°C (575°F) for 24 hours to remove any trace of hydrogen from the samples before testing. Each tensile specimen was radiographed through two directions following ASTM Method E1030. The film radiographs were digitized to allow image analysis software to measure indication length, for presentation purposes and to allow future work on automating the rating process. An example of the digitized radiographs for some of the CF8 tensile specimens is shown in Figure 3-3.

Specific grip wedges for the tensile design used in this project were purchased and received from MTS. UAB's MTS tensile machine is an 810 load frame with hydraulic grips rated at 50 kips. Before testing, MTS certified the LVDT, 50 kip load cell, and 2" extensometers were in working order and within manufacturer's tolerances. The load train was aligned to class 5 (50 μ in max) using the MTS 709 alignment system. The MTS was reconfigured with appropriate grips and calibrated extensometers to test the 8" long tensile specimens.

Initially, several tensile bars were tested and the results reported to the foundry producing the plate. The tensile properties recorded matched the expected results for that alloy, verifying the setup and procedure. A total of 131 tensile specimens were tested from the four steel alloys (70/40, 110/80, 165/135, and CF8). The time/load/strain data was digitally recorded for each specimen. The crosshead speed was varied during each test: 0.04 in/min up to the yield point and 0.20 in/min to failure. These crosshead speeds provide loading rates within the range required by ASTM E08. Figure 3-4 illustrates example stress-strain curves for 10 tensile specimens removed from the 110/80 steel test plate. A standard set of tensile measurements were made on the specimens tested at UAB and placed into a spreadsheet for each alloy. These measurements include 0.2% offset yield strength, ultimate strength, elongation, elastic modulus, total strain at maximum stress, reduction in area, and total strain at failure. Elastic modulus was calculated using linear regression. Graphical methods introduced more data scatter compared to linear regression. Tables 3-1 through 3-4 list the tensile property data for the four cast alloys.

Indications from the digitized radiographs were identified and measured for length in a direction perpendicular to the loading direction. A PowerPoint presentation was produced for each alloy group. This presentation showed for each tensile specimen both radiographic images (with any indications found labeled), a macrograph of the fractured tensile specimen, a table listing the tensile properties and indication lengths.

Figure 3-5 illustrates two tested tensile specimens from the 110/80 steel group. The slides shows radiographs of the specimen from two directions, the broken tensile specimen, the

tensile properties, and the indication lengths if any were observed. The indications were marked on the radiograph. All four presentations were sent to SFSA for review.

Graphs have been produced plotting the effective yield stress and stiffness ratio versus the maximum radiographic indication length. The proposed acceptance criterion with the five grade levels was superimposed over each plot. Figures 3-6 through 3-9 illustrate these graphs for each alloy tested. These plots demonstrate that the proposed acceptance criterion is acceptable and in fact conservative. This was the final deliverable for this task.

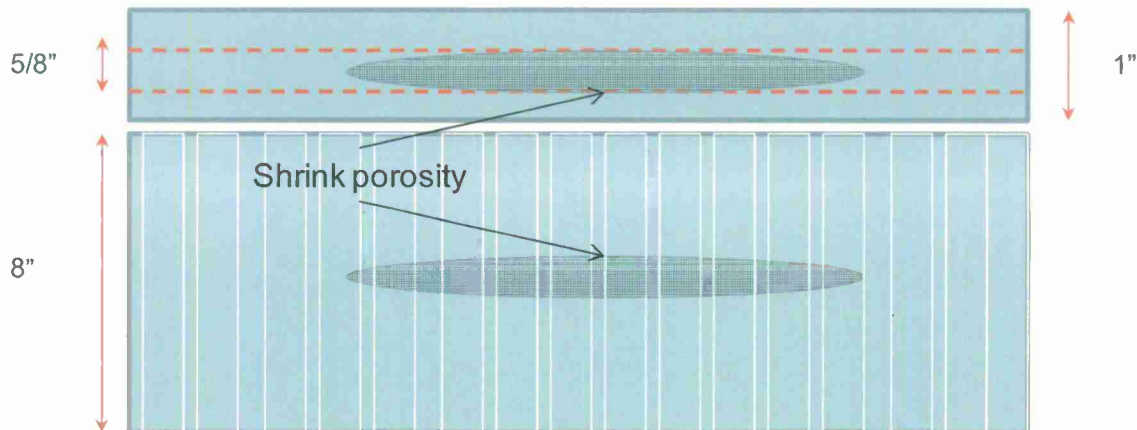


Figure 3-1 Design of 36"l x 8"w x 1"t test plate and approximate location of centerline shrink porosity.

ASTM E 8 - 04

	Dimensions		
	Plate-Type, 1½-in. Wide in.	Standard Specimens Sheet-Type, ½-in. Wide in.	Subsize Specimen ¼-in. Wide in.
G—Gage length (Note 1 and Note 2)	8.00 ± 0.01	2.000 ± 0.005	1.000 ± 0.003
W—Width (Note 3 and Note 4)	1½ + ¼, - ¼	0.500 ± 0.010	0.250 ± 0.005
T—Thickness (Note 5)		thickness of material	
R—Radius of fillet, min (Note 6)	1	½	¼
L—Over-all length, (Note 2, Note 7 and Note 8)	18	8	4
A—Length of reduced section, min	9	2¼	1¼
B—Length of grip section, (Note 8)	3	2	1¼
C—Width of grip section, approximate (Note 4 and Note 9)	2	¾	¾

Figure 3-2 Design of 2" gauge section tensile specimen as per ASTM E08.

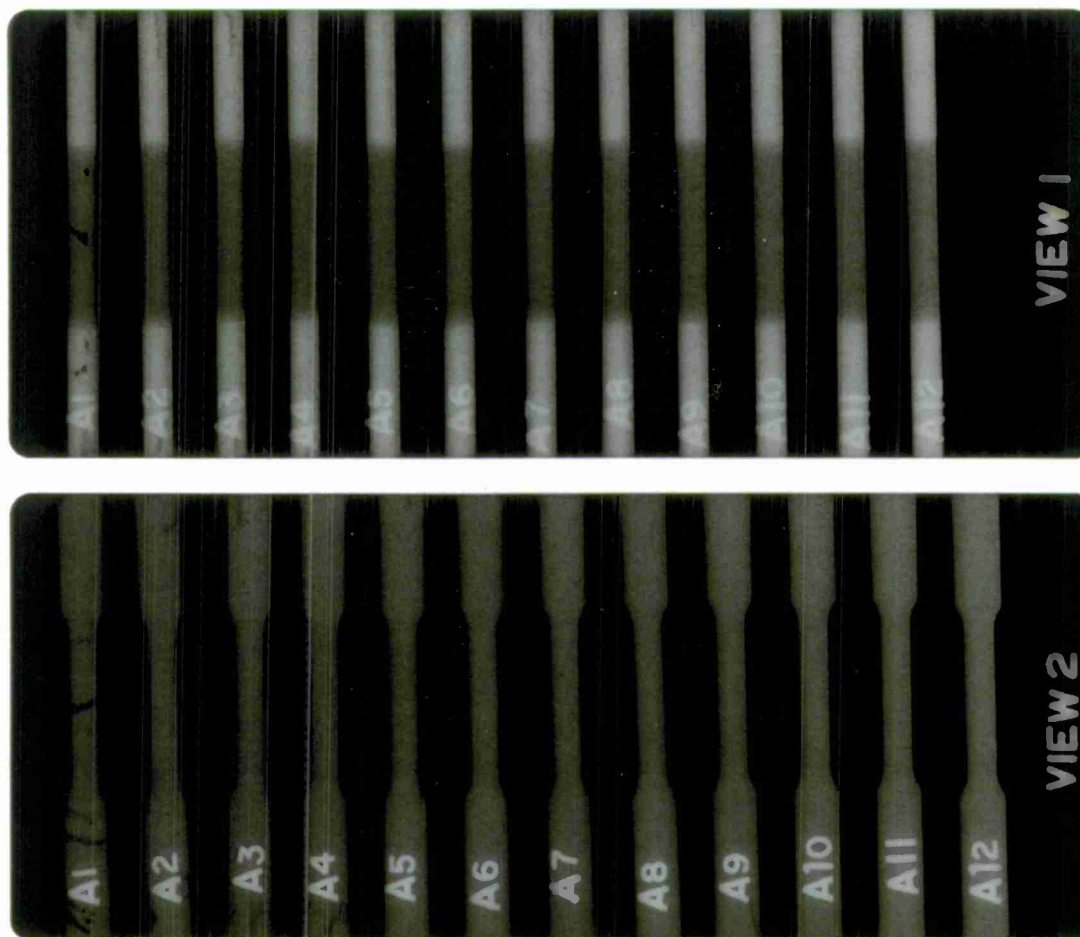


Figure 3-3 Radiograph of 12 CF8 tensile specimens.

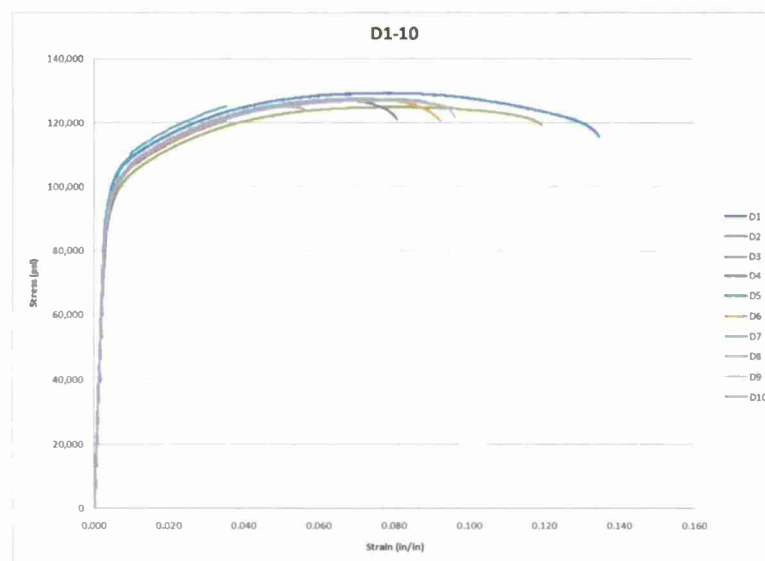


Figure 3-4 Stress-strain curves from 10 tensile specimens removed from the 110/80 steel test plate.

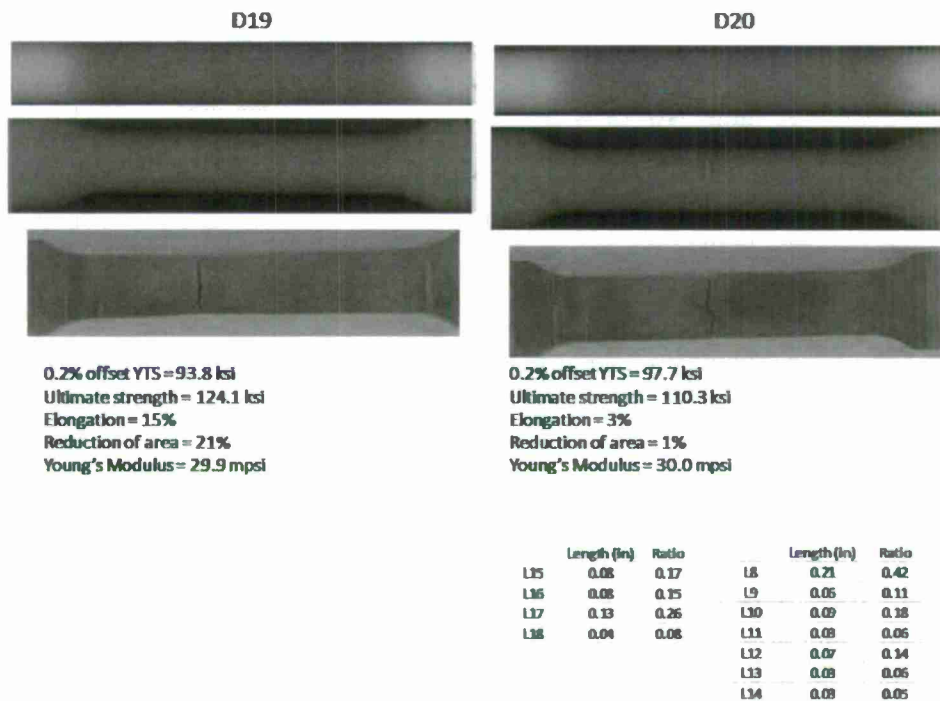


Figure 3-5 Radiographic and tensile property results for two specimens removed from the 110/80 steel test plate.

Table 3-1 Tensile property data for CF8 specimens.

Alloy	Specimen	% Elongation	% C/S Reduction	Elastic Modulus (psi)	0.2% Yield Strength (psi)	UTS(psi)
CF8	A1	19.0	27.0	22,900,000	30,600	61,575
CF8	A2	37.5	28.5	24,200,000	32,100	78,334
CF8	A3	32.5	30.0	N/A	N/A	74,229
CF8	A4	31.3	29.7	25,400,000	32,000	74,495
CF8	A5	35.0	29.8	26,300,000	32,000	74,090
CF8	A6	32.5	26.8	22,140,000	30,400	68,565
CF8	A7	30.0	26.2	22,660,000	31,600	73,096
CF8	A8	28.5	29.0	24,130,000	31,000	70,032
CF8	A9	35.0	25.8	24,080,000	31,400	76,393
CF8	A10	31.7	28.9	25,090,000	31,300	75,713
CF8	A11	31.0	24.8	26,080,000	32,000	74,780
CF8	A12	35.0	29.9	28,260,000	33,000	78,595
CF8	A13	38.5	30.6	27,000,000	32,500	77,737
CF8	A14	41.0	25.4	26,980,000	31,600	77,330
CF8	A15	25.0	15.2	23,960,000	29,900	59,104
CF8	A16	25.0	21.9	26,800,000	31,900	65,685
CF8	A17	29.5	24.0	23,710,000	31,600	68,816
CF8	A18	36.0	27.1	24,090,000	30,600	71,709
CF8	A19	30.0	32.0	27,500,000	32,600	74,653
CF8	A20	31.5	26.8	26,140,000	31,600	74,061
CF8	A21	37.5	32.4	26,280,000	31,800	76,757
CF8	A22	35.0	27.8	27,550,000	32,000	75,110
CF8	A23	30.0	28.2	29,140,000	32,700	71,827
CF8	A24	34.5	26.3	26,030,000	32,800	74,271
CF8	A25	45.0	33.8	27,110,000	31,000	76,690
CF8	A27	36.0	35.4	28,650,000	31,300	72,904
CF8	A28	45.0	37.5	23,910,000	30,300	71,848
CF8	A29	47.5	43.9	20,690,000	28,700	65,534
CF8	A30	22.5	27.0	26,950,000	31,800	54,895
CF8	A31	37.5	46.0	19,640,000	28,800	61,888
CF8	A32	41.0	35.0	25,010,000	31,000	68,290
CF8	A33	45.0	38.3	26,240,000	31,400	71,541
CF8	A34	35.5	29.9	24,210,000	31,500	73,326
CF8	A35	35.0	26.2	23,480,000	31,000	N/A
CF8	A36	29.5	23.4	25,110,000	31,600	N/A

Table 3-2 Tensile property data for 70/40 specimens.

Alloy	Specimen	% Elongation	% C/S Reduction	Elastic Modulus (psi)	0.2% Yield Strength (psi)	UTS (psi)
70/40	B1	32.5	46.3	30,770,000	48,700	81,283
70/40	B2	29.0	34.2	29,930,000	48,150	80,870
70/40	B3	13.0	22.7	29,510,000	46,500	75,896
70/40	B4	12.5	19.5	29,100,000	46,400	74,524
70/40	B5	12.0	21.4	28,980,000	44,600	68,781
70/40	B6	12.5	16.3	29,140,000	44,500	73,520
70/40	B7	10.0	15.4	29,130,000	44,800	72,998
70/40	B8	14.0	21.9	28,590,000	44,300	74,174
70/40	B9	15.0	17.1	29,330,000	44,500	74,259
70/40	B10	15.0	19.8	28,980,000	43,900	73,058
70/40	B11	10.0	13.1	29,000,000	43,000	68,240
70/40	B12	10.5	11.6	28,380,000	43,900	72,116
70/40	B13	10.0	11.1	28,830,000	44,700	69,378
70/40	B14	12.5	18.8	29,700,000	45,600	74,016
70/40	B15	10.5	16.5	28,550,000	44,500	69,200
70/40	B16	12.5	20.8	29,270,000	44,300	68,213
70/40	B17	10.5	17.0	29,010,000	43,000	67,286
70/40	B18	7.5	17.2	29,050,000	44,300	69,712
70/40	B19	8.0	13.9	27,240,000	38,500	58,790
70/40	B20	10.0	10.3	25,120,000	38,000	60,882
70/40	B21	12.5	16.7	28,520,000	42,700	69,260
70/40	B22	15.0	21.7	28,340,000	44,700	73,361
70/40	B23	10.0	10.9	29,590,000	44,300	68,950
70/40	B24	8.0	13.5	27,810,000	42,400	65,437
70/40	B25	N/A	N/A	29,070,000	45,700	66,786
70/40	B26	8.5	9.2	26,250,000	41,600	61,636
70/40	B27	7.0	9.4	28,330,000	40,200	57,238
70/40	B28	12.5	13.3	29,410,000	44,600	74,194
70/40	B29	29.4	46.9	29,900,000	40,700	70,633
70/40	B30	32.5	47.6	29,810,000	43,200	74,441
70/40	B31	32.0	45.4	30,840,000	46,000	78,313
70/40	B32	32.0	41.5	30,350,000	46,100	78,429
70/40	B33	31.0	45.4	30,120,000	45,400	78,446
70/40	B34	31.0	44.6	30,370,000	45,800	78,528
70/40	B35	31.5	49.5	30,460,000	46,000	78,885
70/40	B36	32.5	49.4	30,130,000	48,800	80,816

Table 3-3 Tensile property data for 110/80 specimens.

Alloy	Specimen	% Elongation	% C/S Reduction	Elastic Modulus (psi)	0.2% Yield Strength (psi)	UTS (psi)
110/80	D1	11.6	25.0	30,360,000	100,977	129,189
110/80	D2	4.0	3.4	30,390,000	98,342	98,342
110/80	D3	12.5	15.8	29,670,000	95,500	124,868
110/80	D4	9.5	10.2	27,910,000	98,500	126,700
110/80	D5		N/A	32,890,000	101,000	125,079
110/80	D6	10.6	13.3	31,700,000	99,300	127,228
110/80	D7	11.5	7.2	31,200,000	99,800	127,442
110/80	D8	7.0	6.4	31,050,000	99,200	124,947
110/80	D9	12.0	11.6	30,840,000	98,000	126,846
110/80	D10	11.5	10.0	31,470,000	98,300	127,320
110/80	D11	10.3	13.5	31,200,000	99,500	128,632
110/80	D12	13.5	20.5	30,110,000	98,400	128,121
110/80	D13	12.5	17.3	30,890,000	97,600	126,797
110/80	D14	14.0	16.4	30,440,000	96,200	125,632
110/80	D15	15.0	26.2	30,890,000	94,700	124,470
110/80	D16	12.5	17.9	31,510,000	94,000	123,906
110/80	D17	11.5	12.7	30,460,000	93,000	122,672
110/80	D18	10.0	20.7	30,570,000	94,000	123,034
110/80	D19	14.5	20.8	29,890,000	93,800	124,062
110/80	D20	2.5	1.3	30,000,000	97,700	110,342
110/80	D21	4.5	3.1	29,810,000	98,600	121,121
110/80	D22	5.0	5.5	29,240,000	97,300	121,867
110/80	D23	8.5	7.6	29,840,000	97,800	126,528
110/80	D24	7.5	9.2	29,630,000	97,000	125,401
110/80	D25	15.0	21.7	30,440,000	97,000	126,436
110/80	D26	14.0	16.6	30,200,000	97,500	126,638
110/80	D27	16.1	24.7	30,180,000	96,200	125,397
110/80	D28	13.5	21.0	29,940,000	99,500	128,116
110/80	D35	12.5	24.9	29,970,000	105,800	132,766
110/80	D36	12.5	19.4	30,100,000	107,700	134,241

Table 3-4 Tensile property data for 165/135 specimens.

Alloy	Specimen	% Elongation	% C/S Reduction	Elastic Modulus (psi)	0.2% Yield Strength (psi)	UTS(psi)
165/135	C1	2.0	1.9	29,680,000	168,000	170,151
165/135	C2	2.0	1.8	30,380,000	167,000	169,836
165/135	C3	7.5	7.8	29,700,000	167,000	182,352
165/135	C4	5.0	5.0	29,550,000	168,000	182,074
165/135	C5	7.5	8.2	30,270,000	167,000	181,841
165/135	C6	7.5	11.3	30,110,000	164,000	179,979
165/135	C7	7.5	8.8	30,090,000	163,000	179,457
165/135	C8	8.0	9.6	30,640,000	163,500	179,455
165/135	C9	7.0	8.2	29,930,000	161,000	177,286
165/135	C10	8.0	8.6	30,690,000	157,000	175,571
165/135	C11	2.0	1.4	30,350,000	N/A	107,523
165/135	C12	5.0	6.3	29,660,000	155,000	174,071
165/135	C13	3.0	3.6	29,790,000	155,400	168,814
165/135	C14	5.0	6.3	29,330,000	154,000	172,756
165/135	C15	7.5	10.1	29,400,000	153,400	172,034
165/135	C16	5.0	4.9	30,540,000	157,000	172,460
165/135	C17	7.0	6.5	30,330,000	151,000	168,934
165/135	C18	6.5	7.6	31,120,000	150,000	168,463
165/135	C19	5.0	5.9	30,180,000	154,000	170,550
165/135	C20	2.5	2.5	26,710,000	144,500	144,478
165/135	C21	2.5	2.0	29,690,000	137,400	137,597
165/135	C22	2.5	2.1	29,620,000	156,000	156,364
165/135	C23	5.0	3.9	29,890,000	157,000	171,179
165/135	C24	3.0	2.7	29,710,000	159,000	167,168
165/135	C25	4.5	4.5	30,240,000	160,500	175,876
165/135	C26	9.0	9.5	30,180,000	161,000	178,414
165/135	C27	5.0	3.9	30,050,000	152,000	172,231
165/135	C28	4.0	4.2	30,140,000	173,000	184,102
165/135	C35	7.5	12.6	30,270,000	165,000	181,253
165/135	C36	7.5	12.2	29,660,000	176,000	190,768

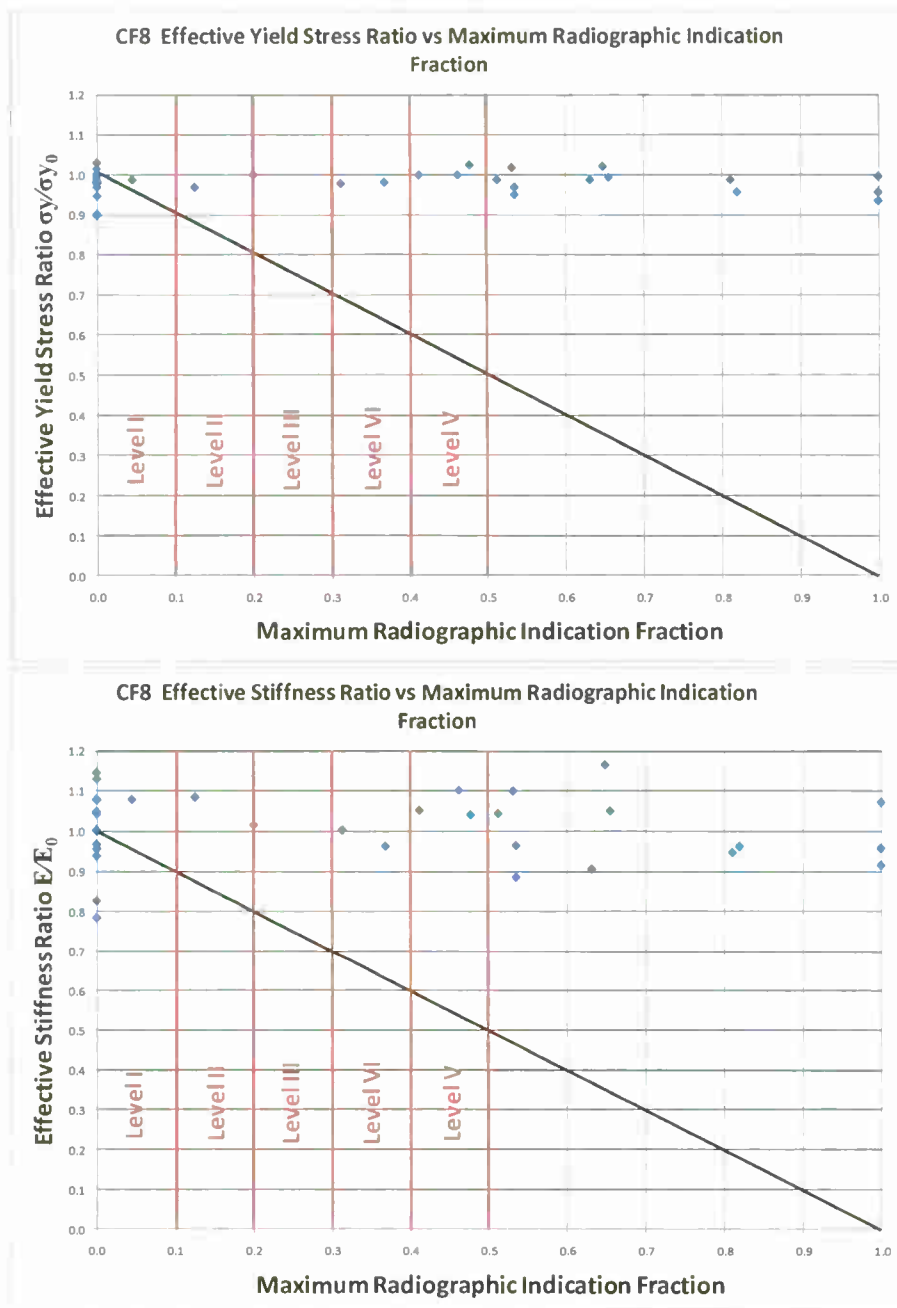


Figure 3-6 Plot of effective yield stress and stiffness ratio versus maximum radiographic indication fraction for CF8 cast steel.

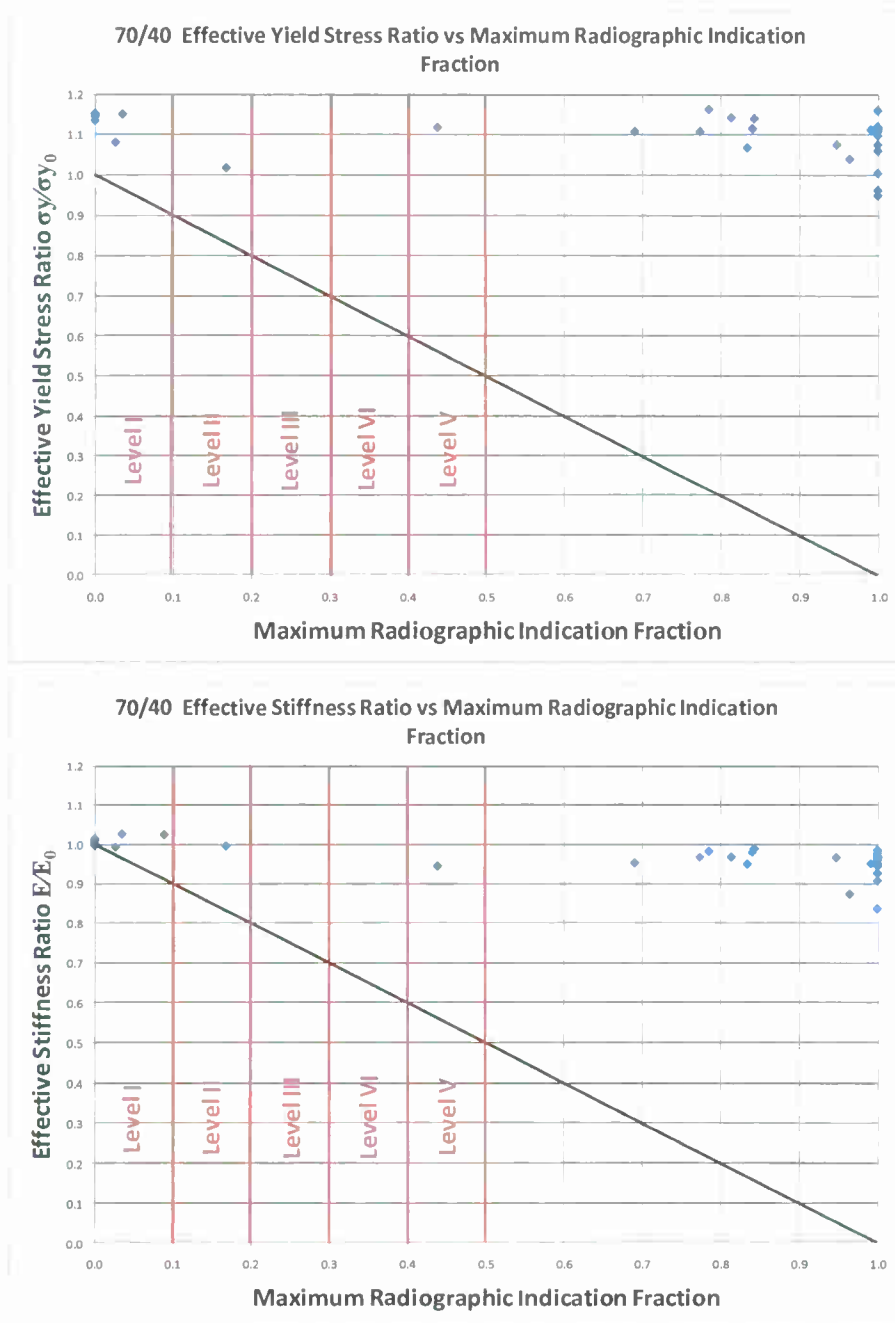


Figure 3-7 Plot of effective yield stress and stiffness ratio versus maximum radiographic indication fraction for 70/40 cast steel.

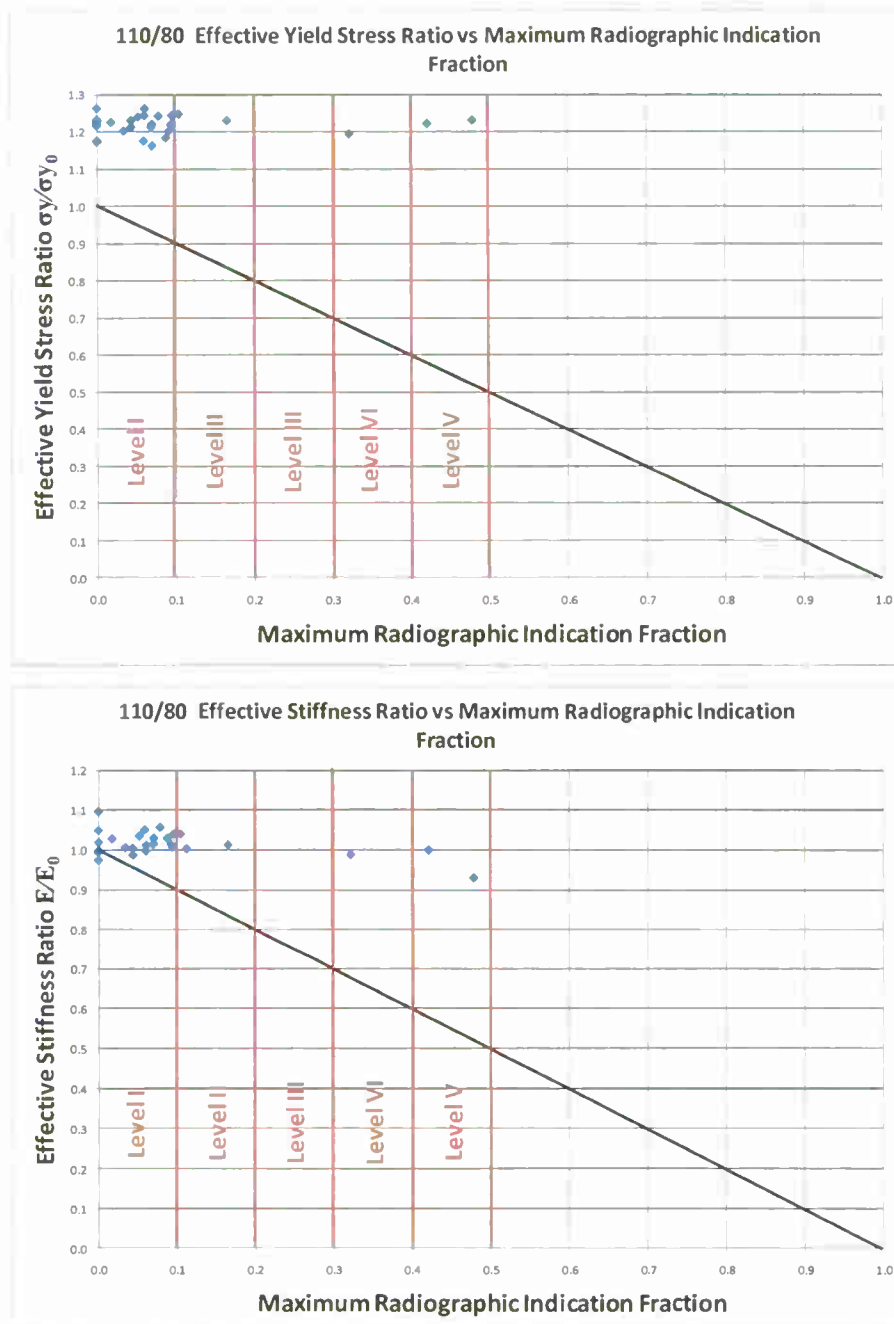


Figure 3-8 Plot of effective yield stress and stiffness ratio versus maximum radiographic indication fraction for 110/80 cast steel.

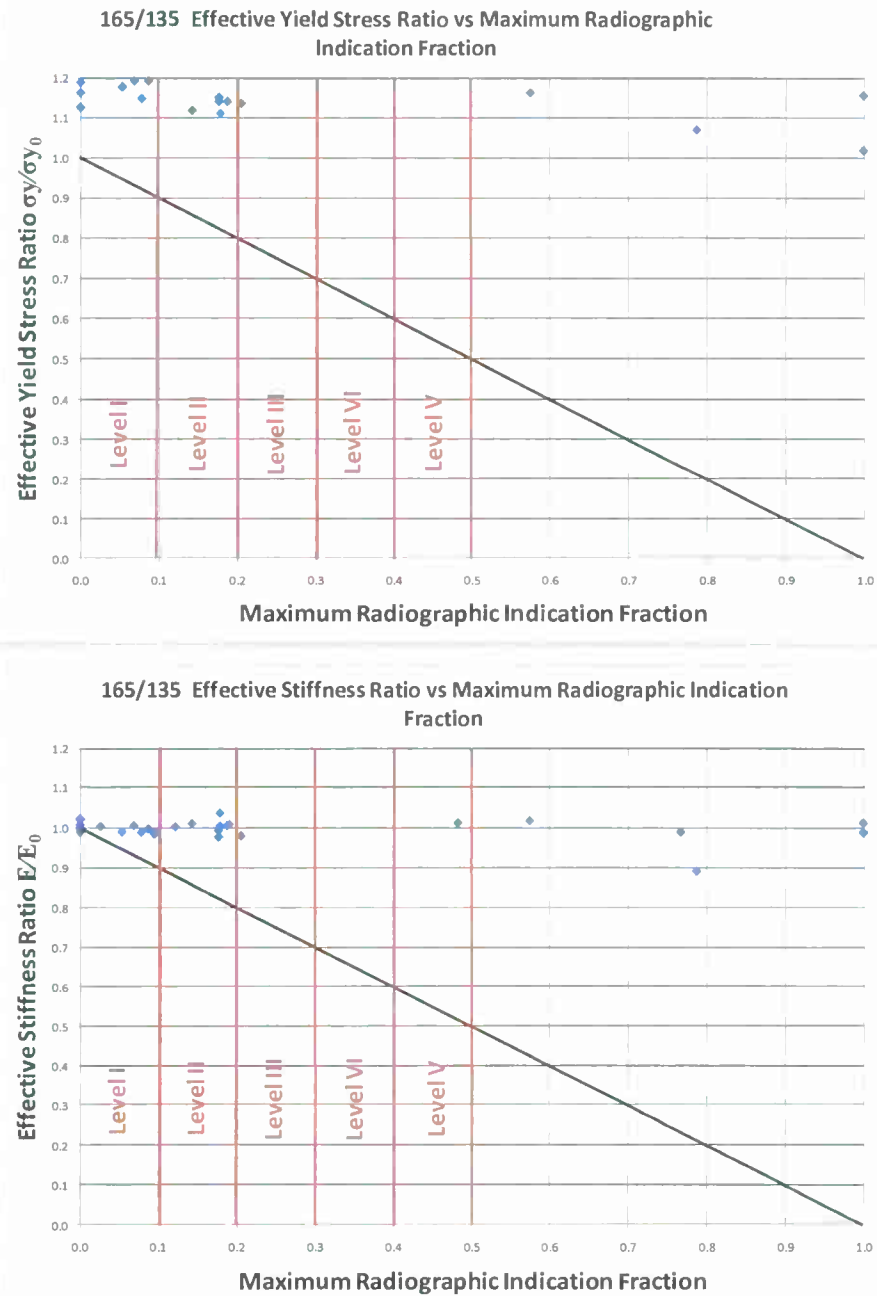


Figure 3-9 Plot of effective yield stress and stiffness ratio versus maximum radiographic indication fraction for 165/135 cast steel.

4. *Effect of Surface Indications on Mechanical Properties in Steel Castings: Principal Investigator Dr. John Griffin, University of Alabama at Birmingham*

Abstract

The objective of this research is to initiate the development of surface indication standards that are based on part performance. The research was limited to the effect of surface indications on the tensile properties in cast steel. The steel was cast and heat treated by production foundries and alloys and was selected to provide a range of tensile strengths either through heat treatment or chemistry. Surface indications were measured both with magnetic particle and liquid penetrant methods to provide indication length and shape. In addition, tensile specimens with no surface indications had artificial indications drilled into the gage section and tested.

Three cast steel grades were selected to provide a range of tensile strength and toughness values. These grades included two carbon and low alloy steels and one high alloy steel. The steels provided a range of yield strengths from 40 to 135 ksi. In addition, ES1 grade steel was selected to provide an ultra-high strength low alloy material for comparison.

The effect of surface indications on tensile strength was directly related to the strength/ductility levels of the steel. Yield and ultimate strengths of steels such as CF8 and ASTM 958 110/80 (minimum yield strength 80 ksi, minimum ultimate strength 110 ksi) were largely unaffected by the natural surface indications collected in this study and only decreased significantly when an artificial indication large enough to reduce the gage net section by 25% was introduced. When tensile strength and hardness increased (ASTM 958 165/135 (minimum yield strength 135 ksi, minimum ultimate strength 165 ksi), ES1), the effect of surface indication length was more pronounced with indication lengths of about 0.1" significantly affecting strength and strength decreasing linearly with increasing indication length. Modulus was largely unaffected by indication length. As would be expected, elongation decreased with increased indication length. The effect was more dramatic with increasing strength of the steel.

Artificial indications produced by drilling flat bottom holes to the centerline of the tensile gage section conservatively matched very well with the natural indications in their effect on tensile properties. This is a welcomed result allowing designers to introduce a repeatable indication in a location of their choosing for either a numerical simulation or usage test.

Objective

International standards organizations (ASTM International, ISO, SAE, ASME, etc.) provide a variety of methods by which surface indications can be quantified or classified to a subjective level for castings (ASTM E125, ASTM E433, ISO BS EN 1369, ISO BS EN 1371, SAE-AMS-STD-2175, MIL-STD-1907, etc.). However, all of these references are based on workmanship, not performance of the part. Parts requiring higher performance are typically subjected to higher workmanship standards without any clear understanding as to whether this actually improves performance. These higher workmanship standards increase the monetary and time cost to the customer.

The objective of this research is to initiate the development of surface indication standards that are based on part performance. This research was limited to the effect of surface indications on the tensile properties in cast steel. The proposed goal was to test tensile specimens containing a range of typical surface indications. The steel was cast and heat treated by production foundries and alloys were selected that provided a range of tensile strengths either through heat treatment or chemistry. Surface indications were measured both with magnetic particle and liquid penetrant methods to provide indication length and shape. In addition, tensile specimens with no surface indications had artificial indications drilled into the gage section and tested. The goal in this case was to determine if a repeatable and easily produced indication mimicked the results from the natural indications. This would provide designers/engineers a method by which to predict the effect of an indication of a particular length on part performance.

The ultimate goal is the development of a manual for castings which provides a methodology to design a cast part that provides satisfactory performance with an adequate survival probability during the design life. This manual will most likely be based on fatigue life, not tensile, since most parts fail by fatigue. This is, of course, beyond the scope of this research but is in line with this task's goals. A design manual previously described would not be unique or unprecedented since one currently exists for welded joint and components from the International Institute of Welding (Fatigue Design of Welded Joints and Components). This manual provides a basis for the design and analysis of welded components composed of structural steel and aluminum loaded by fluctuating forces.

The goals of this strategy will benefit the designer, producer, and customer of castings. The designer will have a methodology to quickly specify a surface indication requirement that satisfies the design life and performance of a casting. The producer will not be burdened with surface quality requirements that add cost and time to production without any benefit to the customer. The customer will benefit from an efficient design requirement that minimizes cost and lead time while satisfying the performance requirements.

Approach

Three cast steel grades were selected to provide a range of tensile strength and toughness values. These grades included two carbon and low alloy steels and one high alloy steel. The steels provided a range of yield strengths from 40 to 135 ksi. The carbon and low alloy steels included an ASTM 958 110/80 (minimum yield strength 80 ksi, minimum ultimate strength 110 ksi), an ASTM 958 165/135 (minimum yield strength 135 ksi, minimum ultimate strength 165 ksi) and a high alloy CF8 cast steel was also included to provide a steel with a different microstructure and modulus but with tensile properties similar to the 70/40 steel. In addition, ES1 grade steel was selected to provide an ultra-high strength low alloy material for comparison.

A 36"l x 8"w test plate was designed to provide a shape with a large cope surface and produce the number of necessary test specimens. The large cope surface provided a range of surface indication lengths for each steel grade. The ES1 steel was provided as a 16" diameter by 4.5" thick billet in a non-heat treated condition. As such, no natural surface indications were available; however, the steel was tested with artificial indications.

Four steel foundries, each a member of the SFSA, agreed to produce all the four alloy grades at the required strength levels. From each 110/80, 165/135, and CF8 plate, 0.050" of steel was removed from the cope surface to straighten the surface and remove any molding irregularities and minimize false surface indications. A 3/4" thick plate was saw cut from the cope surface as shown in Figure 4-1. Each machined plate was marked to designate the strength level as well as the location and orientation of the tensile blanks along the length of the plate as shown in Figure 4-2. The tensile blanks were saw cut from each plate creating approximately 30 tensile blanks per strength level. The number of tensile blanks per strength level/alloy varied because some of the blanks did not complete clean up from the 0.050" cut removed from the cope surface. These blanks were discarded. The remaining blanks were machined to final dimensions as per ASTM A370/E8 sheet type standard specimen (Figure 4-3).

The ES1 steel billet was sectioned to produce tensile blanks such that the center section was avoided as much as possible. The billet center is the most likely location for shrink and segregation anomalies. Therefore, the gage section of the tensile blank was removed from the mid-radius of the billet. Since this particular alloy was not heat treated by the foundry, UAB heat treated the steel using the following procedure: homogenized at 2000°F for 2 hours then air cool, austenitized at 1900°F for one hour then water quenched, tempered at 375°F for four hours then water quenched. Depending on the heat treatment, ES1 steel can reach ultimate strength greater than 250 ksi. Using the 0.5" x 0.5" gage section from the other low and high alloy steels would have produced loads higher than the capability of UAB's tensile frame. Therefore, the ES1 specimen gages were machined to 0.50" x 0.25".

All four surfaces of each tensile specimen gage were inspected using either magnetic particle or liquid penetrant. For magnetic particle inspection, a Parker Research DA-400 contour probe with Parker Research DMP-5 dry magnetic inspection powder was used. For liquid penetrant inspection, Magnaflux Zyglo ZL-60D water washable fluorescent penetrant with a medium sensitivity (sensitivity level 2) was used. Liquid penetrant was only used on the CF8 specimens. Indications from each tensile specimen were photographed to document location and length as shown in Figure 4-4.

Specimens without surface indications were either tested as-is to provide a baseline or tested with an artificial indication. The artificial indications were created by drilling a single flat bottom hole with a diameter of 0.0625", 0.125" and 0.25" to a depth of one-half specimen thickness in the gage section (0.25" depth for 110/80, 165/135, or CF8 and 0.125" depth for the ES1 steel).

Tensile tests were performed on a tensile machine consisting of an MTS 810 50 kip load frame with MTS 647 hydraulic grips, and controlled by a MTS FlexTest SE. The load train was reconfigured with appropriate grips and calibrated extensometers to test the 8" long tensile specimens. Before testing, MTS certified the linear displacement transducer, 50 kip load cell, and 2" extensometers were in working order and within manufacturer's tolerances. The load train was aligned to class 5 (50 µin max) using the MTS 709 alignment system. The time/load/strain data was digitally recorded for each specimen. The crosshead speed was varied depending on the alloy and changed according to the test: ranging from 0.03 to 0.04 in/min up to the yield point and 0.20 in/min to failure. These crosshead speeds provide loading rates within the range required by ASTM E08. Figure 4-5 illustrates

example stress-strain curves for 10 tensile specimens removed from the 110/80 steel test plate. A standard set of tensile measurements was made for each specimen tested at UAB and placed into a spreadsheet for each alloy. These measurements include 0.2% offset yield strength, 0.1% offset yield strength, ultimate strength, proportional limit, elongation, elastic modulus, total strain at maximum stress, and reduction in area.

Indications from the magnetic particle or liquid penetrant photographs were identified and measured for length in a direction perpendicular to the loading direction. Indications from all four sides of the gage section were measured. Length measurements were made using Image Pro-Plus imaging analysis software and the indication lengths were tabulated and stored for subsequent analysis. In addition, the location and length of all measured indications were documented by capturing the annotated photograph. Macrographs of the fractured tensile bar were recorded for comparison and the fracture surface area covered by an anomaly measured as shown in Figure 4-6.

All tensile property data was plotted against both maximum and total indication length to detect any relationships that existed. For the sake of brevity, only 0.2% offset yield strength, ultimate strength, elongation and modulus will be discussed in the body of this report. However, the remaining plots will be presented in the appendices.

Results

110/80 – For this particular alloy strength, two foundries supplied test plates. Since the chemistry and alloy content most likely varied between the foundries to meet ASTM A958 110/80 specification, the summary tensile and indication data was tabulated and plotted distinctly to allow detection of any significant differences. Table 4-1 lists the tensile property and indication data for the 110/80 steel from Foundry 1. Indication data is listed as either the maximum single indication length (perpendicular to loading direction) or the sum of all indications observed in the gage section. Specimens with artificial (drilled) indications are grouped at the bottom of the table. Table 4-2 lists the tensile property and indication data for the 110/80 steel from Foundry 2.

Figures 4-7 through 4-10 illustrate the effect of maximum and total surface indication length on 0.2% offset yield strength, ultimate strength, elongation, and modulus. Plots for the 0.1% offset yield strength, proportional limit, fracture surface area, and total strain at maximum stress are presented in Appendix 4-A. All specimens with artificial indications are plotted in red. The diamond symbols are from Foundry 1 and the square symbols are from Foundry 2. The strength levels in the 110/80 steel from Foundry 1 were higher than that from Foundry 2 although both met the required minimums. Yield strengths were not significantly reduced until maximum indication length reached the maximum of 0.25". In fact, yield strength did not go below the minimum of 80 ksi with any of the naturally occurring indications and only failed the minimum with a 0.25" diameter x 0.25" deep hole drilled into the gage. Ultimate strength showed similar results to 0.2% offset yield strength with only the longest indication lengths reducing ultimate strength below required minimums.

Elongation showed some unusual results in that the artificial indications followed the same trend of the natural indications in the higher strength 110/80 but the lower strength, higher ductility steel was relatively unaffected by the natural indications although

significantly reduced by artificial indications. Tensile modulus was relatively unaffected by both natural and artificial indications.

The artificial indication lengths provided a very good conservative estimate of the effect of maximum natural indication lengths on tensile yield, ultimate, elongation and modulus.

165/135 -Table 4-3 lists the tensile property and indication data for the 165/135 cast steel. Indication data is listed as either the maximum single indication length (perpendicular to loading direction) or the sum of all indications observed in the gage section. Specimens with artificial (drilled) indications are grouped at the bottom of the table.

Figures 4-11 through 4-14 illustrate the effect of maximum and total surface indication length on 0.2% offset yield strength, ultimate strength, elongation, and modulus. All specimens with artificial indications are plotted in red. Plots for the 0.1% offset yield strength, proportional limit, fracture surface area, and total strain at maximum stress are presented in Appendix 4-B. Both yield and ultimate strength were not significantly reduced until maximum indication length reached a length of 0.1" for both natural and artificial indications. Similar to the 110/80, the yield strength did not go below the minimum of 135 ksi with any of the naturally occurring indications and only failed the minimum with an 0.25" diameter x 0.25" deep hole drilled into the gage. Ultimate strength showed similar results to 0.2% offset yield strength with only the longest natural and artificial indication lengths reducing ultimate strength below required minimums.

Elongation showed the expected trend with values decreasing with increasing indication length. Tensile modulus was relatively unaffected by both natural and artificial indications. The artificial indication lengths provided a very good conservative estimate of the effect of maximum natural indication lengths on tensile yield, ultimate, elongation and modulus.

CF8 - CF8 is the lowest strength, highest ductility steel tested in this study. Table 4-4 lists the tensile property and indication data for the CF8 cast steel. Indication data is listed as either the maximum single indication length (perpendicular to loading direction) or the sum of all indications observed in the gage section. Specimens with artificial (drilled) indications are grouped at the bottom of the table.

Figures 4-15 through 4-18 illustrate the effect of maximum and total surface indication length on 0.2% offset yield strength, ultimate strength, elongation, and modulus. All specimens with artificial indications are plotted in red. Plots for the 0.1% offset yield strength, proportional limit, fracture surface area, and total strain at maximum stress are presented in Appendix 4-C. Yield strength was not significantly reduced by any surface indication, natural or artificial, measured in this study. Ultimate strength was unaffected until the artificial maximum indication length reached the maximum of 0.25".

Elongation showed the expected trend with values decreasing from 60% to a minimum of 20% with increasing indication length. Tensile modulus was relatively unaffected by either natural or artificial indications. The artificial indication lengths provided a very good conservative estimate of the effect of maximum natural indication lengths on yield, ultimate, elongation and modulus tensile properties.

ES1 – ES1 is the highest strength, lowest ductility steel tested in this study. Table 4-5 lists the tensile property and indication data for the ES1 cast steel. Since the tensile specimens were from a billet, only artificial indication data was available as a maximum single indication length (perpendicular to loading direction).

Figures 4-19 and 4-20 illustrate the effect of maximum indication length on 0.2% offset yield strength, ultimate strength, elongation, and modulus. Plots for the 0.1% offset yield strength, proportional limit, fracture surface area, and total strain at maximum stress are presented in Appendix 4-D. Yield strength decreased linearly from about 180 ksi to 130 ksi as indication length increased from zero to 0.25". Ultimate strength also decreased linearly from 240 ksi to 150 ksi as indication length increased from zero to 0.25". Elongation decreased from 6% to 3% as indication length increased from zero to 0.125". There was no further reduction in elongation at an indication length of 0.25". Tensile modulus was unaffected with the size of the artificial indications introduced.

Key Findings

- The effect of surface indications on tensile strength was directly related to the strength/ductility levels of the steel. Yield and ultimate strengths of steels such as CF8 and 110/80 were largely unaffected by the natural surface indications collected in this study and only decreased significantly when an artificial indication large enough to reduce the gage net section by 25% was introduced. When tensile strength and hardness increased (165/135, ES1), the effect of surface indication length was more pronounced with indication lengths of about 0.1" significantly affecting strength and strength decreasing linearly with increasing indication length.
- Modulus was largely unaffected by indication length. Both 0.1% offset yield strength and the proportional limit were measured and plotted to see if the linear portion of the stress-strain curves were affected by indication length. The results did not show any conclusive trend.
- As would be expected, elongation showed an affect from surface indications, with decreased elongation decreasing with increased indication length. The effect was more dramatic in the higher strength steels.
- Artificial indications produced by drilling flat bottom holes to the centerline of the tensile gage section conservatively matched very well with the natural indications in their effect on tensile properties. This is a welcomed result allowing designers to introduce a repeatable indication in a location of their choosing for either a numerical simulation or usage test.

Transition

The results of this study will be presented to steel foundries through presentations and papers. However, the target audience for this work should be designers of castings. There are several options that will be explored including standards that relate surface indications to performance and manuals to aid designers in the selection of castings based on performance.

Conclusions

The effect of surface indications on tensile strength is directly related to the strength/ductility levels of the steel. Yield and ultimate strengths of steels such as CF8 and 110/80 were largely unaffected by the natural surface indications collected in this study and only decreased significantly when an artificial indication large enough to reduce the gage net section by 25% was introduced. When tensile strength and hardness increased (165/135, ES1), the effect of surface indication length was more pronounced with indication lengths of about 0.1" significantly affecting strength and strength decreased linearly with increasing indication length.

Modulus was largely unaffected by indication length. Both 0.1% offset yield strength and proportional limit were measured and plotted to see if the linear portion of the stress-strain curves were affected by indication length. The results did not show any conclusive trend.

As would be expected, elongation showed an affect from surface indications, with decreased elongation with increased indication length. The effect was more dramatic in the higher strength steels.

Artificial indications produced by drilling flat bottom holes to the centerline of the tensile gage section conservatively matched very well with the natural indications in their effect on tensile properties. This is a welcomed result allowing designers to introduce a repeatable indication in a location of their choosing for either a numerical simulation or usage test.

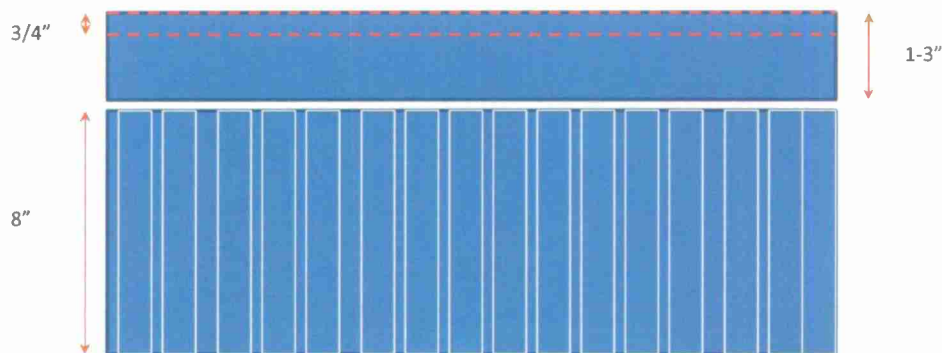
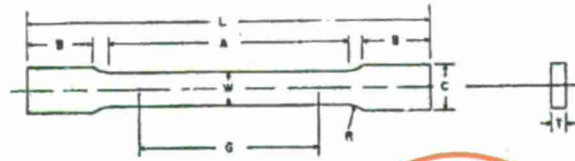


Figure 4-1 An illustration of the cutting plan to remove tensile blanks from a typical cast steel test plate.



Figure 4-2 Photograph of a typical steel test plate after surface preparation and markup for specimen removal.



	Dimensions		
	Plate-Type, 1 1/2-in. Wide	Standard Specimens Sheet-Type, 1/2-in. Wide	Subsize Specimen 1/4-in. Wide
	in.	in.	in.
G—Gage length (Note 1 and Note 2)	8.00 ± 0.01	2.000 ± 0.005	1.000 ± 0.003
W—Width (Note 3 and Note 4)	1 1/2 ± 1/16, - 1/16	0.500 ± 0.010	0.250 ± 0.005
T—Thickness (Note 5)		thickness of material	
R—Radius of fillet, min (Note 6)	1	1/2	1/4
L—Over-all length, (Note 2, Note 7 and Note 8)	18	8	4
A—Length of reduced section, min	9	2 1/4	1 1/4
B—Length of grip section, (Note 8)	3	2	1 1/4
C—Width of grip section, approximate (Note 4 and Note 9)	2	3/4	3/8

Figure 4-3 Final machined dimensions for sheet type tensile specimen from ASTM A370.

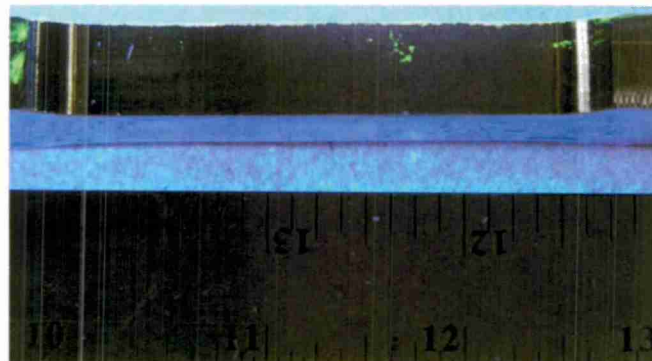
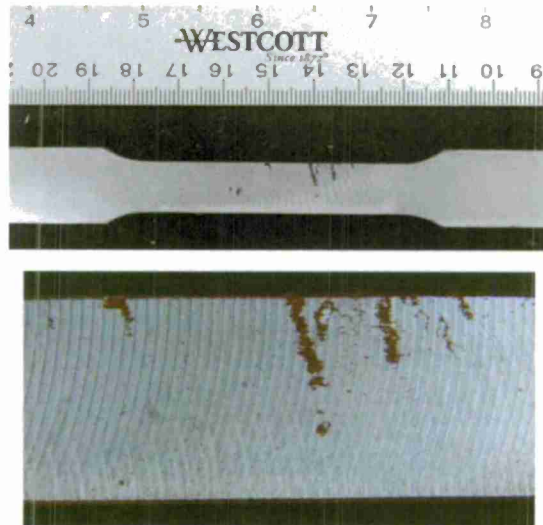


Figure 4-4 Typical magnetic particle and liquid penetrant indications observed on tensile specimen surfaces.

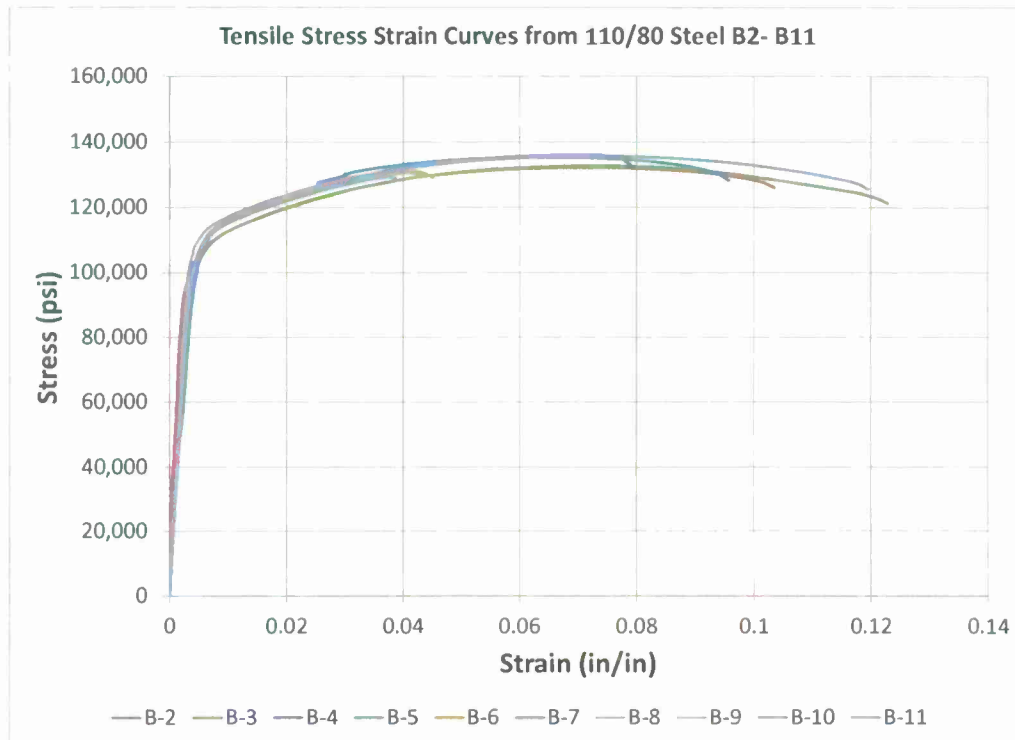


Figure 4-5 Example stress-strain curves for 10 tensile specimens removed from the 110/80 steel test plate.

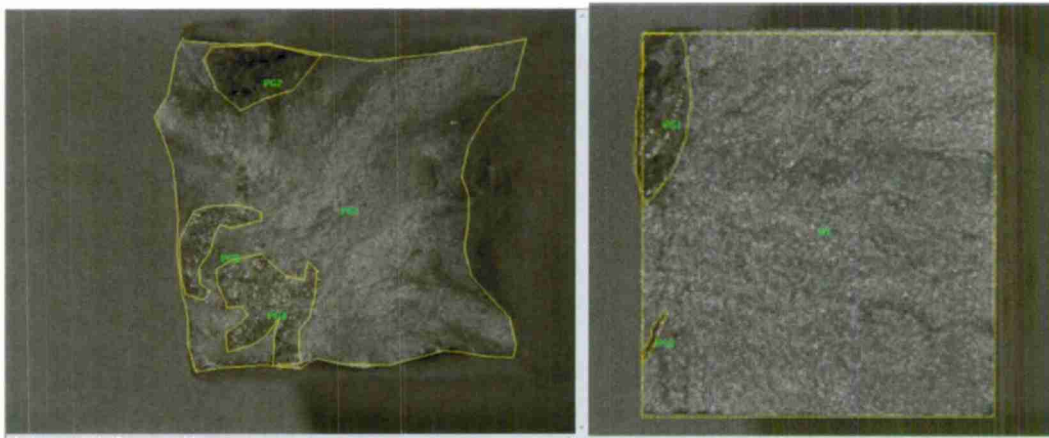


Figure 4-6 Examples of fracture surface indication measurements taken from a CF8 and 165/135 cast steel tensile specimens.

Table 4-1 Summary and Indication Data for 110/80 Cast Steel from Foundry 1.

Specimen	UTS (psi)	Strain at Max Stress (in/in)	Modulus (mpsi)	0.1% Offset Yield (psi)	0.2% Offset Yield (psi)	Proportional Limit (psi)	Elongation (%)	Maximum Indication Length (in.)	Total Indication Length (in.)	Fracture Surface Area (%)
B-1	134,688	0.068						0.000	0.000	
B-2	132,264	0.073		100,235	104,467	33,360	12.5	0.049	0.087	6.7
B-3	132,766	0.074	29.4	100,347	105,082	33,972	13.5	0.066	0.066	0.9
B-4	136,099	0.071	27.8	102,260	108,606	48,456	9	0.000	0.000	
B-5	135,360	0.066	28.6	97,252	106,332	39,679	12.5	0.000	0.000	
B-7	135,836	0.072	30.0	104,412	109,664	53,985	13	0.068	0.074	5.2
B-8	130,681	0.036	33.3	108,458	111,433	51,563	5	0.109	0.109	7.2
B-10	135,563	0.068	31.3	99,261	107,449	34,344	7.5	0.072	0.105	2.7
B-15	135,523	0.068	32.3	105,598	109,486	63,450	8.5	0.067	0.161	4.4
B-16	129,101	0.033	30.8	104,838	108,558	64,514	5	0.085	0.178	4.5
B-17	132,700	0.050	31.6	105,115	108,579	51,731	5.5	0.089	0.279	5.5
B-19	79,368	0.004	27.6			35,979	1.5	0.309	0.571	27.6
B-20	135,960	0.069	28.6	100,631	106,829	50,359	10.5	0.054	0.091	1.3
B-21	119,735	0.017	29.4	100,536	106,330	58,213	1.5	0.161	0.437	2.9
B-22	122,190	0.023	31.6	103,671	108,915	50,518	3.5	0.065	0.170	11.3
B-23	118,382	0.018	28.6	99,710	107,001	49,129	3	0.148	0.310	7.7
B-24	134,378	0.068	33.3	103,893	109,090	84,715	10	0.043	0.043	
B-25	124,334	0.029	29.4	101,779	107,331	63,973	5	0.105	0.333	11.3
B-26	127,525	0.050	28.6	97,658	102,613	53,132	7	0.072	0.072	12.3
B-27	119,915	0.050	30.8	93,257	97,132	40,647		0.104	0.848	
B-28	123,447	0.071	28.6	90,243	95,340	71,008	13	0.066	0.186	21.0
B6	130,995	0.042	29.6	103,394	109,017	49,211	4.5	0.063	0.063	6.3
89	130,540	0.041	30.3	102,862	108,055	45,869	6	0.063	0.063	6.3
811	129,228	0.038	29.4	104,979	108,782	79,121	6	0.063	0.063	6.3
812	118,292	0.021	27.8	91,950	101,037	36,392	4.5	0.125	0.125	12.5
813	119,799	0.020	34.5	102,181	105,759	44,917	3.5	0.125	0.125	12.5
814	118,023	0.020	29.0	96,711	102,177	40,817	3.5	0.125	0.125	12.5
818	99,389	0.016	25.0	78,763	85,291	50,015	3.5	0.250	0.250	25.0

Table 4-2 Summary and Indication Data for 110/80 Cast Steel from Foundry 2.

Specimen	UTS (psi)	Strain at Max Stress (in/in)	Modulus (mpsi)	0.1% Offset Yield (psi)	0.2% Offset Yield (psi)	Proportional Limit (psi)	Elongation (%)	Maximum Indication Length (in.)	Total Indication Length (in.)	Fracture Surface Area (%)
D1-5	111,615	0.089	25.8	92,645	93,051	85,565		0.000	0.000	
D1-9	113,496	0.083	33.3	95,560	95,722	46,260	22	0.000	0.000	0.2
D2-4	115,883	0.070	32.0	96,750	97,070	46,554	19	0.084	0.084	0.8
D2-5	115,768	0.074	32.3	96,096	96,709	49,748	17.5	0.000	0.000	1.4
D2-9	118,264	0.076	32.0	101,093	101,898	49,157	21.5	0.000	0.000	0.7
D2-11	116,691	0.078	31.3	96,915	98,028	61,009	19.5	0.121	0.750	1.3
D3-1	113,540	0.065	40.0	99,749	99,625	32,326		0.193	0.604	
D3-2	111,510	0.089	33.3	93,386	93,348	45,383	23	0.068	0.126	0.0
D3-3	109,662	0.083	29.6	89,849	90,245	82,979	21.5	0.073	0.257	0.0
D3-4	109,258	0.094	30.8	89,475	89,514	56,883	23	0.214	1.209	0.0
D3-5	110,186	0.094	30.8	91,958	91,861	62,971	24	0.103	0.179	0.3
D3-6	110,758	0.090	31.6	91,917	91,758	53,140	23	0.045	0.086	0.0
D3-9	108,094	0.089	31.6	89,083	88,828	52,409	22.5	0.097	0.945	0.2
D3-10	107,510	0.080	29.6	87,511	87,585	45,238	21.5	0.076	0.416	0.0
D3-11	109,881	0.082	31.6	89,846	90,307	45,283	22.5	0.132	0.594	0.1
D3-12	111,729	0.086	31.6	93,729	94,042	61,680	22.5	0.073	0.580	0.0
D3-13	115,430	0.082	32.0	98,662	99,003	49,943	14.5	0.177	0.545	6.2
D1-6	110,226	0.069	33.3	91,482	92,482	46,997	13	0.063	0.063	6.3
D1-8	104,630	0.042	28.6	82,637	87,164	40,222	10	0.125	0.125	12.5
D1-10	86,658	0.029	25.8	64,051	70,211	37,574	7.5	0.250	0.250	25.0
D1-12	106,550	0.038	36.4	88,683	90,457	62,914	9	0.125	0.125	12.5
D1-13	117,151	0.068	28.6	95,761	101,041	45,271	12.5	0.063	0.063	6.3
D2-6	89,896	0.025	26.7	67,724	73,885	39,359	7.5	0.250	0.250	25.0
D2-8	109,142	0.035	30.8	95,296	97,554	27,900	8.5	0.125	0.125	12.5
D2-10	115,793	0.065	30.3	96,983	98,296	46,147	12.5	0.063	0.063	6.3
D2-12	89,616	0.027	27.6	69,240	75,056	41,877	7.5	0.250	0.250	25.0
D2-13	94,363	0.024	28.6	77,935	81,775	46,051	8.5	0.250	0.250	25.0
D3-7	100,583	0.050	29.6	80,207	82,267	39,779	11	0.125	0.125	12.5
D3-8	105,966	0.066	32.0	86,281	86,942	48,632	13.5	0.063	0.063	6.3

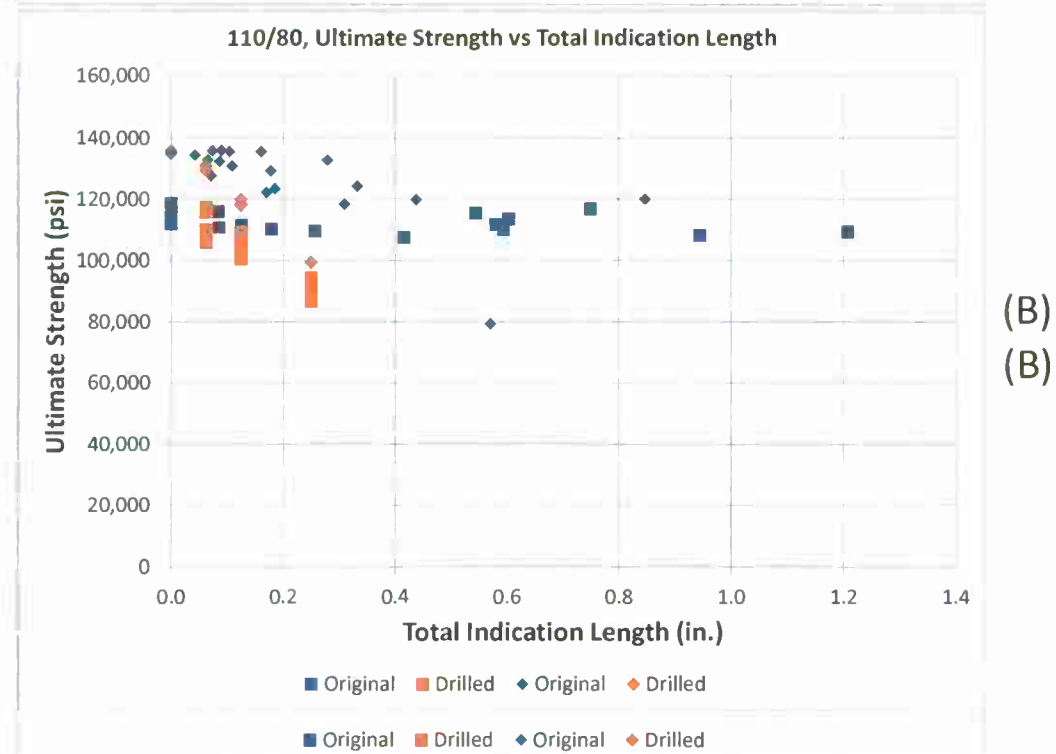
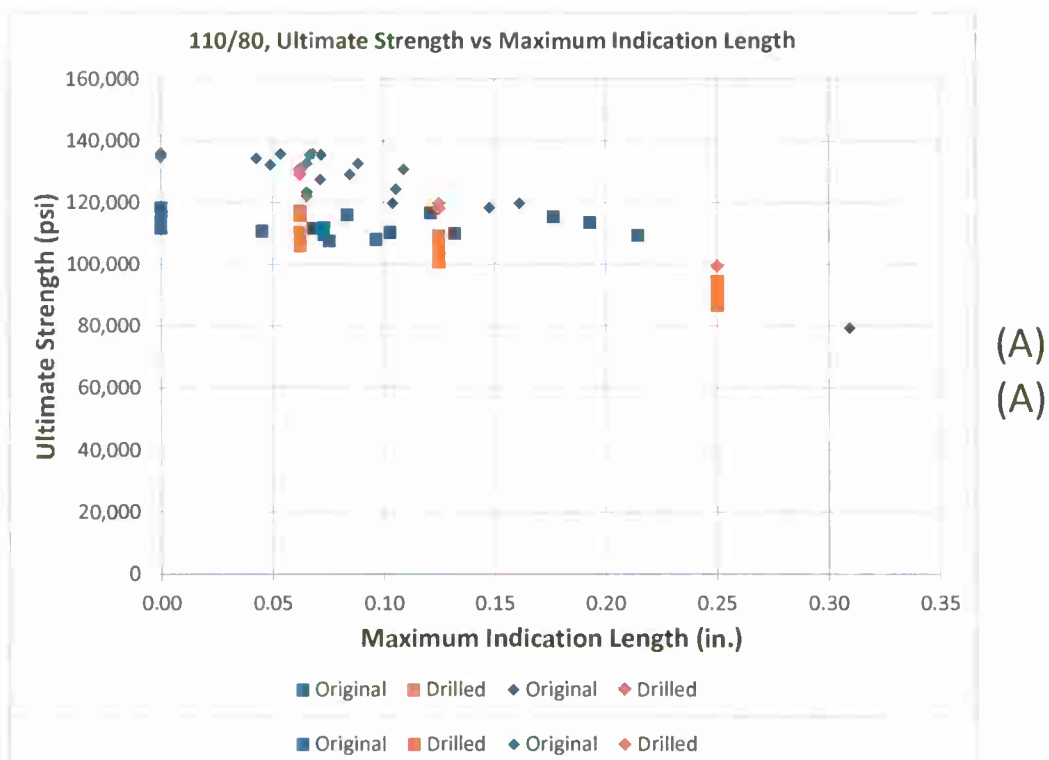


Figure 4-8 Effect of Maximum (A) and Total (B) Surface Indication Length on Ultimate Strength of Cast 110/80 Steel.

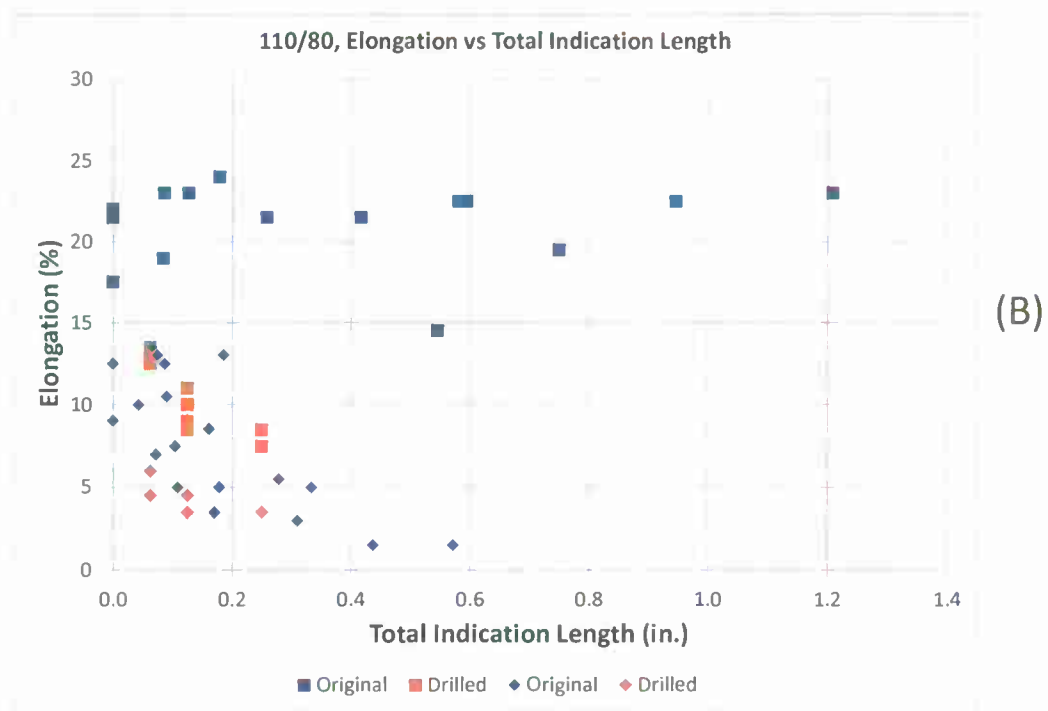
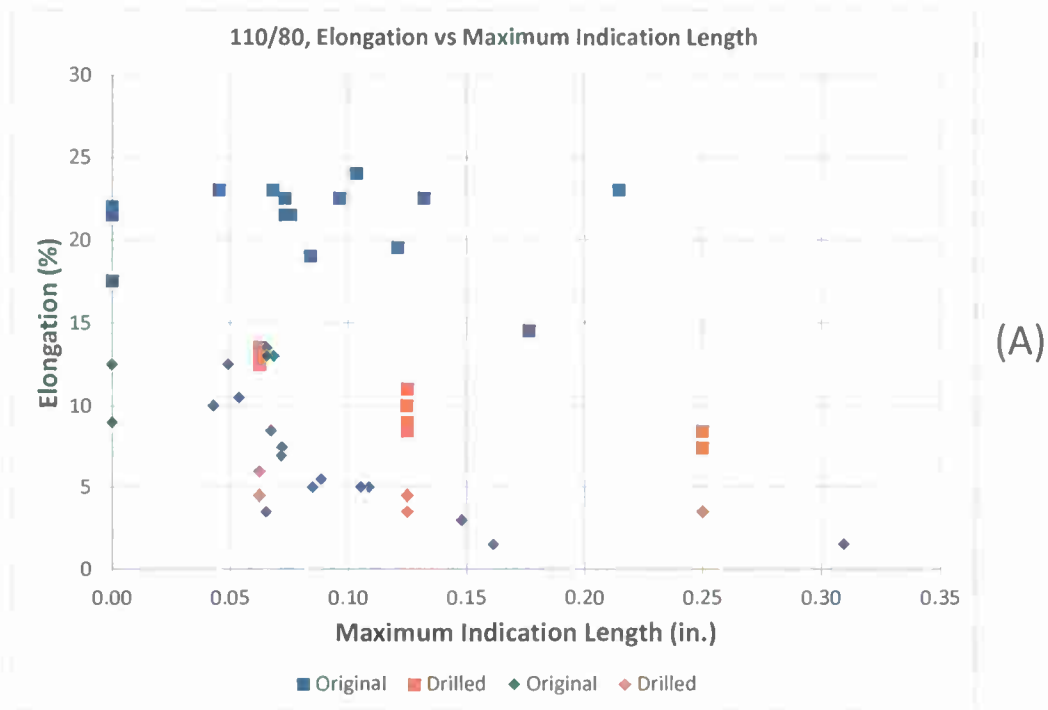
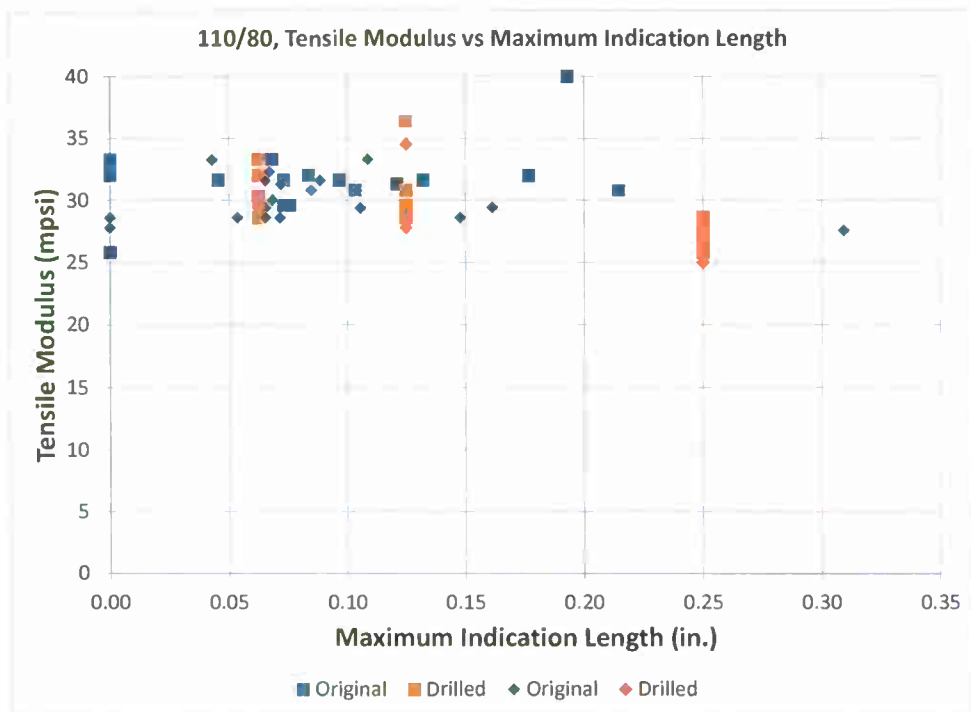
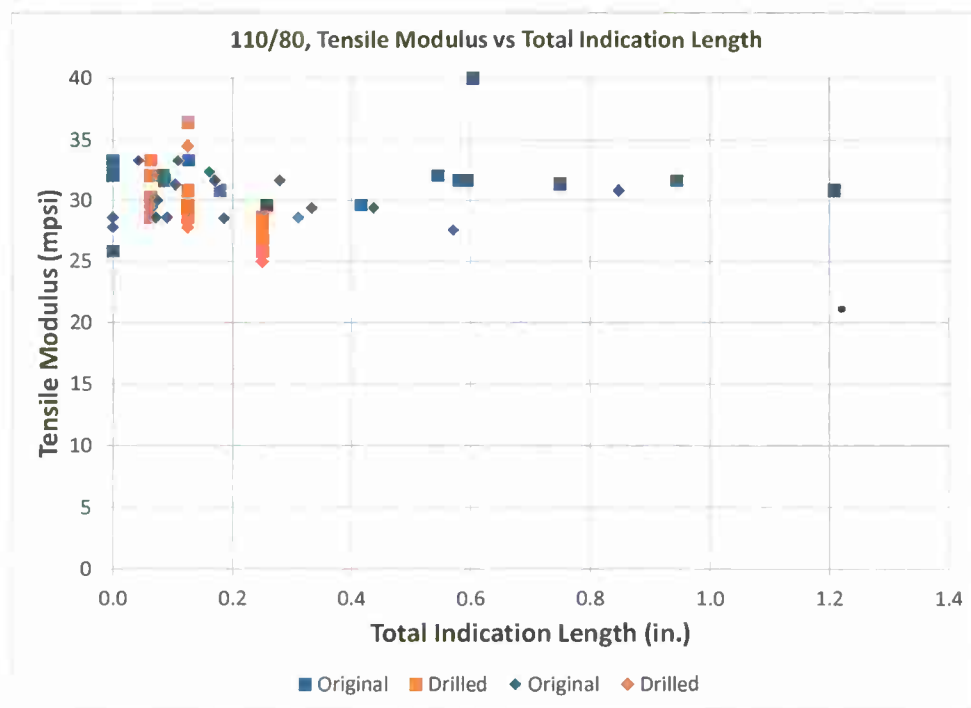


Figure 4-9 Effect of Maximum (A) and Total (B) Surface Indication Length on Elongation of Cast 110/80 Steel.



(A)

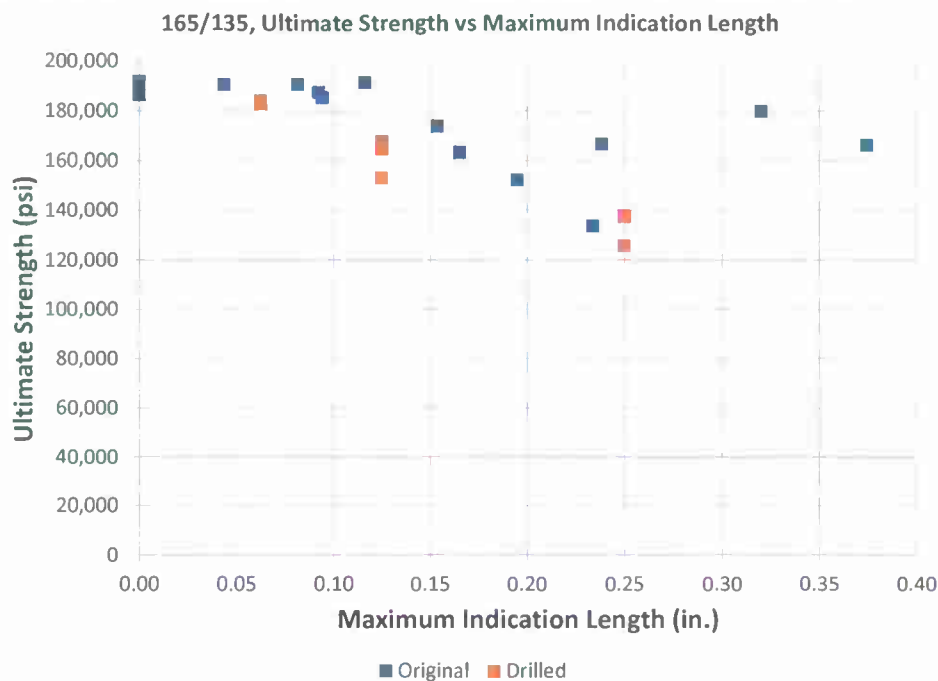


(B)

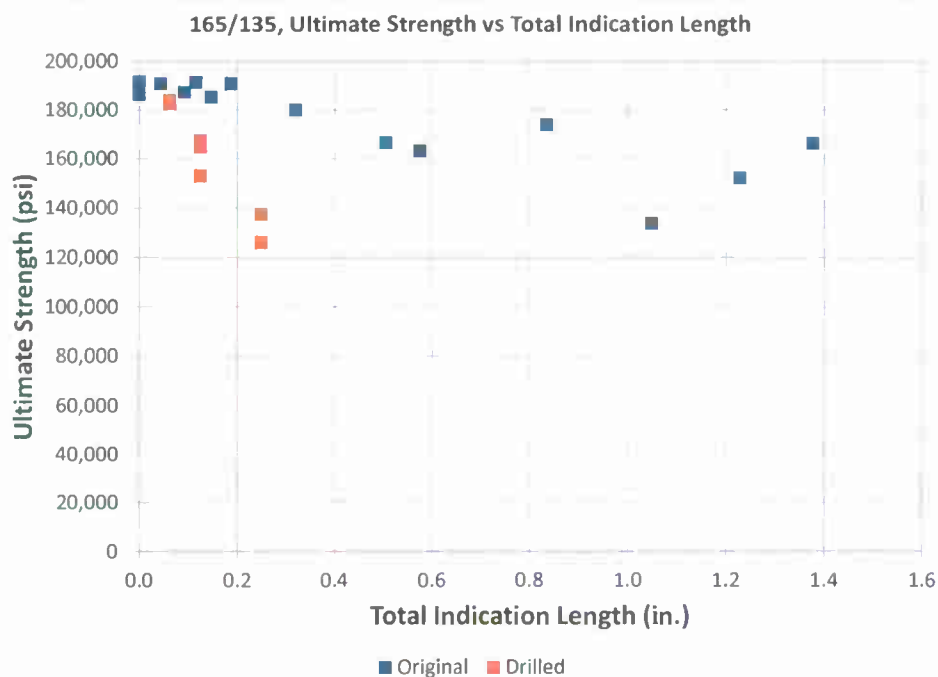
Figure 4-10 Effect of Maximum (A) and Total (B) Surface Indication Length on Tensile Modulus of Cast 110/80 Steel.

Table 4-3 Summary and Indication and Data for 165/135 Cast Steel.

Specimen	UTS (psi)	Strain at Max Stress (in/in)	Modulus (mpsi)	0.1% Offset Yield (psi)	0.2% Offset Yield (psi)	Proportional Limit (psi)	Elongation (%)	Maximum Indication Length (in.)	Total Indication Length (in.)	Fracture Surface Area (%)
A4	190,737	0.046	30	169,380	173,503	77,372	9	0.081	0.189	0.1
A5	191,754	0.044	35	172,346	176,164	45,001		0.000	0.000	
A6	191,394	0.045	29	168,683	174,235	58,476	7.5	0.000	0.000	0.7
A7	191,361	0.046	28.8	171,438	175,975	57,306	8	0.116	0.116	0.0
A8	191,040	0.034	31.7	175,801	175,801	78,471	7.5	0.000	0.000	
A9	191,144	0.039	29	174,661	174,661	45,422	7	0.000	0.000	
A10	189,976	0.033	30	168,679	174,246	61,126	3.5	0.000	0.000	0.4
A13	190,766	0.043	30	168,996	174,317	34,647	5.5	0.044	0.044	0.2
A15	179,878	0.025	26.7	158,873	166,448	54,786	3	0.320	0.320	12.0
A18	152,161	0.006	28.8			39,308	2	0.195	1.228	7.2
A19	185,230	0.022	25.7	163,797	171,237	56,343	2.5	0.094	0.147	3.3
A20	166,603	0.007	28.3			42,866	2.5	0.238	0.505	6.1
A21	133,506	0.005	28			46,435	3	0.234	1.049	50.8
A22	186,292	0.024	27.5	166,528	172,795	57,619	4	0.000	0.000	1.4
A24	187,251	0.017	28	167,392	174,636	44,941	5.5	0.092	0.092	26.9
A25	173,814	0.009	31.7	162,799	169,426	65,579	2	0.154	0.835	32.0
A26	166,190	0.011	30	152,339	160,046	91,017	2.5	0.375	1.377	15.9
A27	163,150	0.020	28	142,979	149,570	105,959		0.165	0.575	
A11	183,794	0.013	33.3	169,354	174,701	78,452	2	0.0625	0.0625	6.3
A12	182,829	0.013	32.5	168,168	173,463	74,197	3	0.0625	0.0625	6.3
A14	183,667	0.015	26.3	165,293	172,544	44,741	3	0.0625	0.0625	6.3
A16	137,494	0.008	28.8	127,272	135,000	81,838	2	0.250	0.250	25.0
A17	164,855	0.010	26.7	152,289	160,755	44,874	2.5	0.125	0.125	12.5
A23	167,566						2	0.125	0.125	12.5
A28	153,096	0.009	30	140,606	148,869	51,836	2.5	0.125	0.125	12.5
A29	125,984	0.009	32	110,737	118,276	62,174	2.5	0.250	0.250	25.0

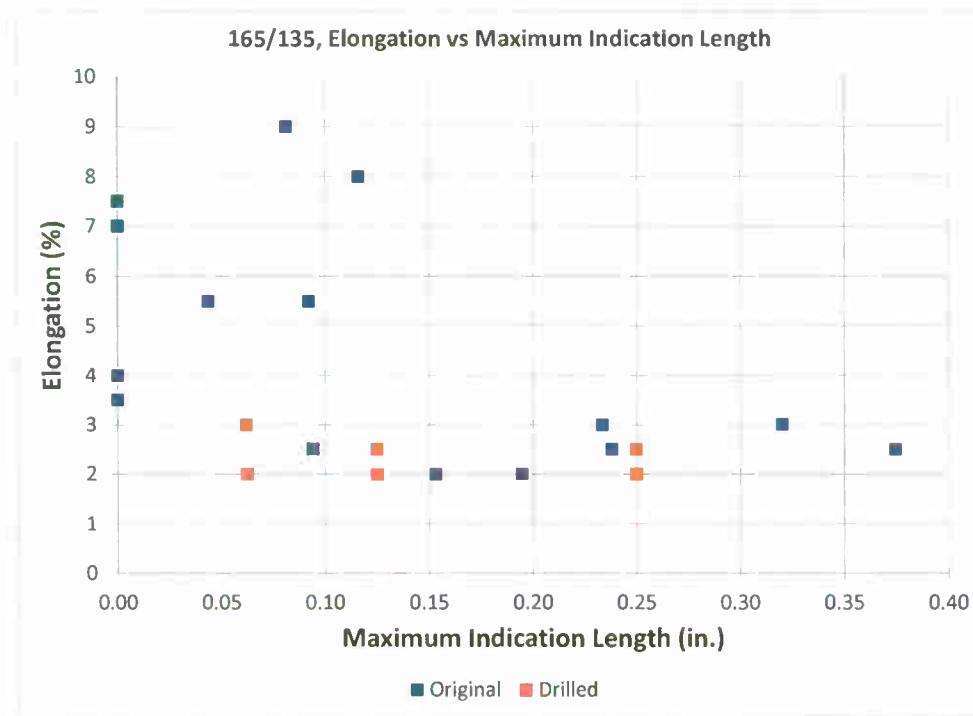


(A)

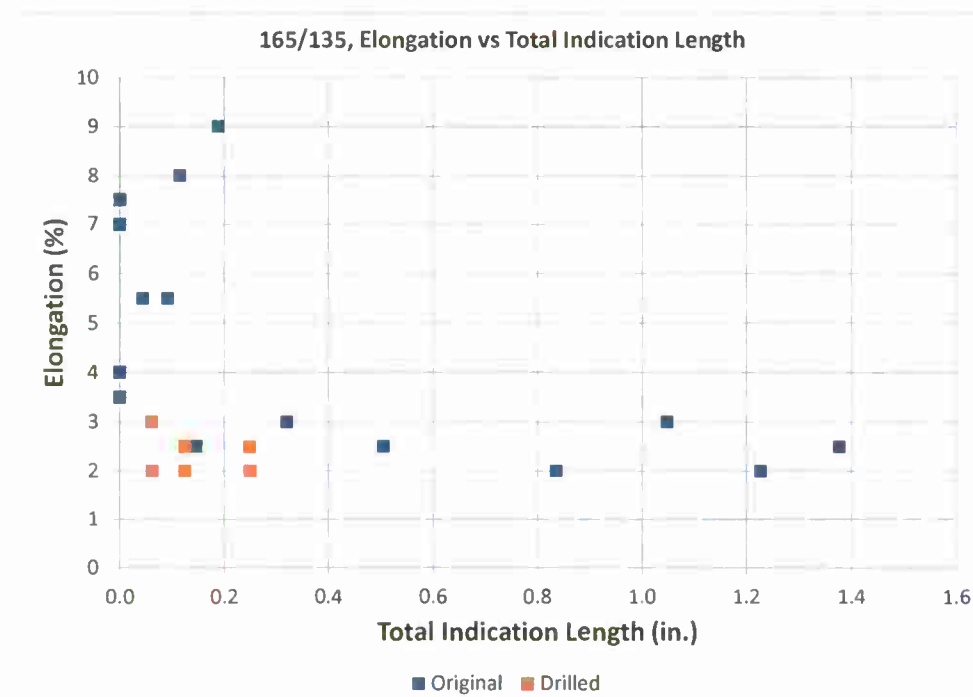


(B)

Figure 4-12 Effect of Maximum (A) and Total (B) Surface Indication Length on Ultimate Strength of Cast 165/135 Steel.

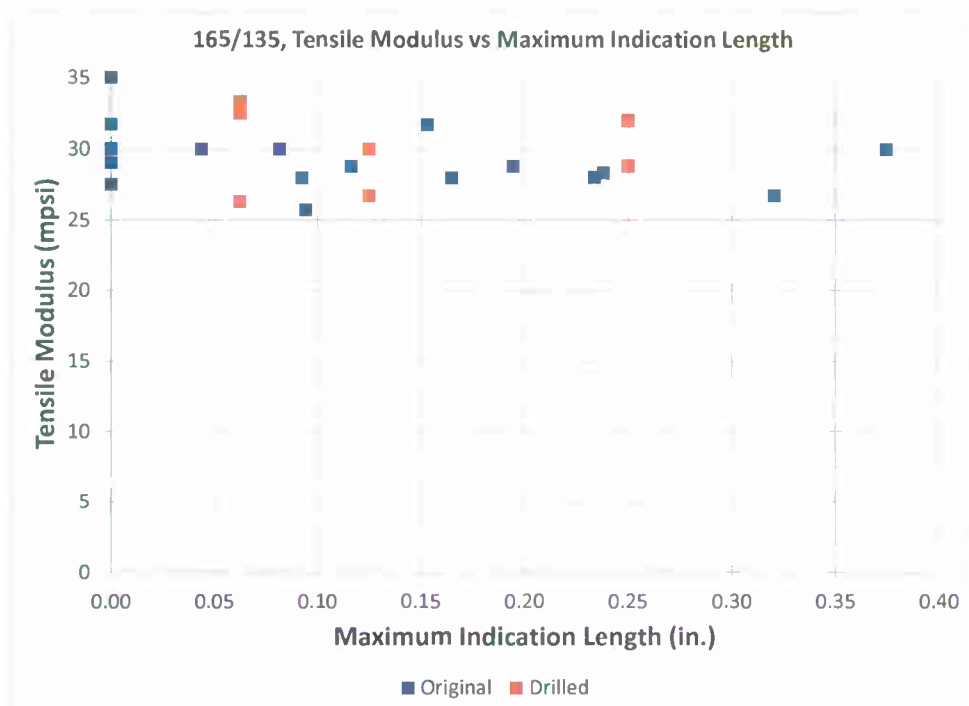


(A)

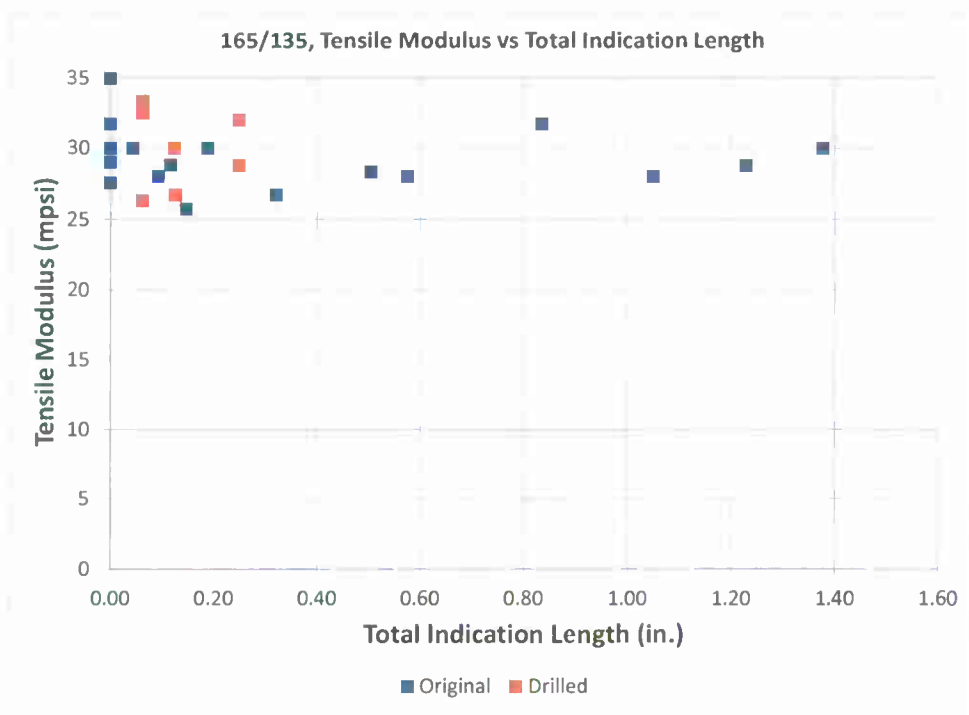


(B)

Figure 4-13 Effect of Maximum (A) and Total (B) Surface Indication Length on Elongation of Cast 165/135 Steel.



(A)

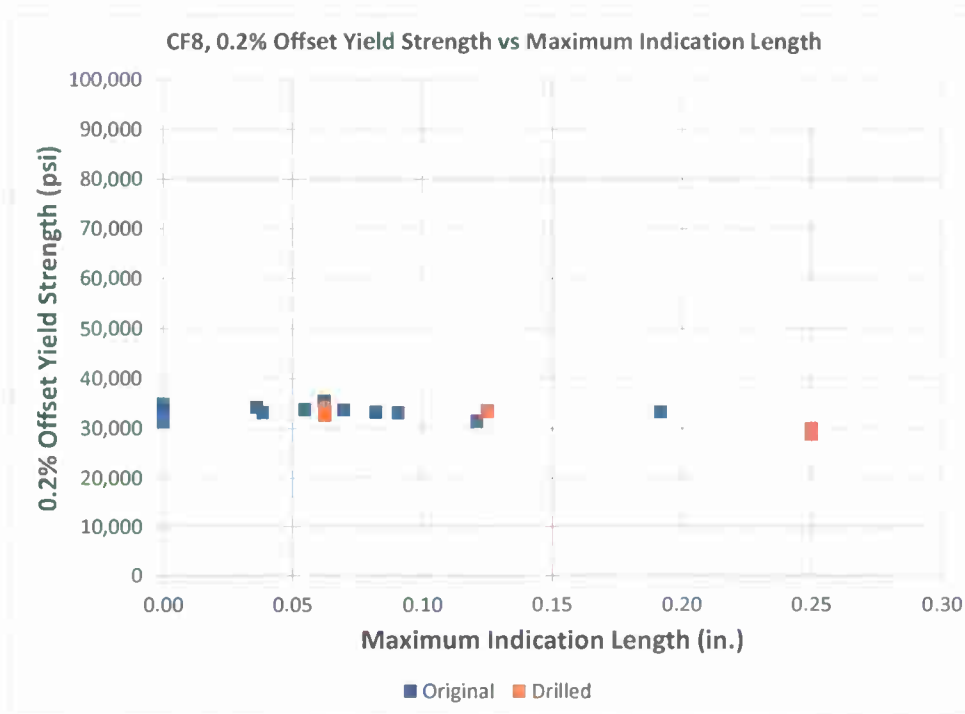


(B)

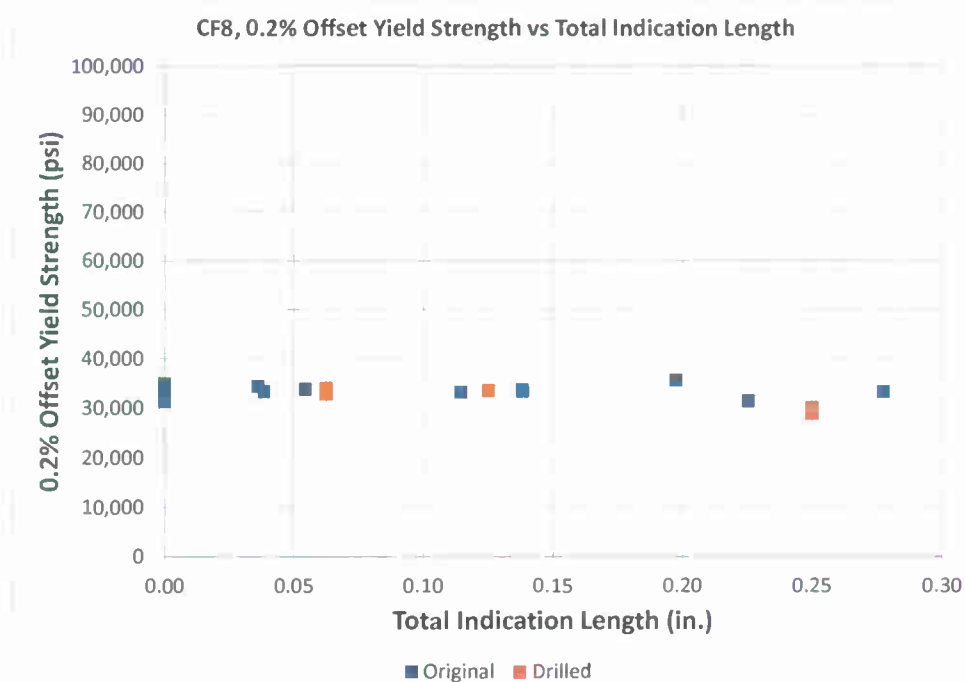
Figure 4-14 Effect of Maximum (A) and Total (B) Surface Indication Length on Tensile Modulus of Cast 165/135 Steel.

Table 4-4 Summary and Indication Data for CF8 Cast Steel.

Specimen	UTS (psi)	Strain at Max Stress (in./in)	Modulus (mpsi)	0.1% Offset Yield (psi)	0.2% Offset Yield (psi)	Proportional Limit (psi)	Elongation (%)	Maximum Indication Length (in.)	Total Indication Length (in.)	Fracture Surface Area (%)
C1	65,843	0.201	25	28,507	31,391	12,599		0.000	0.000	33.4
C2	80,941	0.428	26.3	30,691	33,676	15,313	52	0.070	0.138	0.5
C3	70,549	0.221	26	30,483	33,165	13,287	26	0.038	0.038	11.8
C8	78,716						51	0.000	0.000	0.0
C9	77,775	0.461	23.8	32,037	34,163	15,042	54	0.036	0.036	0.0
C10	78,786	0.328	27.8	31,752	34,444	15,353	45.5	0.000	0.000	0.0
C11	79,285							0.000	0.000	
C14	71,432						28.5	0.072	0.119	0.0
C15	69,248	0.166	28.3	32,896	35,582	16,656	20	0.062	0.197	47.4
C16	78,077	0.353	25	31,127	33,278	22,860	39	0.192	0.278	15.6
C17	76,178	0.393	25	30,514	33,095	17,021	45.5	0.091	0.114	0.6
C19	79,807	0.384	26	30,894	33,626	17,799	54	0.000	0.000	0.0
C23	78,657	0.386	26.5	30,624	32,907	16,526	45	0.000	0.000	0.2
C25	77,752	0.263	23.3	31,240	33,275	18,781	40	0.082	0.138	0.7
C26	75,136	0.362	24.5	28,565	31,405	14,728		0.121	0.225	
C28	75,694	0.419	26.5	31,643	33,773	20,390	48	0.055	0.065	0.0
C31	72,530	0.412	23.5	30,519	33,074	16,745	56.5	0.000	0.000	0.0
C34	77,869	0.377	23.3	32,578	34,914	24,417	44	0.000	0.000	
C35	76,781	0.356	27	30,237	33,859	15,250	35	0.000	0.000	0.0
C36	78,449	0.397	27	31,919	33,921	23,444	47	0.000	0.000	
C4	73,908						30.5	0.125	0.125	12.5
C5	69,098	0.244	26	31,773	34,049	21,268	28.5	0.063	0.063	6.3
C7	57,423	0.159	20	26,663	28,827	16,234	22.5	0.250	0.250	25.0
C12	68,558	0.200	24	31,015	33,570	18,550	26	0.125	0.125	12.5
C13	59,943	0.164	25	27,039	29,366	16,629	23.5	0.250	0.250	25.0
C18	56,602	0.127	23.3	27,880	30,022	17,923	20	0.250	0.250	25.0
C20	78,104	0.455	26.7	30,278	32,663	18,761	48.5	0.063	0.063	6.3
C22	60,943	0.160	20	27,823	29,522	19,495	22.5	0.250	0.250	25.0
C27	72,688						37.5	0.125	0.125	12.5
C29	66,259	0.233	22	31,205	33,327	21,450	28.5	0.125	0.125	12.5
C30	70,017		22				32.5	0.063	0.063	6.3
C32	72,075						29	0.063	0.063	6.3



(A)



(B)

Figure 4-15 Effect of Maximum (A) and Total (B) Surface Indication Length on 0.2% Offset Yield Strength of Cast CF8 Steel.

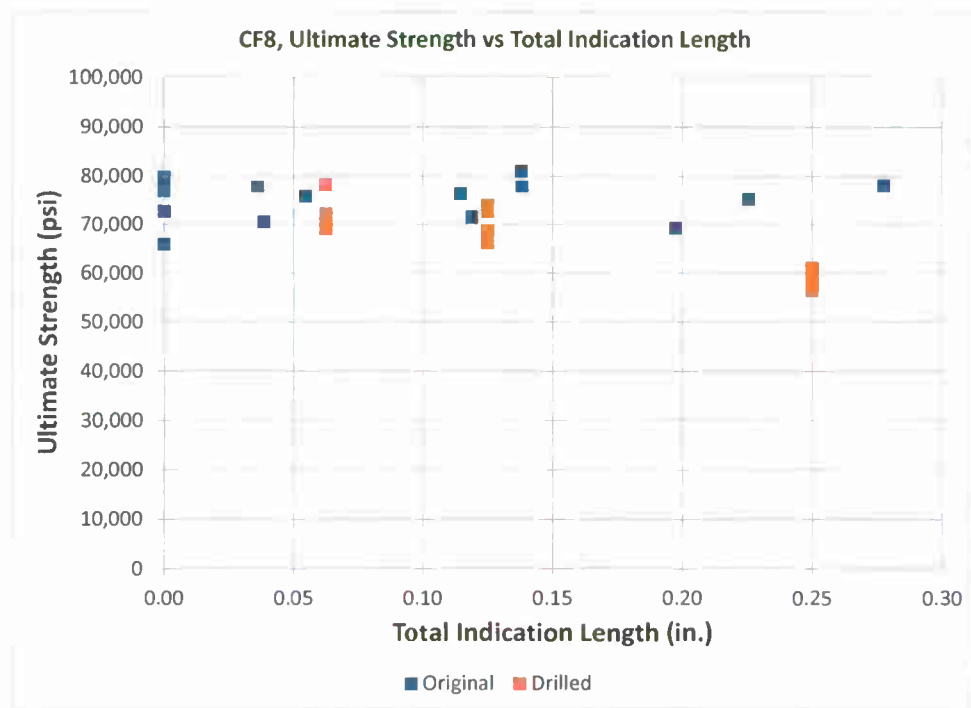
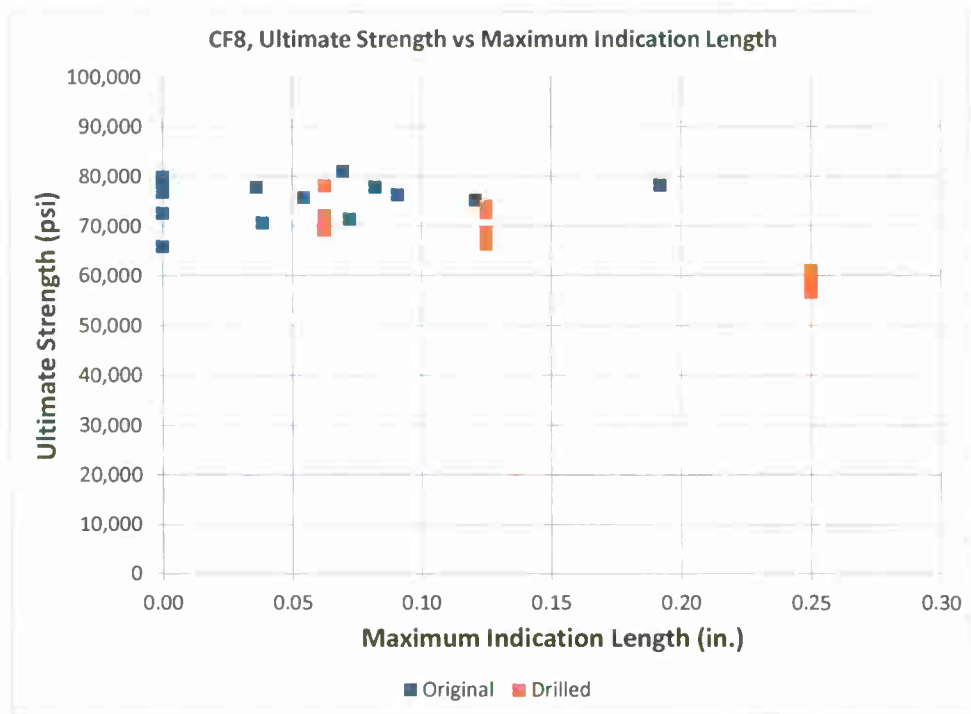
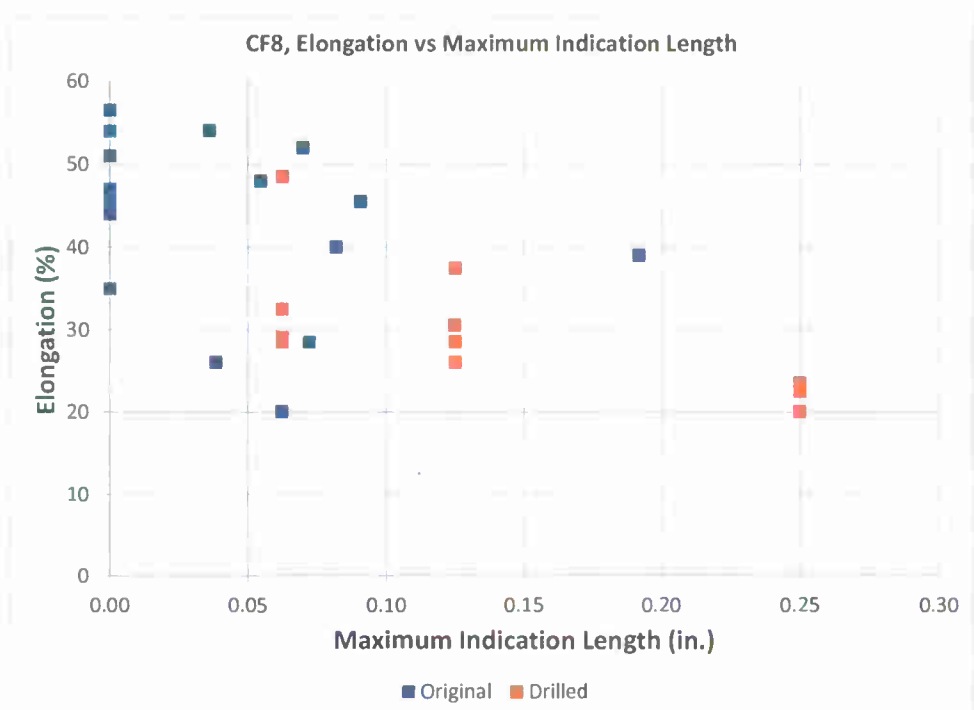
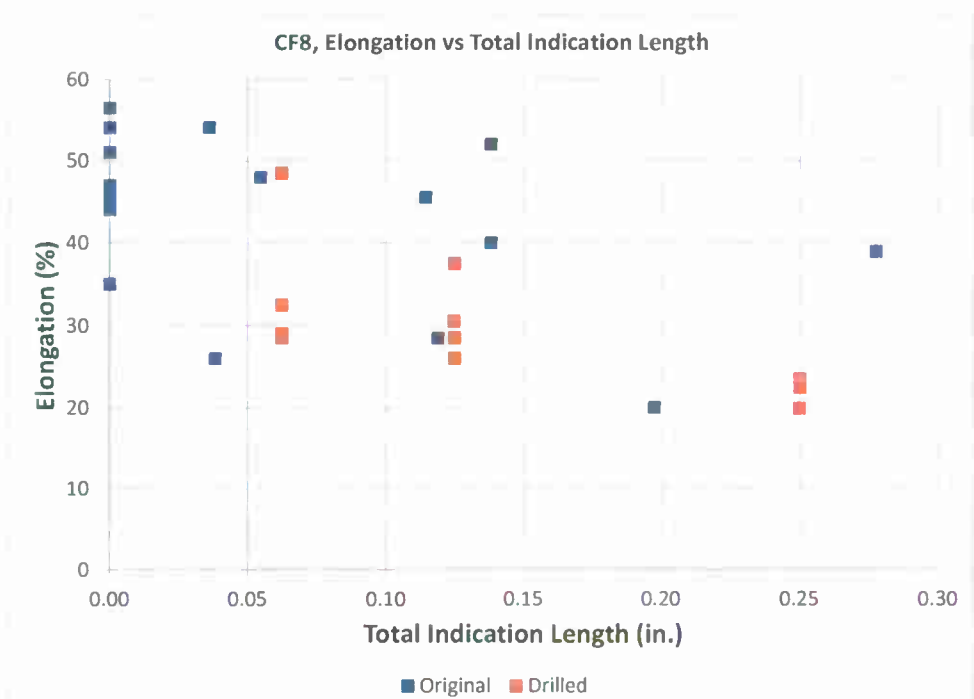


Figure 4-16 Effect of Maximum (A) and Total (B) Surface Indication Length on Ultimate Strength of Cast CF8 Steel.



(A)



(B)

Figure 4-17 Effect of Maximum (A) and Total (B) Surface Indication Length on Elongation of Cast CF8 Steel.

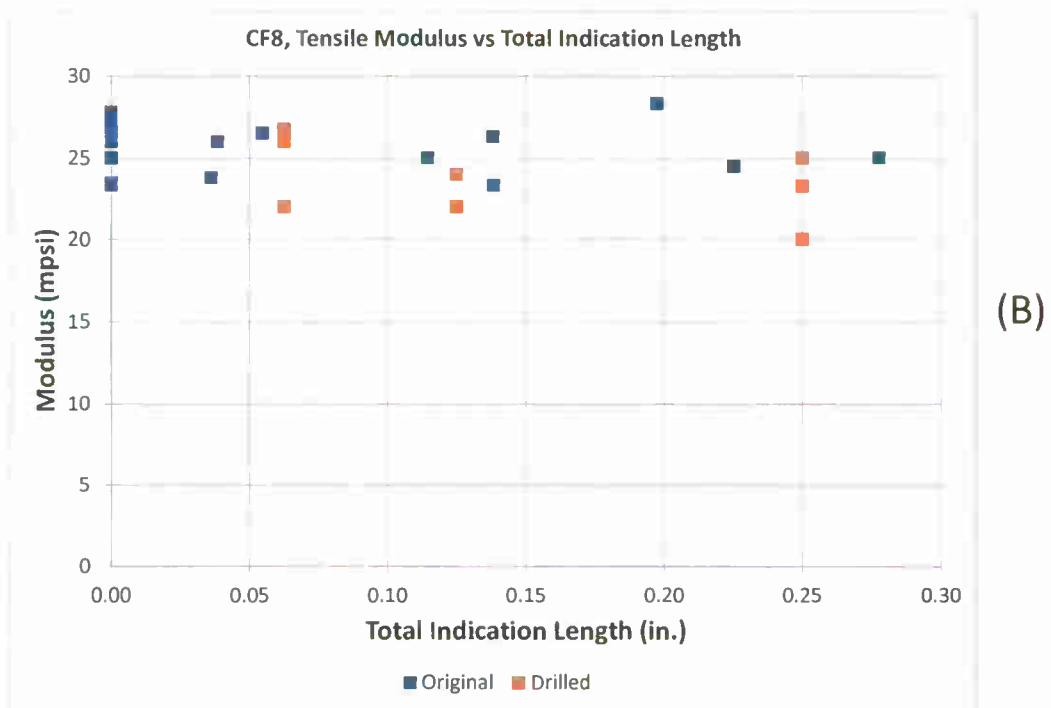
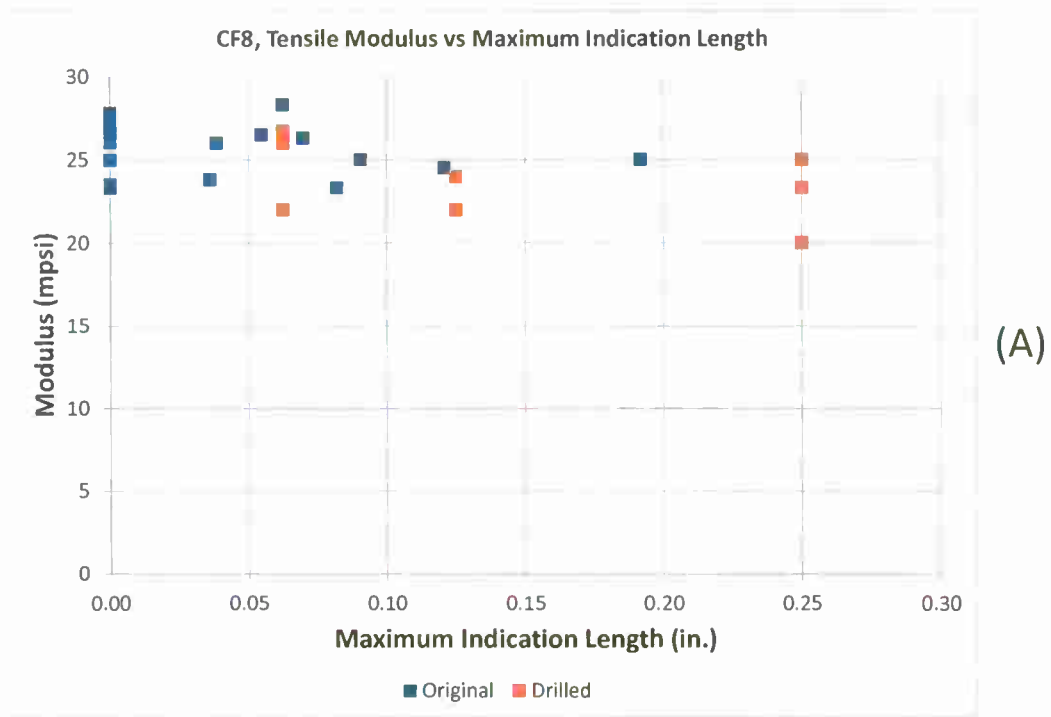


Figure 4-18 Effect of Maximum (A) and Total (B) Surface Indication Length on Tensile Modulus of Cast CF8 Steel.

Table 4-5 Summary and Indication Data for ES1 Cast Steel.

Specimen	UTS (psi)	Strain at Max Stress	Modulus	0.1% Offset Yield	0.2% Offset Yield	Proportional Limit	Elongation	Maximum Indication Length	Total Indication Length	Fracture Surface Area
	(psi)	(in/in)	(mpsi)	(psi)	(psi)	(psi)	(%)	(in.)	(in.)	(%)
ES1-2	240,310	0.036	30.8	164,160	181,900	112150	6.4	0	0	0
ES1-3	230,030	0.0268	30.1	164,900	181,900	121690	5.9	0	0	0
ES1-4	222,060	0.0209	29.2	152,320	174,620	91900	4.4	0.0625	0.0625	7
ES1-5	224,670	0.023	27	147,850	168,470	78180	4.2	0.0625	0.0625	7
ES1-6	220,420	0.0218	31.7	158,520	174,850	94410	4.7	0.0625	0.0625	7
ES1-7	173,690	0.0153	29.3	134,780	150,570	81690	3.7	0.125	0.125	14.5
ES1-8	185,540	0.0152	33.6	148,590	162,410	99770	3.0	0.125	0.125	14.5
ES1-9	176,330	0.0158	30	144,820	156,690	81050	3.4	0.125	0.125	14.5
ES1-10	157,460	0.0167	25.6	112,510	126,630	61550	3.4	0.25	0.25	29
ES1-11	157,640	0.0155	28.6	114,700	131,790	55760	3.0	0.25	0.25	29
ES1-12	132,670	0.0094	26.7	100,920	117,970	58430	4.0	0.25	0.25	29

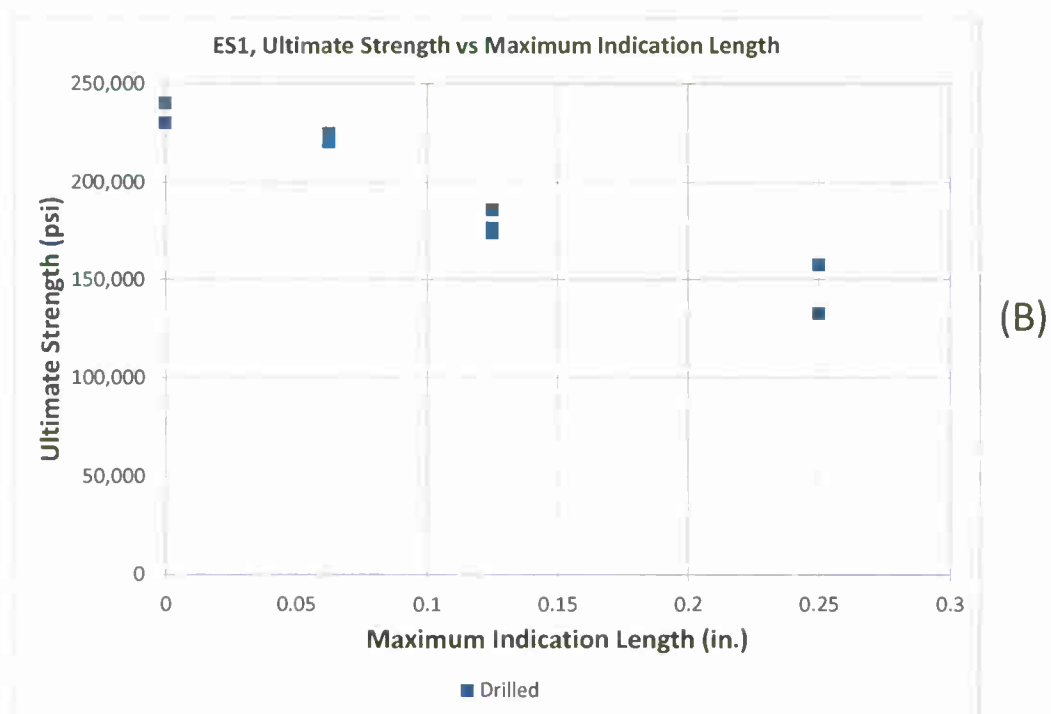
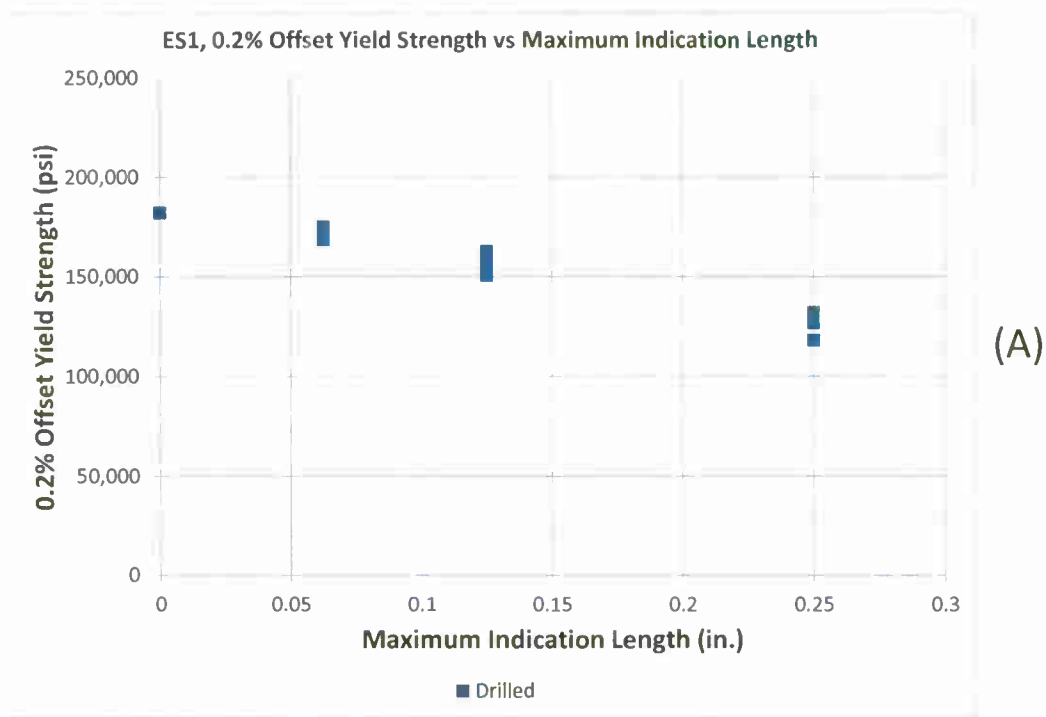


Figure 4-19 Effect of Maximum Surface Indication Length on 0.2% Yield Strength (A) and Ultimate Strength (B) of Cast ES1 Steel.

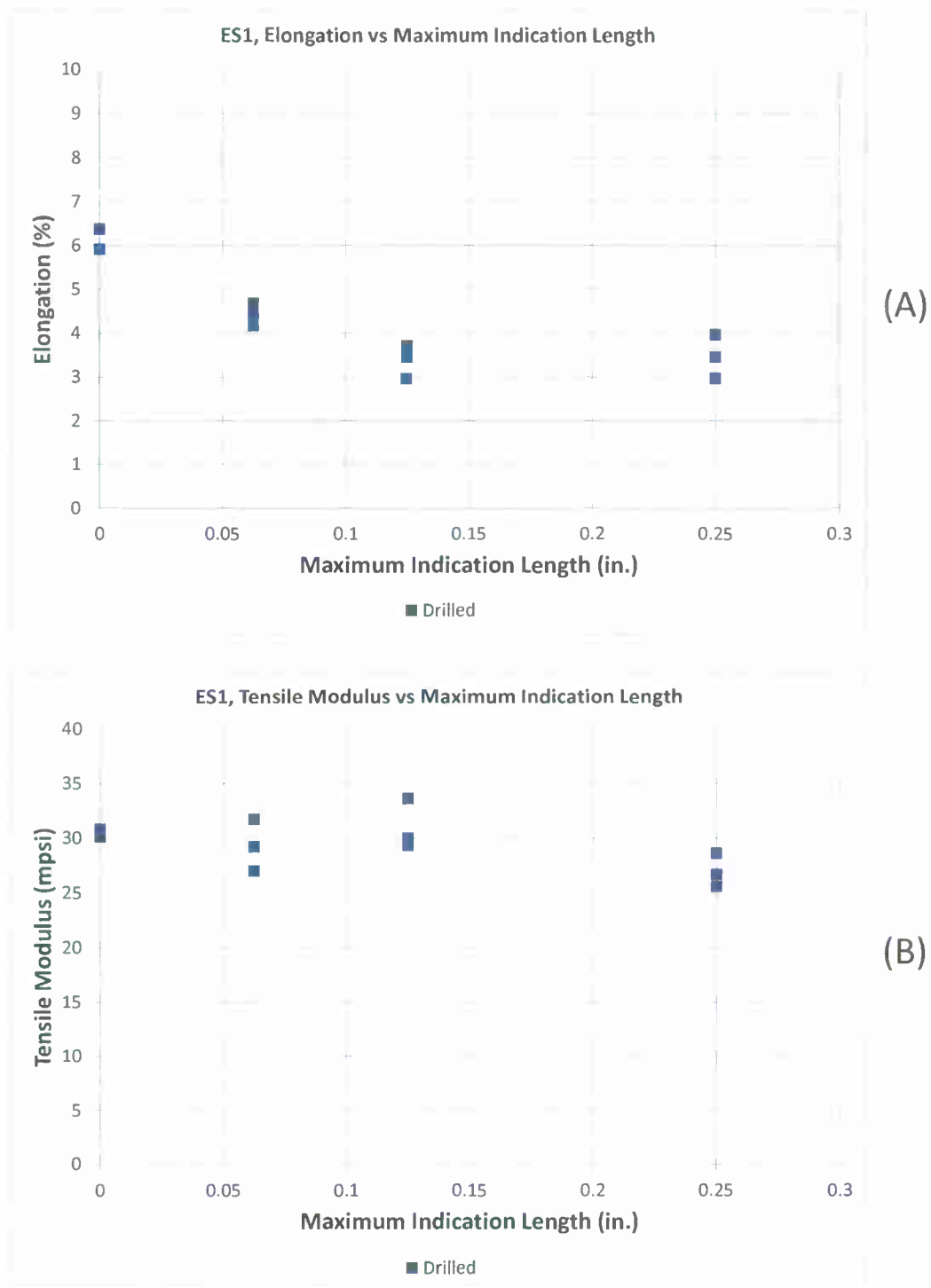


Figure 4-20 Effect of Maximum Surface Indication Length on Elongation (A) and Tensile Modulus (B) of Cast ES1 Steel.

APPENDIX 4-A

Additional Graphs for 110/80 Cast Steel

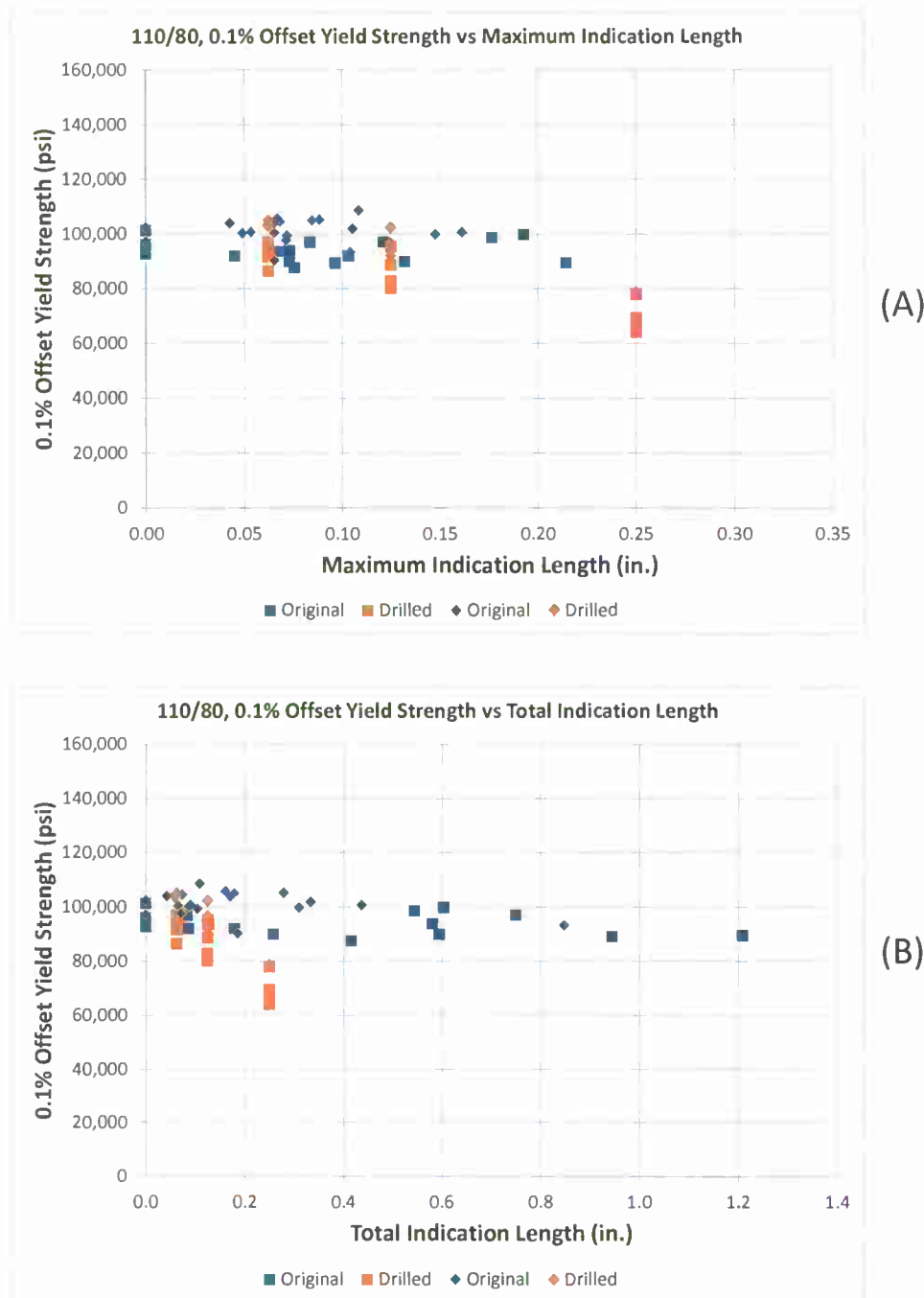


Figure 4-A-1 Effect of Maximum (A) and Total (B) Surface Indication Length on 0.1% Offset Yield Strength of Cast 110/80 Steel.

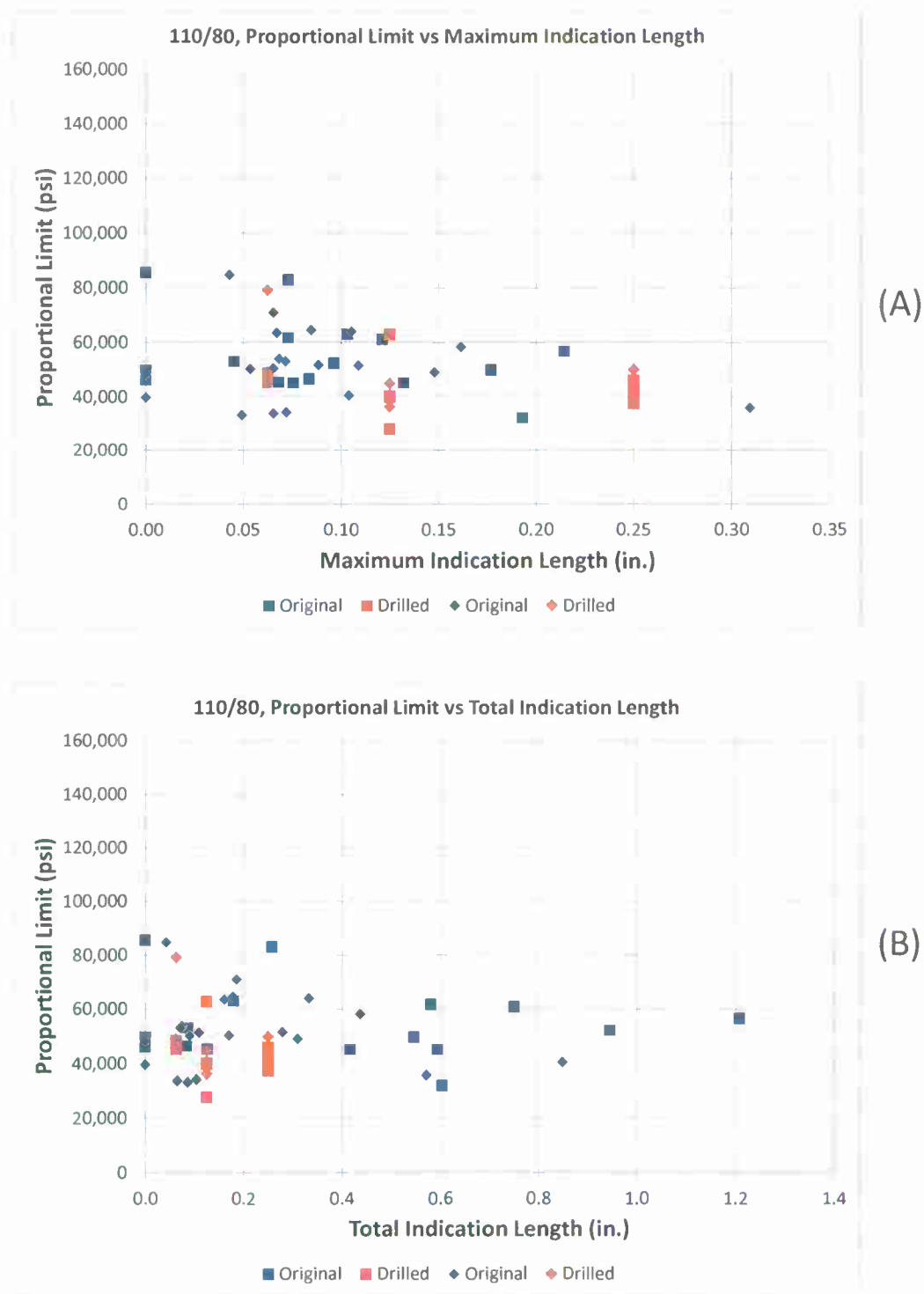


Figure 4-A-2 Effect of Maximum (A) and Total (B) Surface Indication Length on Proportional Limit of Cast 110/80 Steel.

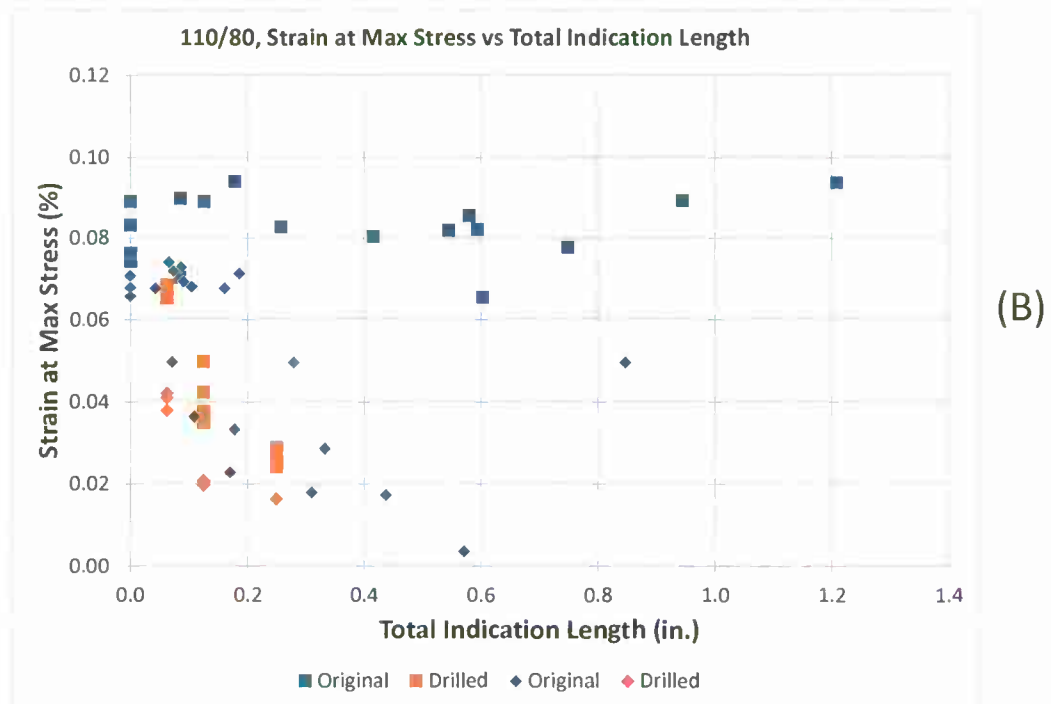
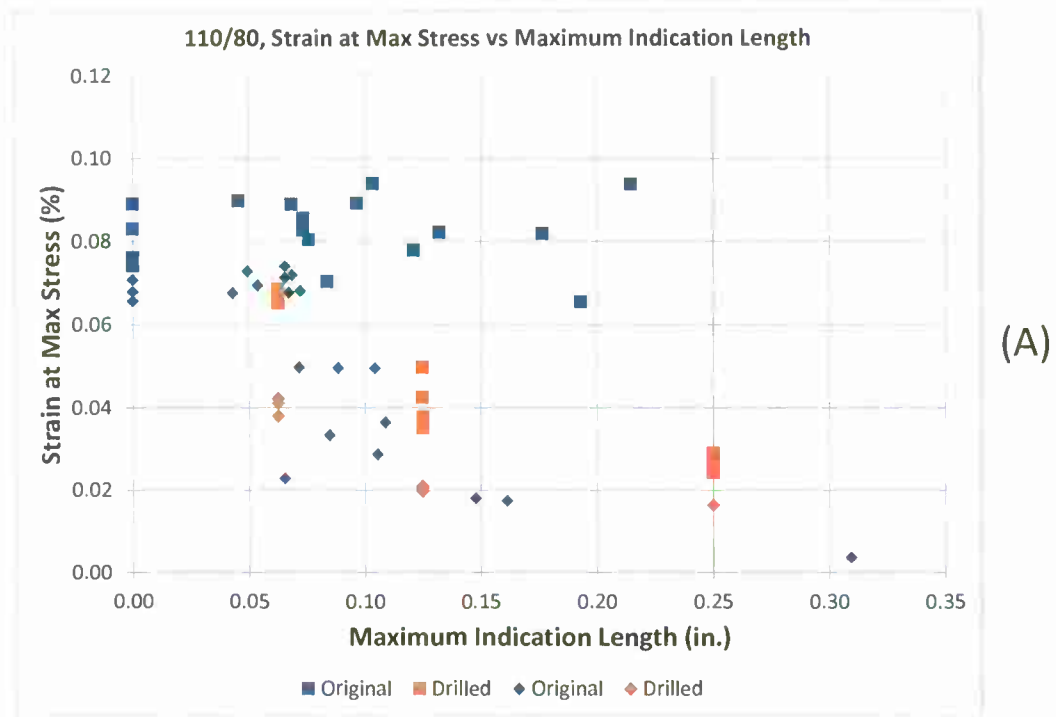


Figure 4-A-3 Effect of Maximum (A) and Total (B) Surface Indication Length on Strain at Max Stress of Cast 110/80 Steel.

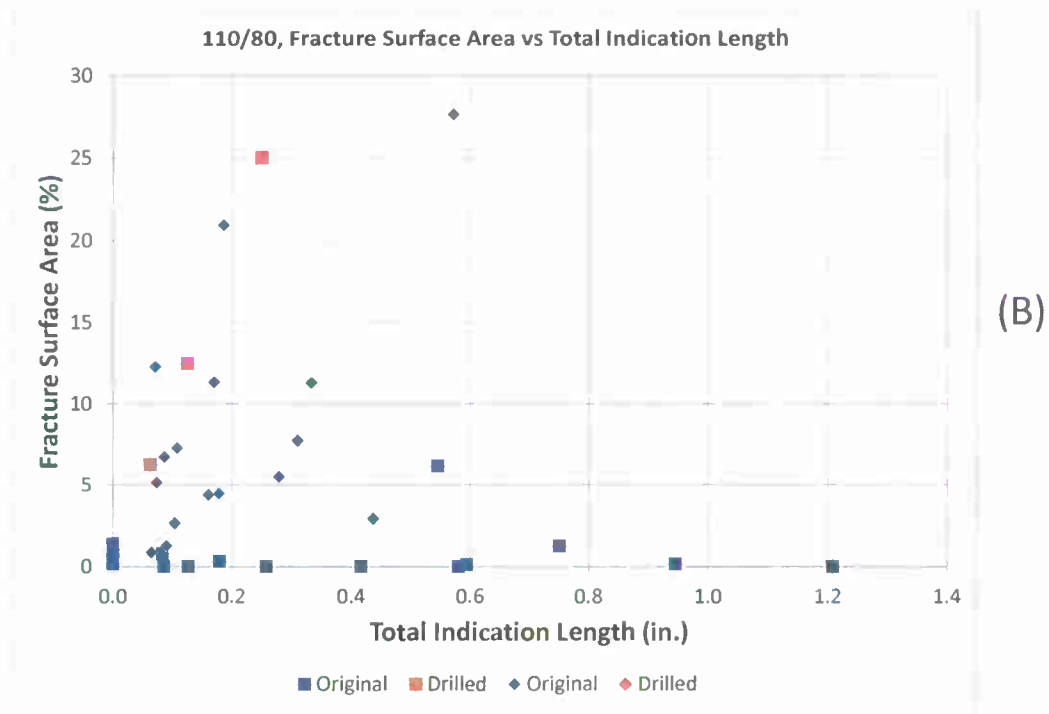
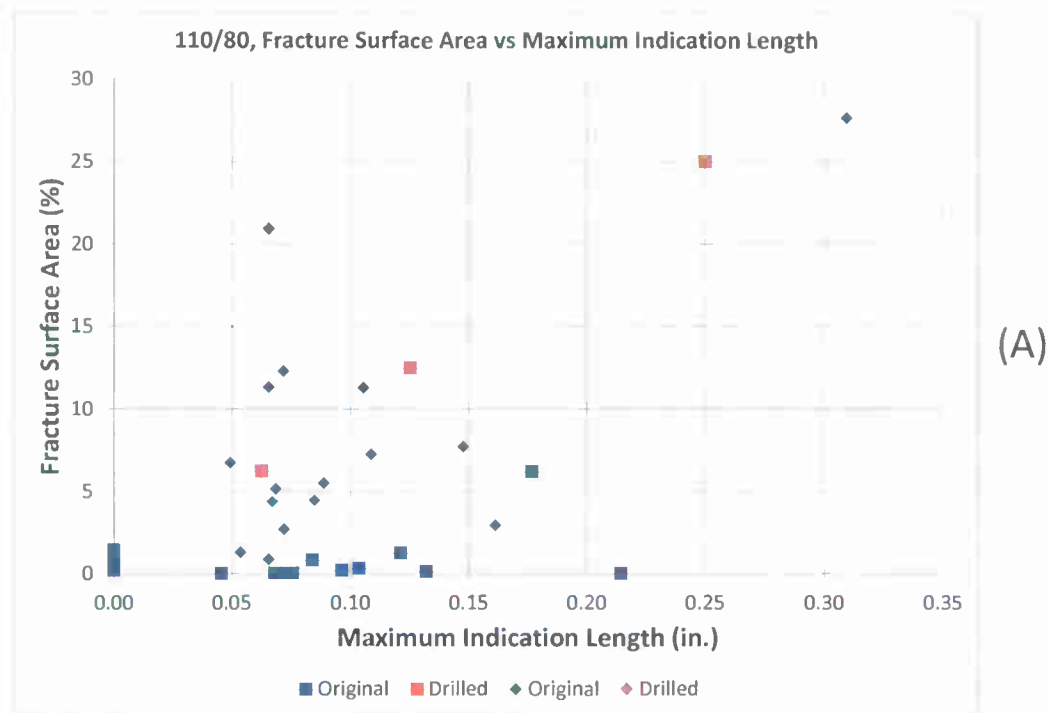


Figure 4-A-4 Effect of Maximum (A) and Total (B) Surface Indication Length on Fracture Surface Area of Cast 110/80 Steel.

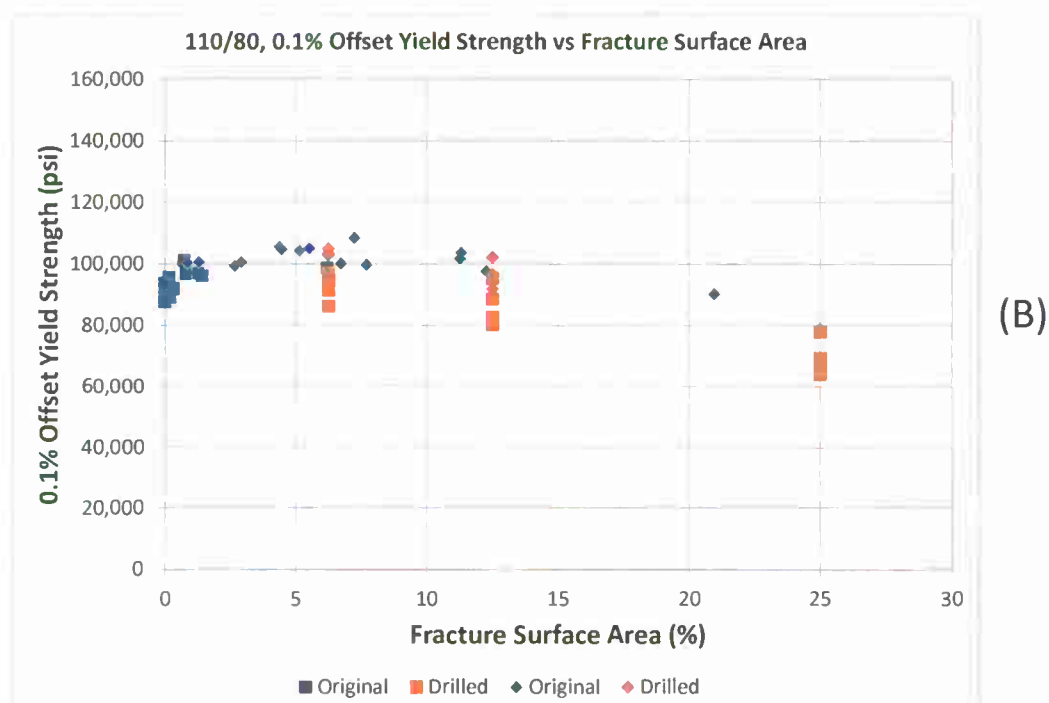
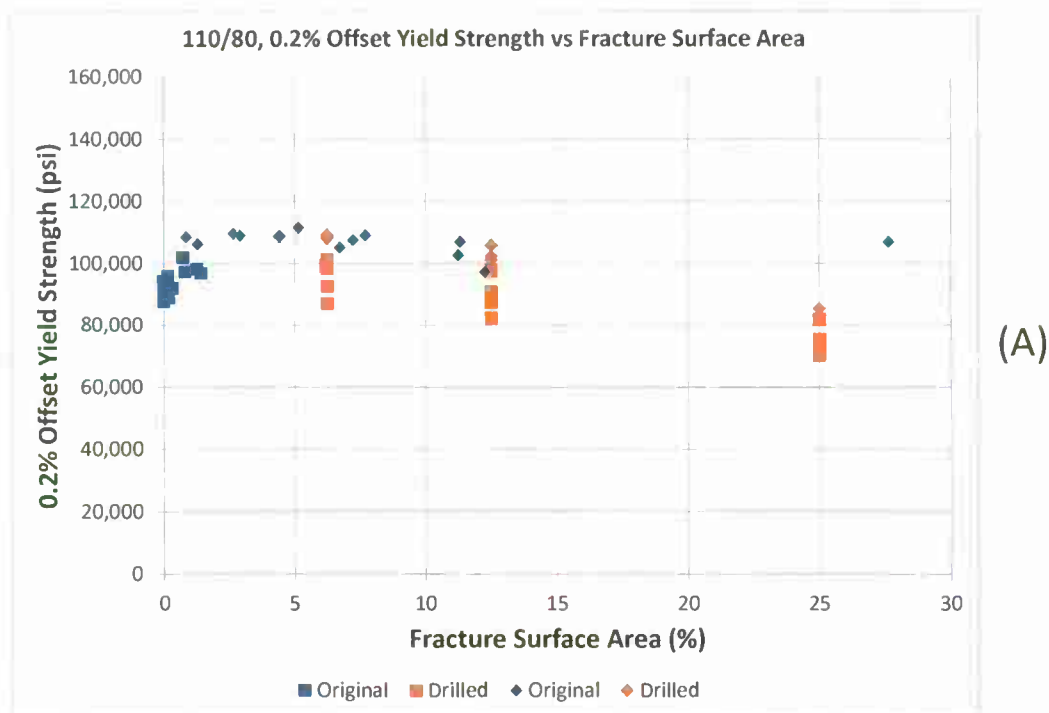


Figure 4-A-5 Effect of Fracture Surface Area on 0.2% Offset Yield Strength (A) and 0.1% Offset Yield Strength (B) of Cast 110/80 Steel.

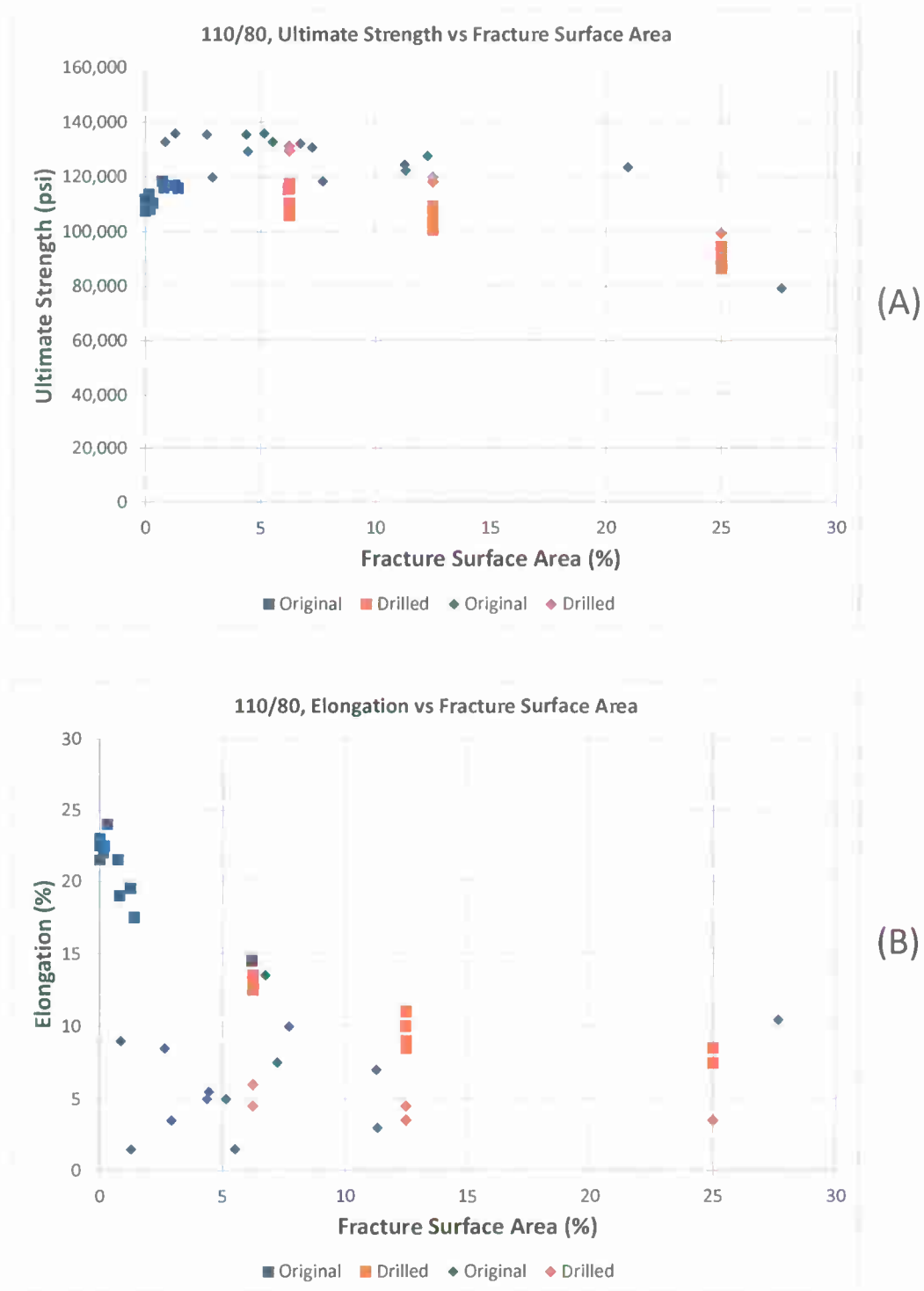


Figure 4-A-6 Effect of Fracture Surface Area on Ultimate Strength (A) and Elongation (B) Cast 110/80 Steel.

APPENDIX 4-B

Additional Graphs for 165/135 Cast Steel

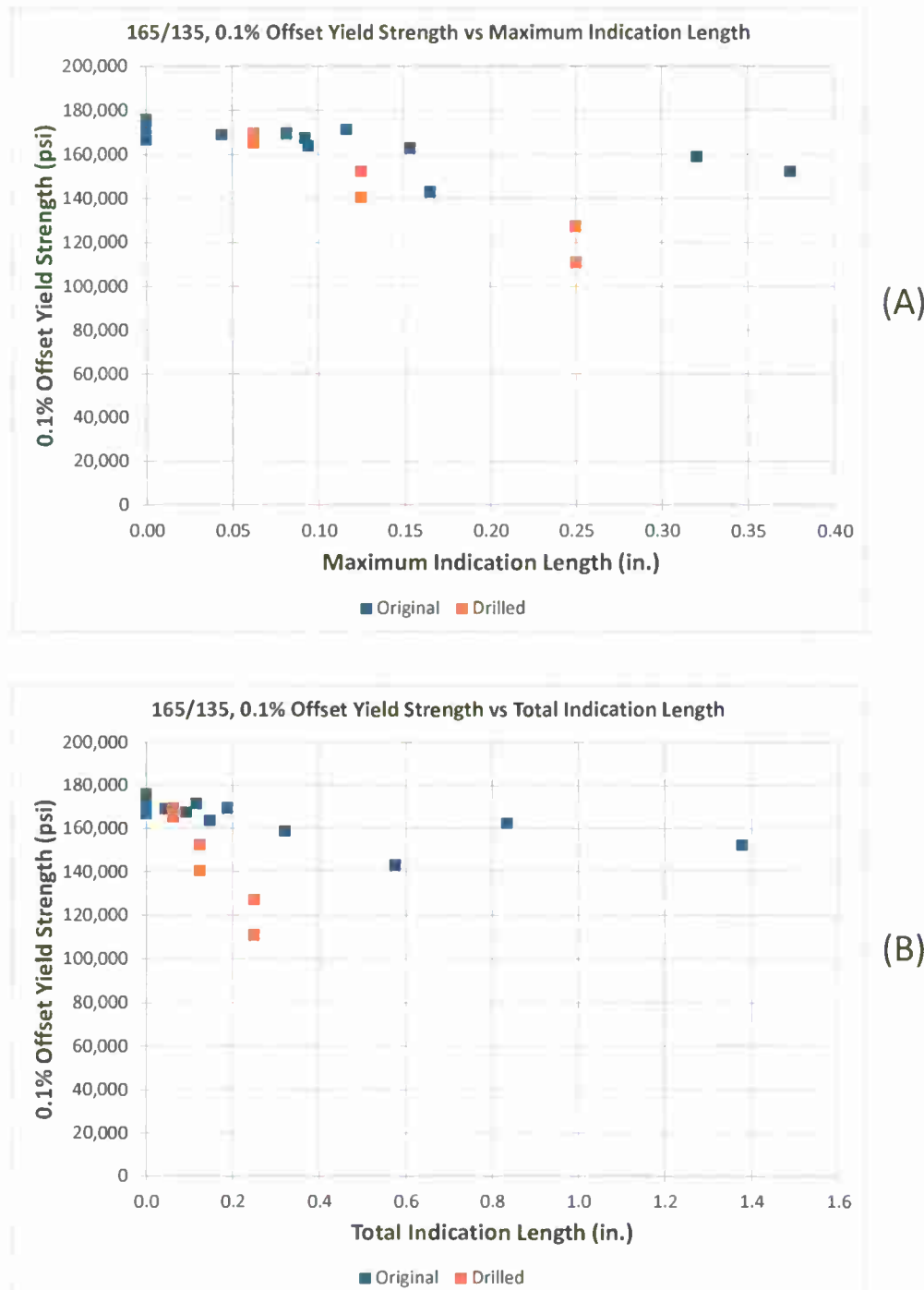


Figure 4-B-1 Effect of Maximum (A) and Total (B) Surface Indication Length on 0.1% Offset Yield Strength of Cast 165/135 Steel.

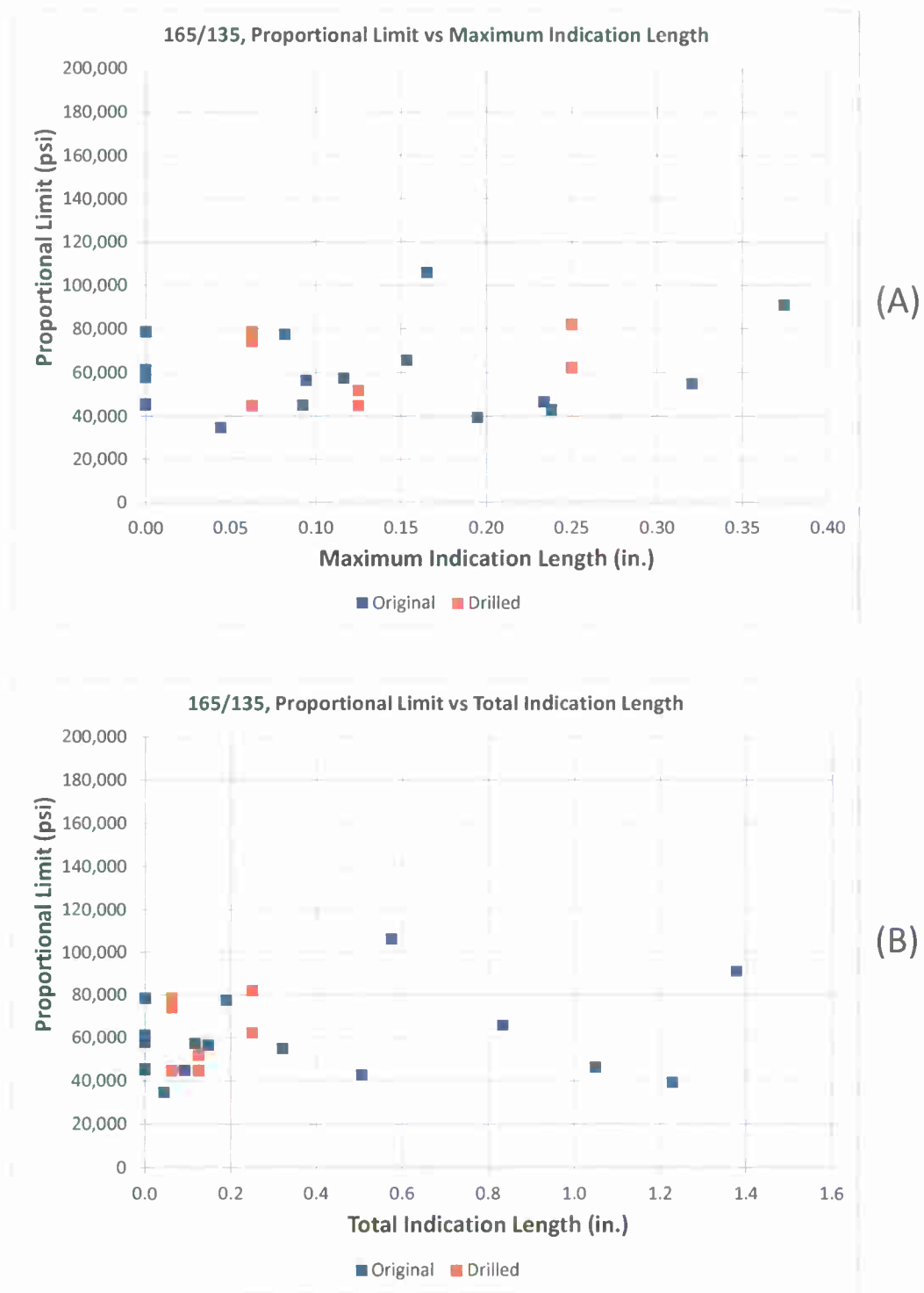


Figure 4-B-2 Effect of Maximum (A) and Total (B) Surface Indication Length on Proportional Limit of Cast 165/135 Steel.

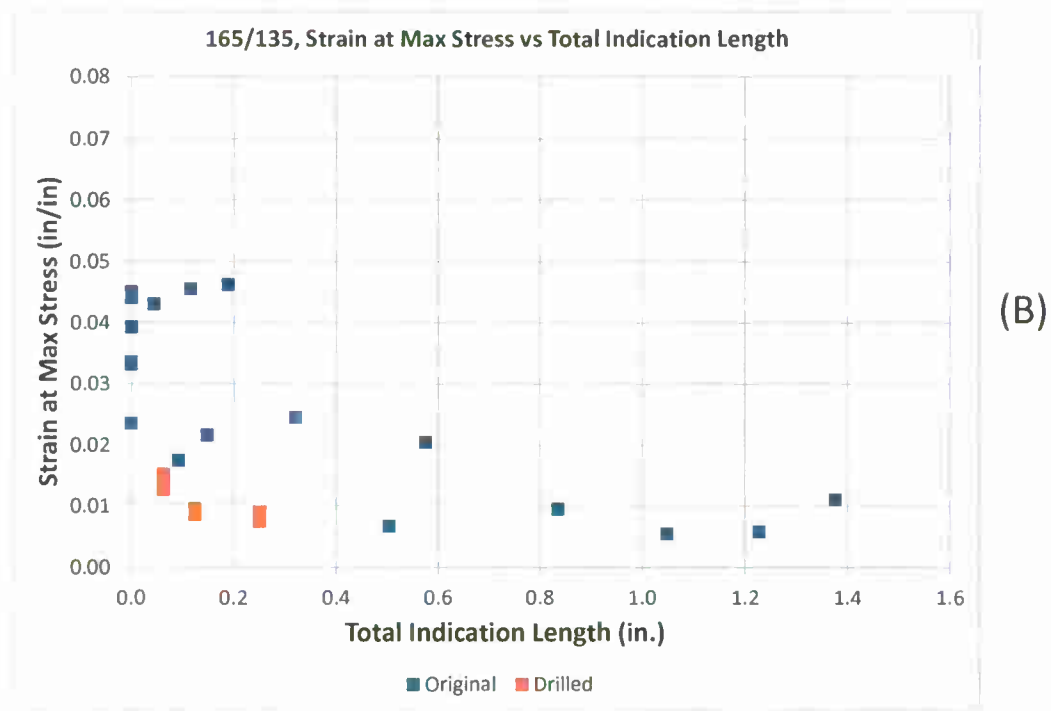
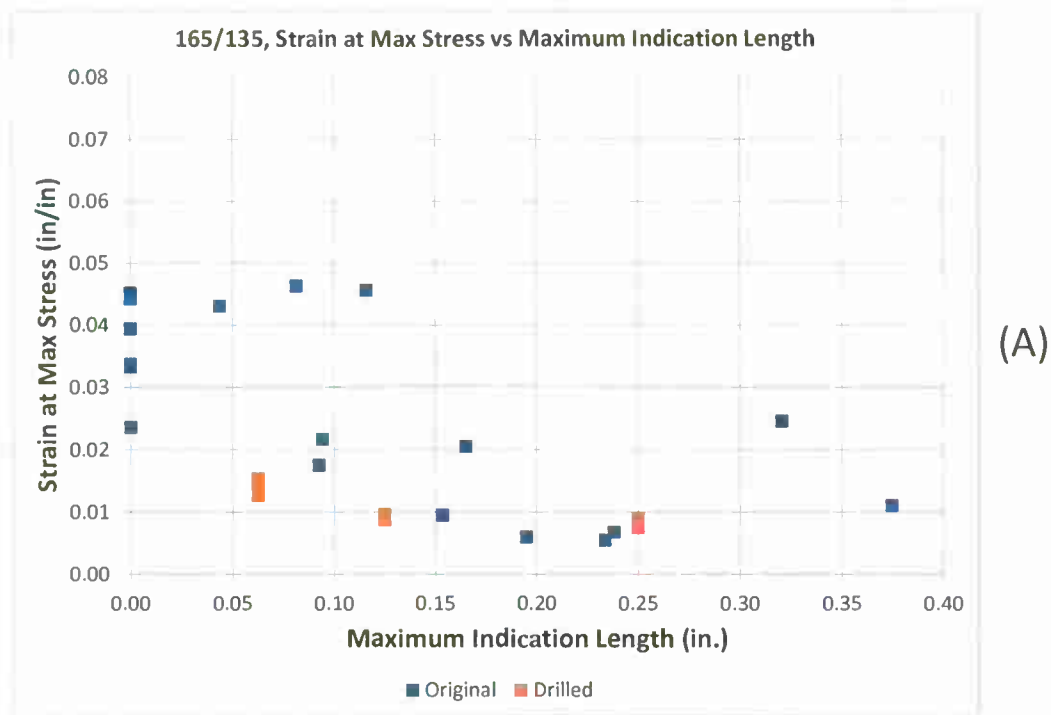


Figure 4-B-3 Effect of Maximum (A) and Total (B) Surface Indication Length on Strain at Max Stress of Cast 165/135 Steel.

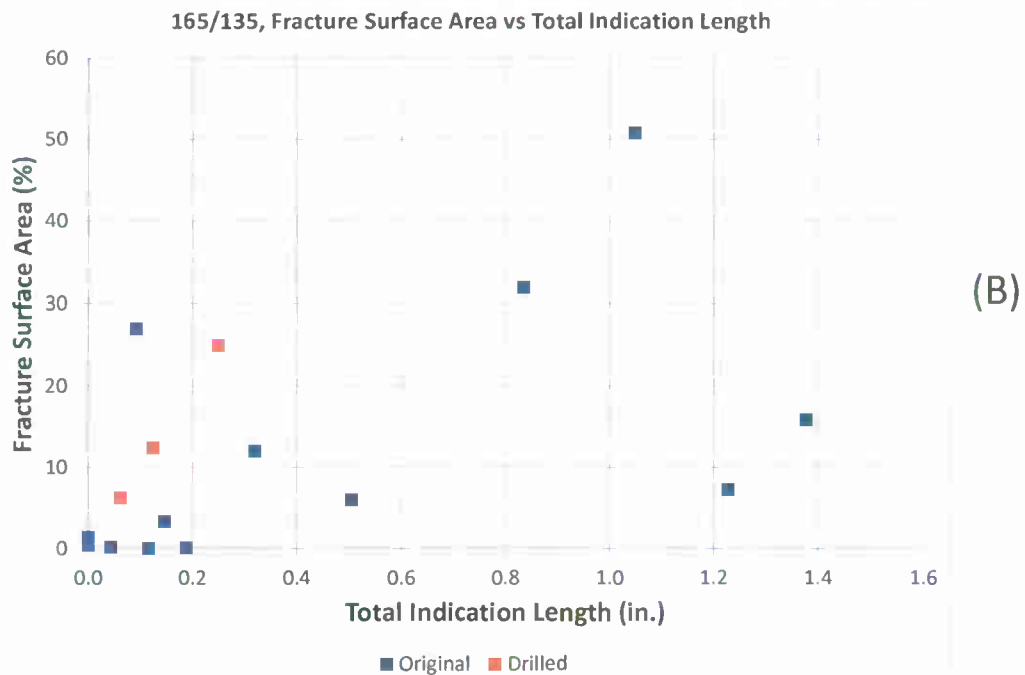
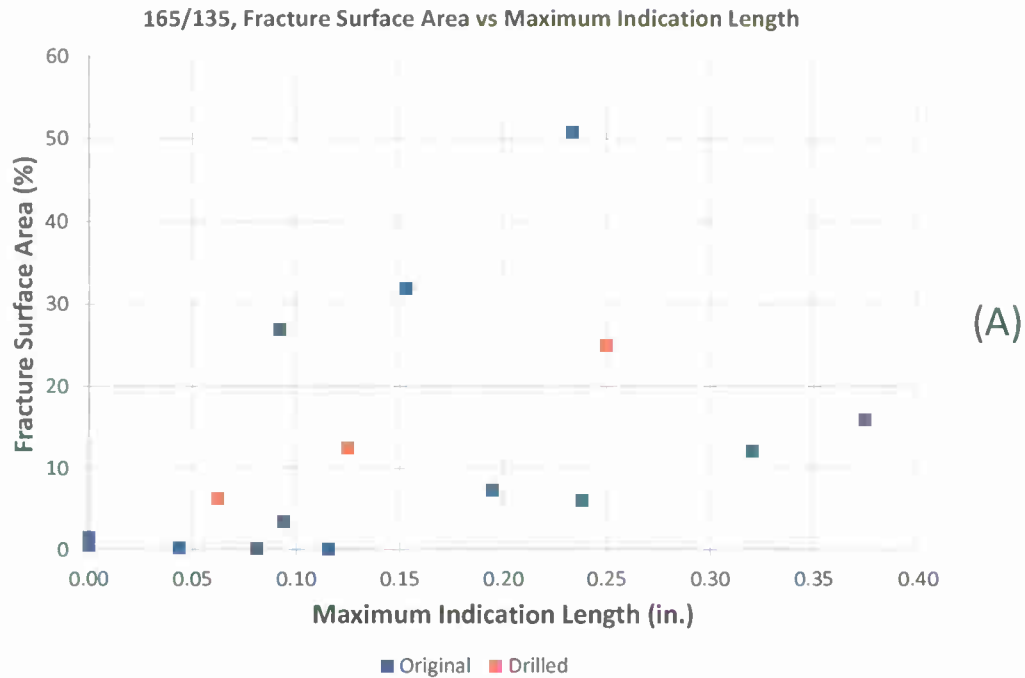


Figure 4-B-4 Effect of Maximum (A) and Total (B) Surface Indication Length on Fracture Surface Area of Cast 165/135 Steel.

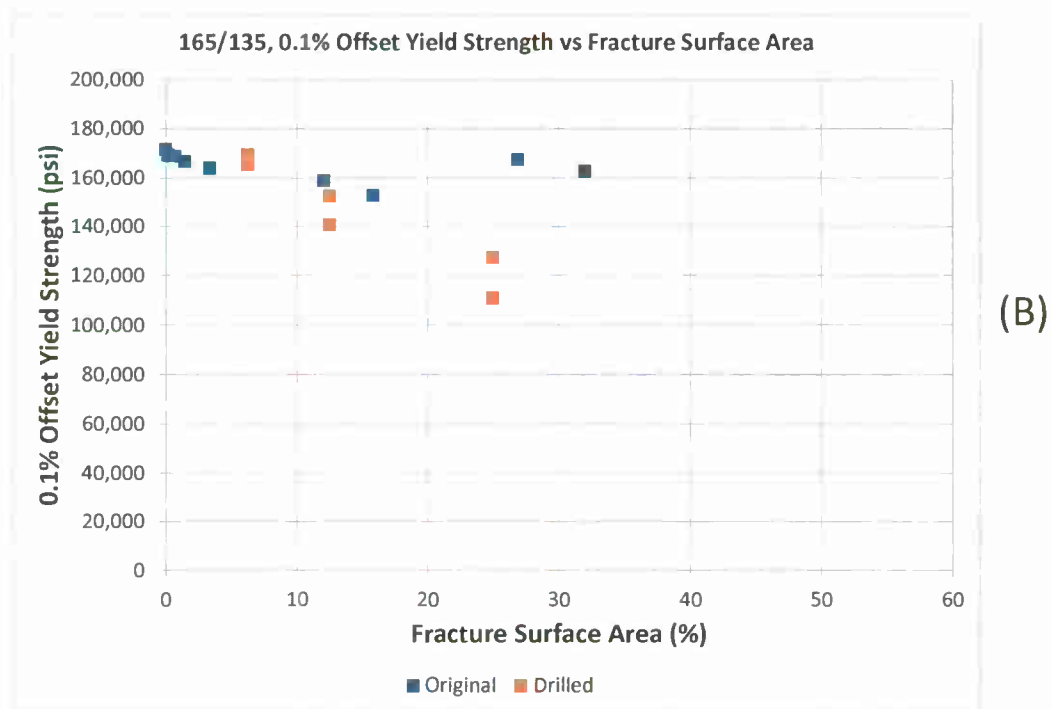
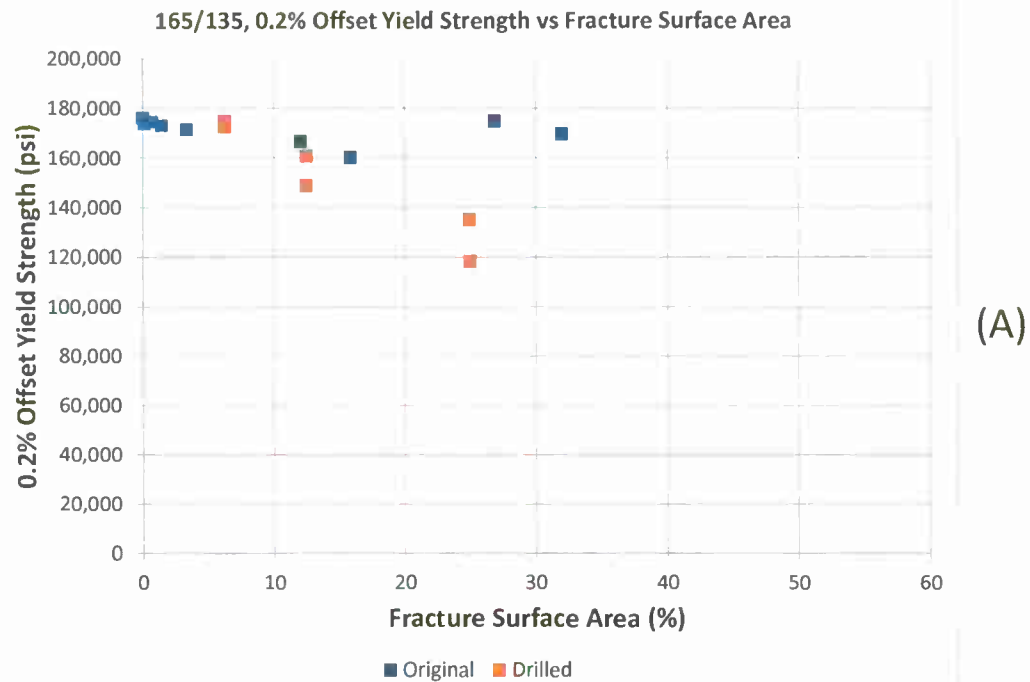


Figure 4-B-5 Effect of Fracture Surface Area on 0.2% Offset Yield Strength (A) and 0.1% Offset Yield Strength (B) of Cast 165/135 Steel.

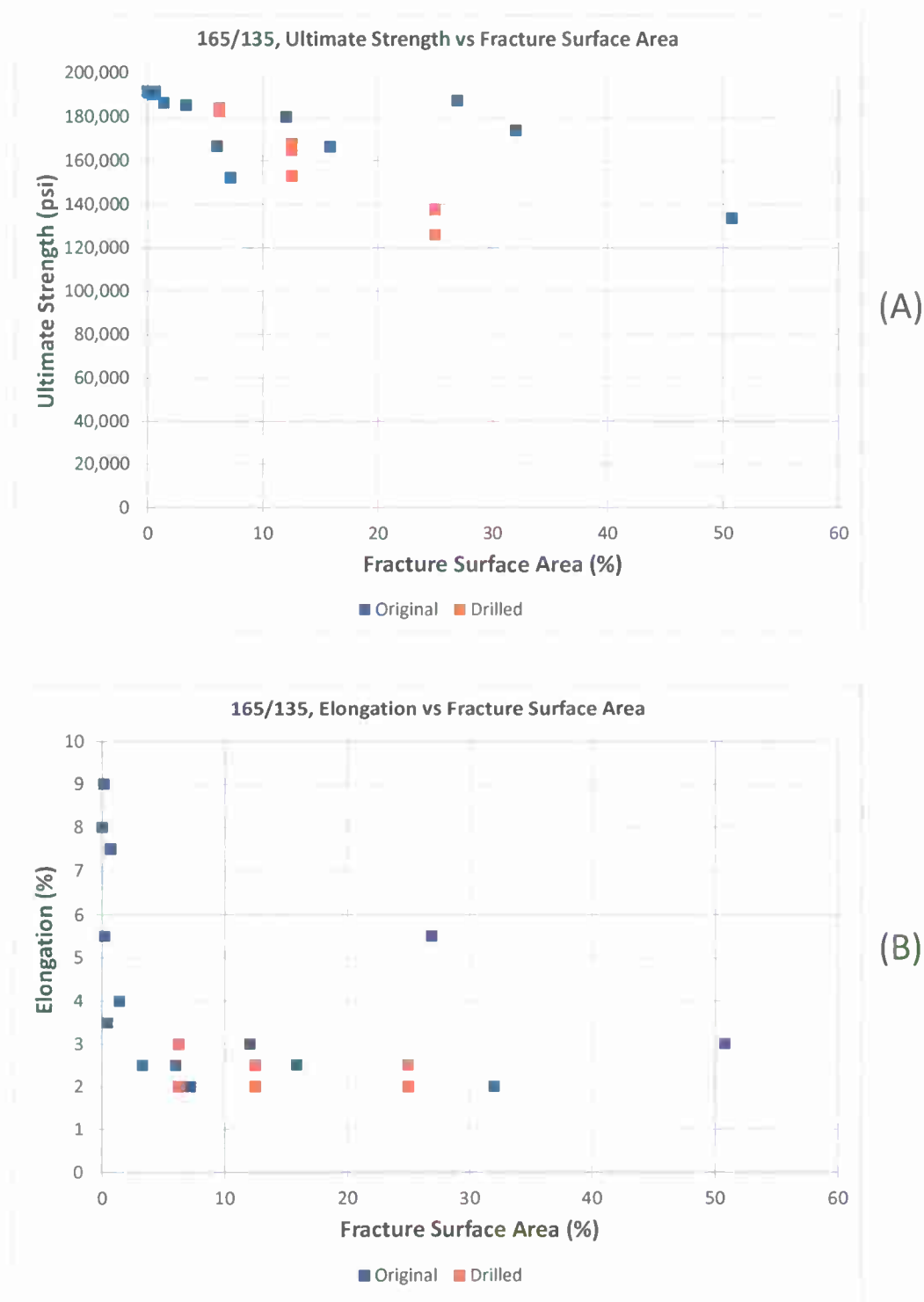


Figure 4-B-6 Effect of Fracture Surface Area on Ultimate Strength (A) and Elongation (B) Cast 165/135 Steel.

APPENDIX 4-C

Additional Graphs for CF8 Cast Steel

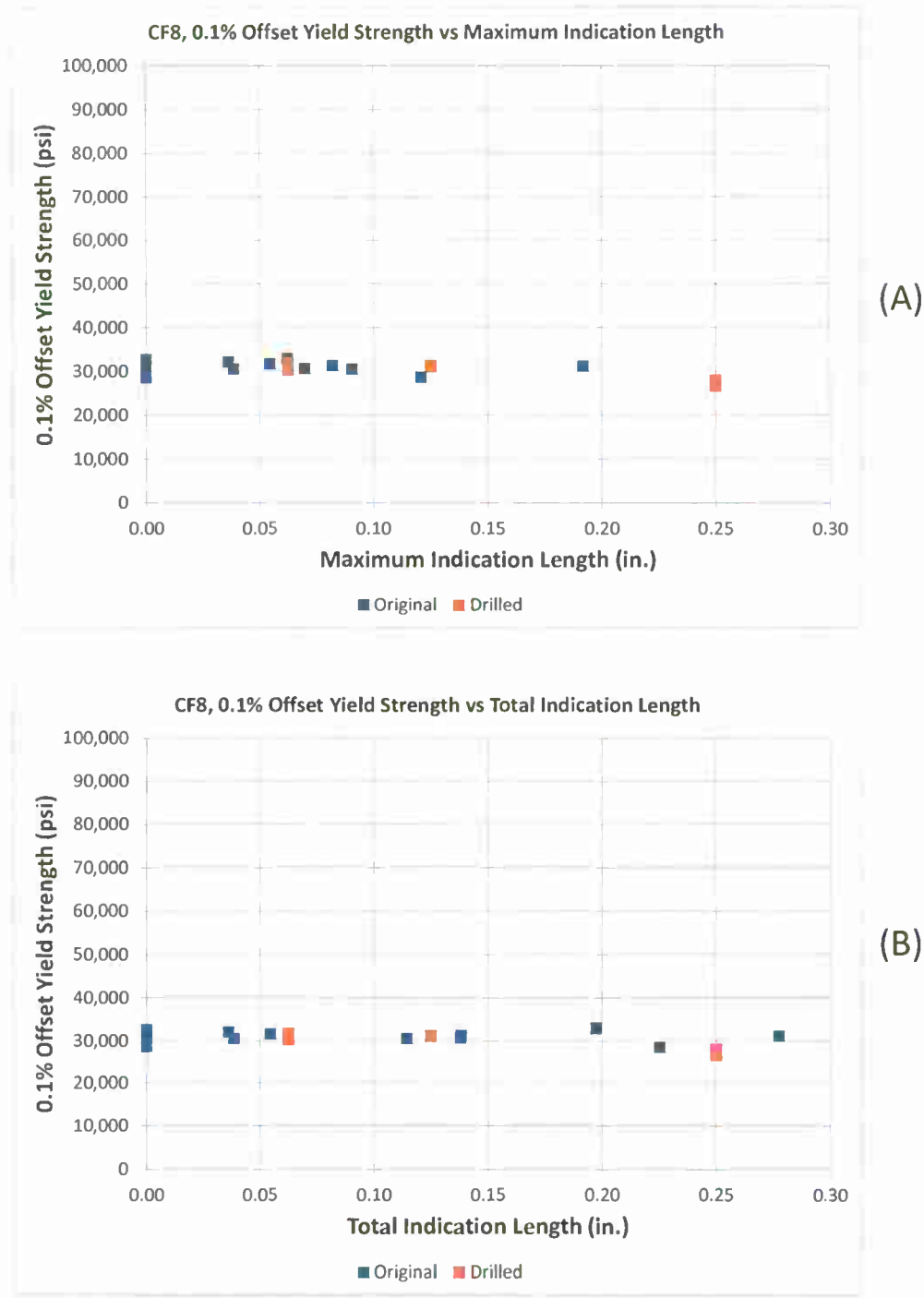


Figure 4-C-1 Effect of Maximum (A) and Total (B) Surface Indication Length on 0.1% Offset Yield Strength of Cast CF8 Steel.

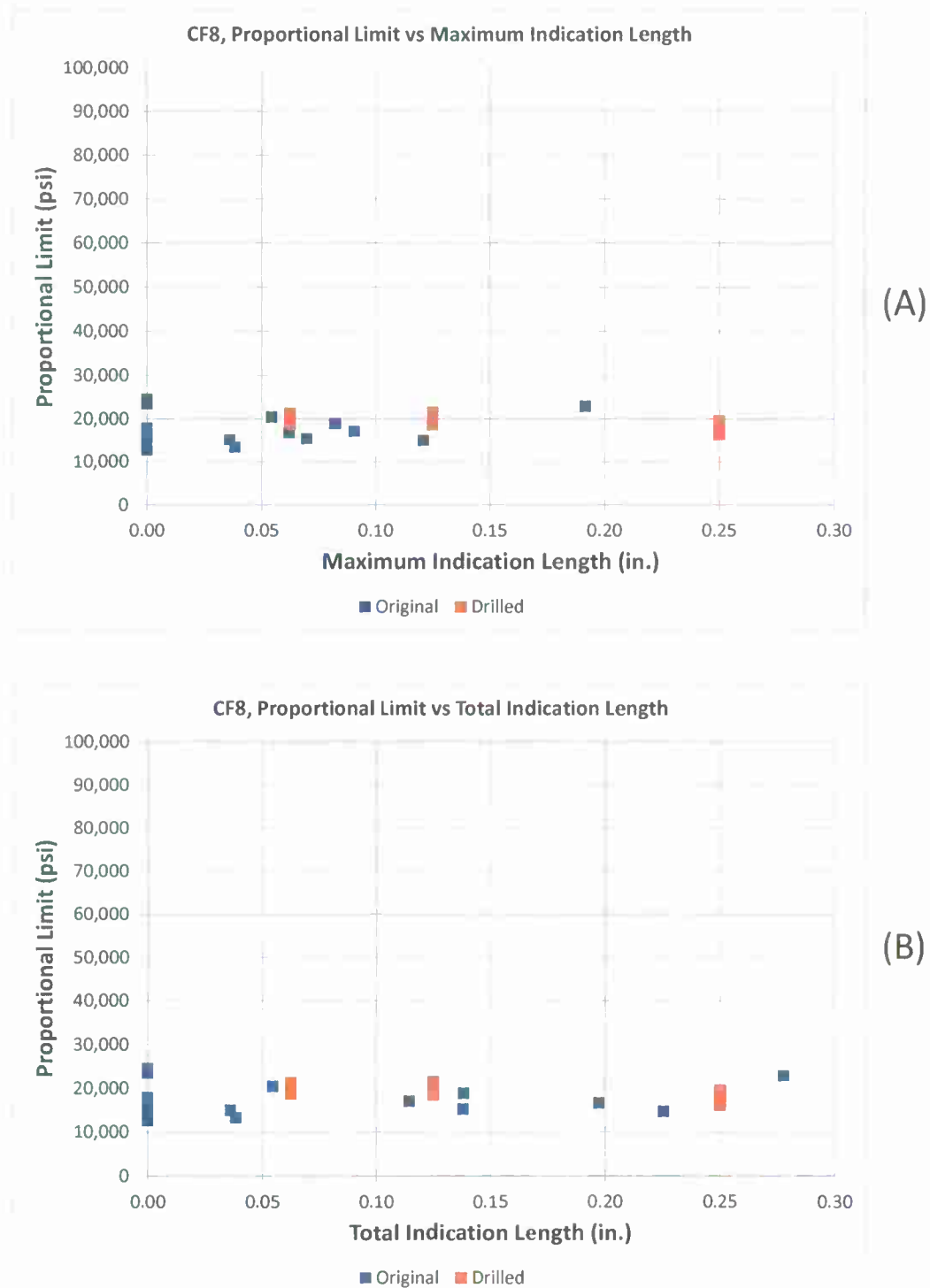


Figure 4-C-2 Effect of Maximum (A) and Total (B) Surface Indication Length on Proportional Limit of Cast CF8 Steel.

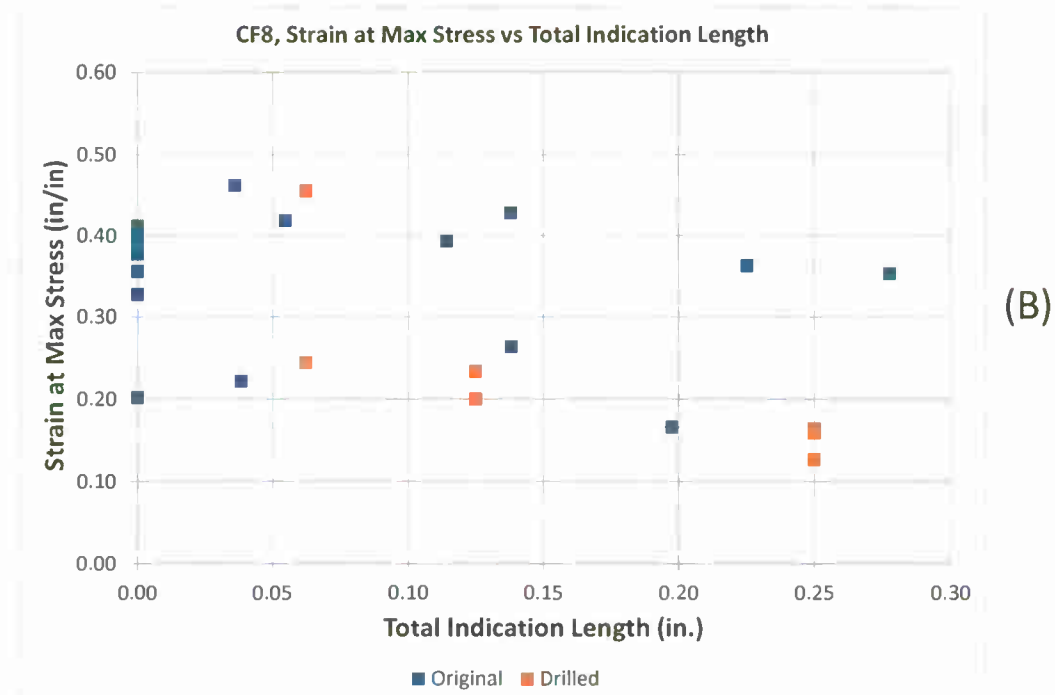
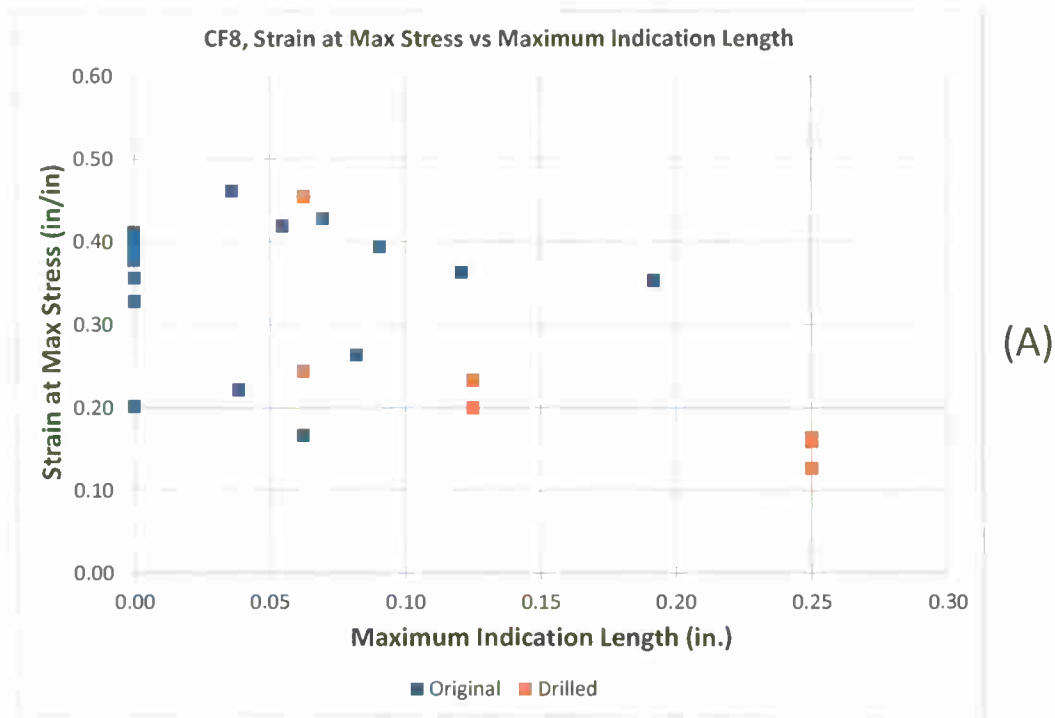


Figure 4-C-3 Effect of Maximum (A) and Total (B) Surface Indication Length on Strain at Max Stress of Cast CF8 Steel.

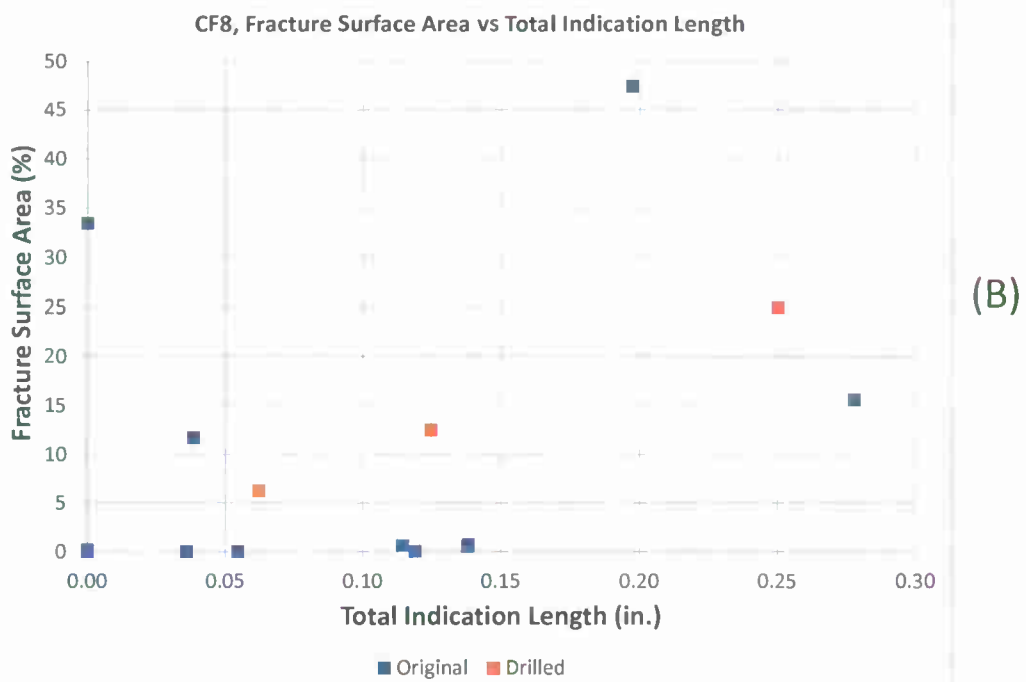
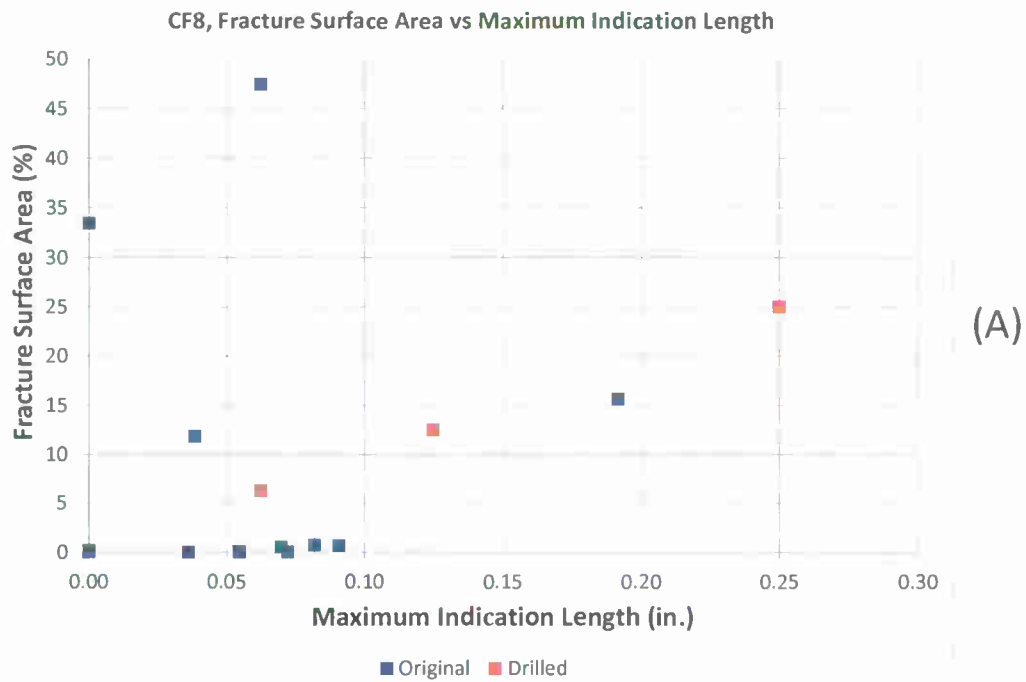


Figure 4-C-4 Effect of Maximum (A) and Total (B) Surface Indication Length on Fracture Surface Area of Cast CF8 Steel.

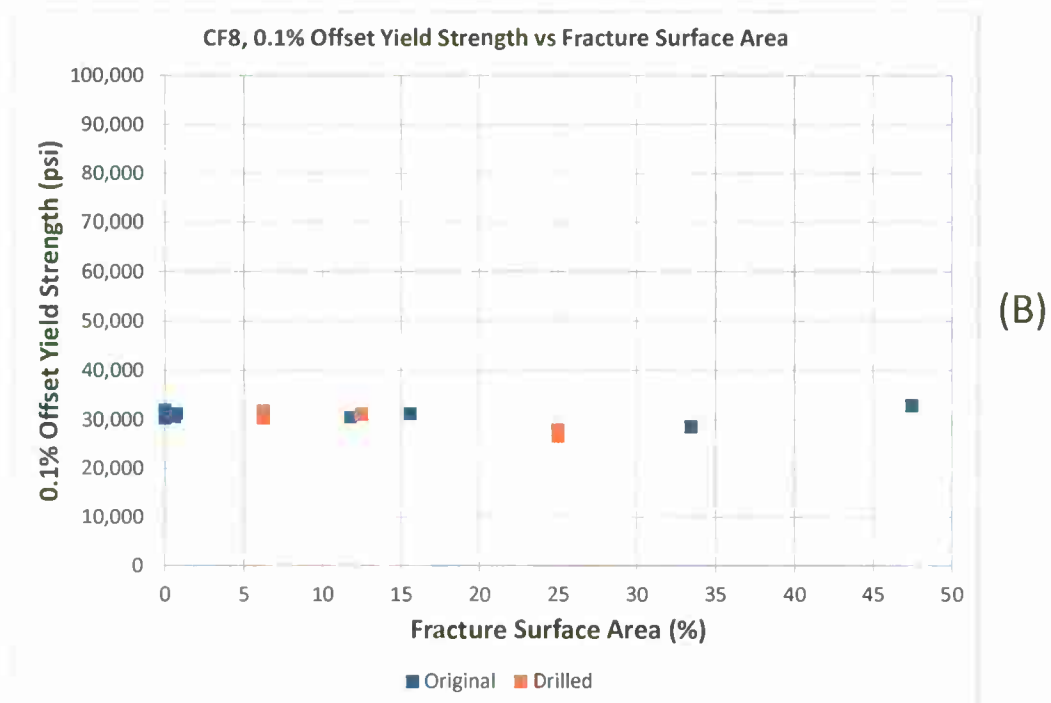
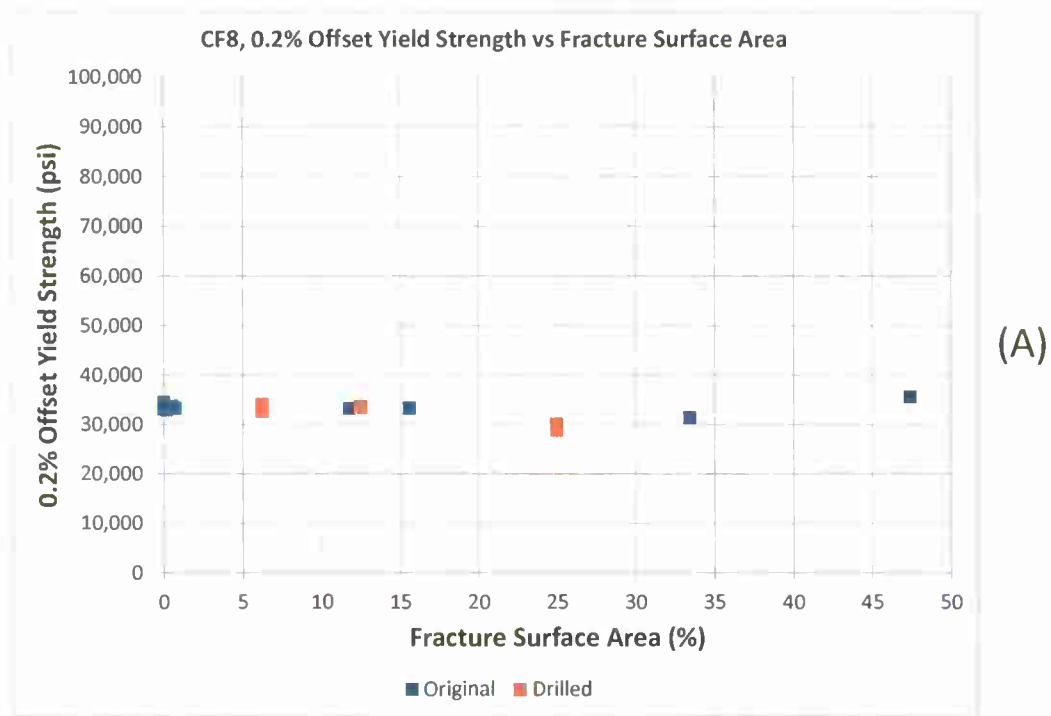


Figure 4-C-5 Effect of Fracture Surface Area on 0.2% Offset Yield Strength (A) and 0.1% Offset Yield Strength (B) of Cast CF8 Steel.

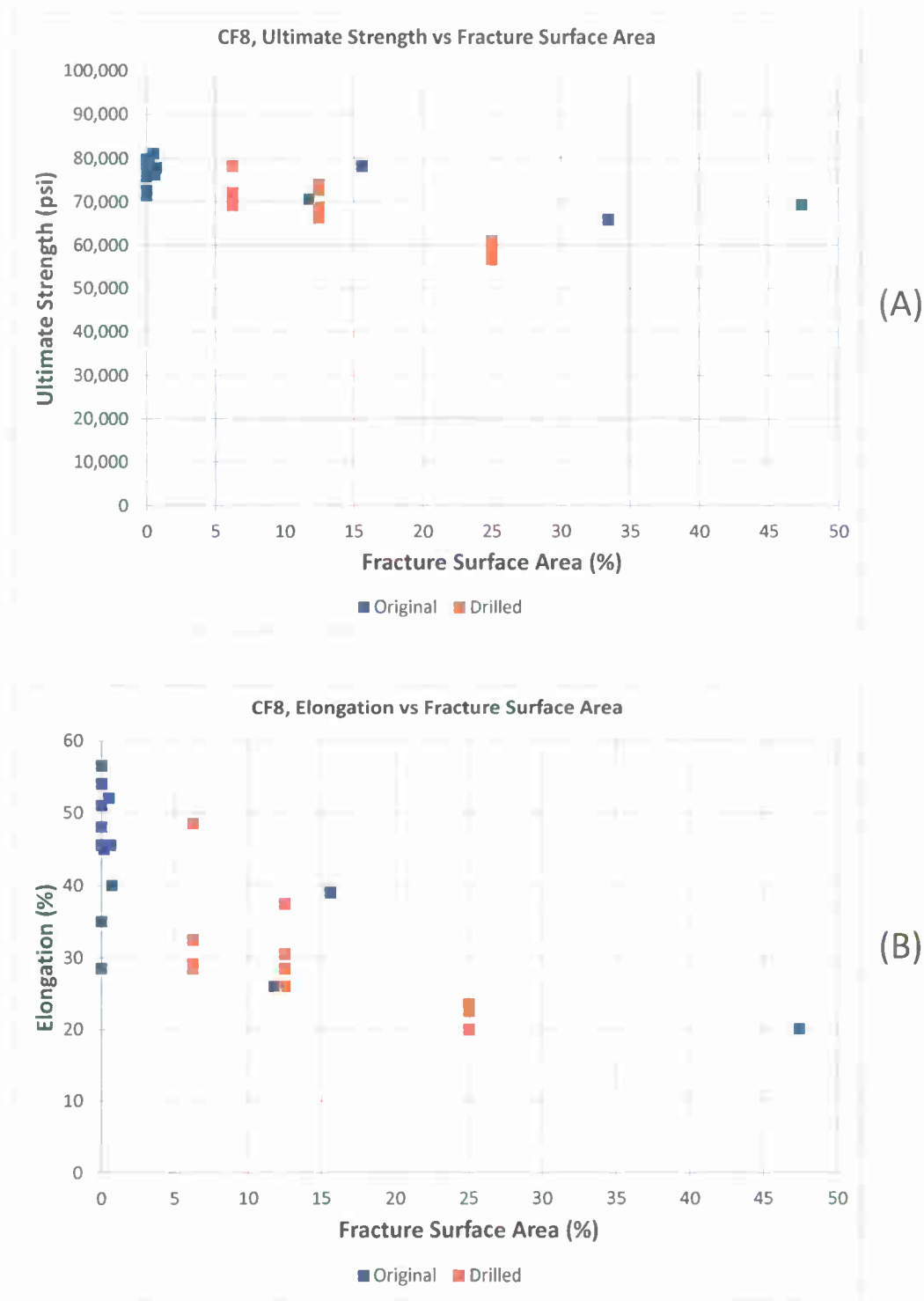


Figure 4-C-6 Effect of Fracture Surface Area on Ultimate Strength (A) and Elongation (B) Cast CF8 Steel.

APPENDIX 4-D

Additional Graphs for ES1 Cast Steel

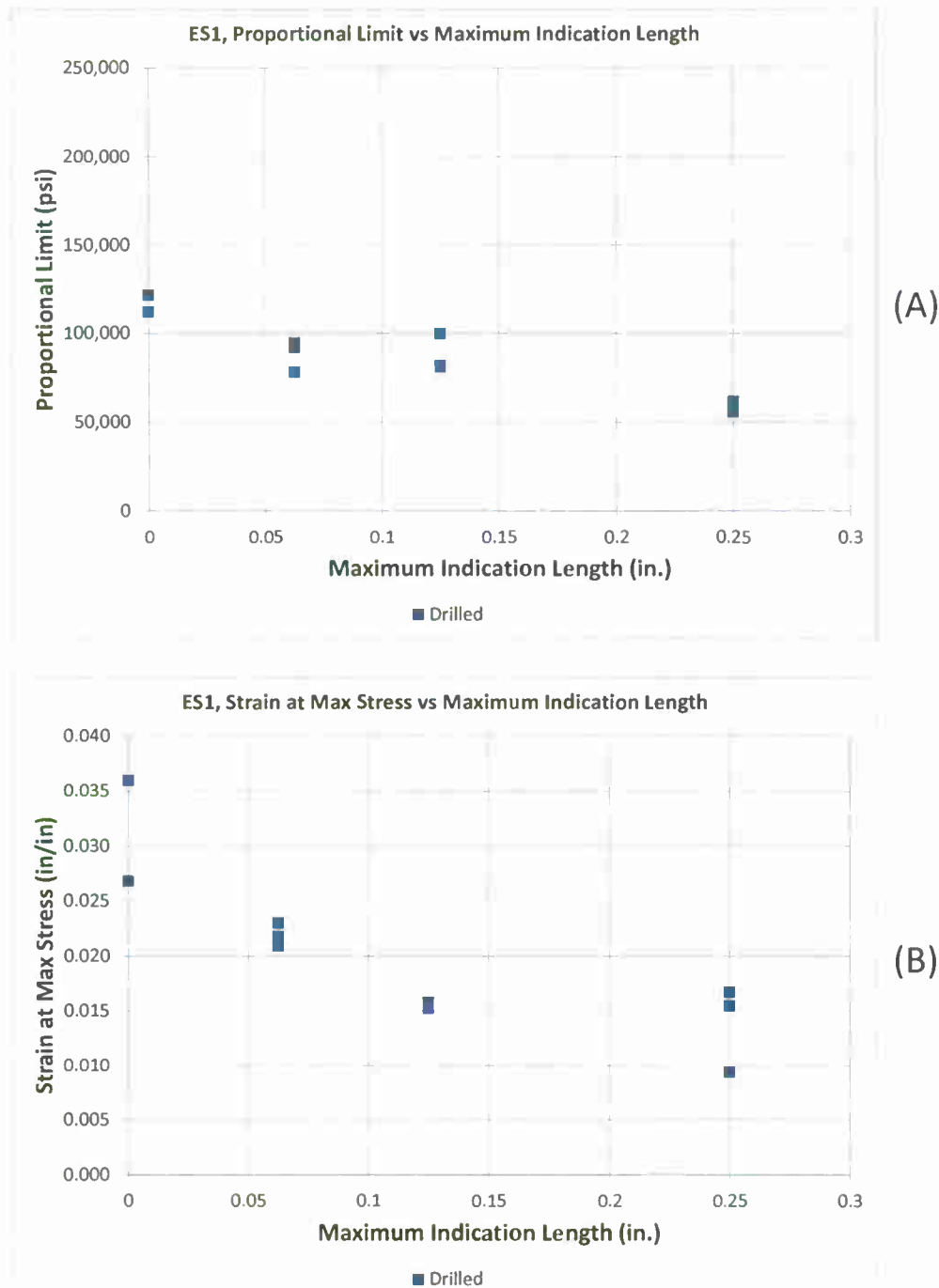


Figure 4-D-1 Effect of Maximum Surface Indication Length on Proportional Limit (A) and Strain at Max Stress (B) of Cast ES1 Steel.

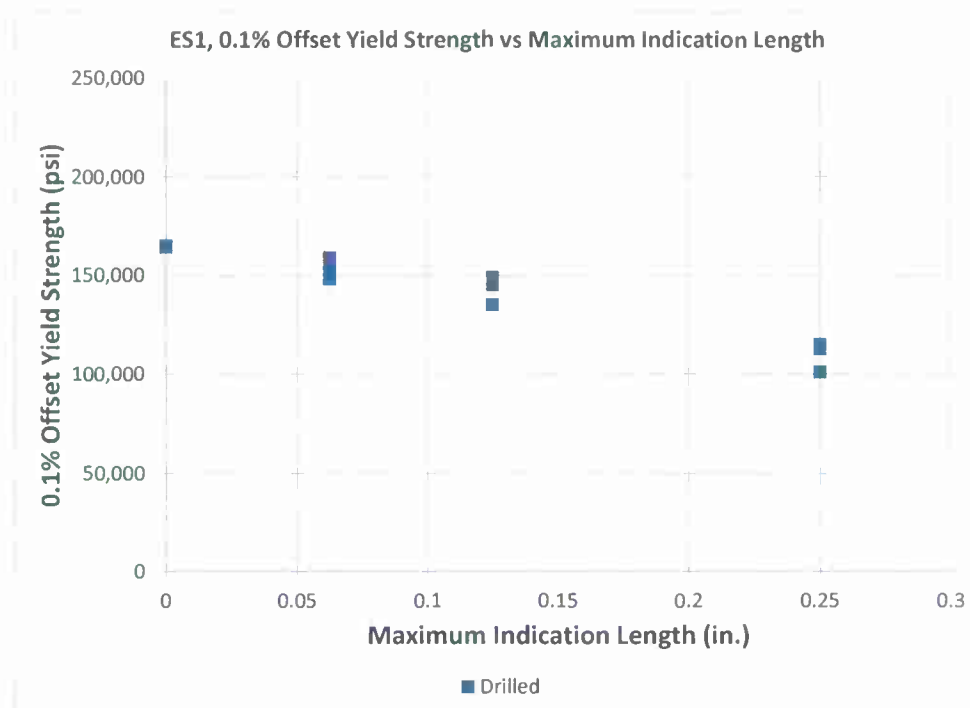


Figure 4-D-2 Effect of Maximum Surface Indication Length on 0.1% Offset Yield Strength of Cast ES1 Steel.

5. Industry Capabilities for Preparedness and Sustainment/Process Capability Improvements for Cast Metals Industry: Principal Investigator Jerrod A. Weaver, Non-Ferrous Founders' Society

The Department of Defense requires that each military service determines their material and parts requirements to attain and sustain operational objectives. As part of this effort, Industrial base capability assessments are a critical component to the DoD's ability to effectively plan for the availability of spare parts for weapon systems support. However, in the absence of data for industry's current capability, assessments may be unreliable, resulting in reduced readiness due to impractical lead times (too long or too short), low material availability, inventory shortfalls, etc.

The cast metals industry plays a key role in manufacturing spare parts for weapon systems support. Coupled with the number of unfilled orders related to castings, required lead times to deliver cast parts, and the diminishing number of metalcasters, there is a clear need to assess this industry's capabilities to improve the military's spare parts management.

The objective of this program was to leverage the Defense Casting Suppliers Database and the Cast Tooling Database created as part of DLA's Castings for Improved Readiness initiative, to gather data from those metalcasters currently supplying defense-related parts. The information collected would be readily accessible to both government personnel and defense contractors to enable the identification of potential supply chain problems so that certain strategies can be enacted to mitigate these risks. In addition, the information can assist in the reduction of backorders, costs, and lead-times, through the enhanced capability of identifying capable casting sources and adjusting production lead-time projections to reflect available industry capability.

As part of the customer requirements phase of the project, NFFS received cooperation through the Army RDECOM Industrial Base Information Technology Team at Rock Island Arsenal (RIA) and the Industrial Base Management Group, part of Life Cycle Management Command (LCMC) at TACOM to determine the data to be collected from the foundries and how to integrate the information within the Army's industrial base systems.

The initial project plan was to conduct a formal industry capability study to include specific industry variables such as capacity utilization, lead-times, production constraints, and workforce issues. But after consulting with the government participants at Rock Island and TACOM coupled with feedback from defense contractors, it was recommended that the focus should be on detailed foundry manufacturing capabilities of those that supply military castings that may not be readily available through existing directories. Furthermore, it was recommended that the information gathered would provide the most benefit in a public domain rather than contained within an Army or DLA system, so that it would be accessible beyond government personnel and easy for industry to provide ongoing updates. To this end, it was determined to expand the Defense Casting Supplier Database and integrate the information gathered through this project.

The new capability information defined by both government and defense contractors included:

Casting Envelope – metalcasters provided their maximum casting size capabilities in terms of length x width x height in units of inches. The casting buyer has the capability to search for specific size dimensions.

Flask Size – for sand casting applications, minimum and maximum flask size is important to determine the metalcasters mold size parameters. The casting buyer has the capability to search specific flask size dimensions.

Approved Sources – as part of the study, foundries provided key OEM and prime companies for which the foundry is currently an approved manufacturing source. There are currently more than 25 OEM/Prime companies that can be searched including Boeing, General Dynamics, BAE Systems, and Raytheon. This capability simplifies the qualification process of a defense contractor seeking an approved foundry source.

Simulation Capability – in addition to those foundries that have rapid prototyping capabilities to deliver on small quantity and surge orders, identifying those metalcasters that employ casting simulation modeling was an important criterion for defense contractors.

Quality Certifications – beyond the ability to search for companies that were certified to ISO 9001, the Army personnel expressed in interest in the ability to search metalcasters that were certified to the TS 16949 automotive standard. Additionally, contractors have been under increased pressure to seek out subcontractors that are ITAR (International Traffic in Arms Regulations) registered so foundries with ITAR registrations were included in the study.

Other information was also gathered including core making processes, monthly production capacity, and percentage of business related to the defense industry. Furthermore, other existing fields were expanded to include materials cast, federal supply classifications, and secondary operations. And because the defense casting supplier database was leveraged, it was feasible to expand the original proposed scope of capability study beyond those foundries that manufacture components for the military to include foundries that produce components for all military services.

The other component of this project was to select an Army weapon system that had both strong anticipated demand and a large number of cast components. The objective was to leverage the NFFS Procurement Solutions Network model to actively monitor the procurements of those cast parts for the weapon system and direct them to both capable casting suppliers and those foundries that may already have tooling available. After review with RIA



Figure 5-1 Defense Casting Supplier Database Search Page

and TACOM, the potential challenge with selecting only one weapon system is that the Army does not often own the tech data for many of the systems they procure and it would be difficult to determine casting content without engineering data provided by the OEM's which is not feasible for this program due to the requirement of extensive funding. As an alternative, multiple weapon systems were selected by RIA and TACOM based upon availability of tech data, supply history, and forecasted demand. The systems chosen were Abrams, Bradley, Small Arms (M249, M240), and mortar parts from Benet. Rock Island provided NFFS a list of parts by NSN for these systems that have procurement activity. The list provided by RIA was approximately 1,800 national stock numbers with both recent procurement history and according to Army systems had forecasted demand. The first step in researching this list to identify those items with casting content was to cross reference the parts with those in the tooling database and the database of confirmed cast parts. The result was only about two percent of the 1,800 parts were in one of these two databases. The next step was to determine the population that was DLA managed and had available tech data packages (TDP). About 600 of the items were DLA managed, and half of those had an Acquisition Method Code (AMC) of 1G which would indicate drawings were available. Another 15% were first time buys through DLA.

The final step was to provide the reduced list of parts to TACOM's LCMC to have them identify cast parts based upon those items that had government accessible TDP's. Though it was conveyed in the planning phase of the project that this level of support could be provided through TACOM, after they conducted some research on a sample population, it was determined that the process for them to review the items was very time consuming and they did not have the resources available for this effort. As a result, NFFS further reduced the list by eliminating items that would not be cast based upon nomenclature and other technical characteristics and incorporated the NSN's as a subset of the population monitored for bid solicitations and will review these items as they are solicited and consequently TDP's will be available. Those items reviewed (average 10 per month with drawings were solicited) and confirmed as cast components have been added to confirmed casting parts database and will be directed to capable casting sources for future procurements.

In conclusion, the expanded capability information has been fully integrated within the Defense Casting Supplier Database (www.defensecastingsuppliers.com) and is readily available to both government and industry, and will updated on a continual basis beyond the timeframe of this project. Similarly, the Army parts have been integrated into the Procurement Solutions Network for Castings and will continue to be researched for casting content and disseminated appropriately to industry. Furthermore, those items that are identified and DLA managed will have the procurement item description (PID) updated to confirm casting as a means to manufacture the item, which will become a permanent record and made available on all future procurements. Based on a recent study through the DLA and the American Metalcasting Consortium, this has historically provided an average of 16% cost reduction and 23% lead-time reductions for fully competitive solicitations.

Project Highlights

- Enhanced resource to identify capable casting suppliers to supply spare parts in both peacetime and wartime

- Ongoing maintenance of supplier capability information and dissemination of casting procurements
- Improved spare parts management to reduce costs and lead-times
- Accessible via the Internet and linked to the DLA Supply Center Assistance Request Page

Process Capability Improvements for the Cast Metals Industry
(www.nffs.org/cpkhome.html)

When quoting new work, foundries typically will quote industry standard tolerances rather than demonstrated in-plant capabilities established by scientific method and data. For example, most foundries will quote dimensional tolerance as +/- .030 inches across the mold half because it is part of the Aluminum Association standard for aluminum castings rather than their actual plant capabilities which are supported by actual data and analysis. This often times leads to acceptance of work that may or may not consistently be within the foundry's process capabilities, contributing to elevated scrap levels and increase PLT and ALT as a result.

The objective of the foundry process capability toolkit was to provide training and methodologies to the casting industry to assist with the identification of actual plant capabilities thru the use of process capability studies. Process capability studies are a statistical method used by engineers to demonstrate the ability of a process to produce output that is within requirements. Process capability is often expressed by use of a process capability index score, such as Cp or Cpk. By carefully measuring the output of a process, and comparing the output to the specification range, one can draw conclusions about the ability of the process to consistently meet specification, or to determine the actual capable tolerances of the process. The foundry process capability toolkit was designed to provide instruction on how to design such a study, collect the appropriate data, perform the necessary calculations and analysis, and to draw conclusion about the process capability based upon the resulting analysis. The toolkit is available to all interested parties via the NFFS website on an on-going basis at no cost.

The foundry process capability toolkit contains the following elements:

1. Web portal (www.nffs.org/cpkhome.html)

The web portal is the home of the foundry process capability toolkit. Since all training materials and other resources are electronic based, the web portal was the most efficient and cost effective method for deploying the toolkit into industry. It is available to any user without restriction and without cost.

2. Process Capability Training Program

The process capability training program is an internet-based training course designed to teach foundry personnel the basic of process capability studies and analysis. The training program consists of a fully animated and narrated training program that is approximately 15 minutes in duration. The training program is programmed in Adobe Flash format and is viewable in any common internet browser, eliminating the need for staff to leave their facility to obtain the training. The content of the training program includes:

- Different types of process capability studies and when to use them
- Process Capability Study Design
- Process Capability Evaluation Process
- Determining Process Capability Index Score
- User examination to test training effectiveness

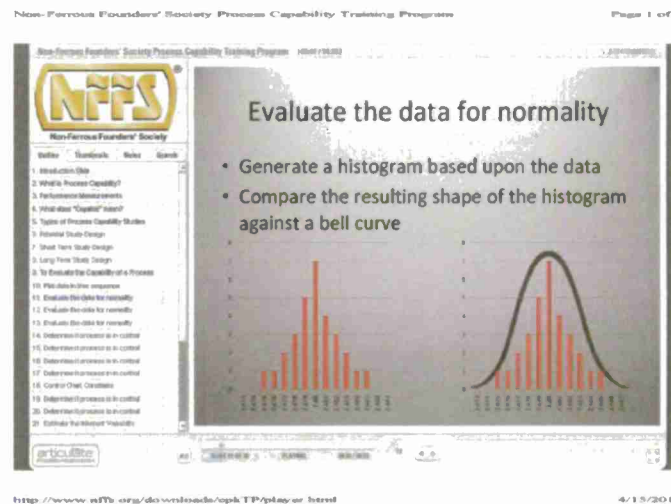


Figure 5-2 Example of slide from training program and software interface

3. Two Process Capability Case Studies

- **Cast Study 1 (Process) - Investment Casting Slurry Viscosity**

An investment casting foundry recently noticed a decrease in the amount of fine detail in several of their casting runs. Analysis of the process variables caused the quality engineers to suspect that the viscosity of the slurry tanks in the shell department was consistently too high and was a potential root cause of the problem. A foundry engineer was asked to determine:

- Is the process within control?
- Is the process capable of meeting the upper and lower specification limits for viscosity?
- Is the process properly centered?

- **Case Study 2 (Casting) - Customer Tooling Change Request**

A foundry has received an engineering change notice from their customer. The customer has requested a change in the overall width requirement of their product and a new measurement tolerance, from the previous requirement of **2.475" (+/- 0.015")** to **2.480" (+0.030 and - 0.000)**. The customer has also requested that the foundry hold the process output (castings) to the minimum side of the tolerance range as much as feasible while maintaining a process capability score of at least 1.33 Cp and 1.33 Cpk. A foundry engineer was asked to determine:

- Is the process presently within control?
- What is the current process capability index score for C_p and C_{pk} ?

- What target dimension should the foundry request of the pattern maker for the tooling dimension to satisfy the customer requirements?

4. Process Capability Failure Resolution Paths

Process capability failures are usually linked to chronic problems in the basic process either in raw materials, process or equipment. Since raising equipment capability usually requires the expenditure of funds, it is prudent to extract all the improvements possible from raw materials and methods first. These guidance documents are designed to help the foundry professional with identification of potential causes of process capability failures within the following broad categories: *Chemistry, Dimensional, Physical Properties and Internal Defects.*

5. Corrective Action Template Procedure/Form

The corrective action procedure is designed to provide to most basic and user friendly method of managing change within the foundry. These template documents are available in MS word format for ease of use, and are compatible with most modern quality management systems.

6. On-line Process Capability Calculator and Charting Assistant

This on-line tool is designed to assist the end user with creating the necessary histograms, control charts and run charts required, and includes an automatic calculation of the process capability index scores (both Cp and Cpk). The end user can input their data and receive the output in a .pdf document that is easily printed and stored no matter the user platform. Screen captures of the input and resulting output of this application is shown below:

Non-Ferrous Founders' Society

Quality Characteristics:

Upper Specification Limit:

Lower Specification Limit:

Sample Size:

Data

10.8 26.1 1.2 30.2 28.6 28.1 1.1 28.1 8.3 24.7 1.0 24.7 1.0 24.7 1.0 24.7 1.0 24.7

Figure 5-3 Input Screen

Page 1 of 3



Data Chart

Quality Characteristic: width
Upper Limit: 18
Lower Limit: 6
Sample Size: 9

Control Chart Limits for X-bar Chart
Centerline (X-bar) 9.6669
UCL 11.8429
LCL 6.1879

Control Limits for R Chart
Centerline (R-bar) 2.8999
UCL 6.2875
LCL 0.0000

Statistics
Standard Deviation (Sigma) 1.8746

Process Capability Indexes
Cp 1.8987
Cpk 1.4286
Zupper 1.8747
Zlower 1.4286

Sample Data
10, 6, 6, 10, 11, 12, 10, 10, 9, 6, 10, 11, 11, 10, 11, 9, 10, 9, 9, 11,
10, 9, 9, 10, 9, 7, 9, 10, 9, 9

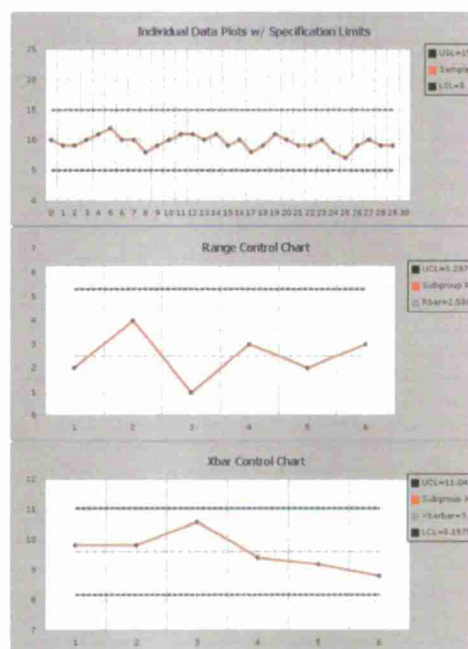
Sample	Subgroup1	Subgroup2	Subgroup3	Subgroup4	Subgroup5	Subgroup6
1	10.0000	12.0000	10.0000	8.0000	10.0000	7.0000
2	9.0000	10.0000	11.0000	10.0000	9.0000	9.0000
3	6.0000	10.0000	12.0000	8.0000	6.0000	10.0000
4	10.0000	8.0000	10.0000	6.0000	10.0000	8.0000
5	11.0000	6.0000	12.0000	11.0000	8.0000	6.0000
X-bar	9.8000	9.8000	10.6000	8.4000	9.2000	8.8000
Min	11.0000	12.0000	11.0000	11.0000	10.0000	10.0000
Max	6.0000	6.0000	10.0000	8.0000	6.0000	7.0000
Range	7.0000	4.0000	1.8000	3.0000	2.0000	3.0000

<http://iMChart.servside.net/>

4/15/2011

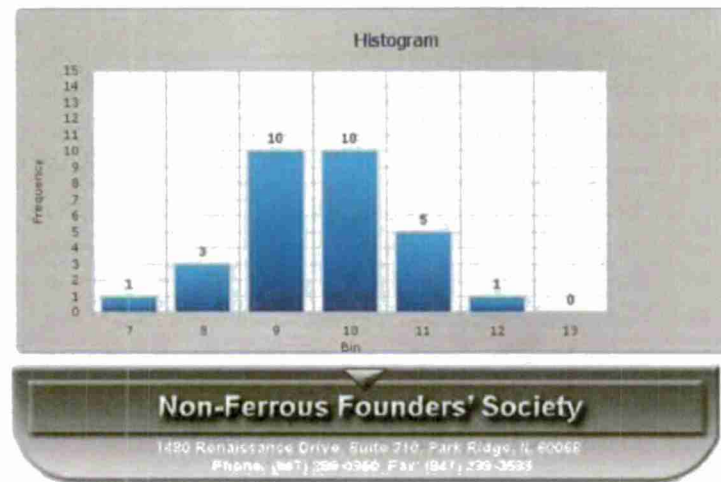
Figure 5-4 Output Screen

Page 2 of 3



<http://iMChart.servside.net/>

4/15/2011



Copyright © 2011 by NFFS. All rights reserved. This project was sponsored by the US Army Contracting Command Joint Munitions & Lethality Contracting Center, Picatinny, NJ on behalf of Benet Laboratories, and was accomplished under Cooperative Agreement Number W15QKN-10-2-0001.

7. Additional Process Capability Resources

Additional links and resources are provided to the end user to assist them with understanding and utilizing process capability studies, and include a control chart table of constants for use in control chart development, and links to various statistical tests used to determine the normality of a data set.

Industry outreach and promotional efforts are multi-faceted. The promotion strategy includes:

- Rollout at AFS Casting Congress, April 2011 (Schaumburg, IL)
- Print ad in *Foundry M&T magazine*, April 2011
- Print ad in *The Crucible* magazine, March/April 2011, May/June 2011
- Promotional handout for inclusion in NFFS membership/industry mailings
- Promotion on NFFS website and within NFFS electronic newsletters
- Coordination with the Foundry Educational Foundation (FEF) to promote the toolkit to FEF schools, professors and students

NFFS expects that the process capability toolkit will become an integral part of foundry operational analysis, leading to increased organizational performance levels. It is anticipated that usage of the toolkit will be between 60 -75 unique IP addresses accessing the toolkit per month. Code has been inserted into the webpage to allow tracking of the usage statistics. NFFS will monitor these usage statistics to evaluate and improve its outreach and promotion efforts.

Project Highlights

- Process Capability Training Program and Web Portal
- Foundry Process Capability Disasters Article: *The Crucible*; July/August 2010
- Roll-out and promotion at AFS Casting Congress, Schaumburg, IL April 2011
- Distributed by the Foundry Education Foundation (FEF) to metal casting professors and students within FEF colleges and universities

6. Advanced Aluminum Metal Matrix Composites for Sand and Investment Casting Applications: *Principal Investigator Kenneth Kremer, M Cubed Technologies, Inc.*

Abstract

Metal matrix composites consisting of silicon carbide (SiC) particles in an aluminum alloy matrix have been well studied due to the unique combination of properties that they present. Most of the physical and mechanical properties can be tailored by shape, size and quantity of ceramic particles in a properly designed aluminum alloy matrix. Manufacturing method and heat treatment can have a significant impact on composite performance. Historically, castable composites have been limited to 30 volume percent particle loadings by gravity pour and 40 volume percent by mechanical or vacuum assist. At 55 volume percent loadings, the stiffness and coefficient of thermal expansion of steel can be duplicated while maintaining a density close to that of aluminum. Forming of 20, 30 and 55 volume % aluminum silicon carbide castable composites in sand molds was demonstrated in a finned thermal management component and tensile bars. Physical and mechanical testing was conducted and discussed to illustrate the range properties possible with increased fractions of ceramic particulate in the composite.

Background

M Cubed Technologies and Net Shape Solutions have worked together to evaluate cast aluminum/silicon carbide metal matrix composites (MMCs) for military and commercial applications. Casting is a desired process (as opposed to machining of wrought metals) as complex, net shape parts can be produced at low cost. MMCs are of interest because of their advantageous properties. Specifically, aluminum/silicon carbide MMCs offer higher stiffness and lower thermal expansion (CTE) than aluminum; and, when the SiC content is high enough, these materials can reach the stiffness of steel while maintaining an aluminum-like density.

A restriction with aluminum/silicon carbide MMCs made by gravity pour casting is that silicon carbide contents have been limited to 30 volume percent. Above this level, casting was not possible because the aluminum/silicon carbide (Al/SiC) melt became too viscous. At only 30 volume percent silicon carbide (SiC) some of the properties are not extremely attractive. One of the goals of this project was to produce Al/SiC cast MMCs with a ceramic particulate content of 55 volume percent SiC using a novel forming process. At this SiC content, a unique combination of properties for a castable composite can be achieved.

Properties of MMCs and various traditional materials are provided in Table 6-1. The virtues of the Al/SiC-55p are clearly evident with a low density, a stiffness (Young's modulus) similar to steel, low thermal expansion (CTE), and high thermal conductivity. Moreover, this material provides Al-like high corrosion resistance (unlike steel). The lower reinforcement content MMC (Al/SiC-30p) is unable to match the stiffness of steel.

Table 6-1 Property Comparison of Al/SiC Cast MMCs and Traditional Metals

Material	Density (g/cc)	Young's Modulus (GPa)	CTE (ppm/K)	Thermal Cond. (W/m-K)
Magnesium (AZ91)	1.8	45	26	72
Al (6061)	2.7	69	25	167
Titanium (6-4)	4.5	114	9.7	85
Steel (4340)	7.8	205	14	44
MCubed Cast Al/SiC-30p	2.8	125	14	160
MCubed Cast Al/SiC-55p	2.9	200	12	160

Existing Thermal Management Materials

There are several types of heat sinks which are commonly used for thermal management in defense electronics, namely finned aluminum heat sinks, copper clad molybdenum (Cu/Mo/Cu) plates and copper/tungsten (Cu/W) plates. Examples are shown in Figure 6-1.

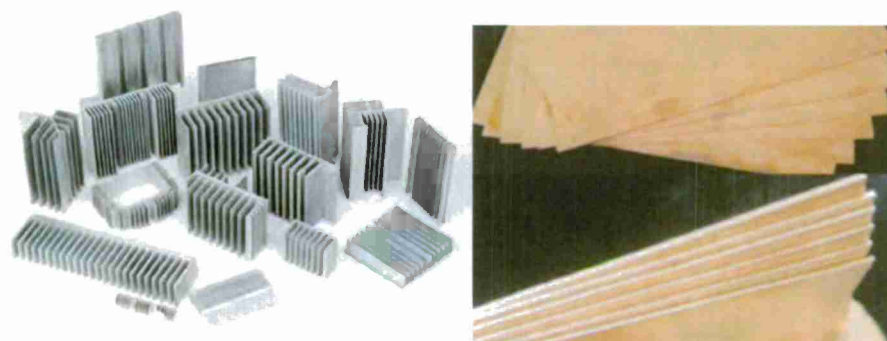


Figure 6-1 Example Thermal Management Devices
LEFT Finned Aluminum Heat Sinks, RIGHT Cu/Mo/Cu Heat Sinks

As shown in Table 6-1, a major problem with aluminum heat sinks is high CTE. Because of this, it is not possible to directly braze the heat sinks to electronic devices because cracking will occur due to differential thermal expansion (i.e., the CTE of typical Al_2O_3 electronic substrates is nominally 10 ppm/K). Another issue with aluminum heat sinks can be cost as most are machined from wrought plate. Wrought plate is generally used to maximize thermal conductivity (i.e., aluminum castings tend to have lower thermal conductivity).

The Cu/Mo/Cu and Cu/W materials have two distinct property advantages. First, they have a low CTE of 6 to 9 ppm/K, which is well matched to ceramic electronic substrates. This allows the substrates to be directly brazed to the heat sink, thus providing maximum heat transfer as opposed to using a conductive paste which has poor heat transfer. In addition, they have a high thermal conductivity, like aluminum, of 160 to 170 W/m-K. However, there are many short comings to these materials. First, they have very high densities of 10 g/cc and 16 g/cc, respectively, making them far from ideal for thermal management uses in defense avionics. Second, because Cu/Mo/Cu is made with a cladding process, it is not well suited to the fabrication of high heat transfer geometries, such as finned heat sinks. Finally,

due to world-wide changes in commodity prices over the past 10 years, devices made from copper and more especially tungsten and/or molybdenum have become very expensive.

Work Plan

- Task #1: Develop casting methods to produce the Al/SiC-55p MMC in complex shape.
- Task #2: Identify a "Demonstration Component."
- Task #3: Produce and test demonstration component.
- Task #4: Characterize properties of various ceramic loadings in the demonstration component and assess vs. metrics.
- Task #5: Conduct 2 webinars summarizing the entire program.
- Task #6: Write 2 technical articles – one article to specifically address an introduction to MMC technology and the second article to report on the one year program.
- Task #7: Write a *Guidance Document* – As a design and manufacturing guideline to address topics pertinent to the consideration of MMC as a material of choice in component design and production in conventional non-ferrous foundries.

The desirable properties for electronic device thermal management are high thermal conductivity, low density, high stiffness, and low coefficient of thermal expansion (CTE) to match the substrates in the electronic device. As shown in Table 6-1, it is difficult to achieve this combination in traditional materials. M Cubed has produced thermal management packages for commercial use in automotive and aeronautic applications to control heat output of advanced electronic packaging. To date, M Cubed has used reaction-bonded Si-Al/SiC materials (i.e., ceramic matrix composites - CMCs) because of their high thermal conductivity, high specific stiffness, tailorable CTE, and complex shape capability. The down side of these materials is low toughness (4 to 6 MPa-m^{1/2}), limited machinability, and high production costs. A cast MMC approach provides some of the same property advantages, but with a higher toughness (13 MPa-m^{1/2}) and inherently lower cost process (e.g., low cost raw materials and net shape fabrication through casting).

The advantages that an aluminum-based cast MMC presents in a thermal management application over competitive materials are numerous. Specifically, the component for the present program was assessed per the following metrics:

- The cost is to be 50% lower than Cu/Mo/Cu and Cu/W.
- Like Cu/Mo/Cu and Cu/W thermal management materials, the CTE of the cast MMC material will more-or-less match the CTE of electronic ceramic substrates.
- Compared to wrought aluminum thermal management materials, the cast Al/SiC MMC will have 50% lower CTE mismatch induced stress when bonded to an electronic ceramic substrate.
- The stiffness should be approximately 180% higher than 6061 aluminum (200 GPa vs. 70 GPa).
- The thermal conductivity should match or exceed that of current Cu/Mo/Cu and Cu/W heat sinks.

- The overall weight of the structure should be 80% lighter when compared to a Cu/Mo/Cu or Cu/W based thermal management system.
- In addition, the aluminum-based MMC will provide:
 - Extreme corrosion resistance
 - Fatigue resistance (unlike aluminum, MMCs show positive high cycle fatigue resistance)

Experimental Procedure

A finned plate was designed for the demonstration component as a generic thermal management heat exchanger which could be formed in a conventional sand mold. The finned plate design is shown in Figure 6-2.

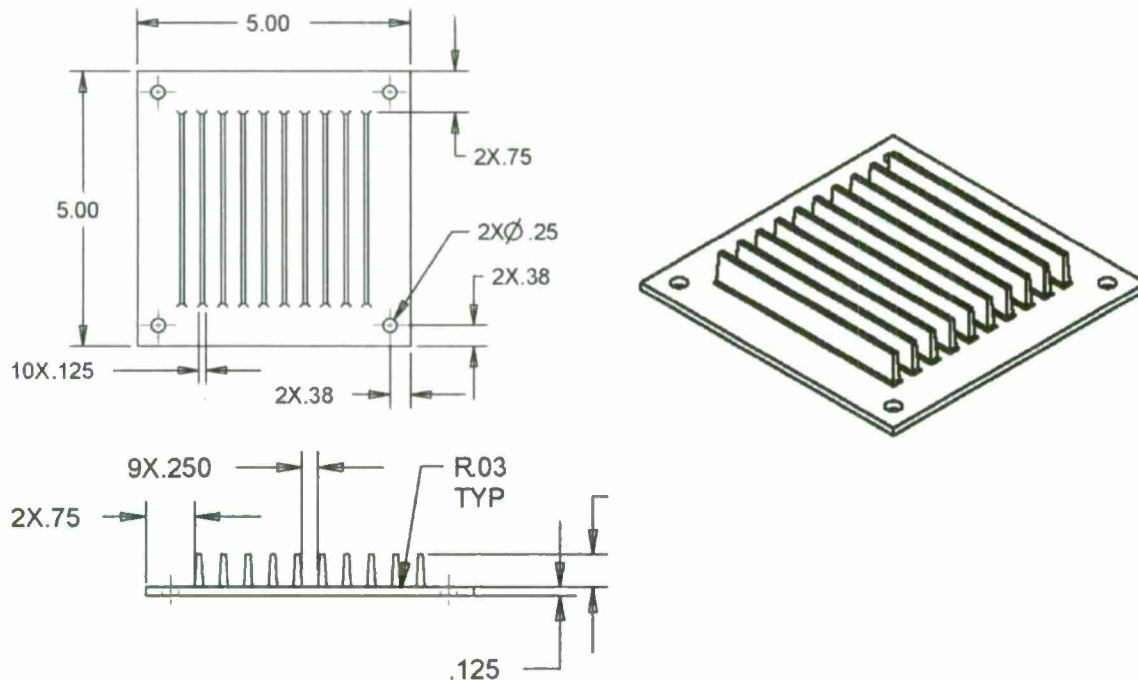


Figure 6-2 Demonstration Component Finned Heat Exchanger Design

The tooling used to make the molds to form the finned plate castings are cope and drag plates with attached mold boxes, shown in Figure 6-3. The mold media is #70 fineness silica sand with sodium silicate binder cured with an ester catalyst. Ceramic particulate loadings for finned plates, tensile bars and test coupons were targeted at 20, 30 and 55 volume percent loadings. A standard alloy similar in chemistry to AA359 loaded with 30 volume percent F500 grit silicon carbide particulate was used. Aluminum alloy was added or removed as necessary to achieve the targeted loadings.



Figure 6-3 Cope and Drag Tooling to Make Finned Plates

The loadings were verified by two quantifiable methods. Density was obtained via a water displacement method per ASTM C135 and Young's modulus was determined by an ultrasonic pulse echo technique per ASTM E494. There is a direct correlation between ceramic particle loading and Young's modulus.

The gating used on all of the castings begins with a simple pouring cup and square downsprue into a well or sump (Figure 6-4). There is a choke just after the well and then a bubble trap ahead of the ceramic foam filter. You can see some evidence of bubbles that rose to the top of the trap during pouring. The filter used to produce all of the test specimens was a 10 pores per inch (ppi) ceramic foam filter. The runner after the filter is in the drag and the gates are in the cope. A runner extension can be seen just behind the finned part. The gating ratios are chosen to ensure non-turbulent flow after the choke.



Figure 6-4 Cast Finned Plate with Gating

Each batch of alloy was prepared in an electric resistance melter with a 600 pound crucible. A resistance melter is used to take advantage of the good temperature control inherent in this equipment. Even though the ceramic is solid, it can react with the aluminum to form aluminum carbide which will adversely affect the properties of the composite. Temperature excursions or hot spots at the crucible wall can allow this reaction to occur. Temperatures for this alloy are kept below 710° Celsius to avoid this reaction. Also, a cover gas of dry ent moisture in the air and hydrogen

absorption. Adjustments were made to the melt as necessary to obtain the correct ceramic loading. The melt was stirred gently to ensure that the particulate was uniformly

distributed before pouring. At all steps of handling the melt, it is very important to not entrain air into the alloy. The bubbles do not float out as quickly and the bubbles do not burst at the surface because the fine silicon carbide particles sustain the bubble walls. When the melt was at temperature and properly stirred, it was hand ladled into multiple sand molds to form the finned plates, tensile bars and sample coupons.

Specimens for all three loadings were prepared for the following testing:

- Density by water displacement, ASTM C135
- Young's modulus by ultrasonic pulse echo technique, ASTM E494
- Thermal diffusivity, ASTM 1461
- Specific heat, Differential Scanning Calorimetry (DSC)
- Coefficient of Thermal Expansion (CTE), ASTM E381
- Tensile properties, ASTM B557-10. The bars were heat treated to a T77 condition (over aged and stabilized). Ten bars were pulled for each of the three loadings.
- Digital thermal image analysis was carried out on the finned plates.

For digital image analysis, the back faces of the finned plates were milled flat. The finned faces were spray painted black to present a face with uniform emissivity to the digital camera. A 2" x 2", 40 watt cartridge heater was adhesively bonded at the center of each plate on the milled surface to apply a constant thermal load. The test set up was arranged as is schematically represented in Figure 6-5. An FLIR SC5000 IR digital camera was used to record the thermal profiles of the samples. This represents the performance of the plates under actual thermal loading in still air. An 80/20 Tungsten/Copper flat plate was also prepared and tested under the same conditions for comparison.

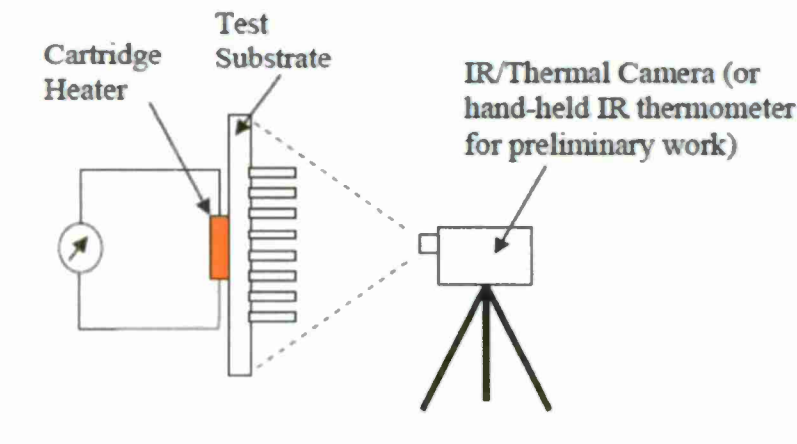


Figure 6-5 Test Schematic for the Thermal Testing.

Results and Discussion

The white area in the photographs of the cast composite microstructures in Figure 6-6 is the aluminum matrix and the dark area is the silicon carbide reinforcing particles. The photomicrograph on the left contains 70 volume percent aluminum/silicon alloy. In contrast, the photomicrograph on the right contains 45 volume percent aluminum/silicon alloy. As more silicon carbide is added the ceramic properties in some cases begin to

predominate. The results of the testing of the graduated loadings change the appearance of the microstructures and the properties of the composite structures (Table 6-2), except in the case of thermal conductivity.

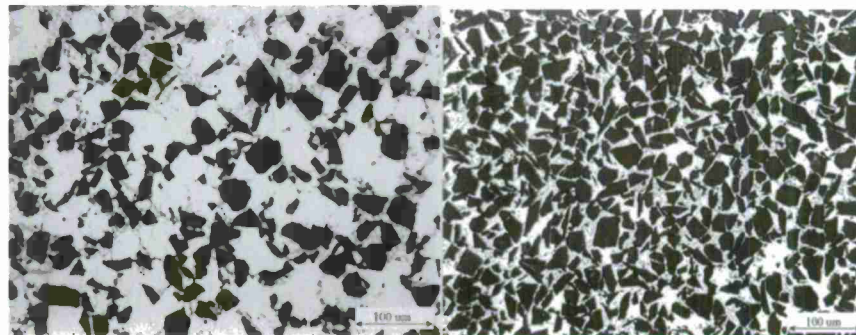


Figure 6-6 Aluminum/30% Silicon Carbide (left) and Aluminum/55% Silicon Carbide.

Table 6-2 Physical and Mechanical Properties of Alloy and Alloy with Ceramic Particulate.

	Matrix Alloy	Al/SiC-20p	Al/SiC-30p	Al/SiC-55p
Density (g/cc)	2.68	2.72	2.79	2.94
Young's Modulus (GPa)	71	106	119	198
Ultimate Tensile (MPa)	312	263	228	210
Elongation (%)	4.6	1.4	0.5	0.3
Coef. Thermal Exp., 20 to 300°C (ppm/C)	21.2	17.1	15.7	11.4
Thermal Conductivity (W/m-K)	134	131	132	127

While there is a slight increase in density (10%) when comparing the matrix alloy to Al/SiC-55p, the Young's modulus increases nearly 3 fold. Notice that the progression in the elastic modulus with loading is not a straight line relationship. The increase in elastic modulus or stiffness is a result of the CTE mismatch (21.2 ppm for aluminum versus 4 ppm for silicon carbide) between the matrix alloy and the ceramic particles. As the matrix alloy solidifies and shrinks around the silicon carbide grains during cooling, the aluminum contracts by a factor of 5 times more than the silicon carbide. Stress fields develop around each of the particles as the aluminum is put in tension. This causes dislocation fields to be generated around each of the grains. These dislocation fields impede slip and flow of the matrix when it is later put under load. As the space between the particles decrease with higher loadings of ceramic, the dislocation fields begin to overlap and this enhances the matrix alloys resistance to slip, thus increasing the effect with greater loadings of ceramic and the modulus. Also, silicon carbide has a much higher modulus than aluminum, namely 70 GPa for aluminum and 410 GPa for SiC. As the applied load is efficiently transferred to the silicon carbide reinforcement by the matrix, the greater modulus contributes to the overall stiffness of the composite. Conversely, elongation decreases very rapidly with

ceramic additions. It approaches failing in a brittle manner after about 20 volume percent silicon carbide. For this reason, there is essentially no difference between yield strength and ultimate tensile strength. However, if the application does not require elongation as primary design concerns, then it is of small consequence.

The tensile strength should have increased with the addition of ceramic reinforcement by the same mechanism of dislocation interaction explained above and transfer of mechanical loading to the silicon carbide. Because there is a steady decrease of tensile strength with silicon carbide loading, it would appear that it would be associated with the silicon carbide particles. Another explanation may be associated with the T77 heat treatment. Most of the other reported work of mechanical properties of Al/SiC composites has been with tested under a T6 condition. While the T6 condition develops greater strength, the composite is less stable for subsequent machining and will typically distort more during secondary operations. The over aged and stabilized casting, therefore, will not meet the same strength levels as T6, but will have lower residual stress and be more amenable to tighter tolerances during removal of material during machining.

The CTE decreases by nearly 50% over the range of compositions. At 55% loading, the modulus and CTE are the same as steel with less than a 10% increase in weight. Matching CTE in two coupled materials will eliminate stress or separation between the two components. This is an important attribute in thermal management. There are a variety of materials in thermal management device designs that must transport thermal energy across several interfaces. Most of these materials have dissimilar CTEs. Because no surface is perfectly flat and smooth, there is always an air gap between the mating surfaces. A thermally conductive paste is used at these interfaces to improve the transport of heat while allowing expansion and contraction. If the CTE of the materials can be matched, the layers can be soldered together with a composition of much higher thermal conductivity allowing more efficient thermal transport.

As can be seen in Table 6-2, even though the CTE changes significantly the thermal conductivity does not vary much. The thermal conductivity of the matrix alloy is 134 W/m-K and for silicon carbide it is 120 W/m-K. The thermal conductivity is a function of matrix and reinforcement conductivity as well as the interfaces between the matrix and the ceramic particles. As the loading of the ceramic increases, there is a balance between the increases in thermal conductivity that the silicon carbide should contribute versus the decrease from more interfaces for the thermal energy to cross.

The last set of characterization tests conducted was digital thermal imaging. The thermal images, of which there is an example in the right corner of Figure 6-3, were analyzed to study performance under actual thermal loading. As can be observed in Figure 6-7, the Al/SiC plates operated at a cooler steady state temperature than the tungsten-copper (W/Cu) plate. A cooler operating temperature means higher system efficiency. The W/Cu plate, which has a higher thermal conductivity (160 W/m-K), naturally increased in temperature more quickly than the composite plates. There is essentially no difference in thermal flux between the MMC plates with increased loading. This can be explained by the lack of variation in thermal conductivity with ceramic loading (Table 6-2).

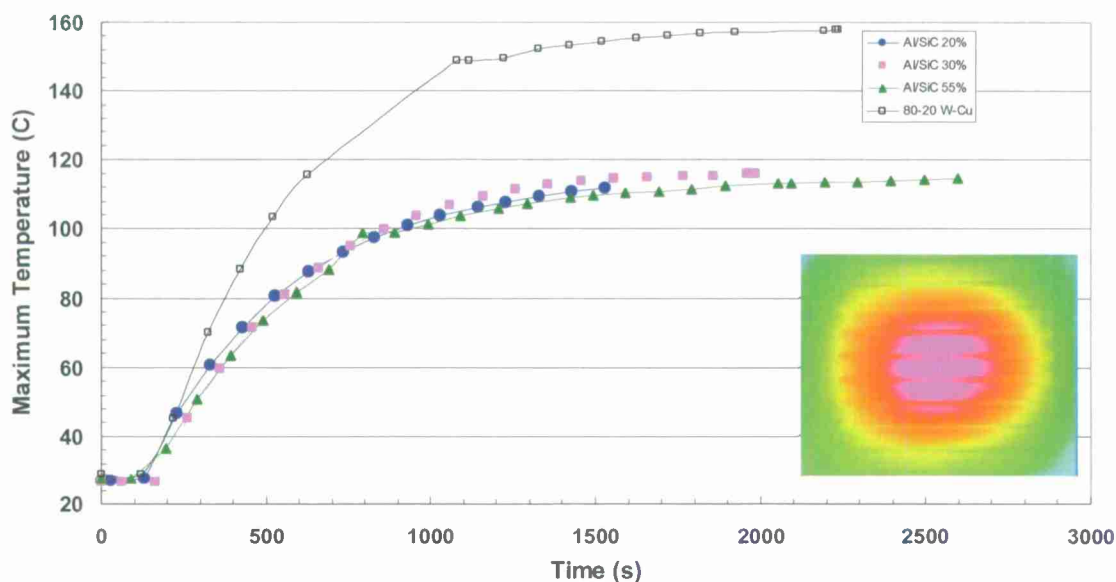


Figure 6-7 Digital Thermal Profiles of Aluminum Composite and Tungsten/copper plates.

Summary of Work and Conclusions

In addition to the production and testing of the three loadings of Al/SiC components and specimens over this one year project, two magazine articles, two webinars and a design and manufacturing document were written as part of the Work Plan. The first article, an introduction to metal matrix composites, was published in July/August, 2011 edition of *The Crucible*. The first webinar, also an introduction to the broad topic of metal matrix composites, was conducted on November 10th, 2011. The final version of the design and manufacturing guideline for aluminum-based metal matrix composites was submitted to NFFS on March 9th, 2011. The guideline is a comprehensive overview for those considering metal matrix composites in a product design or manufacturers considering adding MMCs to their suite of casting materials. The second webinar was focused on the work performed over the last year and was conducted on March 22nd, 2012. The second article, which is also a review of the work performed over the last year and findings, has been submitted to NFFS. This last article is scheduled to be published in a future edition of *The Crucible*.

While the most of the test results were consistent with prior work, the values for thermal conductivity and tensile strength were not expected. The thermal conductivity was expected to be a relatively flat line across the ceramic loadings, but in a higher range than the 130 W/m-K found from testing. Pure aluminum has a thermal conductivity of 220 W/m-K. As alloy additions are introduced to the pure aluminum, the thermal conductivity decreases. This is the case even when higher conductivity metals such as copper and silver are alloyed. In the matrix alloy used in this study, silicon is in the 9 to 10 percent range. Because of the semi-conductor properties of silicon it will have a more significant impact on the thermal conductivity of the composite. Further study of matrix alloys, manufacturing methods and heat treatments will be pursued to gain a better understanding of methods to influence the thermal conductivity of the composite without other adverse side effects.

Further investigation is also warranted with the lower than expected tensile strength. A direct comparison between T6 and T77 will be made with tensile bars cast during the program to determine the impact on mechanical properties.

The outcome of the project findings in comparison to the stated metrics in the introduction are as follows:

- The cost is to be 50% lower than Cu/Mo/Cu and Cu/W.
 - The finished Cu/W (20/80) plate cost \$160.00 per pound. A powder metallurgy process of pressed and sintered powder was used to form the plate. The sand casting approach to form the finned plates used in the study would cost about \$50.00 per pound. Further improvements in economy could be made with large quantities in a die cast approach.
- Like Cu/Mo/Cu and Cu/W thermal management materials, the CTE of the cast MMC material will more-or-less match the CTE of electronic ceramic substrates.
 - The Al/SiC-55p at 11.4 ppm is in the range of Cu/Mo/Cu and Cu/W at approximately 9 ppm.
- Compared to wrought aluminum thermal management materials, the cast Al/SiC MMC will have 50% lower CTE mismatch induced stress when bonded to an electronic ceramic substrate.
 - The reduction in CTE from wrought aluminum alloys at 22 ppm to 11.4 ppm for Al/SiC-55p was discussed earlier. This 50% reduction in CTE will reduce thermal mismatch induced stress by more than half depending on whether the substrate is aluminum nitride or aluminum oxide which have CTEs of 4.5 ppm and 8.4 ppm, respectively.
- The stiffness should be approximately 180% higher than 6061 aluminum (200 GPa vs. 70 GPa).
 - The test value of 198 GPa for Al/SiC-55p meets this goal.
- The thermal conductivity should match or exceed that of current Cu/Mo/Cu and Cu/W heat sinks.
 - The Al/SiC composite values obtained in testing were about 80% of those reported by manufacturers of Cu/Mo/Cu and Cu/W heat sinks. A reduction in alloying elements is one approach to moving closer to the goal of 160 W/m-K.
- The overall weight of the structure should be 80% lighter when compared to a Cu/Mo/Cu or Cu/W based thermal management system.
 - The Al/SiC composites studied had a maximum density of 2.94 g/cc. The Cu/W plate which was used in comparison had a density of 16 g/cc. The minimum density for Cu/Mo/Cu plates is 10 g/cc. The aluminum-based composite is more suitable in applications in which weight is an issue.
- In addition, the aluminum-based MMC will provide:
 - Extreme corrosion resistance
 - Fatigue resistance (unlike aluminum, MMCs show positive high cycle fatigue resistance)

A final goal attained was the demonstration of forming aluminum/silicon carbide components with a 55 volume percent ceramic loading with conventional sand molding in a traditional gravity pour foundry. The properties produced in these components present an interesting combination for applications where the stiffness and CTE of steel is targeted, but the weight of aluminum is a bonus. Added bonuses are the higher thermal conductivity of Al/SiC composites at 130 W/m-K versus 15 W/m-K for 304 stainless steel, better corrosion resistance versus plain carbon steel and greater fatigue resistance versus aluminum.

7. **High Performance Nano-Composite Materials:** *Principal Investigators Stephen P. Udvardy, North American Die Casting Association; Jacob Nuechterlein, Colorado School of Mines; Makhlof M. Makhlof, Worcester Polytechnic Institute*

Abstract

Efforts in this project were applied to the development of castable aluminum base nano-composite material. Three process routes for producing the material were pursued. These include two in-situ routes, self-propagating high-temperature synthesis (SHS) and gas liquid nitridation (GLN), and one ex-situ route, intelligent distributed processing (IDP). The material developed through the SHS route is an Al-4.5% Mg matrix with 10% TiC+SiC particles on the order of 50 nm. The material developed through the GLN route is an Al-5.5% Mg-1.25% Li matrix with 3% AlN particles on the order of less than 200 nm. The IDP material is a 520 Al alloy with 3% 30 nm TiC particles. Castings of the SHS and GLN material were produced, microstructural analyses were conducted and property measurements were made.

Objective

The primary objective of this project was to develop castable high performance aluminum base nano-composite materials that can be used for light weight weapon system components. Two processing routes for the development of nano-composites were initially proposed. The first route was self-propagating high-temperature synthesis (SHS), an in situ process. The second route was intelligent distributed processing (IDP), an ex situ route. Subsequently, a third route was identified and selected for development – gas liquid nitridation (GLN), an in situ process.

The development of aluminum nano-composite materials through one or all of the selected routes is important because current cost-effective and lightweight castable materials do not yield performance characteristics that enable them to replace heavier materials such as iron base materials and higher cost materials such as titanium base materials. Nano-composite materials can provide superior properties compared to other metal matrix composites with micron size reinforcement and the aluminum base nano-composites provide opportunities for approximate 50% weight savings over many iron base materials currently utilized in weapon systems.

Benefits provided to the Department of Defense through this work are intended to be: alternative material for the design of lightweight components that are cost effective; improved performance over standard metal matrix composites; and, superior wear resistance and strength. Benefits are also provided to the foundry and die casting industry. These benefits include: deployment of new technologies; opportunities for market growth; and, ability to meet increasing customer requirements.

The goals of this project were to:

- Down select the specific aluminum base nano-composite material systems for use in die casting
- Define the die casting process parameters for the nano-composite material
- Generate property data for the developed nano-composite material

The proposed project deliverables were:

- A novel technique that will enable die casting of metal matrix composites (MMC) with nano-size particulate uniformly embedded in the matrix.
- Property measurements of the developed composite materials.

Introduction

Aluminum matrix-ceramic particle composite materials have mechanical and physical properties that make them attractive for many applications in the defense, aerospace, automotive and microprocessor industries. Reducing the reinforcement particle size, from the typical micron-size to the nano-size, results in further property enhancements. However, producing these nano-composite materials on a large scale remains difficult despite the numerous attempts that have been made to overcome the typical issues associated with their manufacture. Efforts in this project were applied toward developing robust, economical methods for manufacturing these materials. Figure 7-1 shows the possible means for synthesizing aluminum base nano-composite materials. Once the material has been synthesized, then it may be manufactured into components by semi-solid metal (SSM) processing, squeeze casting, or high pressure die casting. The material synthesis routes selected are highlighted in Figure 7-1 and have been given the labels: (A) self-propagating high-temperature synthesis (SHS), (B) gas liquid nitridation (GLN), and (C) intelligently-distributed processing (IDP). The material systems selected are the Al/TiC, the Al/(TiC + SiC), and the Al/AlN.

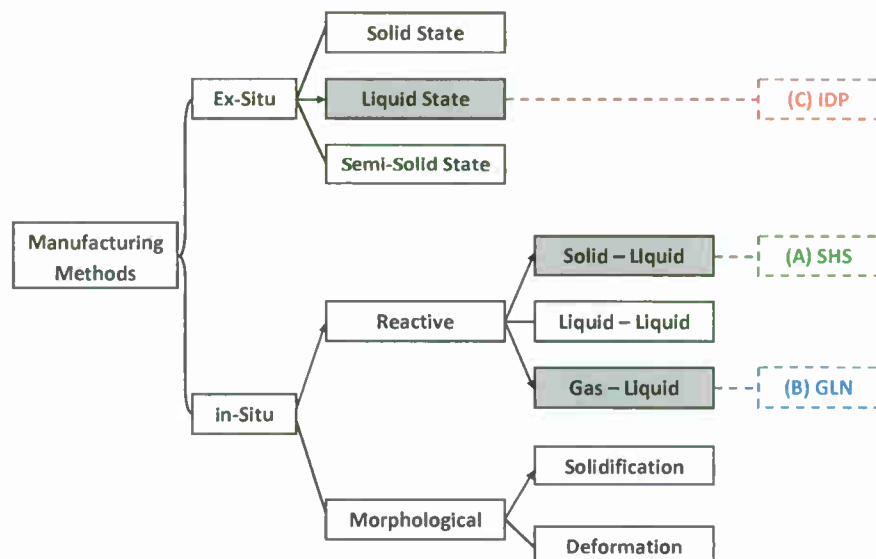


Figure 7-1 Possible routes for synthesizing aluminum base nano-composite materials.

(A) Self-propagating High-temperature Synthesis (SHS)

The following describes the approach, results, and key findings of the SHS portion of this project.

Approach

Self-propagating high-temperature synthesis or SHS is a method of producing ceramic products from powder precursors. When heat is applied to the mixture of reactant

powders, the activation energy for combustion is overcome, triggering a chemical reaction. This exothermic reaction provides energy to the adjacent layer of reactants causing a sequence of reactions that is self-sustaining. These reactions can then be defined by the temperature and velocity of the reaction front. By manipulating the chemistry and reaction conditions, the system can be tailored to produce desired products. Particles of titanium carbide, averaging 1-5 μ m in diameter, have been produced by SHS through propagation of standard combination reactions of elemental titanium and carbon. Through previous SHS efforts in producing aluminum-titanium carbide composites with micron size particles, there was indication that reducing the reaction ignition temperature would reduce the size of the reinforcement particles that are formed and improve strength. Hence, the focus of this work was initially to assess the impact of reaction temperature on reinforcement particle size and the characteristics of the resulting material.

Figure 7-2 shows the overall concept of producing metal matrix composite materials with the SHS process. A compacted pellet of titanium (Ti) and carbon (C) powder is introduced to molten aluminum in a vessel, such as a crucible, and a reaction takes place that converts the Ti and C powder to form titanium carbide (TiC) particulate particles within the molten aluminum matrix metal. After the reaction takes place, the material is either cast into a shape or solidified into a billet as feedstock for future casting. When utilizing only Ti and C powders, the SHS reaction generates micron size TiC particles. This reaction is expressed as:

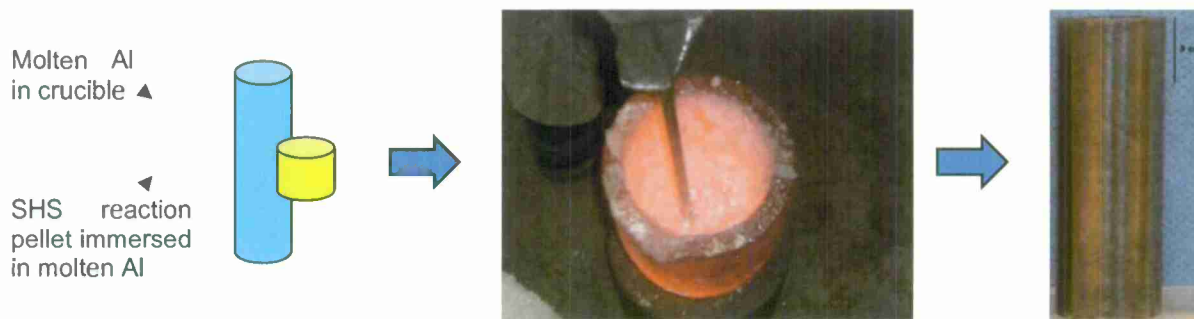


Figure 7-2 Schematic of the powder pellet in molten aluminum, a photograph of the reacted material in the crucible, and a subsequently solidified 1.75 inch diameter billet.

As an initial step in attempting to reduce the temperature of the SHS reaction, diluents such as TiC and Al were utilized in an aluminum-silicon matrix. These had reduced the size significantly, however they also required a lot of time at high temperature to ignite, resulting in particles of about 500nm. Next, copper oxide additions were used to reduce the ignition temperature. The lower ignition temperature decreased the average particle size to less than 400nm.

Microstructural examination of the material revealed that Al_3Ti was being formed along with TiC. It was found that silicon containing aluminum matrices form Al_3Ti preferentially to TiC and since Al_3Ti is an undesirable phase, the matrix was changed to aluminum-magnesium for this reason and also to better wet the particles. Magnesium is a wetting

agent and the amount of magnesium, according to literature, has a significant influence on the rejection or incorporation of the particles from the matrix and the coherency of the composite. (Other alloying elements, such as lithium utilized in the GLN work described later, also act as wetting agents).

As a cost reduction effort, TiO₂ as opposed to pure Ti powder was assessed and found to be a viable alternative. This reaction is shown as:



It was found that the formation of Al₂O₃ (alumina) further reduced the reaction temperature, so adding Al₂O₃ and also pure Al to the melt was studied. Through the following reaction, it was found that TiC particles on the order of 50nm were generated. Figure 3 demonstrates this reduction in particle size when combustion temperature is reduced by diluents.

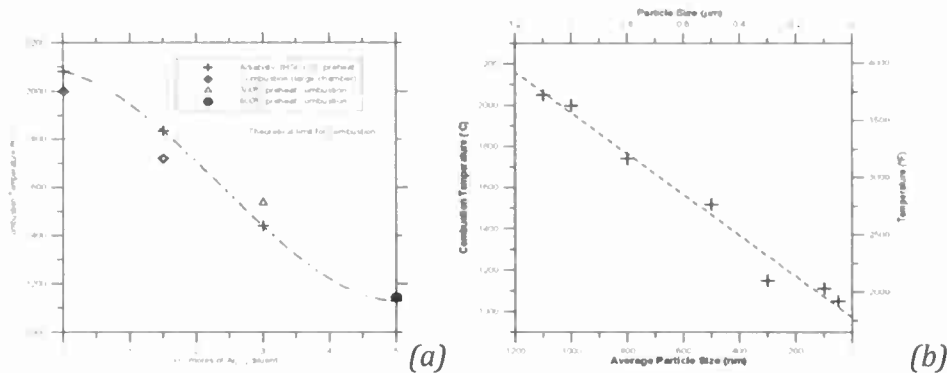


Figure 7-3 (a) Adding diluents such as Al₂O₃ reduces the calculated combustion temperature (Adiabatic temperature) which was calculated using HSC thermodynamic software. The experimental values are also displayed. (b) A reduction in particle size of the titanium carbide with a corresponding reduction in combustion temperature.

The Al₂O₃ particles demonstrated resistance to wetting in molten aluminum. Also, Al₂O₃ is not as strong as some other ceramic phases. Silicon carbide (SiC) is a low density high strength ceramic product so the potential of forming SiC in addition to the TiC was considered even though, due to the relatively low reactivity of the SiC system, the product is difficult to form. Adding silicon to produce silicon carbide reduces the reaction temperature and the TiC reaction was considered to provide enough energy to advance the sluggish SiC reaction to completion. This was found to be the case and through the following reaction, it was also found that particle size was again reduced to an average of 50 nm.



These particles were introduced to the aluminum 4.5% magnesium alloy through the SHS reaction at a volume of 10%. The particles were dispersed in the melt by stirring. Both mechanical stirring and ultrasonic stirring were used. Once the particles were dispersed, the molten composite was poured into a graphite cylinder of 1.75" diameter and 3-4" tall to form billets. Twenty billets of material were produced. These billets were subsequently die

cast by the semi-solid metal (SSM) process into wedge shaped castings at VForge, near Denver, Colorado. The castings were then machined into wear and tensile specimens for testing and measured for hardness.

Results

The most viable SHS reaction for generating TiC reinforcement particle size of 50 nm average considered to be $3\text{TiO}_2 + 4\text{Al} + (3+X)\text{C} + \text{XSi} = 3\text{TiC} + 2\text{Al}_2\text{O}_3 + \text{XSiC}$. Figure 7-4 displays an X-ray diffraction pattern showing that the products are completely developed with no reactants left in the final parts.

Hardness measurements on the Al-4.5%Mg matrix with 10% TiC determined the nano-composite material to be 5 times harder than the unreinforced matrix (108 HRB or 312 HV as opposed to 20 HRB). Microstructural analysis showed that TiC, Al_2O_3 and SiC were reasonably uniformly distributed in the aluminum matrix. Figure 7-5 displays representative microstructures showing particles of titanium carbide in the aluminum matrix at less than 50nm in diameter.

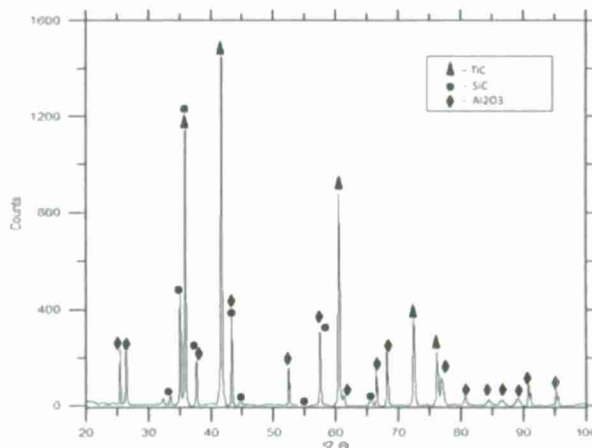


Figure 7-4 X-ray diffraction pattern of powders produced by an SHS reaction

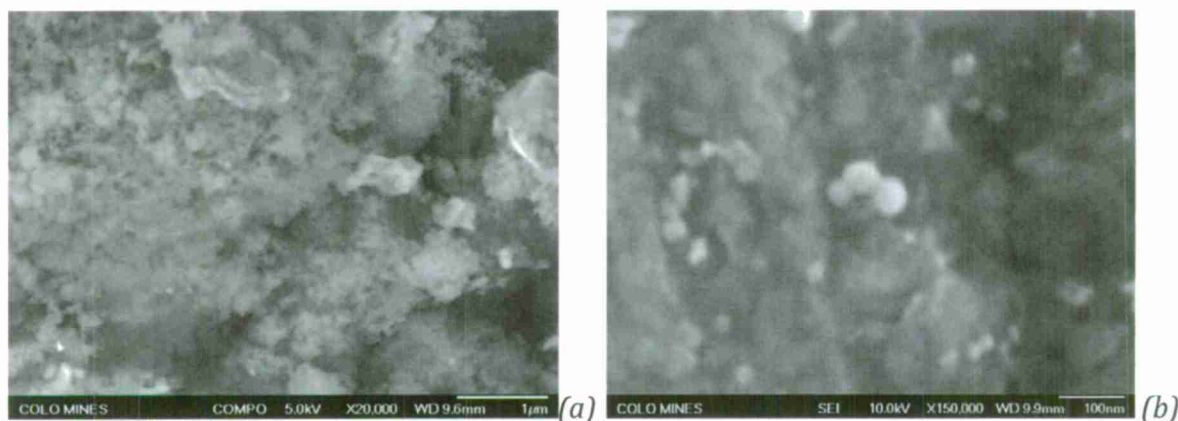


Figure 7-5 - (a) SEM image of powders produced by an SHS reaction demonstrating the small size of the particles. (b) TiC particles in an aluminum matrix at a high magnification to show the morphology and size of the average particles.

Figure 7-6 displays two of the castings produced during the trial at VForge. The trial was for determining the castability of the material and for characterization of the material in the cast condition. Results of this trial indicate that aluminum metal matrix nano-composites show a high propensity for production through this method. The castability of the material was considered to be good and flow was uniform over a fairly wide range of casting temperature.

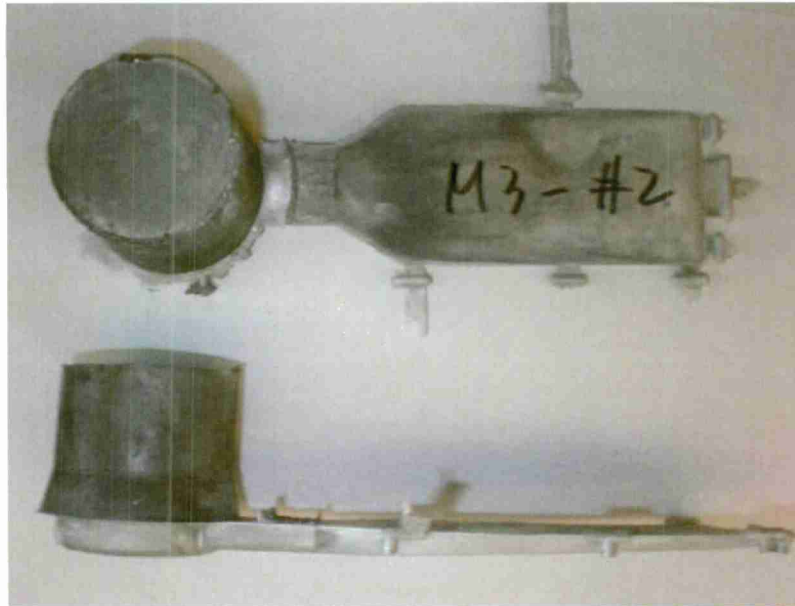


Figure 7-6 Final SSM cast wedge of 10% by volume ceramic particles.

Tensile tests were conducted on specimens removed from the castings. The results show that the nano-particles increase strength over the un-reinforced aluminum matrix and over the matrix reinforced with standard micron-size particles as expected. The ultimate tensile strength (UTS) improvement is 23% over the un-reinforced matrix and 12% over the composite with standard particle size. The yield strength (YS) improvement is 55% over the un-reinforced matrix and 25% over the composite with standard particle size. Ductility (%Elongation) decreased from 3-5% for the matrix and 2-3% for the composite with standard particle size to 1.5%. Hardness of the castings averaged 65 HRB, more than 3 times the matrix, but not quite as hard as the casting feed stock of 108 HRB due to reheating for SSM die casting.

Table 7-1 Tensile data from specimens removed from SHS castings.

	UTS MPa (ksi)	YS MPa (ksi)	Elongation %
Matrix	175 (25.4)	100 (14.5)	3-5
Micron-composite	196 (28.4)	125 (18.1)	2-3
Nano-composite	215 (31.2)	155 (22.5)	1.5

Rubber wheel abrasive wear tests on specimens removed from the castings show that the nano-composite material is much more wear resistant than the micron-composite material yielding a volume loss of material of only 0.108 cubic cm as compared to 0.380 cubic cm. Figure 7-7 shows this as well as a comparison to a high strength low alloy steel and a white cast iron. The nano-composite has the best wear resistance of these materials.

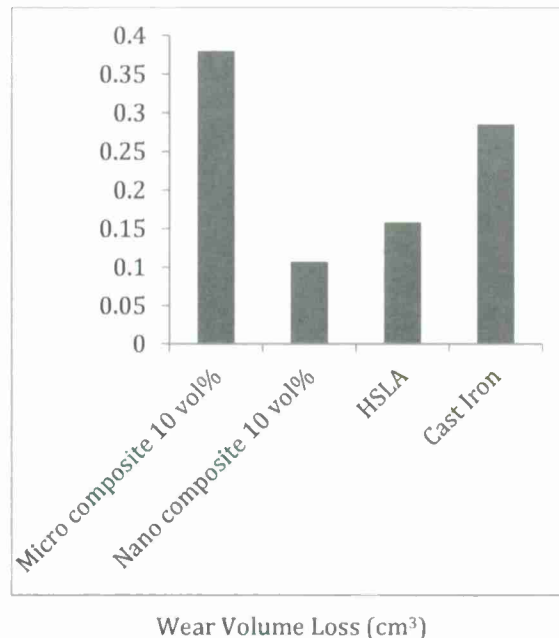


Figure 7-7 Wear resistance of the SHS nano-composite compared to SHS micron-composite, high strength low alloy steel and white cast iron.

Key Findings

- The SHS process produced nano particles of ceramic in an aluminum matrix. This nano-composite material can be produced at a relatively low cost and in a short amount of time. From powders to cast parts can be done in a few hours.
- Titanium carbide, alumina and silicon carbide can be produced through mixing powders and igniting. The SHS reactions go to completion without leaving reactant powders to contaminate the final product. The particles produced are hard and at sizes on average of less than 50nm.
- The particles can be formed in an aluminum alloy of Al-4.5Mg at a large window of volume fractions - from 0-60% ceramic. Good dispersion was only possible when a mixing device was used. The particles wet in the aluminum due to the magnesium additions and hence are good reinforcing agents.
- This material can be SSM die cast with a high level of consistency in the final part. The particles help develop a uniform flow regardless of the temperature. This makes the temperature range for casting these materials large.
- The hardness is increased over the matrix by several times up to hardness levels over 100HRB depending on nano particle volume fraction. The hardness of the nano-composite material is higher than that of metal matrix composite material produced with 1-2 micron sized particles at the same volume fraction.
- The nano-size particles provide for a 25% increase in yield strength and over a three-fold improvement in wear resistance over micron-size particles of the same volume percent in an aluminum matrix.

(B) Gas-Liquid Nitridation (GLN)

The following describes the approach, results, and key findings of the GLN portion of this project.

Approach

The Gas-Liquid Nitridation work was focused on developing the GLN process for synthesizing aluminum-aluminum nitride nano-composites and assessing the effect of the process parameters on the characteristics of the resulting material. The GLN process bubbles nitrogen rich gas through a molten aluminum bath (the matrix) causing a reaction that forms particulate particles of AlN (the reinforcement) within the molten aluminum.

The apparatus shown schematically in Figure 7-8 was designed, built, and used to manufacture ingots of the composite material. In each experiment, 200 grams of the metal alloy are ultrasonically cleaned in acetone and then placed in a graphite crucible that has been previously coated with a boron nitride emulsion. The mullite chamber of the resistance furnace is first evacuated down to 60 mTorr and refilled with UHP Argon at 20 mTorr. This is repeated three times in order to remove as much oxygen as possible from the furnace atmosphere. The chamber is then filled with argon gas at atmospheric pressure and then heating is started. The heating rate is kept constant at 4°C/min in order to avoid excessive thermal stress on the mullite body of the retort. A K-type thermocouple (enclosed in a ceramic tube to prevent its degradation) is placed in the crucible to monitor the temperature. Once the process temperature is reached, the impeller is immersed in the melt and purified nitrogen-bearing gas (nitrogen, ammonia or a combination of both) is injected into the melt. The impeller is connected to an electric mixer (Mixer Direct, 1/15 hp, 115 V) that provides rotation at a constant rpm. Gas purification devices are used to remove oxygen and moisture from the reaction gas down to the parts-per-billion level. Drierite (10-20 mesh) and activated alumina desiccants are used to remove moisture and a high-efficiency oxygen trap (VICI) containing a manganese-based getter material and an oxygen trap (RESTEK) are used to minimize the oxygen content. Plug valves at the beginning and at the end of the gas line isolate the traps in order to avoid contamination from the atmospheric air when they are not being used. Once gas injection is completed, the rotor is extracted from the melt and argon gas is pumped in the chamber to cool the composite material. The composite is left in the

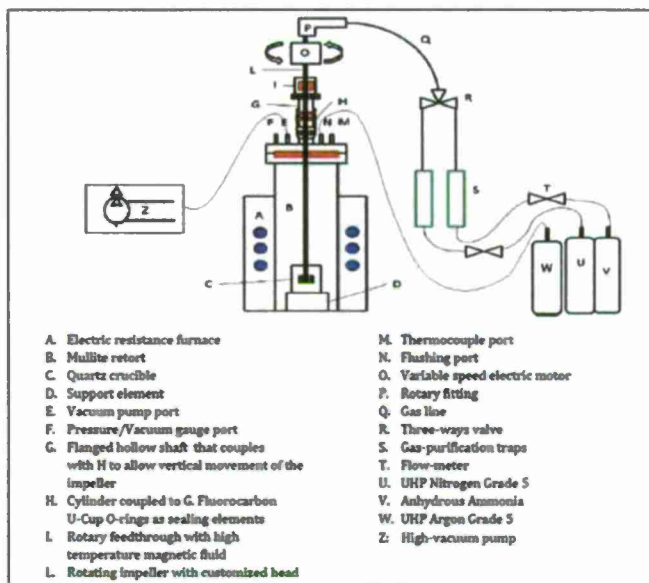


Figure 7-8 Schematic representation of the apparatus used in GLN.

chamber to solidify under the argon atmosphere. This material may then be SSM processed, squeeze cast, or high pressure die cast.

Initially, an Al-Mg matrix was selected due to magnesium's ability to wet particles and provide good cohesion with the reinforcement particles. Efforts to produce AlN particles within matrices of various levels of magnesium were successful; however, the reaction was sluggish. Since lithium (Li) also has the ability to wet particles, Al-Li was next utilized as a matrix and the reaction was found to be greatly accelerated, producing AlN particles in substantially less time. Work was subsequently focused on the Al-Li/AlN system and this comprised the bulk of the work.

A design of experiments was conducted to determine an advantageous level of Li in the matrix, gas mixture, and processing time with a constant impeller rotation speed of 250 rpm. The design of experiments is summarized in Table 7-2.

Table 7-2 Design of experiments for GLN.

Experiment #	Alloy composition	Gas composition	Processing time
1	Al-5 wt% Li	N ₂	2
2	Al-5 wt% Li	N ₂	4
3	Al-5 wt% Li	N ₂ /NH ₃ = 1/1	2
4	Al-5 wt% Li	N ₂ /NH ₃ = 1/1	4
5	Al-5 wt% Li	NH ₃	2
6	Al-5 wt% Li	NH ₃	4
7	Al-2.5 wt% Li	N ₂	2
8	Al-2.5 wt% Li	N ₂	4
9	Al-2.5 wt% Li	N ₂ /NH ₃ = 1/1	2
10	Al-2.5 wt% Li	N ₂ /NH ₃ = 1/1	4
11	Al-2.5 wt% Li	NH ₃	2
12	Al-2.5 wt% Li	NH ₃	4

Samples were taken from the top and the medium-lower sections of the ingots from each experimental run in order to determine the amount of aluminum nitride that formed in these locations. The samples were first ground with silicon carbide paper and then with a diamond suspension. The final polishing was performed with a silica suspension and then the samples were ultrasonically cleaned for 45 minutes in order to remove all contamination that may have been caused by the sample preparation process. The samples were etched with a 10% NaOH solution for 5 seconds in order to improve visualization of the aluminum nitride particles. X-ray diffraction (XRD) was used to confirm the presence of aluminum nitride and a scanning electron microscope (SEM) was used to create photomicrographs of the material. A Matlab-based program [2] was used to analyze the bitmap micrographs and to determine the volume fraction of the aluminum nitride phase, the mean length of the free space between the aluminum nitride particles, the average size

of the aluminum nitride particles, and the average size of the aluminum nitride clusters. In order to ensure statistical validity of the measurements, a minimum of 10 micrographs for each sample were used. Hardness measurements were made by means of a 1.6 mm steel ball and 100 kg total load (Rockwell B). An average of fifteen measurements was made on each sample.

Results

Figure 7-9 shows example SEM photomicrographs of the materials synthesized according to the conditions outlined in Table 7-2 and results from analyzing these photographs are summarized in Table 7-3. Figure 7-10 displays the hardness measurement results showing the improvement over the unreinforced matrix which is approximately 20 HRB.

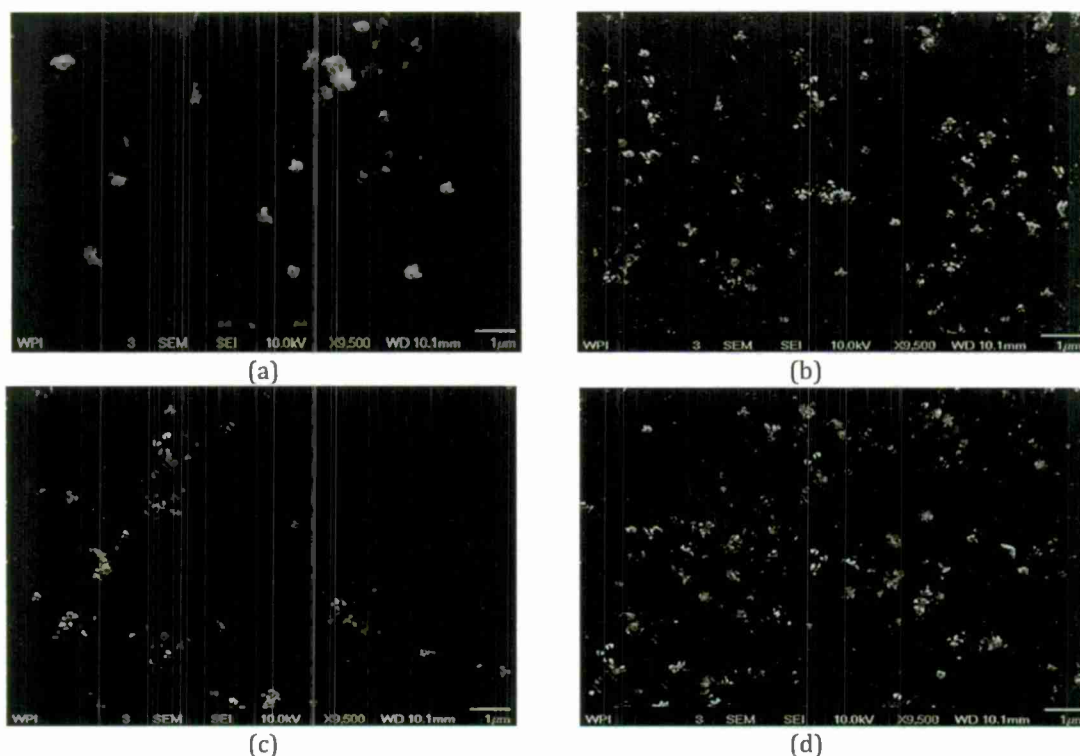


Figure 7-9 SEM photomicrographs of samples from materials processed according to the conditions outlined in Table 2. (a)-(d) are for samples from experiments 2, 5, 10, and 12; respectively.

Table 7-3 Summary of findings.

Experiment #	Volume AlN (%)	Avg. particle size (nm)	Avg. cluster size (nm)	Distribution index
1	No aluminum nitride particles were detected			
2	6.2	643	1540	0.58
3	9.5	489	1327	0.37
4	26.0	453	1552	0.51
5	21.0	274	966	0.82
6	48.0	312	1114	0.74

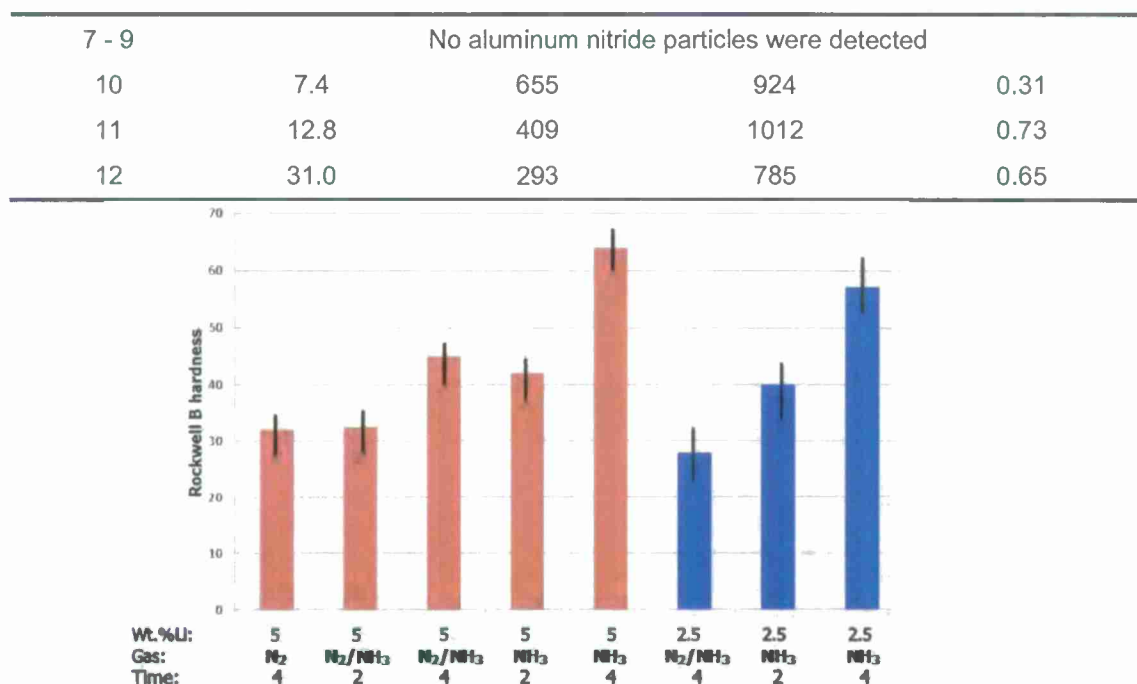


Figure 7-10 Hardness results showing that lithium content, NH₃, and time increase hardness.

Further experimentation (Experiment 13) showed that increasing impeller speed results in a decrease in particle size. Using the parameters from Experiment 10 but increasing the impeller speed to 300 rpm produced AlN particles of 200 nm average in size. Both the average particle size and particle clustering decreased by more than 65% and 50% respectively from the values obtained in Experiment 10. Therefore, in an attempt to further reduce particle size, the apparatus was modified to achieve impeller speeds of 400 rpm and above.

Prior to producing material for a casting trail, sample casts were made in the laboratory and found to have a narrow mushy zone or narrow solidification range. To make the material more conducive to die casting by the SSM and squeeze processes, the solidification range was increased by adding Mg to the Al-Li matrix. Material was then produced for a casting trail to assess castability and generate properties on specimens machined from die castings. An impeller rotation speed of 400 rpm and parameters to produce 3% AlN in an Al-(5-6%) Mg-(1-1.5%) Li matrix were utilized. Disc shaped die castings of the material, approximately 4 inches in diameter and 0.5 inch thick, were successfully produced at Eck Industries using the squeeze process. Properties have yet to be determined.

Key Findings

- The feasibility of producing aluminum alloy matrix-aluminum nitride nano-particle composite materials by means of an in-situ chemical reaction between molten aluminum alloys and a nitrogen-bearing gas was demonstrated.
- A robust apparatus was built, optimized, and used for the demonstration and for establishing the operation window for the process. The apparatus is inexpensive and may be easily scaled up for industrial production of the composite materials.

- The investigations indicate that aluminum alloys with a relatively high lithium content result in a higher volume fraction of aluminum nitride particles. However, melts with relatively lower lithium content produce finer particles – although the particle distribution in these alloys is less homogeneous than in alloys with higher lithium content.
- The investigations also indicate that ammonia is more efficient than nitrogen in nitriding aluminum-lithium alloys. More than 40 volume percent aluminum nitride particles can be produced in an aluminum-5 wt% lithium alloy when the melt is injected with anhydrous ammonia for 4 hours at 1000°C.
- Adding 5-6% Mg to the Al-Li matrix provides for a wider mushy zone and makes the material more conducive to die casting.
- Hardness of the nano-composite material was improved up to in excess of three-fold, depending upon the process parameters. A concomitant increase in yield strength is anticipated.

(C) Intelligently-Distributed Processing (IDP)

The following describes the approach, results, and key findings of the IDP portion of this project.

Approach

The IDP work focused on assessing the feasibility of intelligently distributing the reinforcing particles in a liquid aluminum alloy in order to synthesize aluminum-titanium carbide nano-composites. Making nano-composite articles by adding nano-particles into molten metal is very challenging for two main reasons. One is the difficulty encountered in introducing the nano-particles into molten metal and keeping them suspended in the melt bulk until it solidifies; and the second is dispersing the particles uniformly into the melt. The first difficulty arises because of the large surface area of the particles, their small size, which makes it difficult for them to penetrate the surface of the melt, and many types of particles have poor wettability by the melt. Hence, efforts were applied toward establishing procedures for obtaining a homogeneous distribution of nano-particles within the matrix of an aluminum alloy and optimizing the material's chemical composition for strength and economy.

TiC nano-particles were chosen as the reinforcing particles because they are fairly well wetted by molten aluminum alloys. Also, TiC has mixed covalent and metallic bonds, high elastic modulus, and high hardness (430 GPa and 31 GPa, respectively) and thus its presence in a composite material significantly improves the material's mechanical properties. TiC particles, 30 nm in size, are incorporated into the liquid aluminum alloy by a "flux-assisted process". In this process, a flux – powdered potassium aluminum fluoride, KAlF₄ – is mixed with the particles and then the mixture of particles and flux is added into the molten aluminum alloy. The flux helps to mitigate complications brought about by surface oxidation, and it also reduces the surface tension of molten aluminum alloys, which improves their wetting ability of the TiC particles. Once the TiC particles are introduced in the molten alloy, Lorentz forces, created by the induction coil shown in Figure 7-11, are employed in an attempt to disperse them homogeneously in the melt.

In this work, three potential methods for introducing TiC particles into molten aluminum were selected for investigation: (1) sprinkling the particles or a mixture of particles and flux onto the melt surface, (2) plunging the mixture of particles and flux encapsulated in Al foil into the melt, and (3) plunging into the melt a tablet made from a mixture of particles and flux, which was made by pressing the mixture encapsulated in Al foil in a mold with a pressure of 30 MPa at room temperature. Alloys of Al-Si (A356), Al-Si-Cu (A380), Al-Mg (520), and pure Al were used as matrix material. The initial experiments with flux were conducted with the ratios of particles to flux of 1:0.5, 1:1, 1:2, and 1:5. The resulting materials were analyzed with an optical microscope, a scanning electron microscope (SEM), energy dispersive spectroscopy (EDS), X-ray diffraction (XRD), and a transmission electron microscope (TEM). It was found that a significant fraction of the TiC particles introduced into the melt were detected when the melt composition was Al-Mg or pure aluminum, but not many if any particles were detected when the melt was Al-Cu, Al-Si, or Al-Si-Cu. It was also found that adding the TiC particle by plunging into the melt a tablet made of TiC and flux at a ratio 1:5 gave the best results.

With the TiC to flux ratio of 1:5 providing the most favorable result, a design of experiments was conducted to assess the ability to mix in the TiC particles in the four matrix materials. The design of experiments is summarized in Table 7-4.

Table 7-4 Design of experiments for IDP.

#	Alloy		TiC _p	Flux	Mixing time (min)	Tablet condition
	Type	Weight (%)	Weight (%)	TiC _p :Flux		
1-0	Pure Al	97	3	1:5	10	Whole
1-1	Pure Al	97	3	1:5	10	Broken pieces
1-2	Pure Al	97	3	1:5	5	Whole
1-3	Pure Al	97	3	1:5	20	Whole
1-4	Pure Al	97	3	1:3	10	Whole
1-5	Pure Al	97	3	1:8	10	Whole
1-6	Pure Al	99	1	1:5	10	Whole
1-7	Pure Al	95	5	1:5	10	Whole
1-8	A380	97	3	1:5	10	Whole
1-9	A356	97	3	1:5	10	Whole
1-10	520	97	3	1:5	10	Whole

The resultant material from each experimental run was solidified in a crucible and analyzed for the retention of the TiC particles in the material and uniformity of distribution of the particles. The center location and a location near the edge of the material were analyzed.

Results

Figure 7-12 displays an example X-ray diffraction pattern that shows that TiC is present in the Al-Mg alloy (commercial 520 grade). Seeing TiC in the 520 alloy but not the A380 and



Figure 7-11 Induction coil used to disperse the TiC in the aluminum alloy melt.

A356 alloys may be attributed to the fact that Mg enhances the wetting of TiC by aluminum by eliminating the oxides that may be present at the liquid- particle interface and by decreasing the viscosity and the surface tension of aluminum.

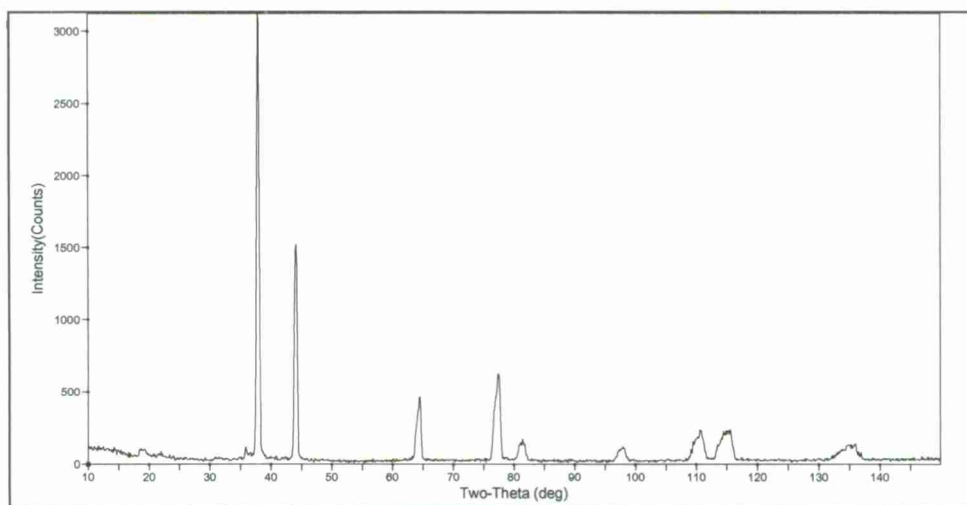


Figure 7-12 X-ray diffraction pattern for TiC particles introduced into 520 alloy. The material was prepared using a particle to flux ratio of 1:5.

Figure 7-13 shows the distribution of the 30 nm TiC particles in the pure aluminum matrix as an example. It was found that a uniform distribution, as shown on the right, could be obtained near the center location of the material. However, a high degree of agglomeration of particles near the wall of the crucible and sticking of the particles to the wall of the crucible was noted. In an attempt to overcome the agglomeration, aluminum powder was added to the TiC and flux in the tablet. This assisted in reducing the agglomeration near the crucible wall but not to a satisfactory level and regardless of mixing time and the application of both mechanical and electromagnetic stirring/mixing. Since uniform distribution of the 30 nm TiC particles in molten Al was not achieved with the IDP process, material for casting was produced by this method.

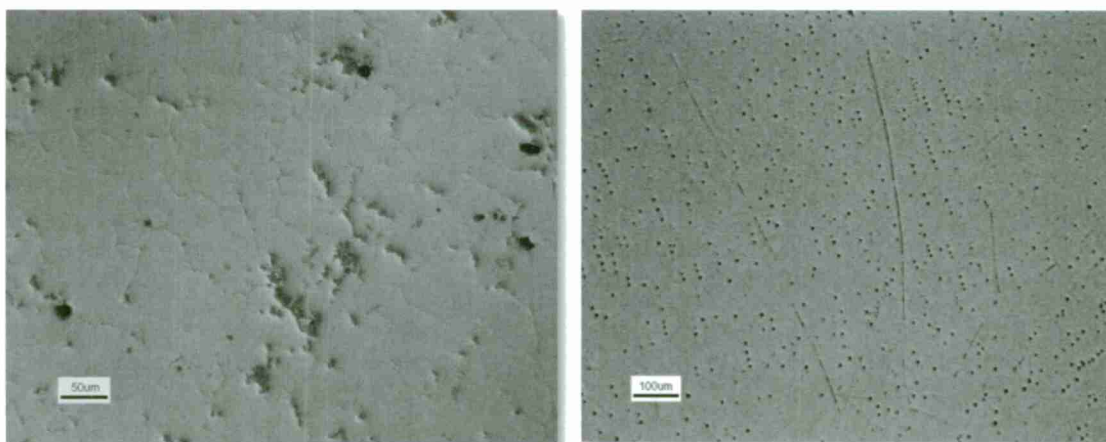


Figure 7-13 Microstructures of nano-particles in aluminum showing moderate agglomeration (left) and uniform distribution (right).

Figure 7-14 shows that incorporating TiC nano-particles into the metal matrix does increase the hardness of the material from 46 HV to about 107 HV (approximately 60 HRB) for more than a two-fold improvement.

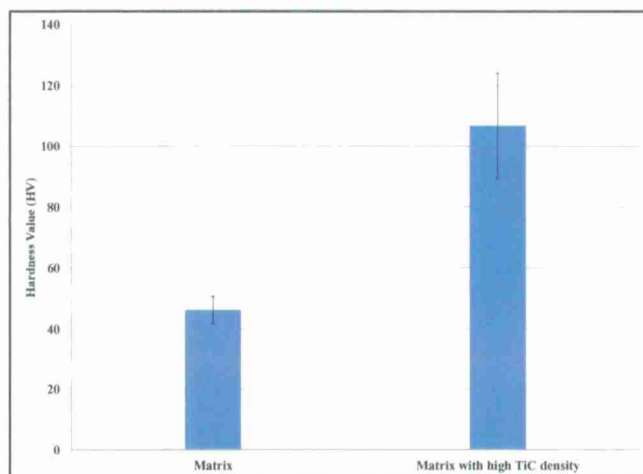


Figure 7-14 Measured hardness for (Al-Mg)-TiC composite prepared by the pressed tablet method.

Key Findings

Although it is considered to be feasible to produce aluminum alloy matrix-TiC nano-particle composite materials by intelligently distributing the reinforcing particles in a liquid aluminum alloy, a few issues remain to be resolved. These include improving the dispersion of the nano-particles in the composite and controlling the amount of residual flux in the final product as some residual flux was periodically noted. Nevertheless, the results obtained indicate that:

- The $KAlF_4$ -assisted process has potential for manufacturing nano aluminum-TiC composite materials because of the beneficial role that $KAlF_4$ plays in enhancing wetting of TiC by liquid aluminum.
- Adding TiC nano particles to the melt by sprinkling them on the surface of the melt in open air leads to degradation of the particles as a result of their oxidation while adding the particles under the melt's surface and wrapping them in aluminum foil reduces the oxidation of the particles and enhances their incorporation into the matrix. Therefore, adding the nano TiC particles mixed with $KAlF_4$ into the melt in the form of a pressed tablet is the recommended method to synthesize nano Al-TiC composites.
- Among all of the investigated alloys, Al-Mg alloys show the greatest potential for incorporating TiC nano particles. Mg enhances the wettability of TiC by liquid aluminum by reducing the surface tension and viscosity of Al and by mitigating the effect of oxides at the TiC/Al interface.
- Lorentz forces induced in the melt by means of an induction coil shows potential in improving the dispersion of the particles in the bulk of the melt.

- TiC nano-particles strengthen the Al-Mg matrix and the pure aluminum matrix as indicated by a significant increase in their hardness.

Conclusions and Recommendations

Castable aluminum base nano-composite materials were developed through three processing routes. The SHS route, which produced the Al/TiC+SiC nano-composite, is the most mature followed by the GLN route, which produced the Al/AlN nano-composite material. The IDP route, which produced an Al/TiC nano-composite, is the least mature. Castings were successfully produced from material that was produced by both the SHS and GLN process routes. Due to the degree of non-uniformity of particle distribution material for casting was not produced by the IDP route. Hence, two novel techniques have been developed that enable die casting of metal matrix composite material with nano-size reinforcement particles adequately distributed within the matrix.

Property measurements show that the SHS Al/10% TiC+SiC nano-composite yields an ultimate tensile strength, yield strength and elongation of 31.2 ksi, 22.5 ksi and 1.5%, respectively, as compared to 25.4 ksi, 14.5 ksi and 3-5%, respectively, for the unreinforced matrix.

Hardness was determined to be 65 HRB average after SSM casting as compared to the unreinforced matrix of approximately 20 HRB. These properties exceed those of the SHS composite material with micron size particles and wear resistance of the nano-composite was determined to be 3 times greater than the SHS micron-composite. Hardness of the GLN Al/3% AlN nano-composite was determined to be as high as approximately 65 HRB as compared to approximately 20 HRB for the unreinforced matrix.

Recommendations for future work are to: 1) generate additional property data for the SHS and GLN nano-composite materials; 2) cast components from the SHS and GLN nano-composite materials for component performance testing; and 3) further develop the IDP process route to overcome the agglomeration issue and cast material for characterization. Consider an alternate or addition mixing method for the IDP nano-composite material, such as ultrasonic mixing.

8. **High Strength, High Toughness, Cast Aluminum Alloy:** *Principal Investigators Robin D. Foley, University of Alabama at Birmingham*

Abstract

The wrought 7xxx series alloys are among the highest strength aluminum alloys. Casting these alloys typically results in two microstructural defects: 1) intermetallics and 2) micro-porosity. Six experimental Al-Zn-Mg-Cu alloys were cast under 1MPa (10 atmospheres) of pressure. Zinc concentrations of 8 and 12wt% and Zn/Mg ratios of 1.5 to 5.5 were tested. Copper was held constant at 0.9%.

Heat treating of the alloys was optimized for maximum hardness. Samples were solution treatment at 441°C (826°F) for 4 hours before ramping to 460°C (860°F) for 75 hours and then aged at 120°C (248°F) for 75 hours.

X-ray diffraction showed that the age hardening precipitates in most of these alloys was the T phase ($\text{Mg}_{32}\text{Zn}_{31.9}\text{Al}_{17.1}$). DSC confirmed that lower alloy contents resulted in easier intermetallic dissolution during solution treatment and that precipitation began at higher temperatures during aging.

Chilled Al-8Zn-1.4Mg-0.9Cu solidified under pressure resulted in an alloy with yield strength of 468MPa (68ksi), tensile strength of 525MPa (76ksi) and elongation of 9%. Two military castings were successfully produced with this composition.

Objective

There is an ongoing need to reduce the weight and cost of military weapon systems. High strength, high toughness, cast aluminum alloys could meet this need in applications such as armor and structural components. Advanced, ultra high strength, cast aluminum alloys can have exceptionally high strength but suffer from a lack of ductility. It is hypothesized that the lack of ductility is caused by the combination of two microstructural features; an interdendritic network of intermetallic particles and randomly dispersed microporosity. These microstructural features are caused by the solidification characteristics of these alloys including a long freezing range and very little isothermal solidification, which produces significant segregation of alloying elements and prevents adequate feeding during solidification.

The objective of his project was to develop an ultra-high strength (>600 MPa yield strength), cast aluminum alloys with reasonable tensile ductility (>8%) based on the Al-Zn-Mg-Cu system without the addition of expensive alloying additions.

Introduction

Advanced, high strength, cast aluminum alloys have been studied extensively in recent years [1-18]. These alloys have exceptionally high strength but relatively low ductility. It has been hypothesized that the lack of ductility is a result of two micro-structural features: 1) an inter-dendritic network of un-dissolved intermetallic particles and 2) randomly dispersed micro-porosity. The microstructural features are a result of solidification characteristics typical of cast Al-Zn-Mg-Cu alloys, which include a long solidification range and segregation during solidification. These factors result in the formation of brittle intermetallics and micro-porosity.

Cast and Wrought Properties in Aluminum Alloys

The most commonly used cast aluminum alloys are based on the Al-Si binary alloy system and include A319 (Al-Si-Cu), A356 (Al-Si-Mg) and A357 (Al-Si-Mg). Compositions of these alloys are shown in Table 8-1 [1]. The solidification range in these alloys are approximately 60 to 90°C (140 to 194°F), and yield strengths range from 165 to 290MPa (24 to 42ksi) while elongations range from 2 to 8% as shown in Table 8-2 [1].

Table 8-1 Composition ranges (wt%) of aluminum casting and wrought alloys [1].

Alloy	Cu	Mg	Mn	Fe max	Si	Ti	Ag	V	Zr	Zn
201	4.0 to 5.2	0.15 to 0.55	0.2 to 0.5	0.15	0.10 max	0.15 to 0.35	0.4 to 1.0	-	-	-
A206	4.2 to 5.2	0.15 to 0.35	0.2 to 0.5	0.10	0.10 max	0.15 to 0.30	-	-	-	-
BAC 100™	5.00 to 6.25	0.2 to 0.5	0.2 to 0.65	0.15	0.15 max	0.02 to 0.04	0.4 max	0.05 to 0.25	0.05 to 0.25	-
A319	3.0 to 4.0	0.10 max	0.50 max	1.00	5.5 to 6.5	0.25 max	-	-	-	1.0 max
A356	0.20 max	0.25 to 0.45	0.10 max	0.20	6.5 to 7.5	0.20 max	-	-	-	0.10 max
A357	0.20 max	0.40 to 0.70	0.10 max	0.20	6.5 to 7.5	0.10 to 0.20	-	-	-	0.10 max
Wrought 7042	1.3 to 1.9	2.0 to 2.8	0.20 to 0.40	0.20	0.20 max	-	-	-	0.11 to 0.20	6.5 to 7.9
Wrought 7075	1.2 to 2.0	2.1 to 2.9	0.30 max	0.50	0.40	0.20	-	-	-	5.1 to 6.1
Wrought 2519	5.3 to 6.4	0.05 to 0.40	0.10 to 0.50	0.30	0.25 max	0.02 to 0.10	-	0.05 to 0.15	0.10 to 0.25	0.10 max

Table 8-2 Aluminum alloys and their mechanical properties (for cast alloys, properties are from separately cast test bars) and liquidus and solidus [1].

Alloy	Yield MPa (ksi)	UTS MPa (ksi)	Elongation (%)	Liquidus Temp. (T _L) ±2°C (°F)	Solidus Temp. (T _S) ±2°C (°F)
201-T6	484(70)	435(63)	7	650 (1200)	535 (995)
201 - T7	414 (60)	462 (67)	4.5	650 (1200)	535 (995)
A206 - T7	347 (50)	436 (63)	12	650 (1202)	570 (1058)
A319 - T6	165 (24)	250 (36)	2.0	605 (1120)	515 (960)
A356 - T6	165 (24)	227 (33)	3.5	615 (1135)	555 (1035)

A357 – T62	290 (42)	360 (52)	8	615 (1135)	555 (1035)
Wrought 7042 – T7	503 (73)	583 (85)	12	629 (1164)	467 (873)
Wrought 7075 – T6	503 (73)	572 (83)	11	635 (1175)	477 (890)

Higher strength cast aluminum alloys include A206 and 201, both Al-Cu-Mg alloys. Additions of 0.4-1.0wt% silver are added to alloy 201 for increased strength. Alloy A206-T7 has both higher yield strength (345MPa (50ksi)) and elongation (12%) than the Al-Si alloys. The solidification range for this alloy is around 80°C (176°F), and it is commonly cast by high quality aluminum foundries. Alloy 201-T7 has a higher yield strength than those found in A206-T7 at 414MPa (60ksi), but the elongations are lower. The solidification range is 115°C (239°F), making it is more challenging to cast. The addition of silver also makes alloy 201 expensive.

The strengths of cast 201 and A206 are still well below those obtained in wrought 7XXX (Al-Zn-Mg-Cu) alloys as shown in Table 8-2. These alloys achieve yields strengths around 500MPa (72ksi) while maintaining elongations of 10-12%. The downside to the 7xxx series aluminum alloys is their poor stress corrosion cracking resistance and generally poor fatigue strength.

Alloying Effects in Cast Aluminum Alloys

The Al-Zn-Cu-Mg wrought alloys are the highest strength aluminum alloys. Zinc additions alone do not significantly increase strength [2]. However, zinc increases the solution potential of other alloying elements in aluminum so that intermetallics formation can be reduced, increasing strength and ductility [2].

The addition of magnesium to the Al-Zn binary alloy results in the formation of the intermetallic η ($MgZn_2$), which responds well to aging, increasing the strength potential of the alloy [2]. Increasing the volume percent of η ($MgZn_2$) from 0.5% to 12% in quenched sheet has been shown to increase both ultimate and yield strength [2]. Increasing free magnesium further increases strength but decreases elongation and increases the likelihood of stress corrosion cracking [2].

Additions of copper to Al-Zn-Mg alloys increase the resistance to stress corrosion cracking, but increases quench sensitivity and decrease the resistance to general corrosion [3]. It is believed that additions of copper greater than 1wt% also increases the aging rate by increasing the amount of super-saturation, resulting in the nucleation of S phase ($CuMgAl_2$). [2]

In Al-Zn-Mg-Cu alloys, small amounts of iron can result in poor ductility. Iron combines with other elements and results in insoluble, brittle intermetallic constituents that reduce ductility [2].

The Al-Zn-Mg-Cu alloys achieve high strengths through solid solution and precipitation hardening. To maintain strength and ductility in these alloys, the formation of porosity and brittle intermetallics during solidification must be minimized or eliminated. Porosity reduces ductility. Porosity can be minimized by proper gating and risering, the use of chills, solidification under pressure (SUP) and Hot Isostatic Pressing (HIPing). Large

intermetallics reduce the strength of the alloys by limiting the alloying available for precipitation hardening and reduce ductility by forming an interconnected network of brittle phases. If the cooling rate is low, or if alloying levels are high, the intermetallics are challenging to dissolve during solution treatment. Intermetallics size can also be minimized by the use of chills.

Phase Stability and Heat Treatment

The simple aluminum-copper binary phase diagram (Figure 8-1 [4]) helps to illustrate the issues associated with intermetallic formation during solidification in high strength aluminum casting alloys. To minimize intermetallic formation, alloys must have compositions below the eutectic range (less than 6% for the binary aluminum-copper system). In practice, the intermetallic constituent in question must be even lower because non-equilibrium solidification can cause segregation which will increase the amount of the intermetallic constituent in the areas that solidify last. As the alloy solidifies, a copper-rich solute is rejected from the aluminum-rich dendrites into the remaining liquid. This segregation can increase the copper concentration of the liquid to over 6% and result in eutectic formation when overall compositions are below the eutectic range. Larger, eutectic intermetallics that form during non-equilibrium solidification may not dissolve during solution treatment and this limits the alloying available for precipitation hardening. In addition, non-equilibrium eutectic formation also limits the solution treatment temperature because localized melting can occur in these low melting temperature regions.

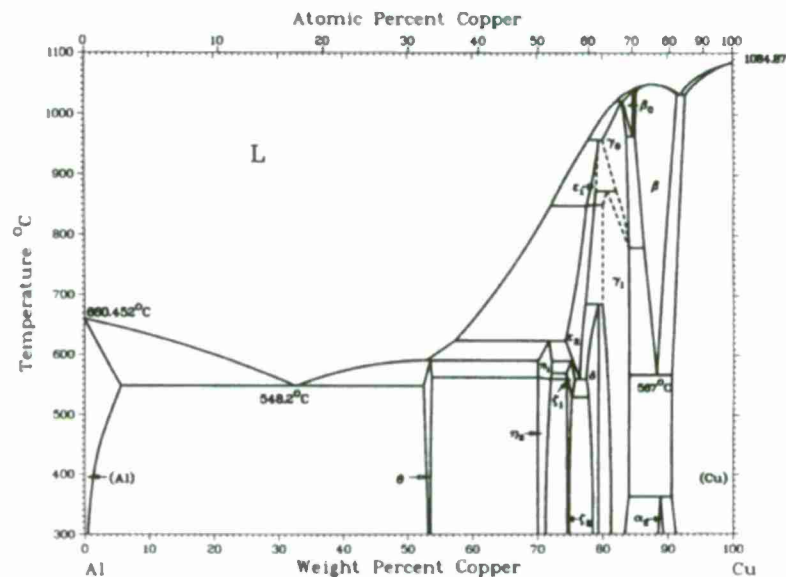


Figure 8-1 The aluminum-copper binary phase diagram [4].

The aluminum, zinc, and magnesium ternary liquidus projection also aids in understanding the formation of intermetallic formation based on starting composition (Figure 8-2 [4]). In low total alloy amounts (~ less than 10wt%) the MgZn₂ (η) phase will be present as predicted by most literature. For high alloy contents, T phase (Mg₃₂(Zn,Al)₄₉) will be present [5]. 7xxx alloys have a number of phases that can form during solidification including η (MgZn₂ in which aluminum and copper can substitute for zinc), S (Al₂CuMg) and T ((Mg₃₂(Zn,Al)₄₉) [2]. The S phase Al₂CuMg is more likely to form at higher copper concentrations and is slow to dissolve; in addition, non-equilibrium melting of this phase can occur between 485-490°C (905-914°F) [2].

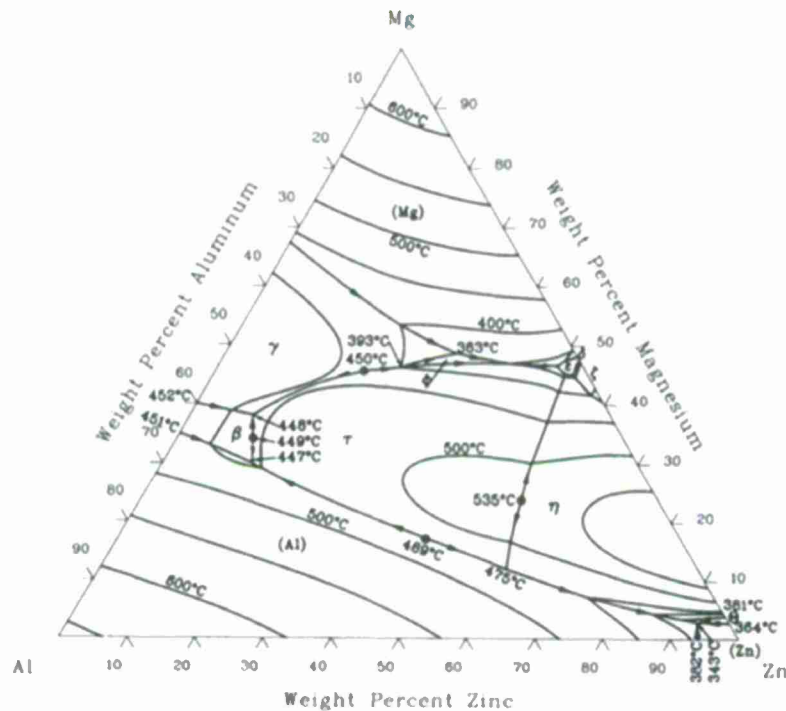


Figure 8-2 The aluminum, zinc, magnesium ternary liquidus projection [4].

High zinc and magnesium concentrations may result in interconnected intermetallics, which may not dissolve during solution treatment. Increasing the alloy concentration increases strength, so finding the practical point of insolubility will greatly advance our current knowledge base on cast Al-Zn-Mg-Cu alloys.

Solution Treating

The purpose of solution treating is to dissolve the second phases that form during solidification to maximize the amount of solute (copper, magnesium, and zinc) in solid solution within the aluminum matrix. This maximization occurs just below the eutectic temperature. In practice, the temperature must be lower to avoid localized melting. Cast 7xx alloys have been shown to exhibit incipient melting if the temperature is not carefully maintained [6].

Aging

Age hardening of Al-Zn-Mg-Cu alloys begins with the super saturation of the aluminum matrix (α SS) [4]. In 7xxx series alloys, a number of precipitates can form. A low temperature initial aging period results in the redistribution of solute atoms within the solid solution lattice to form clusters of Guinier-Preston (GP) zones that are considerably enriched in solute. This local redistribution results in distortions of the lattice planes, increasing the material's strength proportionally to the size and number of GP zones.

Above room temperature, GP zones with high Zn/Mg ratios transform into the transition precipitates η' and/or T' [2]. These metastable precipitates are partially coherent with the {111} matrix plane [2] and are precursors to the equilibrium precipitates η (MgZn_2) and T

($Mg_{32}(Zn,Al)_{49}$) which are shown in Equation 2. The η ($MgZn_2$) phase is more likely to form at lower magnesium and zinc concentrations

$$SS \rightarrow GP \text{ zones (Spherical)} < \frac{\eta' \rightarrow \eta}{T' \rightarrow T} \quad \text{Equation 1 [2]}$$

The possible transition routes are oversimplified in equation 1 as the transition phase η' may actually form over a range of considerable composition range ($Al+T$ and $Al+\eta$). Increasing the time or temperature results in a more rapid transformation to the equilibrium η ($MgZn_2$) and/or T ($Mg_{32}(Zn,Al)_{49}$) phase(s). If the copper concentration is above 1wt%, then copper and aluminum can substitute for zinc in the η ($MgZn_2$) phase to form S phase (Al_2CuMg) [2].

If significant silicon is present in an Al-Zn-Mg-Cu alloy, Mg_2Si can form at the grain boundaries. This phase cannot be dissolved during solution treatment. In wrought alloys, it results in fracture during hot forming [3].

Al-Zn-Mg-Cu Chemistries

Recent studies of cast Al-Zn-Mg-Cu based alloys have shown that high yield strength and ultimate strength are possible. However, the ductility is unacceptably low and needs improvement before these alloys can be used commercially [6,7]. The goal of this research was to maximize strength while maintaining a minimum of 8% elongation. The effect of zinc on aluminum alloy containing 1.5% copper and 1% and 3% magnesium in 1.6mm (0.064in) thick sheet, which has been heat treated and aged is shown in Figure 8-3 [2]. The results indicate that additions of 8-12wt% zinc should result in 8% elongation since the curve appears to level off at about 10% elongation at zinc concentrations above 7wt%.

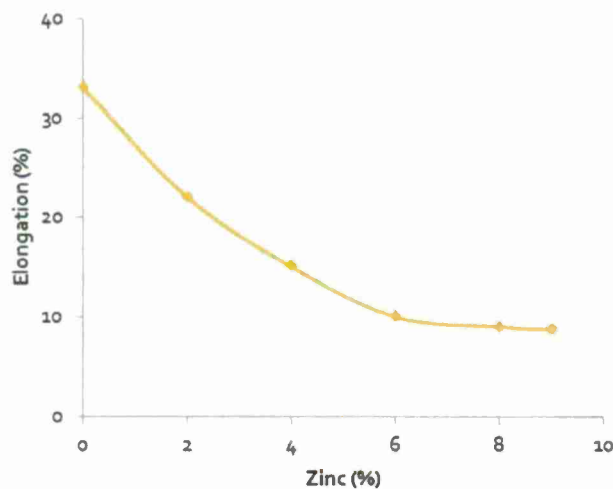


Figure 8-3 Elongation versus zinc content (wt%). [2]

Maximizing yield and ultimate tensile strength requires high zinc and magnesium alloy concentrations. Figure 8-4, shows the effects of zinc and magnesium concentration on the tensile and yield strength of heat treated and aged 1.6mm (0.064in) thick sheet [2]. As the zinc concentration increased from 0 to 9wt%, the yield and ultimate tensile strength increased [2]. Increasing magnesium from 1 to 3wt% increased the yield and tensile

strength [2]. The η (MgZn_2) phase is the primary strengthening precipitate in 7xxx series wrought alloys. The ratio of Zn/Mg to achieve this precipitate is 5.39wt% and the ratios achieved in this study ranged from 0 to 9wt% [2].

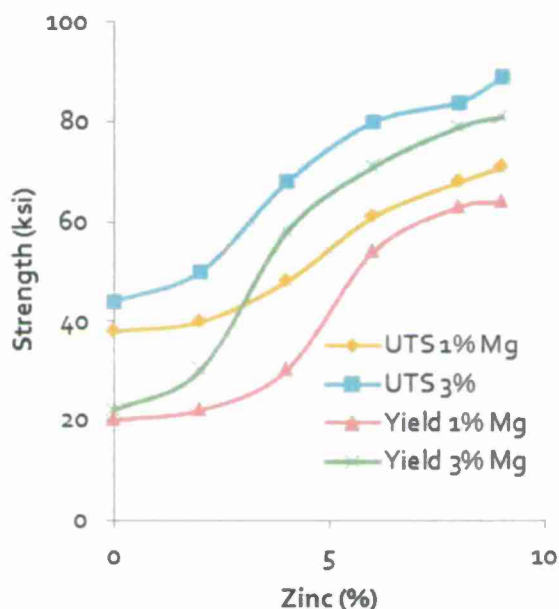


Figure 8-4 Strength versus zinc content (wt%). [2]

SUP/HIPing

Cast aluminum alloys are prone to shrinkage and hydrogen porosity, which can limit the strength and elongation. As the temperature of liquid aluminum increases, so does the solubility of hydrogen within the aluminum. Hydrogen porosity is the result of the difference in solubility in liquid and solid; hydrogen is readily soluble in liquid aluminum alloys but relatively insoluble in the solid, as shown in Figure 8-5[19].

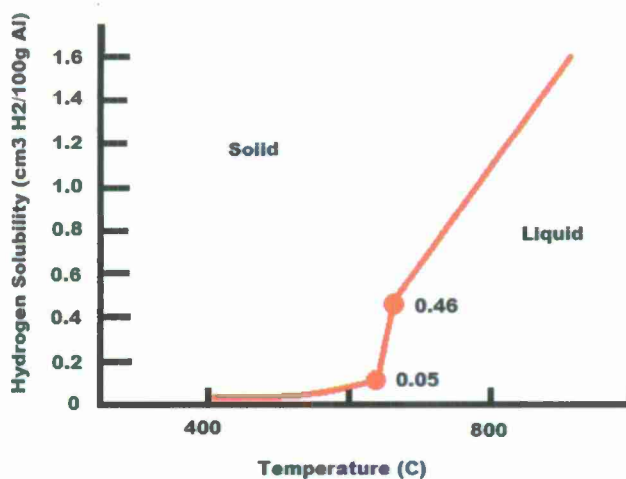


Figure 8-5 Hydrogen solubility in aluminum versus temperature. [19]

There is only limited data documenting pore size reduction by solidifying aluminum alloys under pressure since the specialized equipment necessary to perform such studies is not readily available. The results of one such study stated that "solidification under pressure reduced porosity and helped densify the solidifying metal." However, that study provided only mechanical property and no porosity data [20]. Both shrinkage porosity and hydrogen porosity can be reduced by applied isostatic pressure during solidification. Pressure can improve feeding, physically push dendrites closer together, increase the solubility of hydrogen in the solid, and decrease the size of bubbles (pores) in the liquid (Figure 8-6) [21].

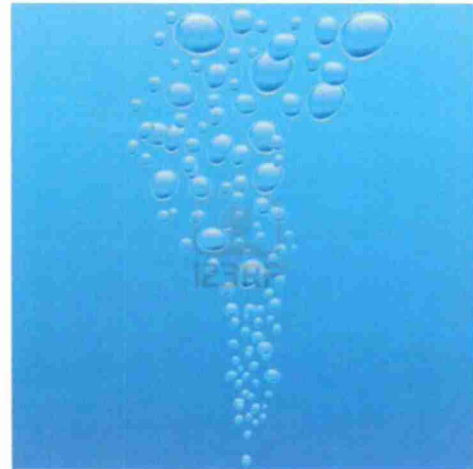


Figure 8-6 Bubble size versus pressure. [21]

By increasing the pressure between 0.1 to 1.0MPa (1 to 10 atmospheres) the porosity can be reduced and resulting mechanical properties can be increased in cast aluminum alloys.

The Castyril R process or pressure solidification process was patented in 1989 by Pechiney in France [22]. It entailed pouring a casting inside a pressure vessel and increasing the pressure until solidification was completed. Currently, Mercury Marine produces approximately 20,000 cylinder blocks a year using this process [23].

This application of additional pressure during solidification should result in decreased and or eliminated hydrogen porosity in the cast metal, which increases the resulting mechanical properties.

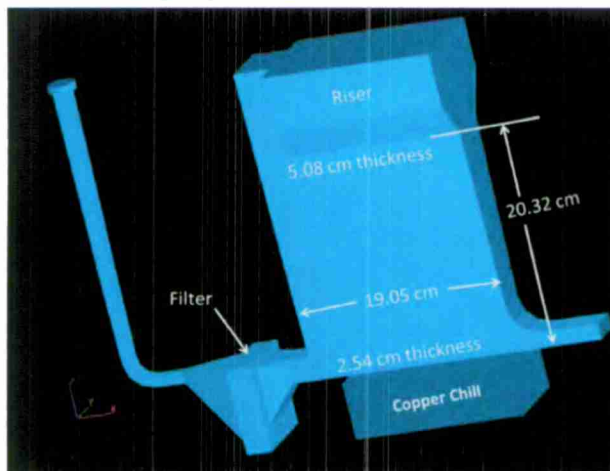


Figure 8-7 Design and Dimension of UAB Wedge casting.

Shrinkage porosity occurs when there is no easy pathway for liquid metal to flow in-between growing dendrites; thus, areas become isolated and pores form. The application of pressure during solidification may help to push liquid metal farther into the channels between dendrites and exert a force that pushes the dendrites together. Both mechanisms can reduce the size and amount of shrinkage porosity.

Experimental Methods

Casting

The experimental Al-Zn-Mg-Cu alloys were cast at UAB in a wedge shaped casting that produced smooth laminar filling and were properly chilled and risered to produce a sound casting. The design and dimensions of the wedge casting are shown in Figure 8-7. A plug-pour basin was used to reduce pouring rate variations and entrained oxides for the wedge castings.

Heats that weighed 9.5kg (21lb) were crucible melted in a resistance furnace. A master alloy containing low iron and copper (Al-0.9Cu-0.08Fe) was used as the base alloy. From this base alloy, additions were made to result in the desired chemistry. Each heat was degassed for between 20-60 minutes with argon rotary degassing. A reduced pressure test sample was taken after degassing for each heat and checked to ensure proper degassing. Grain refinement additions of 0.02wt% Ti were added. Copper chilled chemistry samples were taken for each heat.

The pressure vessel at UAB was used for the experimental alloy wedge castings. The pressure vessel was 1.2 meters in diameter and 1.8 meters in height, which provides sufficient working space to easily produce large castings, such as a cylinder block (Figure 8-8). The pressure vessel is rated at 10MPa (100 atmospheres) maximum pressure. After pouring, the pressure vessel was closed with the mold inside and pressurized to 1MPa (10 atmospheres) pressure using a mixture of dry compressed air and compressed nitrogen gas. Peak pressure of 1MPa (10 atmospheres) was achieved in ~90 seconds after pressurization was initiated. Some castings sections were HIPed to provide a porosity free base line material. HIPing was performed by Bodycote by heating to $453^{\circ}\text{C} \pm 4^{\circ}\text{C}$ at $103\text{MPa} \pm 3.5\text{MPa}$ ($847^{\circ}\text{F} \pm 9$ at $15,000\text{ psi} \pm 500\text{psi}$) for 2-4 hours in inert gas.



Figure 8-8 UAB pressure vessel.

Eight heats of Al-Zn-Mg-Cu alloys were poured between $730\text{-}760^{\circ}\text{C}$ ($1350\text{-}1400^{\circ}\text{F}$). The target chemistries were chosen to allow for investigation into the effects of zinc, magnesium and Zn/Mg ratio on the mechanical properties of cast Al-Zn-Mg-Cu alloys (Table 8-3). Zinc concentrations of 8 and 12wt% and Zn/Mg ratios of 1.5 to 5.5 were tested. Copper was held constant at 0.9wt% to minimize copper related intermetallics while gaining stress corrosion cracking resistance and increased strength. The low alloy casting (3) and high alloy casting (4) were cast under 0.1MPa (1 atmosphere) and 1MPa (10 atmospheres) to allow for a comparison on the effects of pressure during solidification.

Table 8-3 Target chemistries for each of 6 alloys.

Alloy	Zn	Mg	Zn:Mg	Cu	Fe
1	8	5.3	1.5	0.9	<0.08
2	8	2.3	3.5	0.9	<0.08
3 *	8	1.5	5.5	0.9	<0.08
4 *	12	8	1.5	0.9	<0.08
5	12	3.4	3.5	0.9	<0.08
6	12	2.2	5.5	0.9	<0.08
7075	5.1-6.1	2.1-2.9	1.8-2.9	1.2-2.0	

*Denotes cast under pressure and in air.

Two additional 8Zn-1.4Mg-0.9Cu military castings were produced to demonstrate that this alloy could be used to produce commercial parts. One casting, a helicopter missile launch rail bracket, was solidified under 1MPa (10 atmospheres) pressure. The other, a structural mounting plate for a military vehicle, was solidified conventionally.

Heat Treating

Samples were heat treated at UAB in a recirculating air furnace with a thermocouple attached to the samples to accurately control specimen temperature. Solution treatment studies were conducted with the goal of reducing and eliminating intermetallic particles. Samples were solution treated at 441°C (826°F) for 4 hours followed by 460°C (860°F) for 75 hours.

Aging was conducted to determine the maximum hardness. Samples were naturally aged at room temperature for greater than 24 hours then artificially aged at 120°C (248°F) and 150°C (302°F) for between 0 and 120 hours. Hardness was measured at varying times with a New Age HB3000B Brinell Hardness tester at 500kg load and a 10mm diameter ball.

Tensile Testing

Tensile bars that were 9mm diameter x 36mm gage length were tested in accordance with ASTM E8/B557 (2011, 2010) [24,25] on an MTS 810 servo hydraulic tension/compression tester using an extensometer. This data was used to determine mechanical properties such as 0.2% offset yield strength, ultimate tensile strength and elongation to fracture.



Figure 8-9 Casting produced with lines showing where each tensile blank was cut from.

Samples were removed from the four locations at distances ranging from 0.8cm (0.3in) to 6.7cm (2.6in) from the chill (Figure 8-9). As the distance from the chill increased, the cooling rate in the samples decreased. Samples for HIPing were removed from a section rotated 90 degrees from the chilled and SUP tensile samples. The center of the HIPed tensile bars were at a distance more than 5cm (2in) from the chill so the cooling rate in these regions were lower than seen in the thickest SUP samples. From each wedge casting, two specimens were removed from locations adjacent, 2.9cm (1.1in), 4.8cm (1.9in), and 6.7cm (2.6in) from the chill and four HIPed samples were analyzed.

Microstructural Analysis

Microstructural analysis was conducted on selected tensile samples using optical microscopy. Samples approximately parallel to and just below the tensile fracture surfaces were removed and polished.

Intermetallic measurements were made by taking optical images of the microstructure at a magnification of 500x. Image analysis was conducted by utilizing color thresholding to separate the second phase particles from the matrix to determine their volume percent and feret length.

Tensile fracture surfaces were examined with a Zeiss Stemi 6 stereo microscope. Projected fracture surface oxide volume percent's were measured.

SEM analysis of the tensile bar fracture surfaces and metallography samples were conducted at UAB. An FEI-FEG 650 SEM equipped with an EDAX TEAM SDD 30mm² energy dispersive x-ray detector (EDS) was used.

Secondary and backscattered electron imaging were used to examine the samples. With EDS analysis, the entrained oxides and elements present in the intermetallic particles were identified. Projected fracture surface porosity measurements were also performed on the tensile fracture surfaces.

X-ray diffraction (XRD) was performed on the polished tensile samples of solution treated and aged Al-Zn-Mg-Cu alloys. XRD was performed using a Siemens D-500 Diffractometer with Cu radiation and graphite monochromater. Scans were performed at 40kV and 30mA between 2 θ of 20° and 90°, utilizing a step size of 0.05° and a dwell time of 60 seconds. Total scan times for each samples was about 24 hours. XRD was used to identify the second phase particles and texturing of the aluminum matrix.

Both solution treatment and aging Differential Scanning Calorimeter (DSC) tests were conducted on the experimental cast Al-Zn-Mg-Cu alloys. The DSC used was a TA Instruments DSC Q100. For the solution treating study, samples were heated from room temperature to 500°C (932°F) at a rate of 20°C/min (36°F/min) and then cooled back to room temperature at the same rate. For the aging study, samples were solution treated and then tested at a rate of 5°C/min (9°F/min) to 200°C (392°F). Sample size for DSC was dictated by the DSC equipment capacity and was less than 3.5mm diameter and 2mm in length. The results were analyzed using TA Instruments Universal Analysis 2000 program. Points of inflection, peak positions and area under the peaks were all determined.

Results/Key Findings

Mass spectrometry analysis of each chemistry button was conducted and the results are shown in Table 8-4. The results were close to the desired compositions for the alloys.

Table 8-4 Actual chemical compositions for each alloy determined using spectrometer analysis.

Alloy	Zn (wt%)	Mg (wt%)	Cu (wt%)
1	7.9	4.9	0.9
2	8.1	2.1	0.9
3-0.1MPa	7.9	1.4	0.9
3-1MPa	8.2	1.4	0.9
4	13.1	7.3	1.0
5	12.5	3.4	0.8
6	12.4	2.0	.63

Table 8-5 contains thermal analysis data for each alloy. Thermal analysis curve for the alloys with the highest and lowest alloying additions are shown in Figure 8-10. The liquidus

(T_L) is the temperature at which solidification began and is identified as the end of the first rapid cooling rate. Solidification in most of the alloys was completed with the formation of some eutectic as there was some recalescence followed by a subsequent leveling off of the cooling curve. Completion of solidification was indicated when the temperature began to decrease again. The solidus temperature (T_S) and time spent there are indicative of the amount of intermetallics formed. Volume fractions of as-cast intermetallic phases are undesirable as they will be difficult to dissolve during the solution treating phase and will lower strength and ductility. The eutectic can form because the composition is within the eutectic region or due to segregation that occurs during solidification.

Table 8-5 Thermal analysis results for each alloy.

Alloy	Zn (wt%)	Mg (wt%)	Cu (wt%)	$TL \pm 2^\circ C$ ($^\circ F$)	$TS (\pm 2^\circ C)$ ($^\circ F$)	Solidification Range $TL - TS^\circ C$ ($^\circ F$)	Time at Solidus (sec)
1	7.9	4.9	0.9	618 (1144)	472 (882)	146 (262)	30
2	8.1	2.1	0.9	629 (1164)	467 (873)	162 (291)	10
3	8.2	1.4	0.9	637 (1179)	457 (855)	180 (324)	2
4	13.1	7.3	1.0	590 (1094)	473 (883)	117 (211)	89
5	12.5	3.4	0.8	626 (1159)	466 (871)	160 (288)	26
6	12.4	2.0	0.6	624 (1155)	463 (865)	161 (290)	16

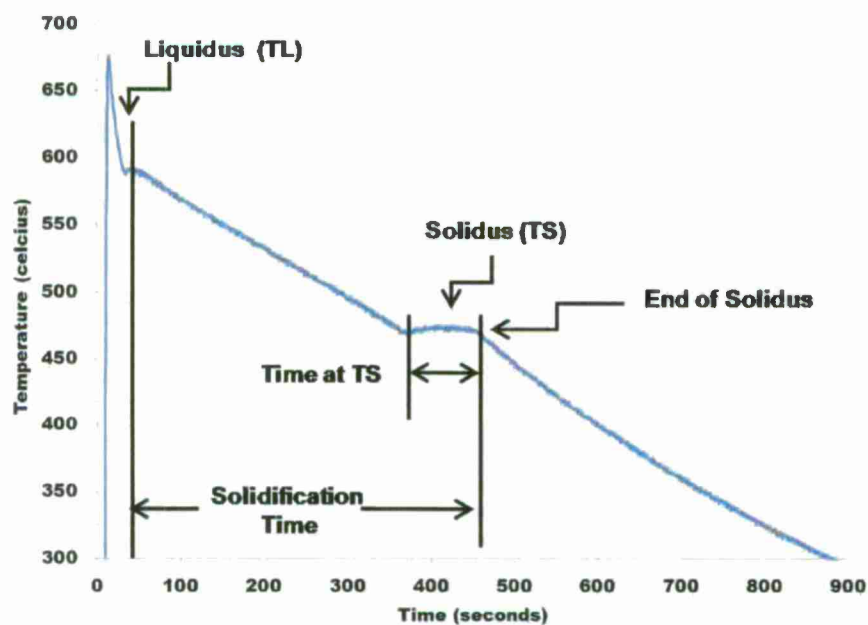


Figure 8-10a Cooling curve for alloy 4 (7.9Zn-4.9Mg-0.9Cu).

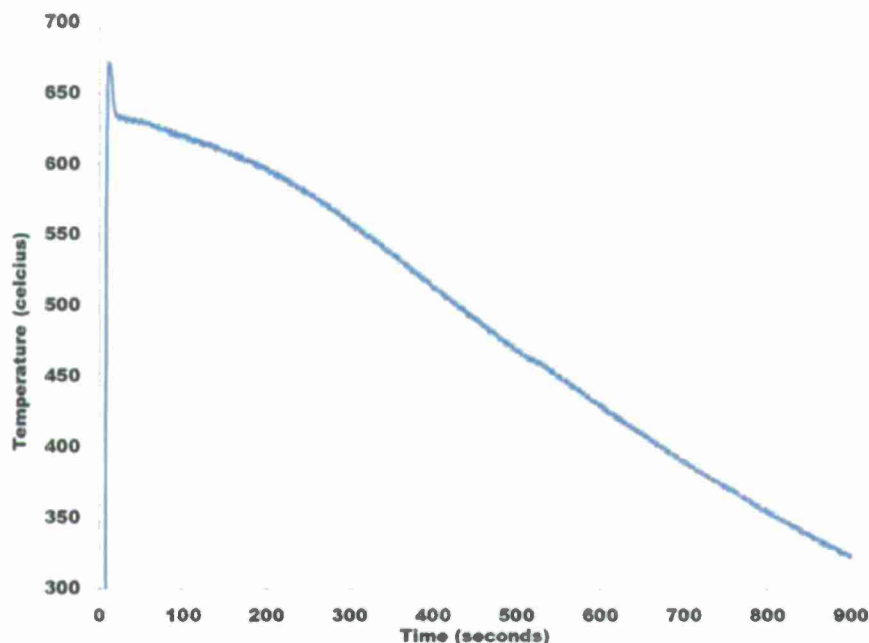


Figure 8-10b Cooling curve for alloy 3 (8.2Zn-1.4Mg-0.9Cu).

The solidus and liquidus temperature were approximately constant with zinc concentration. As magnesium increased from 2 to 7.3wt%, the liquidus temperature decreased from 637 to 590°C (1179 to 1094°F) while the solidus temperature increased from 457 to 473°C (855 to 883°F) leading to an increase in the solidification range from 147 to 180°C (223 to 324°F). The largest solidification range was seen at the lowest alloy additions of 8.2Zn-1.4Mg (alloy 3) at about 180°C (324°F) while the smallest was seen at the highest alloy additions of 13.1Zn-7.3Mg (alloy 4) at 117°C (211°F).

The three alloys with the high zinc concentration had longer times at T_s when compared to the low zinc alloys. Also, the time spent at T_s decreased with decreasing magnesium concentration at constant zinc concentrations. Alloy 3 (lowest alloy concentration) had the shortest time spent at T_s (0 ± 2 seconds) while alloy 4 (highest alloy concentration) had the longest time spent at T_s at 89 seconds.

SEM Characterization

Representative SEM images of the as-cast microstructure of the alloy with lowest alloying additions (alloy 3-1MPa (8.2Zn-1.4Mg)) and the highest alloying additions (as cast alloy 4 (13.1Zn-7.3Mg)) are shown in Figures 8-11a and 8-11b. The image magnification of alloy 4 (13.1Zn-7.3Mg) is higher to show the eutectic structure. All the alloys exhibited some eutectic intermetallics although the amount was greatly reduced in the lower alloy compositions. As zinc and magnesium contents increased, the size and amount of interconnected eutectic intermetallic increased. The cooling curve and microstructure of alloy 4 (14.1Zn-7.3Mg) with the highest alloying additions indicated that the alloy was in the eutectic range and that the large as-cast intermetallics could not be dissolved. Therefore, no further analysis was performed on alloy 4 (13.1Zn-7.3Mg).

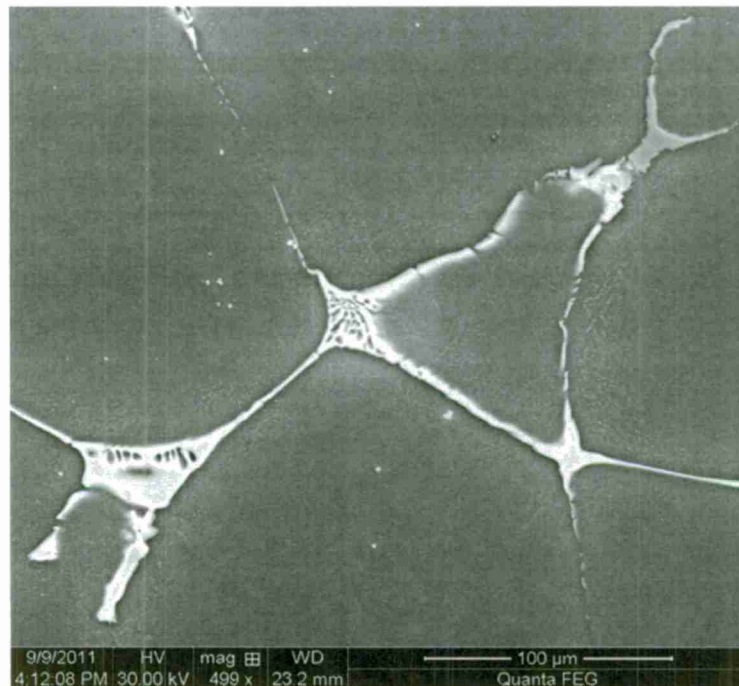


Figure 8-11a As cast microstructure of alloy 3-1MPa (8.2Zn-1.4Mg) showing intermetallic phases.

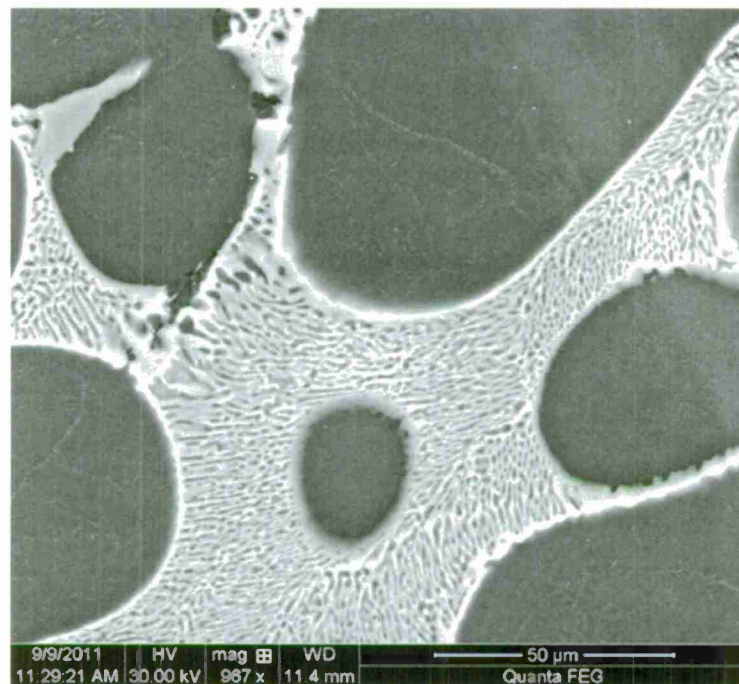


Figure 8-11b As cast microstructure for alloy 4 (13.1Zn-7.3Mg) showing intermetallics phases.

Following solution treatment and aging, some fraction of the as-cast intermetallics remained in all of the samples. SEM-EDS analysis was performed on all the alloys and two different as-cast intermetallic phases were identified. A representative SEM image of the intermetallics in alloy 2 (8.1Zn-2.1Mg) is shown in Figures 8-12. The matrix contained

aluminum, zinc, magnesium and copper (red outline in Figure 8-13). The majority of the as-cast intermetallic phase contained aluminum, zinc, magnesium and copper (blue area in Figure 8-13) with a higher zinc, magnesium and copper concentration than seen in the matrix. A smaller amount of an intermetallic-inclusion phase was also identified and contained aluminum and iron with trace amounts of zinc, magnesium, copper and nickel (Figure 8-14).

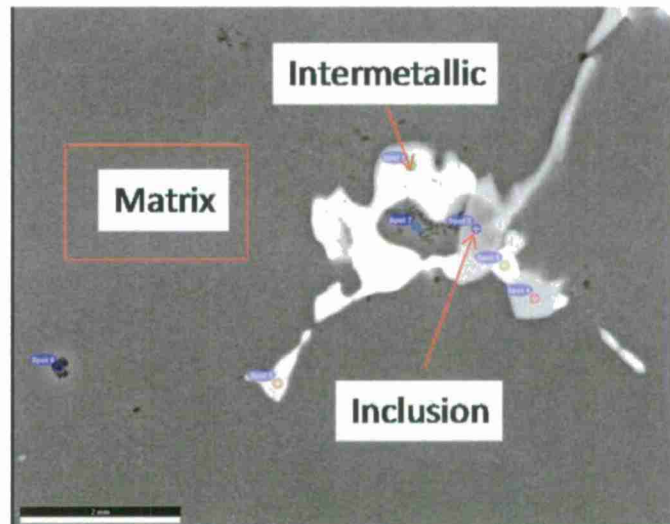


Figure 8-12 Representative backscatter scanning electron micrograph (compositional contrast) of the intermetallics found in the samples.

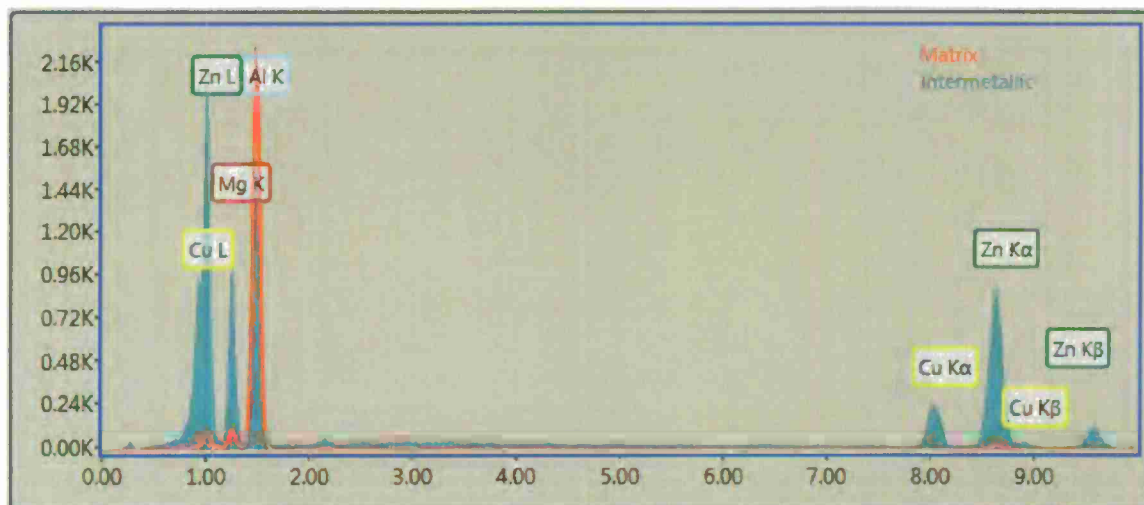


Figure 8-13 EDS results for both the aluminum matrix (red outline) and the intermetallic (blue).

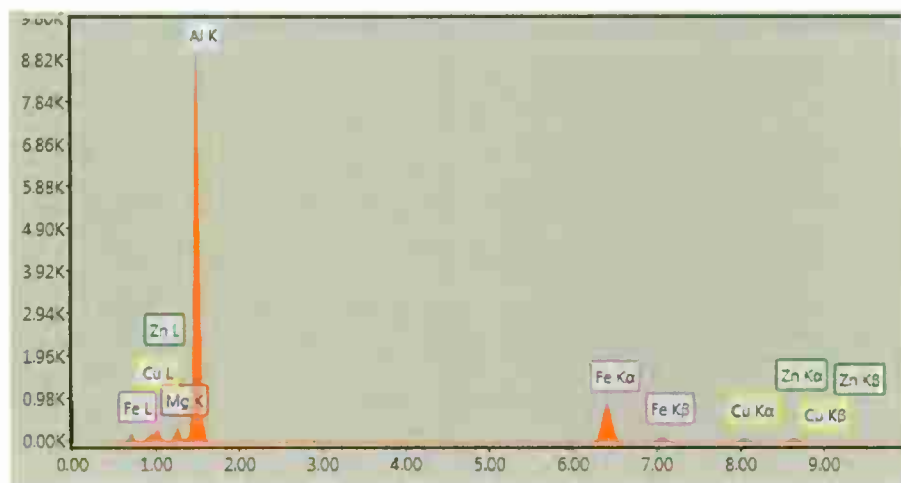


Figure 8-14 EDS results for the intermetallic containing iron and trace amounts of nickel (possible inclusion).

The size of the intermetallic particles in the as cast structure varied with cooling rate (faster cooling rate, smaller intermetallics) The smaller the intermetallics, the easier they were to dissolve during solution treatment. The iron containing intermetallic (inclusion) did not dissolve during solution treatment and therefore this phase can only be minimized by a reduction in total iron content requiring purer aluminum and alloying elements.

Aging Results

Aging at 120°C (248°F) for times between 0 – 120 hours resulted in the Brinell hardness values shown in Table 8-6 (Figure 8-15). All alloys showed a rapid increase in hardness between 0 and 2 hours. Alloy 1 (7.9Zn-4.9Mg), alloy 2 (8.1Zn-2.1Mg), alloy 5 (12.5Zn-3.4Mg) and alloy 6 (12.4Zn-2.4Mg) also showed a modest increase in hardness when further aged up to 120 hours. The hardness of alloy 3 (8Zn-1.4Mg) leveled off between 24 and 96 hours when aged at 120°C (248°F). Alloy 5 (12.5Zn-3.4Mg), the remaining alloy with the highest alloying additions, had the highest hardness at all times with a peak hardness of 183BHN. Alloys 1 (7.9 Zn-4.9Mg) and 6 (12.4Zn-2.4Mg) were similar in hardness and had a peak hardness of 169 and 170BHN respectively. Alloy 3-0.1MPa (7.9Zn-1.4Mg) was run twice and showed good repeatability and had a maximum hardness of 152BHN at 24 hours. Alloy 3-1MPa (8.2Zn-2.1Mg) and solidified at 1MPa of pressure) had a peak hardness of 144BHN at 96 hours. There was a small increase in peak hardness at higher zinc concentrations and peak hardness also increased with magnesium concentrations up to 3.4% (Figure 8-16a and b).

Table 8-6 BHN (500kg) for samples solution treated and aged at 120°C (248°F) for varying times (hrs).

Time (Hours)	Alloy Designation (Alloy # - MPa)						
	1-1 7.9Zn 4.9Mg	2-1 8.1Zn 2.1Mg	3-1 8.2Zn 1.4Mg	3-0.1 7.9Zn 1.4Mg	3-0.1 7.9Zn 1.4Mg	5-1 12.5Zn 3.4Mg	6-1 12.4Zn 2.4Mg
0	126	111	116	100	103	144	140
1	144	135	122	121	119	160	156
2	153	144	125	127	127	168	161
4	156	144	127	130	130	171	163

8	161	148	135	136	136	175	164
24	165	151	136	152	152	177	168
48	164	154	143	144	143	180	169
72	169	155	141	144	142	180	169
96	170	156	144		141	181	171
120	169	158	140		142	183	170

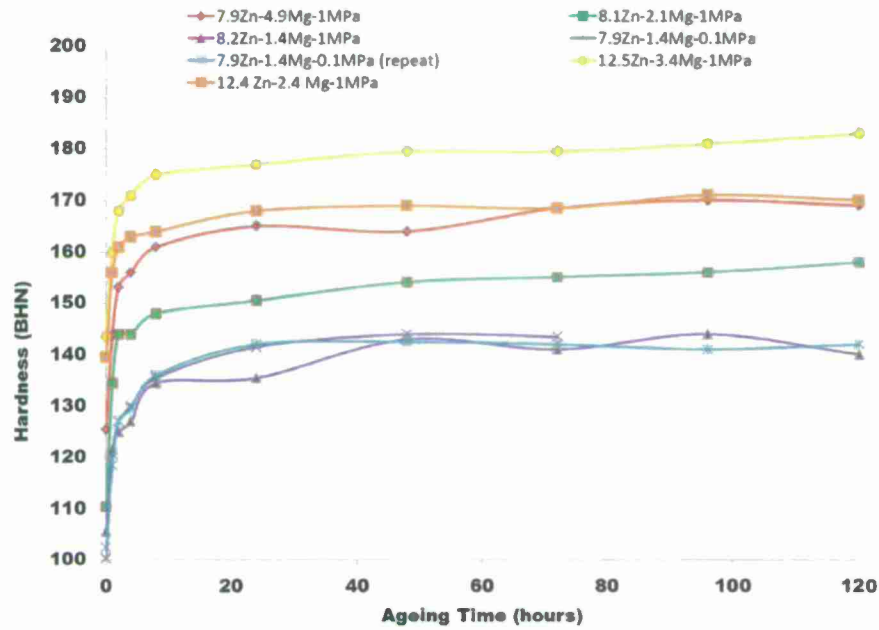
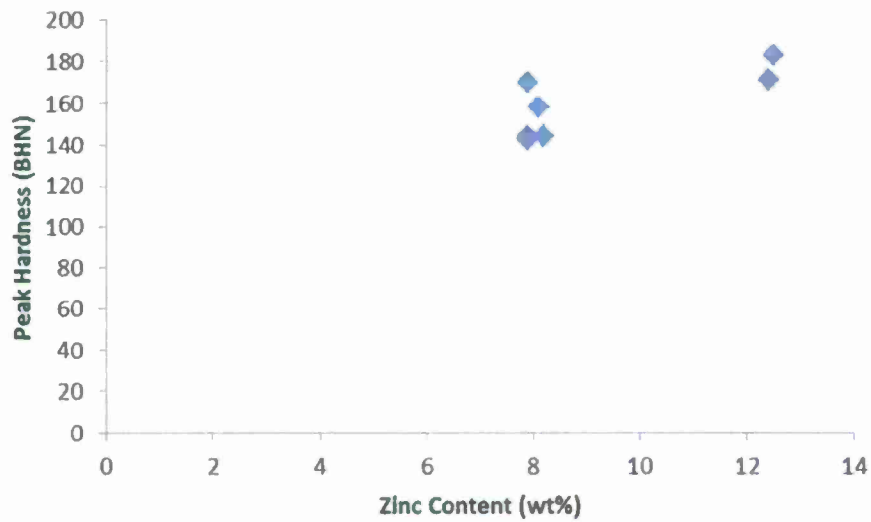
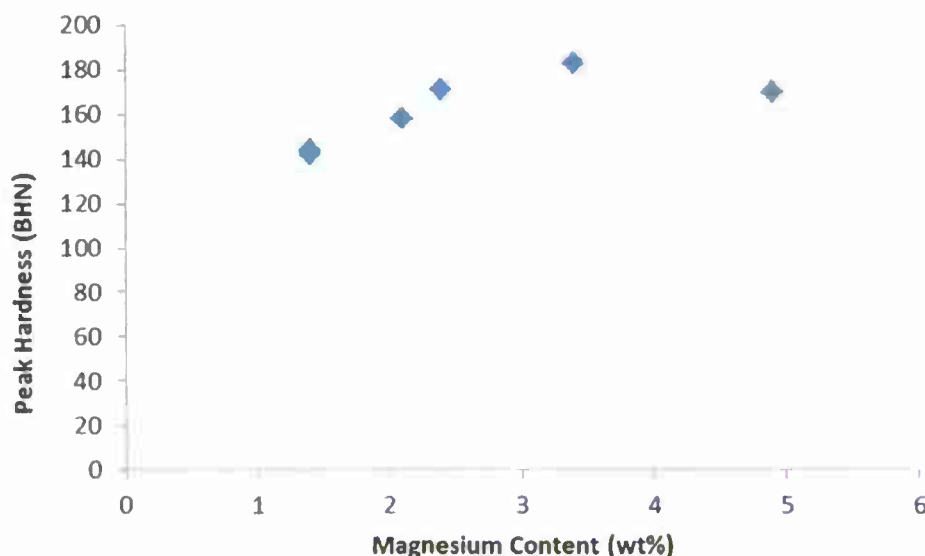


Figure 8-15 Hardness versus time for 120°C (248°F) aging.



(a)



(b)

Figure 8-16 Peak hardness versus (a) zinc and (b) magnesium content after aging at 120°C (248°F).

Aging at 150°C (302°F) resulted in peak hardness in about 8 hours as shown in Table 8-7 and Figure 8-17. For all alloys, maximum hardness was achieved before 24 hours and began to drop off linearly. Alloy 5 (12.5Zn-3.4Mg) had the highest peak hardness of 178BHN but overlapped with alloy 1 (7.9Zn-4.9Mg) after 96 hours. Alloy 6 (12.4Zn-2.4Mg) dropped in hardness to less than that of alloy 1 (7.9Zn-4.9Mg) between 4 and 8 hours. Comparing peak hardness to zinc concentration showed a small increase with increasing zinc concentration and peak hardness increased slightly with magnesium content until 3.4wt% and then appeared to taper off (Figure 8-18a and b). These results are in agreement with the results from aging at 120°C (248°F).

Table 8-7 BHN (500kg) for samples solution treated and aged at 150°C (302°F) for varying times (hrs).

Time (Hours)	1-1 7.9%Zn 4.9%Mg	2-1 8.1%Zn 2.1%Mg	3-1 8.2%Zn 1.4%Mg	5-1 12.5%Zn 3.4%Mg	6-1 12.4%Zn 2.4%Mg
0	124	119	103	141	137
1	159	148	133	171	165
2	162	150	137	172	165
4	165	155	141	175	167
8	168	157	143	178	166
24	167	157	139	175	160
48	161	151	131	167	153
72	158	147	127	161	149
96	155	143	124	155	146
120	150	140	120	150	144

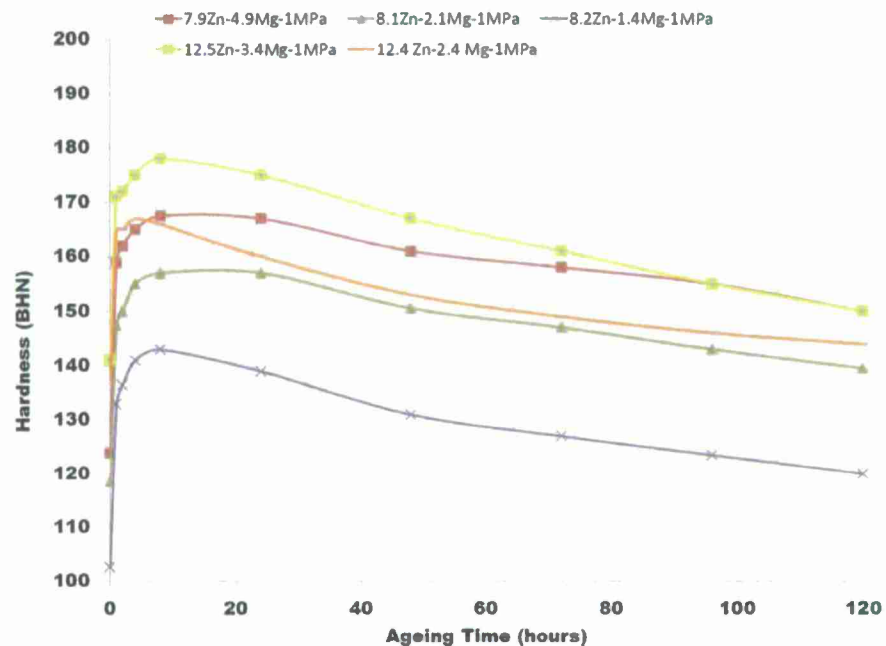
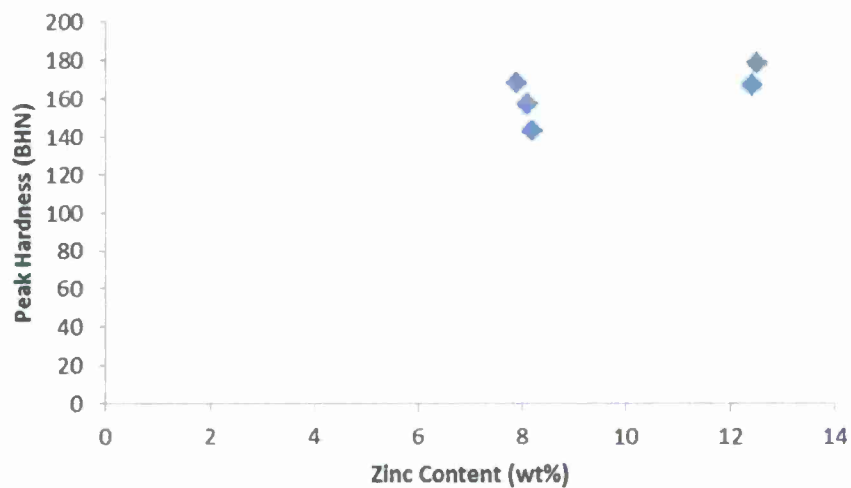
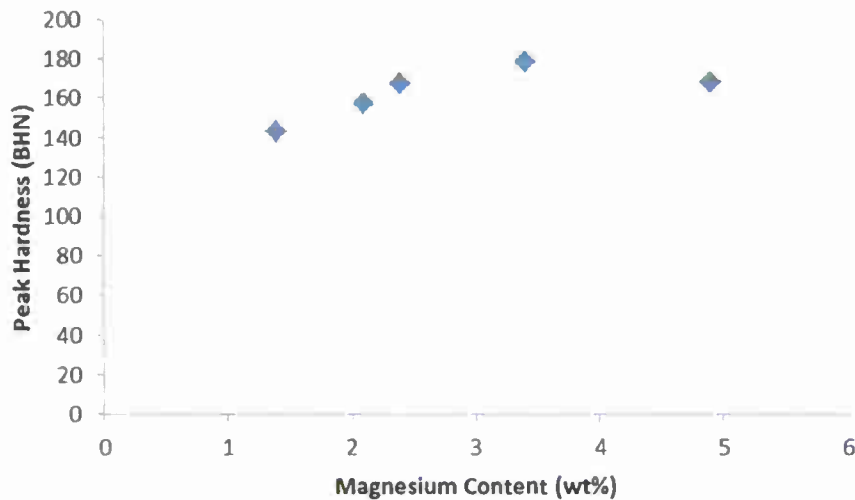


Figure 8-17 Hardness versus aging time at 150°C (302°F) showing a steep drop off after 8 hours.



(a)



(b)

Figure 8-18 Peak hardness versus (a) zinc and (b) magnesium content after aging at 150°C (302°F).

The peak hardness at 120°C (248°F) was somewhat higher than peak hardness achieved at 150°C (302°F). The largest difference was found in the alloys containing 12wt% zinc. The 8wt% zinc alloys were only 1-2BHN higher when aged at 120°C (248°F) versus 5BHN at 150°C (302°F).

XRD

Representative x-ray diffraction scans from the solution treated and aged samples are shown in Figures 8-19 through 8-21. In all the samples, the results showed that the aluminum matrix was highly textured.

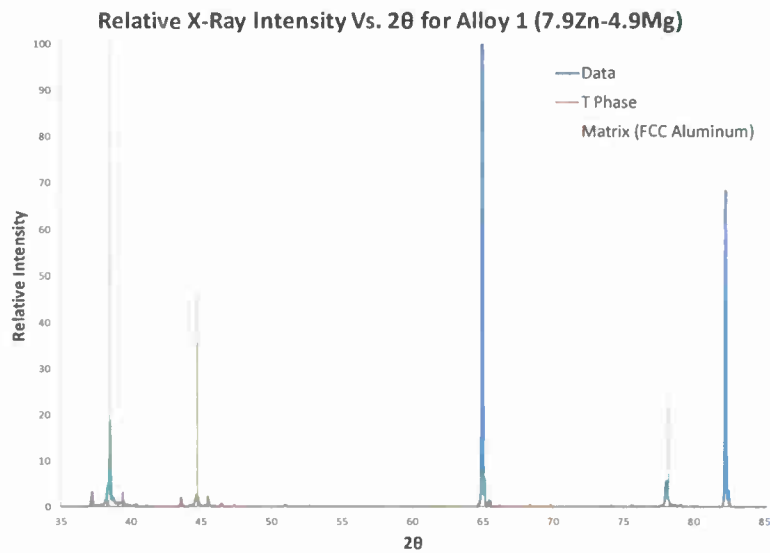


Figure 8-19 XRD results (background subtracted) for alloy 1 (7.9Zn-4.9Mg) showing a match with the intermetallic T-Phase ($\text{Mg}_{32}\text{Zn}_{31.9}\text{Al}_{17.1}$).

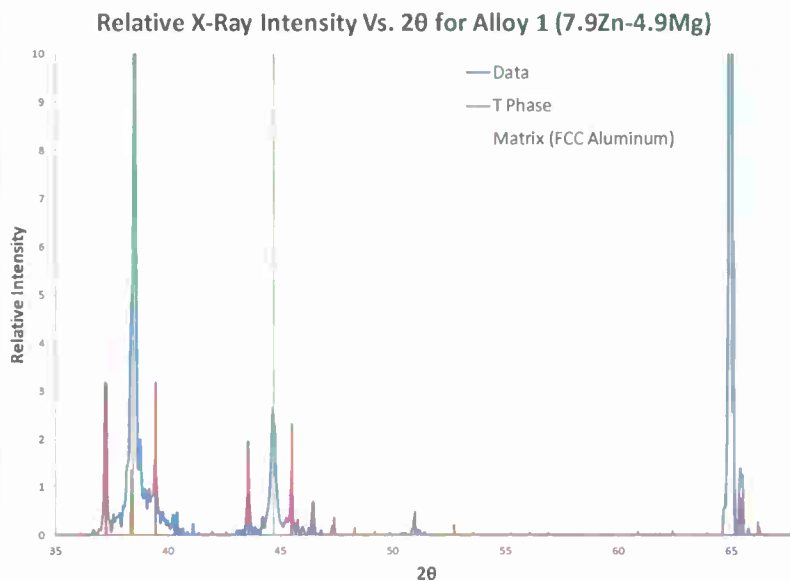


Figure 8-20 Zoomed XRD results (background subtracted) for alloy 1 (7.9Zn-4.9Mg) showing a match with the intermetallic T-Phase ($\text{Mg}_{32}\text{Zn}_{31.9}\text{Al}_{17.1}$).

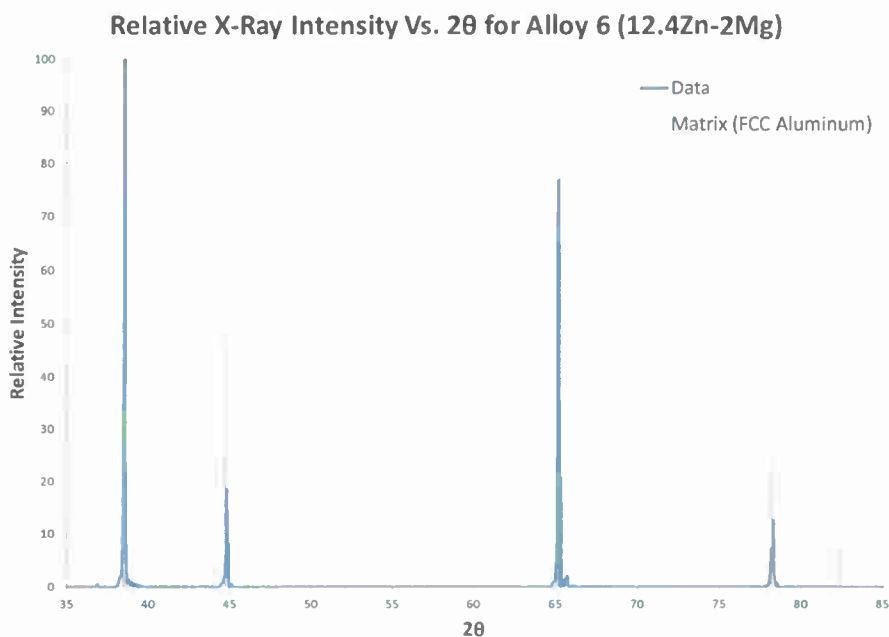


Figure 8-21 XRD results (background subtracted) for alloy 6 (12.4Zn-2Mg).

In alloys 1 (7.9Zn-1.4Mg), 2 (8.1Zn-2.1Mg), and 5 (12.5Zn-3.5Mg) the predominant age-hardening phase was identified as T phase. This phase has a body centered lattice with a lattice parameter of about 1.4nm. In the Al-Mg-Zn system, the formula for T phase is $(\text{Mg}_{32}(\text{Zn},\text{Al})_{49})$ and copper can substitute into the lattice [5]. In alloys 3 (8Zn-1.4Mg) and 6 (12.4Zn-2Mg) no significant peaks from the age-hardening phase were identified. Only a single peak that matched with T phase was seen in alloy 6 (12.4Zn-2Mg) x-ray diffraction

scan and no intermetallic peaks were visible in alloy 3 (8Zn-1.4Mg) scans. Additional, longer x-ray scans may be required to verify the age-hardening precipitate phase in these alloys.

DSC

Differential Scanning Calorimeter was used to conduct a solution treatment simulation study of each alloy. Typical results are shown from alloys 2 (8.1Zn-2.1Mg) in Figure 8-22. The first peak is most likely from the dissolution of an intermetallic that formed during solidification; the second peak is due to precipitation from solid solution; while the third peak represents the dissolution of that precipitate.

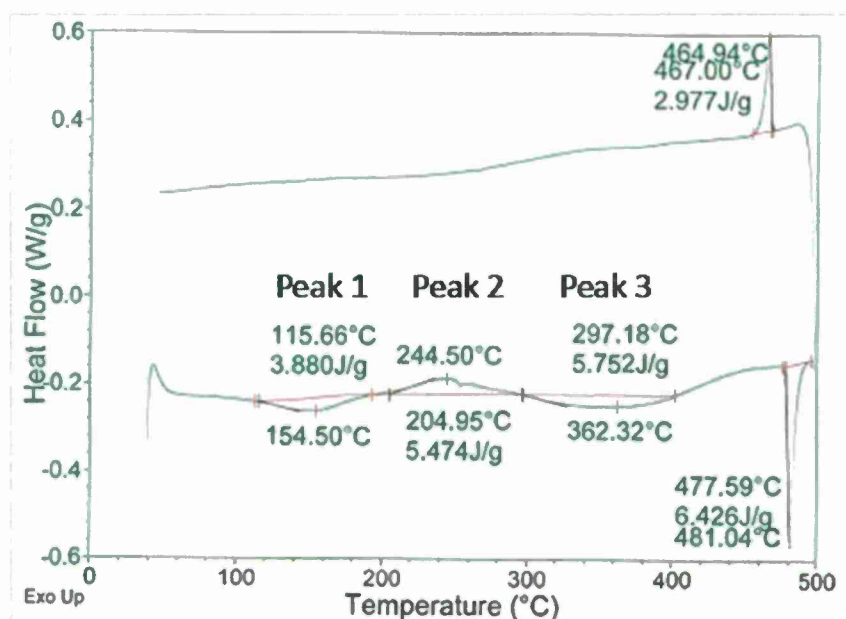


Figure 8-22 DSC curve for the "solution treatment study" of as cast alloy 2 (8.1Zn-2.1Mg).

The solution treatment study found that as alloy content increased, the size of the reaction peaks decreased and the starting temperatures of the reactions increased in temperature. This is likely caused by faster dissolution and coarsening rates for smaller intermetallics. Table 8-8 shows the temperature of each peak for the alloys.

Table 8-8 DSC results for "Solution Treating Study" of as cast samples with peak locations in Celsius.

Alloy	Zn (wt%)	Mg (wt%)	Cu (wt%)	Peak temperature		
				Peak 1 °C (°F)	Peak 2 °C (°F)	Peak 3 °C (°F)
1-1MPa	7.9	4.9	0.9	NA	253 (487)	NA
2-1MPa	8.1	2.1	0.9	154 (309)	244 (471)	362 (684)
3-0.1MPa	7.9	1.4	0.9	141 (286)	216 (420)	380 (716)
3-1MPa	8.2	1.4	1.0	149 (300)	206 (403)	341 (646)
5-1MPa	12.5	3.4	0.8	151 (304)	243 (469)	390 (734)
6-1MPa	12.4	2.0	0.63	152 (306)	Na	385 (725)

DSC results for the aging study on the solution treated sample showed two peaks (Table 8-9). The first peak is most likely due to the formation of a transition precipitate while the

second peak is its dissolution. As magnesium concentration increased, the starting temperature of the transition precipitate formation decreased independent of zinc concentration. The dissolution temperature of this phase decreased with increasing magnesium concentration for the low zinc samples (8wt%) but did not change for the high zinc (12wt%) samples. Alloy 2 (8.1Zn-2.1Mg) had a significantly different temperature for the precipitate dissolution. It is not known why this occurred. A representative DSC curves from the aging study are shown in Figure 8-23.

Table 8-9 DSC results for "aging study" of previously solution treated samples with the peak location in Celsius.

Alloy	Zn (wt%)	Mg (wt%)	Cu (wt%)	Solution Treated DSC Results	
				Peak 1 C (°F)	Peak 2 C (°F)
1-1MPa	7.9	4.9	0.9	92 (198)	166 (331)
2-1MPa	8.1	2.1	0.9	101 (214)	150 (302)
3-0.1MPa	7.9	1.4	0.9	110 (230)	170 (338)
3-1MPa	8.2	1.4	1.0	108 (226)	-
5-1MPa	12.5	3.4	0.8	-	167 (333)
6-1MPa	12.4	2.0	0.63	107 (225)	167 (333)

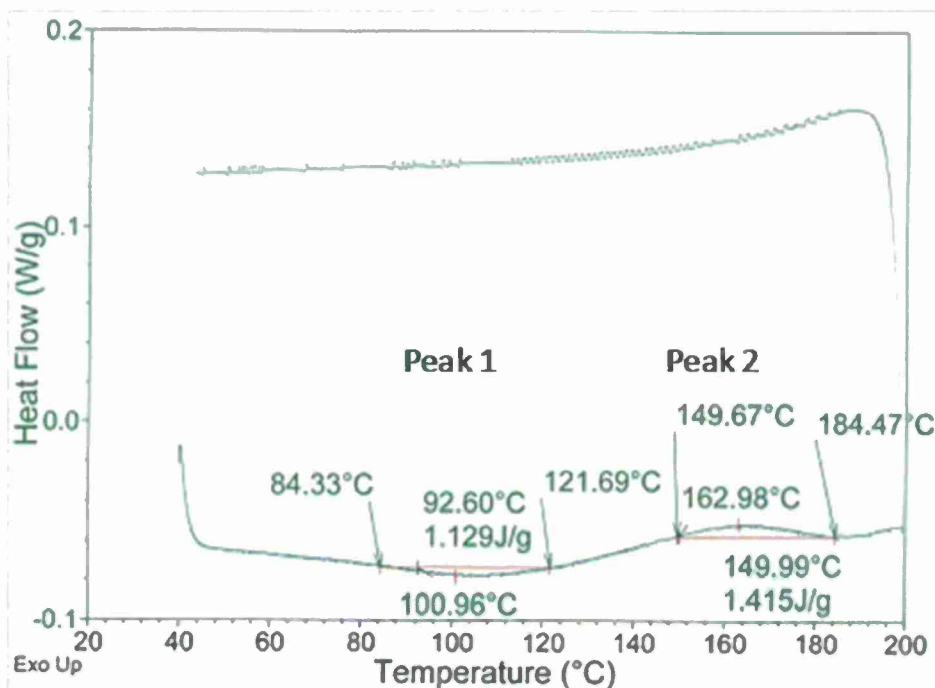


Figure 8-23 DSC curve for the "aging study" of solution treated alloy 2 (8.1Zn-2.1Mg).

Tensile Properties and Microstructural Characterization

Tensile results for all alloys and conditions are summarized in Table 8-10. The tensile properties for the SUP samples and the corresponding atmospheric samples for alloy 3-0.1MPa (7.9Zn-1.4Mg) are shown in Figure 8-24. The properties for the chill and HIPed samples are illustrated in Figures 8-25 and 8-26 respectively. In the SUP, chill and HIPed

samples, both of the alloys with 12.5% zinc (alloys 5 and 6) and the alloy with 8% zinc and 5% magnesium (alloy 1) had very low ductility and failed before yield. Only the two alloys with lower alloy content, alloy 2 (8.1Zn-2.1Mg) and alloy 3-1MPa (8.2Zn-1.4Mg), reached yield during tensile testing. Of these two alloys, the higher zinc alloy (alloy 2, 8.1Zn-2.1Mg) had higher strength but lower ductility. In this alloy, the yields ranged from 538 to 490MPa (78 to 71ksi) and the elongation ranged from 1.7 to 3.6%. Alloy 3-1MPa had the lowest alloying additions at 8.2% zinc and 1.4% magnesium, and this alloy showed the best combination of strength and ductility. Yield strengths in this alloy averaged about 465MPa (67ksi) and elongations ranged from 5 to 9%. Additional discussion of the effect of microstructure and processing conditions will focus on Alloy 3-1MPa.

Table 8-10 Average Mechanical properties of Al-Zn-Mg-Cu Tensile Bars.

Alloy	Zn (%)	Mg (%)	Cu (%)	Condition	Yield	UTS	% Elongation
1	7.9	4.9	0.9	SUP	*	312	0.3%
				Chill (SUP Casting)	*	371	0.7%
				HIP (SUP Casting)	*	269	0.8%
2	8.1	2.1	0.9	SUP	538	565	3.6%
				Chill (SUP Casting)	490**	524	1.7%
				HIP (SUP Casting)	522	567	3.4%
3-0.1MPa	7.9	1.4	0.9	Atmospheric	450	466	2.1%
				Chill (Atmospheric)	*	0	0 %
				HIP (Atmospheric)	461	495	4.0%
3-1MPa	8.2	1.4	0.9	SUP	464	505	5.8%
				Chill (SUP Casting)	468	525	9.0%
				HIP (SUP Casting)	464	508	5.3%
5	12.5	3.4	0.8	SUP	*	324	0.9%
				Chill (SUP Casting)	*	432	1.1%
				HIP (SUP Casting)	*	353	0.8%
6	12.4	2	0.6	SUP	*	578	1.5%
				Chill (SUP Casting)	576**	576**	2.1%**
				HIP (SUP Casting)	*	510	0.5%

*Failed before yield **Only one bar's data used, since other failed before yield.

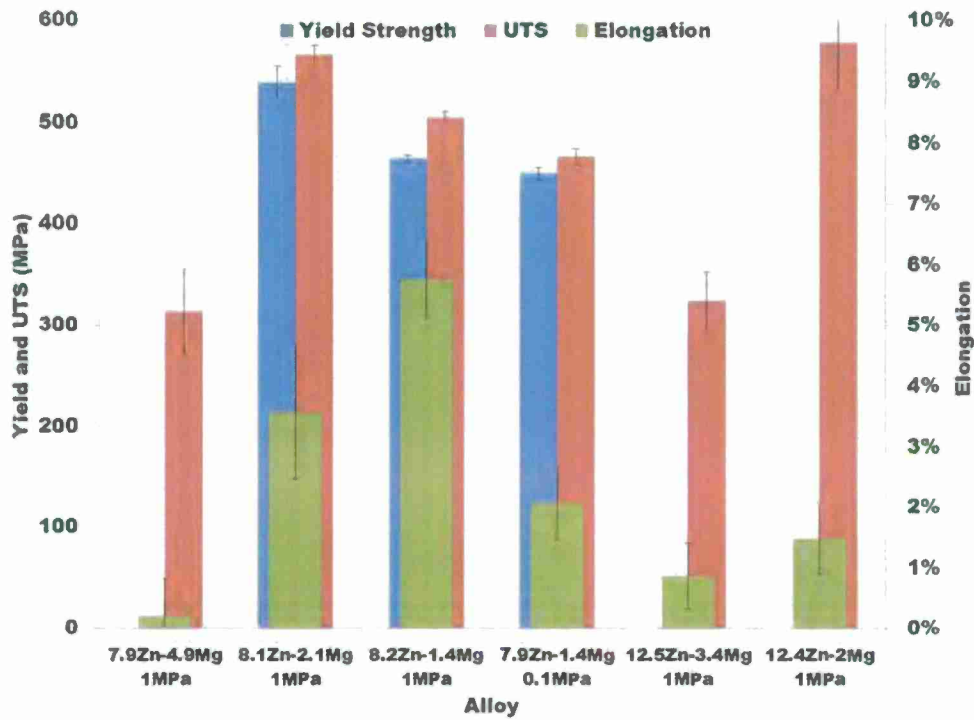


Figure 8-24 Tensile properties of samples 1.9-4.5cm (0.75-1.75in) from the chill in the wedge castings.

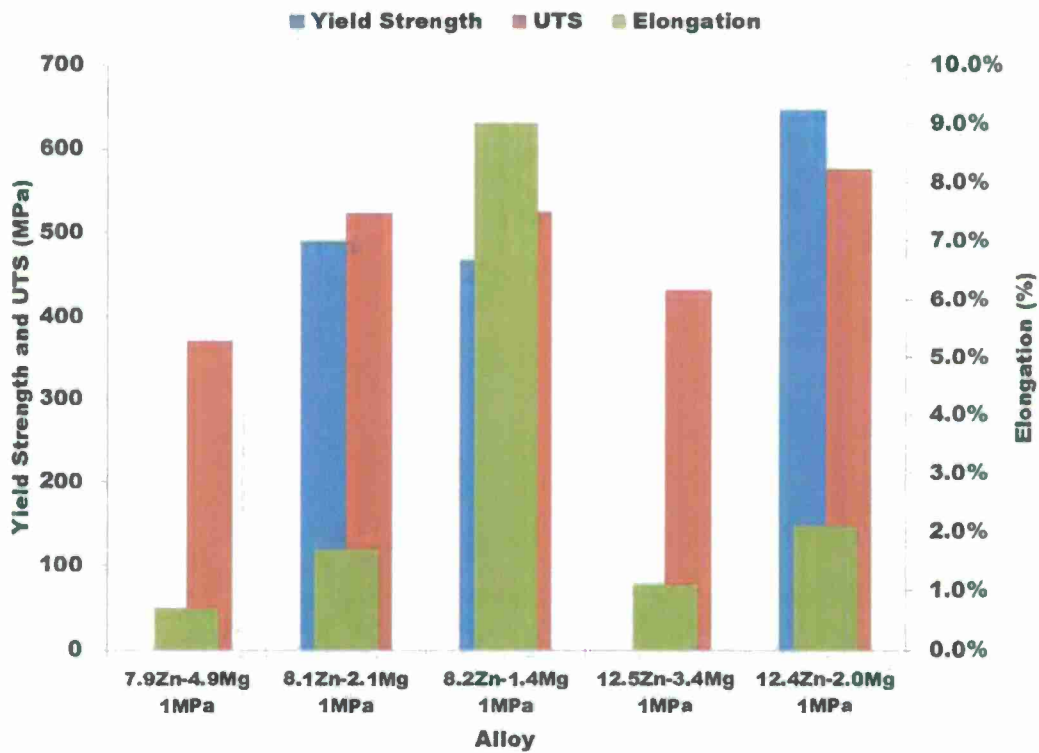


Figure 8-25 Tensile properties of samples next to the chill in the wedge castings.

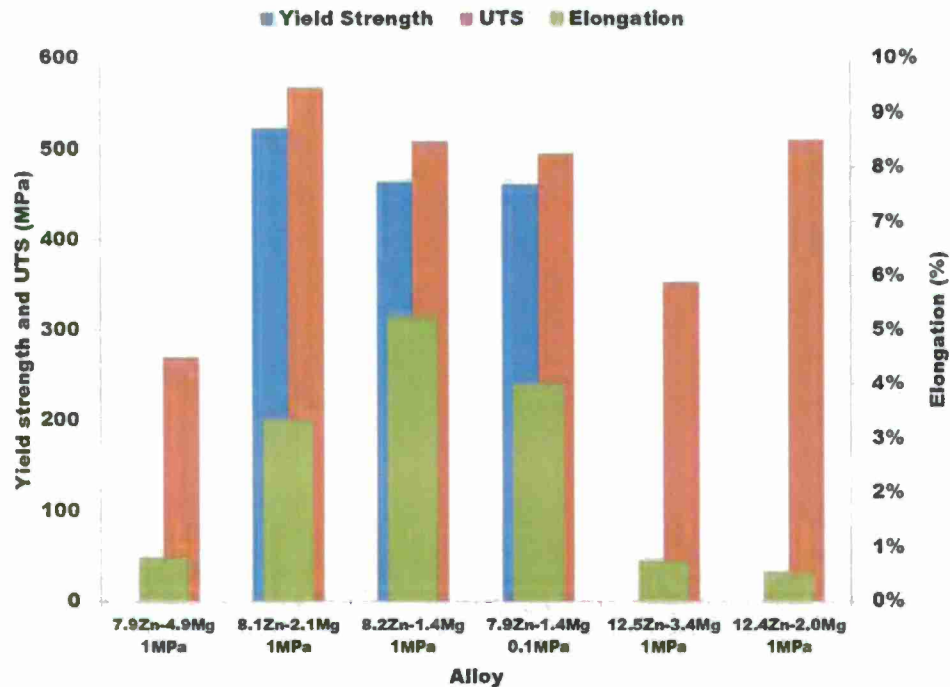


Figure 8-26 Tensile properties of the HIPed samples in the wedge castings.

The effect of SUP and distance from chill on percent elongation in alloy 3-1MPa (8.2Zn-1.4Mg) and 3-0.1MPa (7.9Zn-1.4Mg) are shown in Figure 8-27. Note that the sample closest to the chill would not experience the full effect of pressurization since solidification is completed before the full pressure is applied. In the SUP casting, the chill sample had the highest elongation at about 9% and at greater distances from the chill, the elongation dropped down to around 5 to 6%.

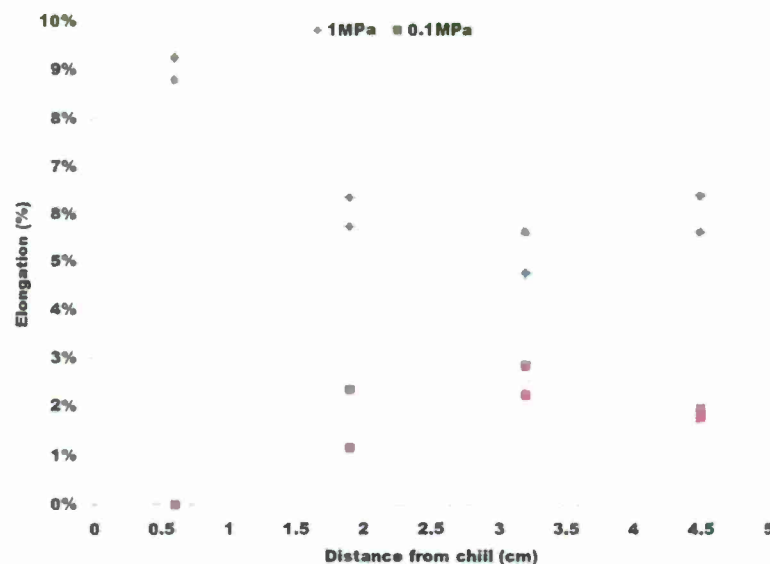


Figure 8-27 Effect of distance from chill on percent elongation of alloy 3-1MPa (8.2Zn-1.4Mg) and 3-0.1MPa (7.9Zn-1.4Mg).

It was expected that the chilled sample in the conventionally solidified wedge would have similar elongation values to that of the SUP chill sample. In addition, the elongation would be expected to be lower in the remainder of the 0.1MPa wedge because of higher porosity concentration. Away from the chill, the elongation was lower in the 0.1MPa wedge (Figure 8-27). However, the elongation was 0% in the chill sample solidified at 1atmosphere pressure. Examination of the alloy 3-0.1MPa chill fracture surfaces showed that they were both almost completely covered in an oxide film as illustrated in Figure 8-28. Polished samples and fracture surfaces from this wedge at greater distances from the chill also showed many oxide films although the amount was greatly reduced from what was seen in the chill samples (Figure 8-29). It is not known why these films formed in this casting.



Figure 8-28 Stereo microscope image of fractured tensile surface from alloy 3-0.1MPa (7.9Zn-1.4Mg), chill sample. Fracture surface is almost completely covered with an oxide film.

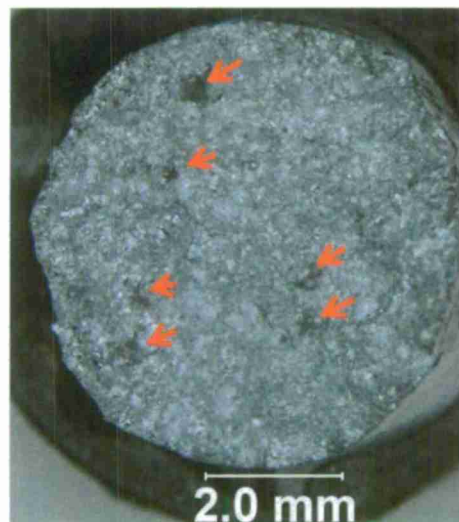


Figure 8-29 Stereo microscope image from alloy 3-0.1MPa (7.9Zn-1.4Mg), sample 2.0cm from chill. Fracture surface has numerous oxide films on surface.

The effect of distance from chill on yield and ultimate strength in alloy 3-1MPa (8.2Zn-1.4Mg) and 3-0.1MPa (7.9Zn-1.4Mg) is shown in Figure 8-30. Data from the 0.1MPa (1 atmosphere) chill sample were not included. The SUP chill samples had the highest yield and ultimate strengths and the yield and ultimate strengths were higher in the SUP samples compared to the conventionally cast specimens. There was a small decrease in the yield and ultimate strength with increasing distance from the chill in the SUP samples.

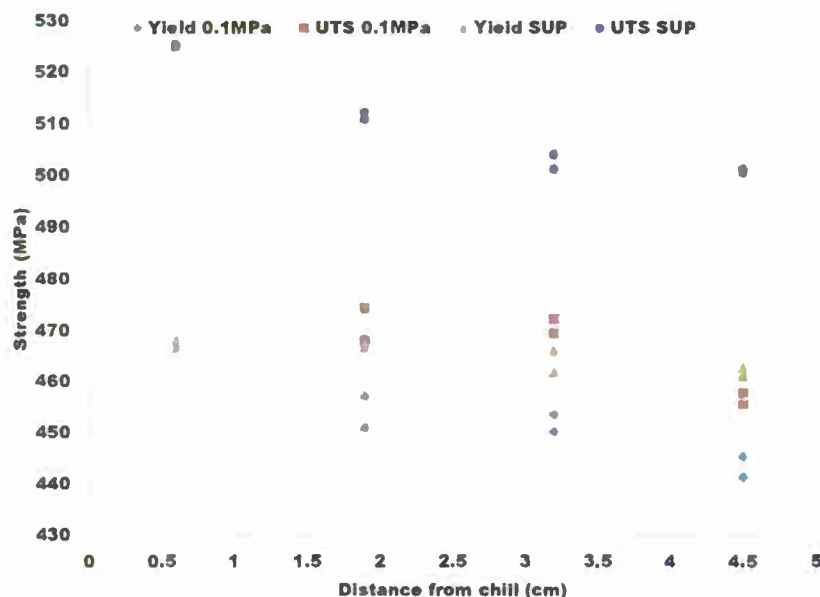


Figure 8-30 Yield and ultimate tensile strength versus distance from chill in alloy 3-1MPa (8.2Zn-1.4Mg) and 3-0.1MPa (7.9Zn-1.4Mg) wedge castings.

The increase in tensile properties when comparing the SUP and atmospheric castings is attributed to the absence of large oxide films and the application of pressure [20-23, 26]. The increase in properties seen in the chilled SUP casting is likely caused by the increase in cooling rate. This should reduce the size of as-cast intermetallics and aid in dissolution during solution treatment. The higher cooling rate will also decrease the overall grain size, which should also improve mechanical properties.

Mechanical properties of HIPed tensile bars are shown in Table 8-10. Graphs of the effect of HIPing on the yield strength, ultimate tensile strength, and percent elongation of alloy 3-1MPa (8.2Zn-1.4Mg) and 3-0.1MPa (7.9Zn-1.4Mg) are shown in Figures 8-31 through 8-33. In the samples solidified conventionally (0.1MPa pressure), the average yield and ultimate strength was slightly higher in the HIPed samples. The average percent elongation of the HIPed sample was also higher in the 0.1MPa casting after HIPing. However, the scatter in HIPed 0.1MPa elongation was very large, probably due to oxide films found throughout this sample. In the SUP samples, there was no significant difference in the yield, ultimate and tensile strengths of the samples before and after HIPing.

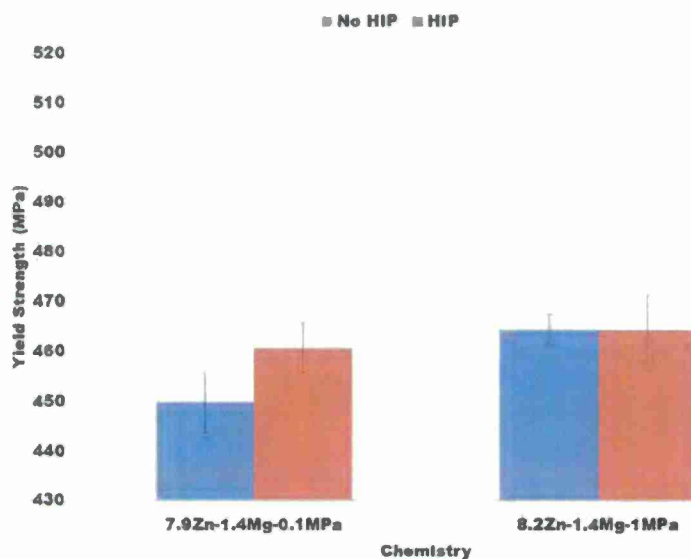


Figure 8-31 Effect of HIPing on yield strength of alloy 3-0.1MPa (7.9Zn-1.4Mg) and 3-1MPa (8.2Zn-1.4Mg).

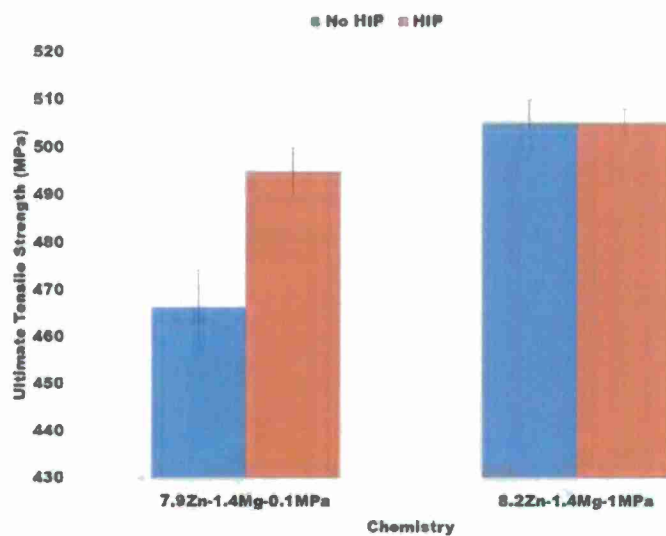


Figure 8-32 Effect of HIPing on ultimate tensile strength of alloy 3-0.1MPa (7.9Zn-1.4Mg) and 3-1MPa (8.2Zn-1.4Mg).

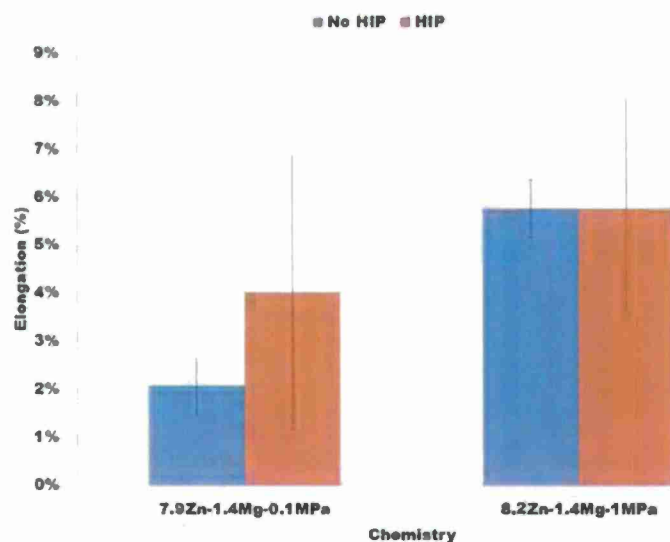


Figure 8-33 Effect of HIPing on percent elongation of alloy 3-0.1MPa (7.9Zn-1.4Mg) and 3-1MPa (8.2Zn-1.4Mg).

Hot Isostatic Pressing of the experimental alloys decreased the size and amount of porosity. Figure 8-34 shows the effect of SUP and HIPing on the Alloy 3-1MPa (8.2Zn-1.4Mg) castings. Both solidification under pressure and HIPing reduced the porosity but the pores were not completely eliminated. The combination of both processes gave the smallest pore size. HIPing will not eliminate pre-existing oxide films or large intermetallics.

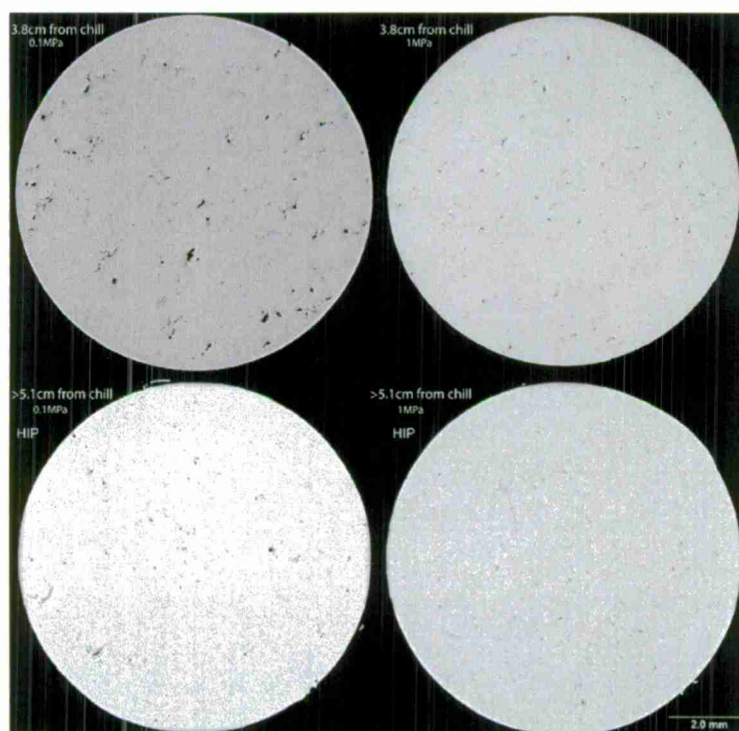


Figure 8-34 Effects of HIPing on alloys 3-0.1MPa (7.9Zn-1.4Mg) and 3-1MPa (8.2Zn-1.4Mg). HIPing only marginally affected the porosity in the alloy previously solidified under 10 atmospheres of pressure.

Projected fracture surface porosity and oxide film measurements were performed on all alloy 3-1MPa (8.2Zn-1.4Mg) tensile samples. The effects of these anomalies on percent elongation are shown in Figure 8-35. The 0.1MPa chill samples are not included. Higher anomaly concentrations on the fracture surface reduced the ductility of the samples. However, in a number of the SUP samples, there were no anomalies found on the fracture surface, and the elongation of these samples was still lower than the SUP chill samples. Figure 8-36 shows the microstructure of the chilled and HIPed 1MPa (10 atmosphere) sample. The HIPed tensile bars were machined from blanks with a much slower cooling rate compared to the chill samples tensile bars and the intermetallic size significantly increased as the cooling rate decreased (Figure 8-37). These results indicate that the brittle intermetallics affected the ductility of the samples. Higher solidification cooling rates are required to ensure ductility in this alloy, even when porosity is eliminated.

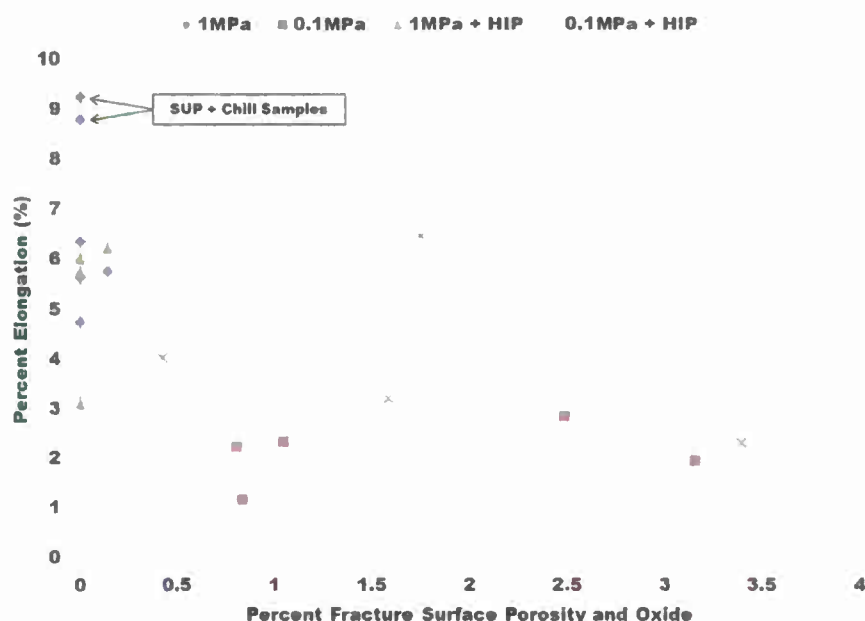


Figure 8-35 Effect of fracture surface porosity and oxide films on percent elongation of alloys 3-1MPa (8.2Zn-1.4Mg) and 3-0.1MPa (7.9Zn-1.4Mg) samples.

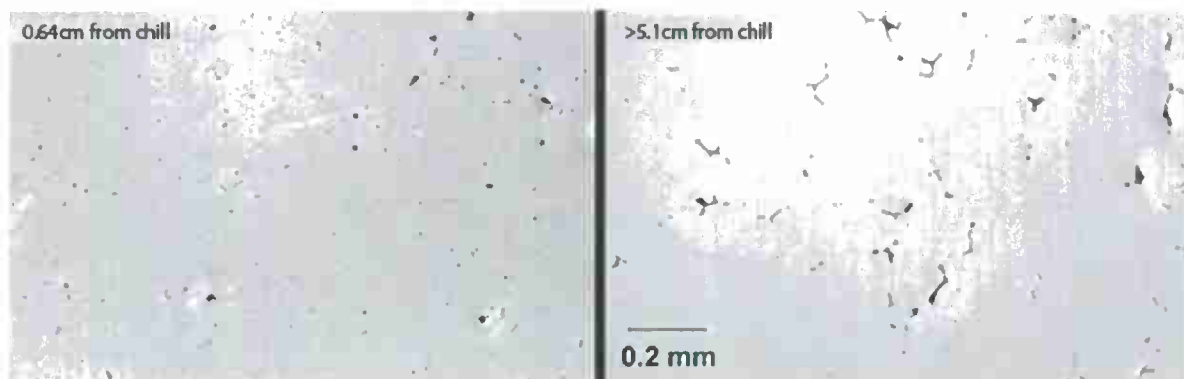


Figure 8-36 Microstructure of chill and HIPed sample in SUP alloy 3-1MPa (8.2Zn-1.4Mg) casting.

Average Intermetallic Length

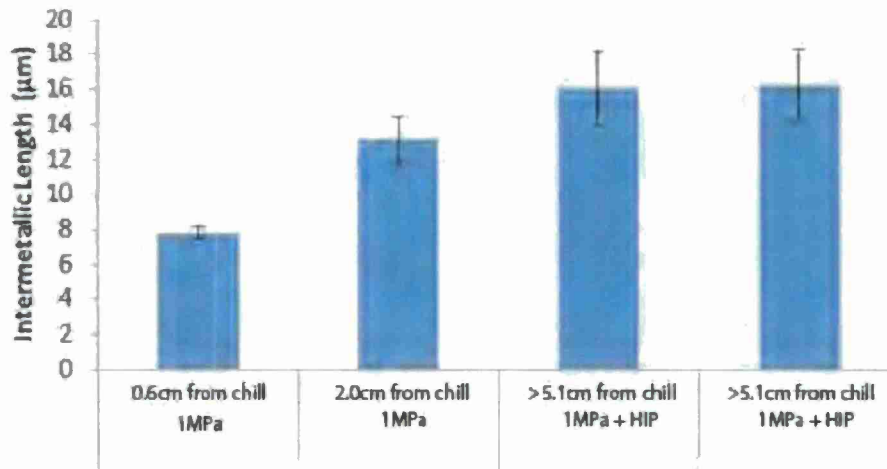


Figure 8-37 Average intermetallic size in SUP alloy 3-1MPa (8.2Zn-1.4Mg) casting.

Production of Military Castings with Cast Al-Zn-Mg-Cu Alloy

The 8Zn-1.4Mg-0.9Cu alloy had the best combination of strength and ductility so this alloy was chosen to demonstrate the castability of the Al-Zn-Mg-Cu. UAB completed a project with AMRDEC to examine the possibility of converting a 7075-T73 aluminum fabrication (Hellfire Missile Launch Rail Bracket) to a casting. The original design (Figure 8-38) was fully machined and was time consuming and expensive to produce. Figure 8-39 shows the 8Zn-1.4Mg-0.9Cu casting that was produced. The casting was solidified under pressure and no hot tearing or significant porosity was detected.

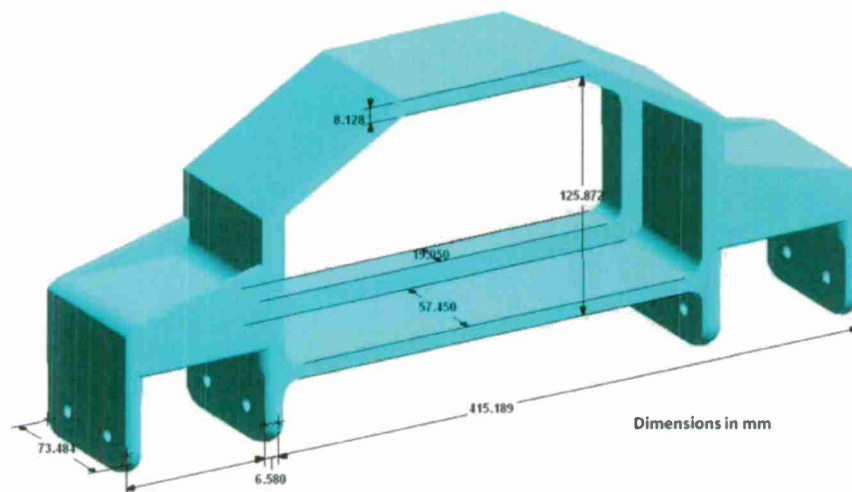


Figure 8-38 Original Design of 7075-T73 aluminum fabrication (Hellfire missile launch rail bracket).

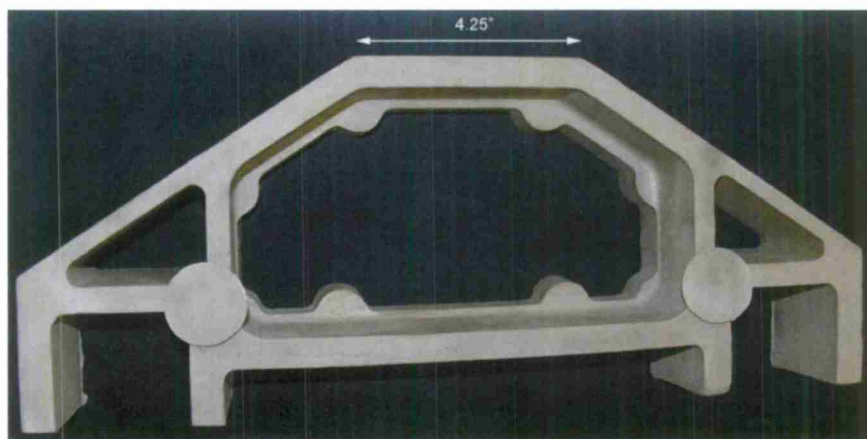


Figure 8-39 Hellfire missile launch rail bracket casting solidified under pressure (1MPa) with the 8Zn-1.4Mg-0.9Cu alloy composition.

A second commercial casting section was produced without the application of pressure. This casting was a structural mounting plate for a military tactical vehicle. The pattern was loaned to UAB by Eck Industries, Inc. and Eck produces this part with 206 aluminum. A macrophotograph of the casting is illustrated in Figure 8-40. Again, the commercial casting was successfully produced with the experimental 8Zn-1.4Mg-0.9Cu. The part completely filled, there was no hot tearing and no significant porosity on the casting surface. These results indicate that the experimental alloy can be produced with proper casting technology.



Figure 8-40 Structural mounting plate casting for military tactical vehicle solidified conventionally with the 8Zn-1.4Mg-0.9Cu alloy composition.

Transition

Military castings were successfully produced with the Al-Zn-Mg-Cu alloy with the best combination of strength and ductility. Presentation of the research was given at the AFS

aluminum research committee meetings. Two presentation/papers were submitted for the 2013 AFS World Congress.

Conclusions and Recommendations

Six cast Al-Zn-Mg-Cu alloys were produced with zinc concentrations of 8 and 12%, and Zn/Mg ratios of 1 to 5.4%. Copper was limited to 0.9% to improve stress corrosion cracking.

At the highest alloy content (13.1Zn-7.3Mg) a large amount of eutectic structure formed, such that no solution treating temperature and time would have re-dissolved it, short of re-melting. Castings produced with lower alloying additions contained less intermetallics.

SEM EDS analysis showed the intermetallic particles had two different chemistries including an intermetallic phase with aluminum that was rich in magnesium, zinc, and copper; and an intermetallic phase that contained aluminum, iron, magnesium, and silicon with traces of zinc, nickel and copper. The first intermetallic was significantly dissolved during heat treatment while the second was stable. These results indicate that the iron concentration should be minimized in these samples to increase ductility.

X-ray diffraction showed that the age hardening precipitates in these alloys matched well with T phase ($\text{Mg}_{32}\text{Zn}_{31.9}\text{Al}_{17.1}$), a cubic crystal structure.

DSC confirmed that lower alloy contents resulted in easier intermetallic dissolution. This is likely due to the smaller, more isolated intermetallic distribution. Precipitation began at a higher temperature in the lower alloy samples. This is likely caused by the amount of alloy in solution and its readiness to reprecipitate.

Heat treating of ultra-high strength cast Al-Zn-Mg-Cu has been optimized for maximum hardness. Samples were solution treatment of 441°C (826°F) for 4 hours before ramping to 460°C (860°F) for 75 hours and then aged at 120°C (248°F) for 75 hours.

Six Al-Zn-Mg-Cu alloys were produced. Zinc concentrations ranged from 8 to 12% and magnesium concentrations ranged from 1.4 to 5%. All alloys were solidified under 1MPa of pressure and poured into a well risered, filtered, and properly gated, wedge-shaped mold with a large chill on the thinnest section of the wedge to provide a variety of cooling rates. In addition, wedges with the highest and lowest alloying additions were conventionally cast at 0.1MPa pressure (atmospheric).

Tensile samples were tested from various locations in the wedge to provide a range of cooling rates. HIPed samples were tested for comparison purposes. The composition with the highest alloying content (Alloy 4 (13.1Zn-7.3Mg)) was in the eutectic range and had large intermetallics which would not dissolve during solution treatment. Because of this, tensile bars were not analyzed from this alloy.

Elongations were very low in alloys 1 (8Zn-5Mg), 5 (12Zn-3Mg) and 6 (12Zn-2Mg). These alloys failed before 0.2% offset yielding. Alloy 2 (8Zn-2Mg) provided the highest strength, however its elongation was limited. The best combination of strength and ductility was obtained at the lowest alloying additions in alloy 3-1MPa (8.2Zn-1.4Mg).

The conventional cast wedge produced with alloy 3-0.1MPa (7.9Zn-1.4Mg) contained unusually high level of oxide films in both the tensile fracture surfaces and polished

microstructure. The source of these oxides is unknown and their presence makes the tensile data suspect.

Solidification under pressure reduced the porosity in alloy 3-1MPa (8.2Zn-1.4Mg) compared to the conventionally cast alloy. Furthermore there was some reduction in porosity in the HIPed samples in both the conventionally and SUP cast wedges. However, HIPing only improved the conventionally cast tensile properties.

The best properties were achieved in the low alloy casting 3-1MPa (8.2Zn-1.4Mg) with the highest solidification rate. In the chilled SUP casting, a yield strength of 468MPa (68ksi), tensile strength of 525MPa (76ksi) and elongation of 9% was achieved. Ductility and strength decreased as the cooling rate decreased. These results show that intermetallics are dominating the ultimate strength and elongation when porosity is minimized. Higher solidification cooling rates are required to ensure ductility in this alloy, even when porosity is eliminated.

References

1. ASM International. *ASM Handbook: Properties and Selection: Nonferrous Alloys and Special-Purpose Materials*. Materials Park: ASM International. 1990. Print.
2. Hatch, John. *Aluminum: Properties and Physical Metallurgy*. Metals Park: American Society for Metals. 1984. 143-155, 226-240. Print.
3. Davis, Joseph. ed. *ASM Specialty Handbook: Aluminum and Aluminum Alloys*. Materials Park: ASM International. 1993. 706-711. Print.
4. ASM International. *Metallography, Structures and Phase Diagrams, Metals Handbook*. Metals Park: American Society for Metals. 1973. 259. Print.
5. Auld, J., Williams, B. "X-Ray powder data of T Phases Composed of Aluminum & Magnesium with Silver Copper or Zinc." *Acta Crystallographica: Crystallographic Journals Online*. 1966: 21, 803. Web. Oct. 2012.
6. Senkov, O., Druschitz, A., Senkova, S., Kendig, K., Griffin, J. "Ultra-High Strength Sand Castings from Aluminum Alloys 7042." TMS 2011 Annual Meeting and Exposition. Warrendale: TMS. 2011. Print.
7. Druschitz, Alan. Griffin, John. "Advanced Cast Aluminum Alloys." *Shape Casting: 3rd International Symposium*, Warrendale: TMS. 2009. 53-60. Print.
8. Stumpf, H. Unpublished Research at Alcoa Laboratories. 1965-1971.
9. Clinch, M., Harris, S., Hepples, W., Holroyd, N., Lawday, M. and Noble, B. "Influence of Zinc to Magnesium Ratio and Total Solute Content on the Strength and Toughness of 7xxx series Alloys." *Materials Science Forum*. 2006: vol. 519-521. Print.
10. Rokhlin, L., Dobatkina, T., Bochvar, N., Lysova, E. "Investigation of phase equilibria in alloys of the Al-Zn-Mg-Cu-Zr-Sc system." *Journal of Alloys and Compounds*. 2004: 10-6. Print.
11. Raghavan, V. "Al-Mg-Zn (Aluminum-Magnesium-Zinc)," *Phase Diagram Evaluations: Section II, Journal of Phase Equilibria and Diffusion*. 2007: Vol. 28, No. 2. Print.

12. Andreatta, F., Lohrengel, M., Terryn, H., de Wit, J. "Electrochemical Characterization of Aluminum AA7075-T6 and Solution Heat Treated AA7075 using a Micro-Capillary Cell." *Electrochimica Acta*. 2003: 3239-3247. Print.
13. Shastry, C., Levy, M., Joshi, A. "The Effects of Solution Treatment Temperature on Stress Corrosion Susceptibility of 7075 Aluminum Alloys." *Corrosion Science*. 1981: Vol. 21. 673-688. Print.
14. Clinch, M., Daval, R., Harris, S., Hepples, W., Holroyd, N., Lawday, M., Noble, B. "A Microstructural Engineering-Based Approach to 7xxx Series Alloy Optimization." Institute of Materials Engineering Australasia Ltd, Materials Forum. 2004: vol. 28. Print.
15. Senkov, Oleg. Senkova, Svetlana. Mendiratta, Madan. Miracle, Daniel. "Method of Making a High Strength Aluminum Alloy Composition." U.S. Patent # 7,048,815. 2006.
16. Druschitz, Alan. "High strength, high toughness, weldable, ballistic quality, castable aluminum alloy, heat treatment for same and articles produced from same." US patent Application 20070102071. 2007. Print.
17. AMS-A-21180A. "Aluminum Alloy Castings, High Strength, Area Meca." Warrendale: SAE International. 2005. 23. Print.
18. Starink, M. J. Wang, S. C. "A model for the Yield Strength of Overaged Al-Zn-Mg-Cu Alloy." *Acta Mater*. 2003: Vol. 51. 5131-5150. Print.
19. Askeland, D., Phule', R. ed. *The Science and Engineering of Materials*. Stamford: Cengage Learning. 2008. 5th ed. Print.
20. Ruff, G., Prucha, T., Barry, J., and Patterson, D. "SAE Technical Paper No. 2001-01-0411: Pressure Counter Pressure Casting (PCPC) for Automotive Aluminum Structural Components." Warrendale: Society of Automotive Engineers. 2001. Print.
21. Borovkov, Maxim. Bubbles in water: vector illustration. 123rf.com. web. Image ID: 2146464. June. 2012.
22. Thomas, J.A. "The Castyrall R Process - Improvements to the Lost-Foam Process Development in Light Alloy Castings." Stratford-upon-Avon: Conference Proceedings at Moat House International Hotel. 1989. Print.
23. Donahue, R. "New Developments that Improve Competitiveness and Open Market Opportunities." Lost Foam Casting Congress. 2001. Print.
24. ASTM International. "ASTM B557-02 Standard Test Methods of Tension Testing Wrought and Cast Aluminum and Magnesium Alloy Products." West Conshohocken: ASTM International. 2010. Print.
25. ASTM International. "ASTM E8-04 Standard Test Methods for Tension Testing of Metallic Materials." West Conshohocken: ASTM International. 2011. Print.
26. Uram, S., Fleming, M., and Taylor, H. "AFS Transactions: Effect of Pressure during Solidification on Microporosity in Aluminum Alloys." Schaumburg: American Foundry Society. 1958: Vol. 66. 129-134. Print.

9. **Developing an Improved Combination of Strength and Permeability for Investment Shells used with Foam Patterns:** *Principal Investigators Dr. Von L. Richards, Missouri University of Science and Technology*

This research is needed for thin section fill and dimensional reproducibility for DoD-relevant steel castings, such as muzzle brake and breech components (loading trays and raven breech nozzle for example).

The objective of this project is to optimize and deploy ceramic mold shell materials for expendable foam patterns such as machined foam or chemically expanded foams produced in low cost master tooling.

Abstract

The use of highly rigid foam for medium to large investment castings of limited production runs has a number of advantages for military castings. While dimensional reproducibility with the rigid foams is significant advantage, the foam rigidity also leads to quality challenges due to shell cracking during pattern removal.

This project developed a thermal/mechanical property database for investment shells and foam patterns in the temperature range covered by the pattern "burn-out" process. Concurrently a coupled thermal-mechanical Finite element model was developed to predict shell cracking during pattern removal. The model was then applied to designing a test article pattern which embodied geometrical features that have been observed to be problem areas in producing large (300pound) complex castings such as the NLOSC muzzle brake.

The test article was then used with laboratory-produced shells to confirm the model. Industrial shells were produced on the test article to further evaluate the effect of shell parameters and firing parameters on shell cracking as a confirmation/refinement step. Finally to translate the results to industry, a shelling/firing trial was conducted in an industrial foundry based on the predictions of the FE model. The metric of zero shell cracking defects was achievable using the results of the model.

Two additional side benefits were also produced during the course of this project – an improved shell edge strength test and quantitative verification the benefit of flash firing with excess oxygen on eliminating pattern residue in shells and eliminating environmental HCN.

Approach

During the first year a preliminary finite element method (FEM) model was developed to predict shell stresses during foam pattern removal prior to investment casting. The preliminary FEM model was used to assist in designing a test article pattern which embodied features that had been observed to create shell cracking defects in prior prototype DOD castings such as the NLOSC muzzle brake. The test article included similar wall thicknesses to those found on the 300 pound casting and internal pockets of similar size to those found to be typical defect locations. The preliminary FEM model was used to test the sensitivity of the test article design to pattern and shell variables thought to be important. Hard tooling was built to produce the test article at FOPAT.

The initial model was also used in parametric studies to help identify important variables for the study of pattern removal and shell build parameters. At the same time property testing and property test development was begun using shells produced in the MST foundry and FOPAT foam materials of selected densities.

During the second year, modeling and parametric studies were continued. One of the co-sponsor foundries in American foundry society observed with another less rigid foam that there was a reduction in shell cracking if they aged the pattern after the shell build but before burn-out. Therefore the behavior of foams with aging at various low temperatures was also studied to see if the observation was valid and could be incorporated into the FEM model. After refinement of the FEM model, Shell building and pattern burn out studies were conducted with MST produced shells to test the improved model and the effect of pattern aging between shell build and burnout. In preparation for industrial confirmation trials, the measurement methods developed in year one were applied to industrial ly produced shells from co-sponsoring foundries during the second year.

A designed experimental matrix of industrially produced shells using the test article pattern was produced at two co-sponsoring foundries. These shells were treated for pattern removal by a matrix of processes including slow firings, flash firing, and aging or not aging before firing. The merged matrix of shell build parameters, and pattern removal parameters were also simulated in the FEM model. Once it was determined that he FEM model simulated the results of industrial shells well, selected sets of conditions were repeated at an industrial foundry and the shell cracking results were compared to the model predictions as industrial confirmation.

Results/Key Findings: Year 1

During Year 1 of the project, the following tasks were completed:

Task 1. Beta version of model of pattern removal stress for FOPAT high rigidity foam

Bullet items:

- The preliminary version of a finite element model was developed to simulate stress from flash firing of FOPAT foams in shell molds for pattern removal.
- Preliminary confirmation test results did not agree with the model although interesting results regarding the location of high stress areas were found.
- Beta version of model of pattern removal stress for FOPAT high rigidity foam was developed with taking into consideration pattern geometry and additional data on foam behavior during firing.

Results:

The previously developed finite element model has been extended by considering the effect of internal corner of the ceramic shell on crack formation during the foam pattern removal process. Figure 9-1 shows the foam pattern and ceramic shell with round corners. The radius of the round corners is assumed to be 2 mm. To obtain accurate solutions, small-size elements have to be assigned in the corner regions, thus substantially increasing the number of elements resulting in increased computational cost. Two approaches have been evaluated to mesh the parts. Figure 9-2 shows the model meshed using tetrahedron

elements. Compared to tetrahedron element, brick elements provide accurate solutions with reduced number of elements. Brick element can only be used for simple geometric shapes. To simplify the geometry, the component must be partitioned into several regular shaped pieces before meshing. Figure 9-3 shows the components meshed using brick elements. Table 9-1 lists the type and the number of elements based for the two approaches.

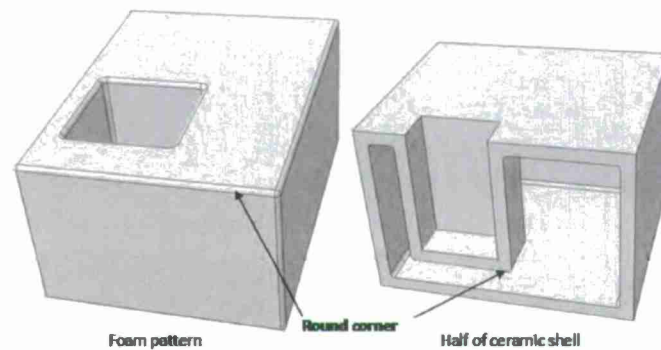


Figure 9-1 Foam pattern and ceramic shell with round corners.

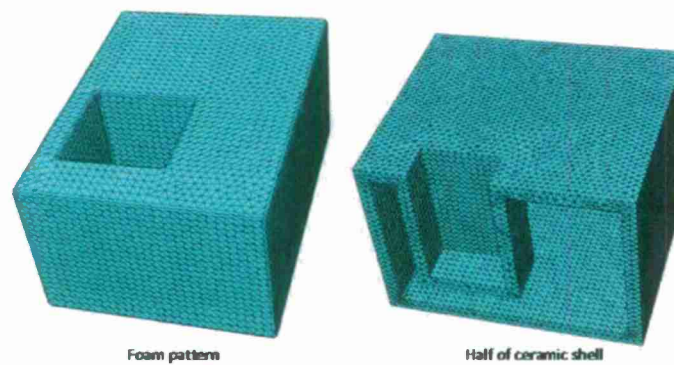


Figure 9-2 Parts meshed using tetrahedron elements.

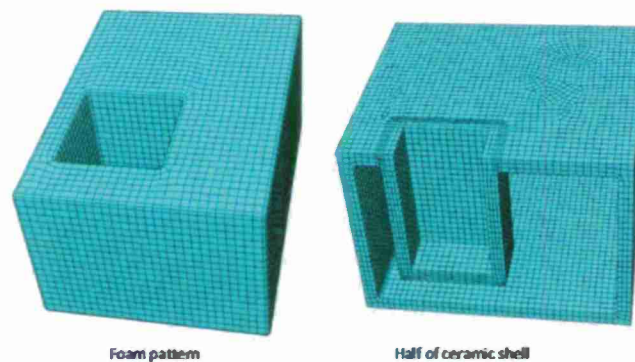


Figure 9-3 Parts meshed using brick elements.

Table 9-1 Type and number of elements in the finite element models.

Mesh Approach	Part	Element Type	Number of Elements
Tetrahedron Elements	Ceramic shell	C3D4 (A 4-node linear tetrahedron)	178,721
	Foam pattern	C3D4 (A 4-node linear tetrahedron)	140,205
Brick Elements	Ceramic shell	C3D8R (8-node linear brick, reduced integration, hourglass control)	32,295
	Foam pattern	C3D8R (8-node linear brick, reduced integration, hourglass control)	28,424

Task 2. Design tooling for FOPAT foam test article

Bullet items:

- Special pattern was designed (Figure9-4).
- Variations in geometry allowed us to simulate different levels of stress in internal corners.

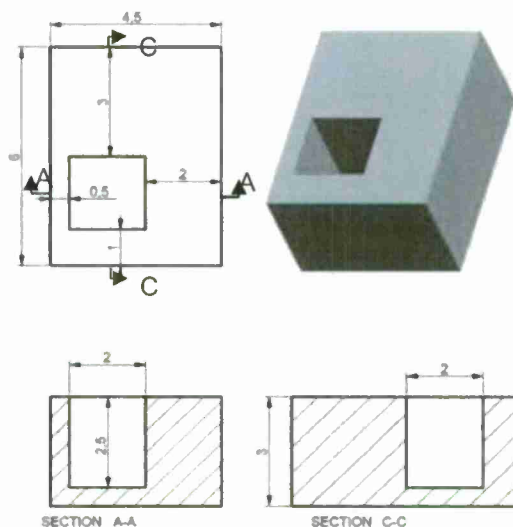


Figure 9-4 Designed FOPAT pattern.

Task 3. Model refinement and parametric studies of high density foam

Bullet items:

- The development of a revised edge test model was continued under the High performance program, but it was applied to shells produced under this program as well. It was found that the model reported in the literature contained a significant error and did not include the edge curvature effects.
- Since the modeling and design work were completed on the test article for Fopat material, the finite element work has been refocused on shell edge testing with is applicable to both the High Performance Alloy project and the SWC program, so it will not be reported under the SWC at this time. However the testing methodology

for the industrial shells used for the SWC program in option year 1 will utilize this method.

- Simulation of stresses in ceramic was done.
- Possible crack formation conditions were analyzed.

Results

Case: continuous heating. For continuous heating, the oven temperature starts from 20°C and the heating rate is 3°C/min. With the continuous heating, the ceramic shell fails after 27min 30s. The temperature distribution of different cross-sections at this time is shown in Figure 9-5. The decomposition of the inside foam does not occur at this time. The maximum principal stress distribution of the ceramic shell is shown in Figure 9-6. The maximum value of the principal stress is located at one of the inner corners of ceramic shell shown in Figure 9-2. The position of the maximum stress is based on the larger sections of foam material that can expand during the continuous heating process. Figure 9-7 shows the definition of various corners inside the shell. Results indicate that the stress values at corners A, B, C and D are higher than other locations. Table 9-2 lists the stress values at various corners inside the ceramic shell.

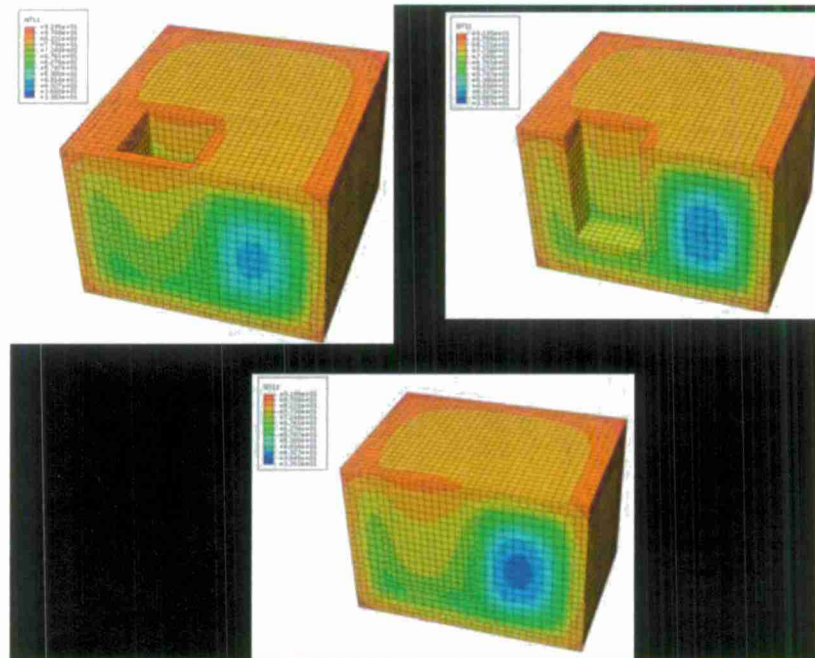


Figure 9-5 Temperature distribution in different cross-sections (time = 28min 30s).

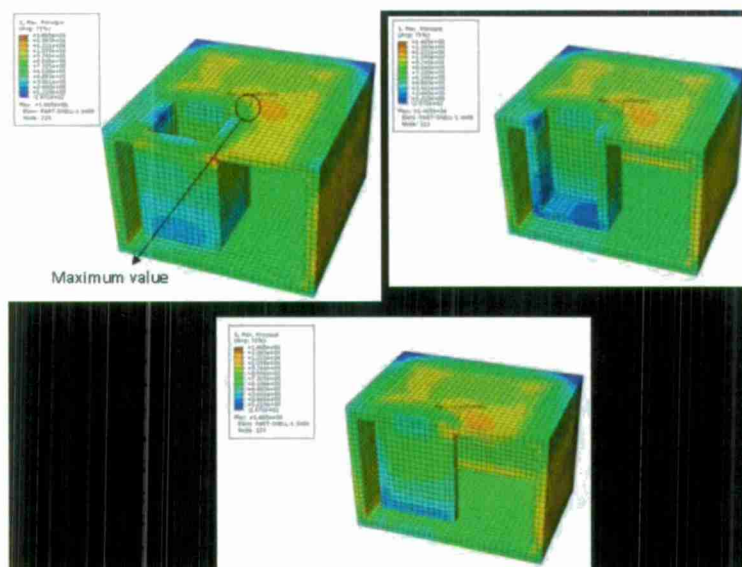


Figure 9-6 Maximum principal stress distribution of the ceramic shell (time = 28min 30s).

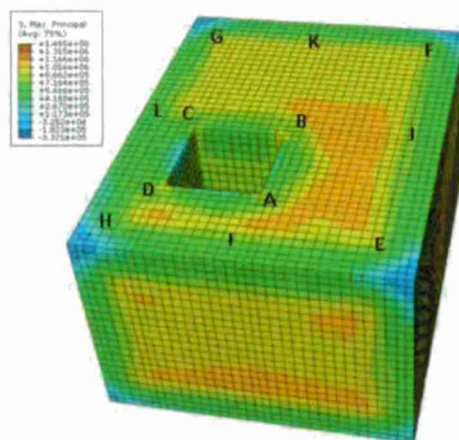


Figure 9-7 Location of internal corners in ceramic shell.

Table 9-2 Stress value at various internal corners of the shell (continuous heating).

Shell inside corner No.	Max principal stress (MPa)	Mid principal stress (MPa)	Min principal stress (MPa)
A	1.327	0.703	0.012
B	1.465	0.755	0.034
C	1.070	0.575	-0.019
D	0.977	0.548	-0.032
E	0.382	0.320	-0.018
F	0.375	0.315	-0.020
G	0.377	0.319	-0.020
H	0.382	0.313	-0.024
I	0.965	0.803	-0.054
J	0.964	0.811	-0.042
K	0.941	0.787	-0.044
L	0.834	0.705	-0.067

Case: flash firing. A finite element model considering internal radius of ceramic shell has been developed. The radius of the round corners is assumed to be 2 mm. For providing accurate solutions with fewer elements, brick elements have been used to mesh the foam and shell. Flash firing is used as the heating method and the oven temperature is assumed to be 600°C. The decomposition of the foam starts after about 82 seconds. The temperature distributions at different cross-sections are shown in Figure 9-8. For flash firing, the temperature of ceramic shell rises quickly while the foam inside still retains the original temperature over much of its volume due to the low thermal conductivity of foam. The stress distribution is shown in Figure 9-9. The extreme stress value is located at one of the internal corners of the ceramic shell. However, the simulation results show that the shell does not fail during flash firing (oven temperature = 600 °C). The stresses at corners "A", "B", "C" and "D" are higher than other locations. These corners are the most vulnerable places for failure (Table 9-3).

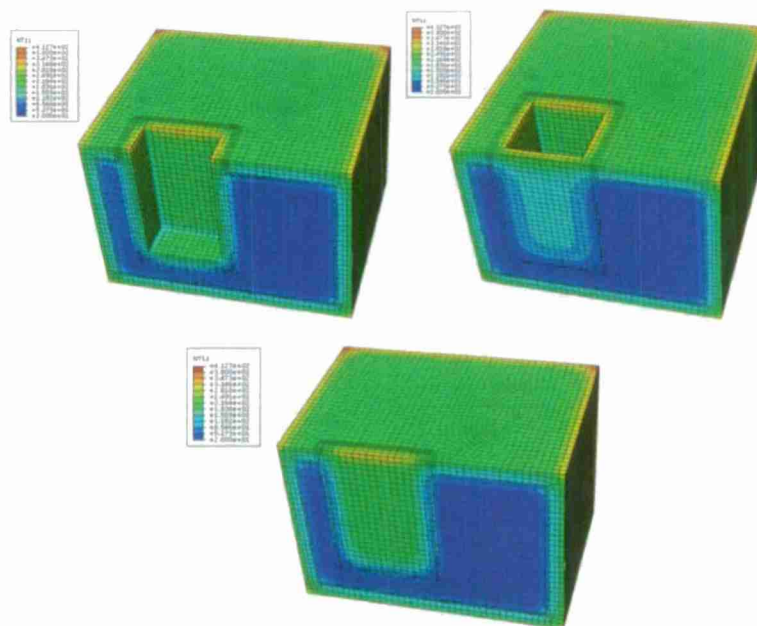


Figure 9-8 Temperature distribution at different cross-sections (time = 82s).

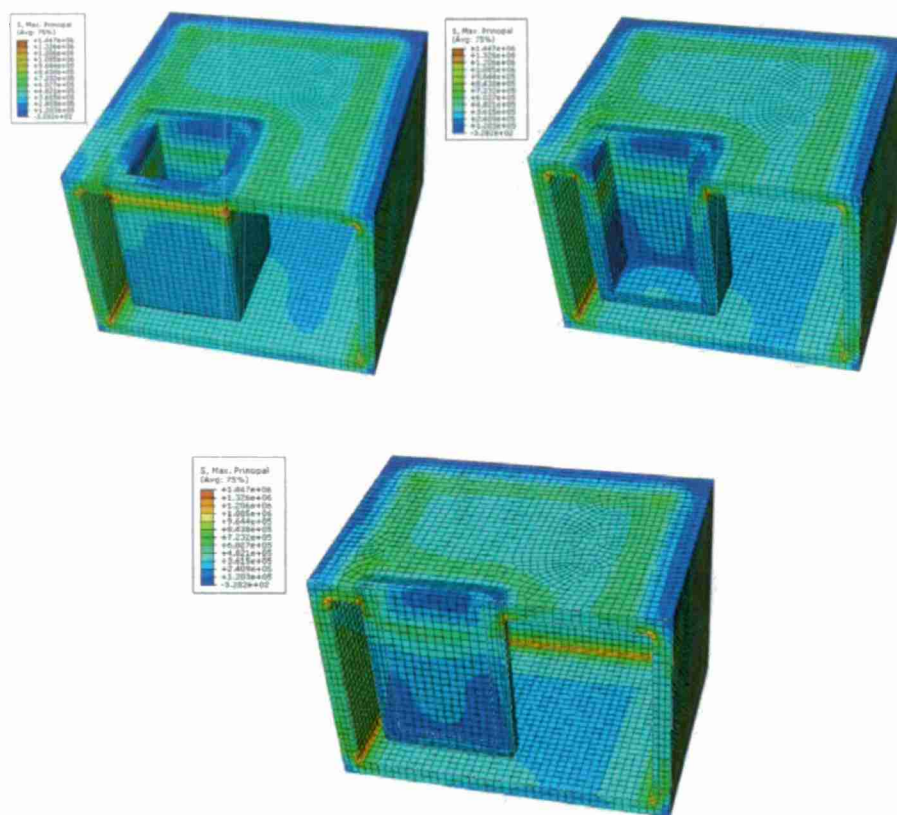


Figure 9-9 Maximum principle stress distribution of the ceramic shell (time = 82 s).

Table 9-3 Stress value at various internal corner of the shell (flush fire).

Shell inside corner No.	Max principle stress (MPa)	Mid principle stress (MPa)	Min principle stress (MPa)
A	1.447	0.436	-0.111
B	1.309	0.411	-0.110
C	1.378	0.467	-0.137
D	1.412	0.451	-0.138
E	0.718	0.679	-0.190
F	0.713	0.676	-0.192
G	0.713	0.673	-0.197
H	0.737	0.686	-0.188
I	1.345	0.600	-0.226
J	1.285	0.547	-0.226
K	1.264	0.530	-0.226
L	1.334	0.610	-0.246

Task 4. Build tooling and buy foam pattern

Bullet items:

- Universal die set for production of FOPAT patterns with different geometry internal pockets was designed (Figure 9-10)
- FOPAT patterns were ordered and built.

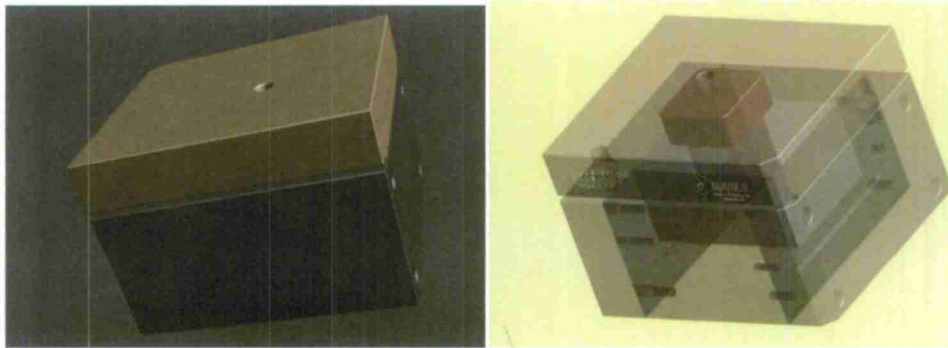


Figure 9-10 Universal die set for production of FOPAT patterns.

Task 5. Missouri S&T shell building

Bullet items:

- Shell building process was implemented at Missouri S&T
- Ceramic shells with different layer numbers (five and seven) have been produced on test articles and are being tested

Results

Shells were produced by dipping the FOPAT patterns into the prepared slurry. The slurry was made of colloidal silica binder and fused silica flour. All coatings were applied at 800 ± 100 cP viscosity. The patterns were submerged in the slurry until completely covered and then removed and suspended over the slurry for approximately 50 seconds. During this time the pattern was rotated and allowed to drip from different points to promote an even coating. A uniform distribution of stucco was then applied using the rainfall method. This was done by continuously rotating the pattern so that all surfaces were directly impacted by the falling stucco until no more stucco would adhere to the surface. The stucco for the prime coat was granular zircon (-100+200 mesh) and the stucco for the back-up coats was fused silica (-30+50 mesh). The seal coat used no stucco. The samples were dried for at least four hours between coats. Shells with three backup coats were developed. After the seal coat was applied the samples dried for another 24 hours at 100°C in a convection furnace with fan used to maintain the temperature at 100 C.

Task 6. Property testing of Missouri S&T shell

Bullet items:

- The strength and elastic modulus of the shells were determined using three point bend testing performed at room temperature
- Shell cracking test was performed using different pattern firing processing

Results:

Six samples were tested and compared to previous results (Table 9-4). The tip of the testing fixture had a radius of 0.12".

Table 9-4 Strength, density and porosity of shells.

Property	New 5 Layer Shell	5 Layer Shell	Industrial Shell
Average Shell Thickness (mm)	4.1 ± 0.3	3.5 ± 0.26	8.29 ± 0.77
Average Maximum Stress (MPa)	7.9 ± 1.2	4.39 ± 0.5	4.80 ± 1.18
Average Elastic Modulus (MPa)	6491 ± 2106	3411 ± 518	1689 ± 427
Bulk Density Average (g/cm ³)	-	1.92 ± 0.22	1.61 ± 0.05
Open Porosity (%)	-	25.96 ± 3.81	27.3 ± 2.2

All of the shells having 5 layers broke during the drying procedure and the shell had a higher modulus and maximum stress than previous builds (Figure 9-11). These results show that there were some discrepancies in the shell build for these shells. It is likely that there was some settling of the slurry due to insufficient mixer placement. These results also show that the current drying procedure will not work for larger samples due to the higher amount of expansion.



Figure 9-11 Crack formed in the shell during drying at 100°C.

A new set of more strong shells was prepared and tested in burnout. These shells had 2.5x2.5x2 inch dimensions samples of each density of FOPAT. Shells were flash fired at 800C for flash fire and during continuous heating at 3 C/min ramp rate. The test showed that high percentage of flash fires broke likely due to water in the shells. To avoid cracks in next test, a 24 hour drying process was followed by flash fire. No ramp rate samples broke - likely due to underestimation of strength of shell and/or foam "aging" during the initial ramp. The fact that the samples did not break may relate to the effects of foam aging shrinkage in the initial stages of slow heating. This was not included in original the model so we are revising the model to incorporate this feature.

Task 7. Build tool and buy foam pattern

Bullet items:

- A special tool was build and 50 foam pattern complicated geometry were produced.

Task 8. MST shells building

Bullet items:

- Seven layer shells around patterns complex geometry were made.

Results:

Shells were produced by dipping the patterns into the prepared slurry. The slurry was made of colloidal silica binder and fused silica flour. All coatings were applied at 800 ± 100 cP viscosity. The patterns were submerged in the slurry until completely covered and then removed and suspended over the slurry for approximately 50 seconds. During this time the pattern was rotated and allowed to drip from different points to promote an even coating. A uniform distribution of stucco was then applied using the rainfall method. This was done by continuously rotating the pattern so that all surfaces were directly impacted by the falling stucco until no more stucco would adhere to the surface. The stucco for the prime coat was granular zircon (-100+200 mesh) and the stucco for the back-up coats was fused silica (-30+50 mesh). The seal coat used no stucco. The samples were dried for at least four hours between coats. Shells with 5 backup coats were developed. After the seal coat was applied the samples dried for another 24 hours in one of three conditions: 60 C, 40 C, or ambient. Drying at 60 and 40 C occurs in a convection furnace with fan maintained at temperature. Ambient drying occurred in a dehumidified lab.

Task 9. Properties testing on MST shells

Bullet items:

- Shell properties were tested at room temperature
- Properties data were introduced in FEM model for prediction stress in the shell during pattern removal

Results:

The strength and elastic modulus of the shells were determined using three point bend testing performed at room temperature. The tip of the testing fixture had a radius of .12". Five samples seven layer shells were tested. The average 3-point bend strength of the shells was 7.2 MPa and the average thickness was 6.4 mm.

Task 10. Property measurements FOPAT foam

Bullet items:

- Elevated temperature modulus of elasticity of FOPAT foam is being measured as input to modeling the drying and pattern burnout heat-up stresses
- Thermal expansion of FOPAT foam was measured
- FOPAT decomposition analysis emphasizes the importance of high oxygen for health and safety.

Results

Thermal expansion. The thermal expansion of the FOPAT, high density foam was studied experimentally. The objective of this experiment was to better understand how the high density pattern foam reacts to heating. By testing the foam under different loading

pressures, the maximum pressure it would exert on the foam during firing can be approximated. By using different heating profiles it was hoped that a way to weaken the foam at lower temperatures would be possible. Three different densities of foam were selected and tested under a range of loading conditions. The pressure loading on the foam below 2.7KPa had no effect on thermal expansion, but a major drop in maximum expansion was noticed when loading pressure has increased to 5.9KPa. Holding the foam at constant heating for prolonged time caused the foam to linearly contract at a very slow rate, but upon increased heating the maximum elongation was not decreased.

Foam samples were cut and milled into 2.75 inch long 0.7 inch diameter cylinders. Two 0.64 inch diameter aluminum disks were places on both ends of the foam and were inserted into a 0.75 inch diameter glass tube submerged in an oil bath. A small hole was present in the end of the tube to allow oil flow inside for improved heating of the sample. Another tube was placed on the upper aluminum disk and filled with controlled amounts of steel shot to exert different loading pressures on the foam samples. The expansion of the foam samples were monitored through the linear movement of the upper tube using a laser proximity probe. The temperature of the oil bath was indirectly controlled through a hot plate located below the oil bath, which heating the oil at an average of 1°C per minute. The average temperature of the foam samples was collected by averaging the reading of two thermocouples inserted in the oil bath, one of which was inserted in a spare foam sample and the other thermocouple was left exposed to the oil.

When tested under loading pressures of 1.1 KPa, 1.9 KPa, and 2.7 KPa the thermal expansion of the foam remained the same. All the variation in the maximum elongation of those samples appears to be random and not a factor of loading pressure. When samples were tested under a 5.9KPa loading pressure a substantial decrease in expansion was noticed. At that level of loading, the 7.5 lbs/ft³ density foam reached a maximum elongation of 0.001 and the 10.5lbs/ft³ density foam extended to an elongation of 0.002 (Figure 9-12).

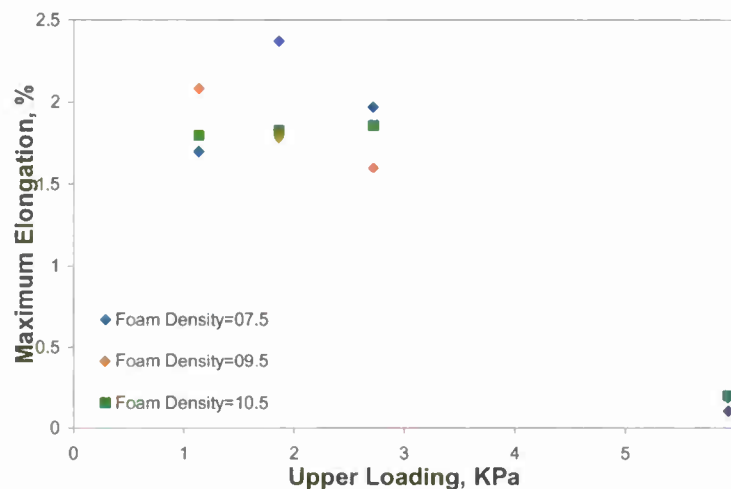


Figure 9-12 Maximum foam expansion under different pressure loads.

Over the full temperature range tested two distinct regions of differing thermal expansion can be noticed for the less constrained samples (Figure 9-13). At temperatures below 90°C

the thermal expansion coefficient tends to be between $50\text{-}60 \times 10^{-6} / ^\circ\text{C}$, but above that temperature the coefficient value gradually increases with an average value ten times the low temperature value. The temperature at which the foam samples reached their maximum elongation was determined not to be related to either their density or the loading pressure for samples tested under 2.7 KPa or less. When a pressure of 5.9 KPa was used, the foam displayed the same coefficient of thermal expansion, but the temperature of maximum elongation was lowered to $50\text{-}55^\circ\text{C}$.

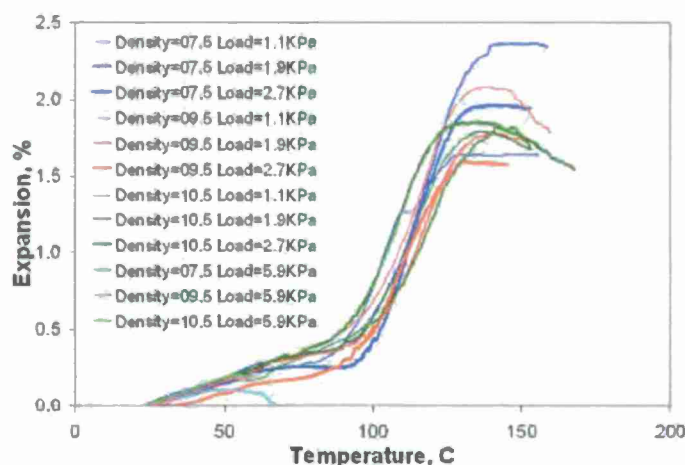


Figure 9-13 Thermal expansion curves.

When foam samples were left in a heated oil bath for extended periods of time, the foam contracted at a slow rate (Figure 9-14). When the oil temperature stabilized, the foam either rapidly returned to its original length and then gradually contracted at a rate of $0.0135\% / \text{hr}$, or it stayed at the expanded length and contracted at nearly ten times the rate noted above. The reason for the different contracting rates is not currently determined. Even though the foam had contracted over time, the maximum elongation and the corresponding temperature did not decrease (Figure 9-15.). On the contrary, the foam samples put through this heating profile expanded to a greater length than previously and the temperature of maximum elongation was higher than before and for some samples it was higher than could be safely maintained with the used oil bath. Upon cooling back to room temperature, a difference final sample length was noticed. The higher density foam shrunk more than the lower density foam. The sample that was tested under 2.9 KPa of pressure showed four times the amount of shrinkage as the sample under 1.1 KPa of pressure.

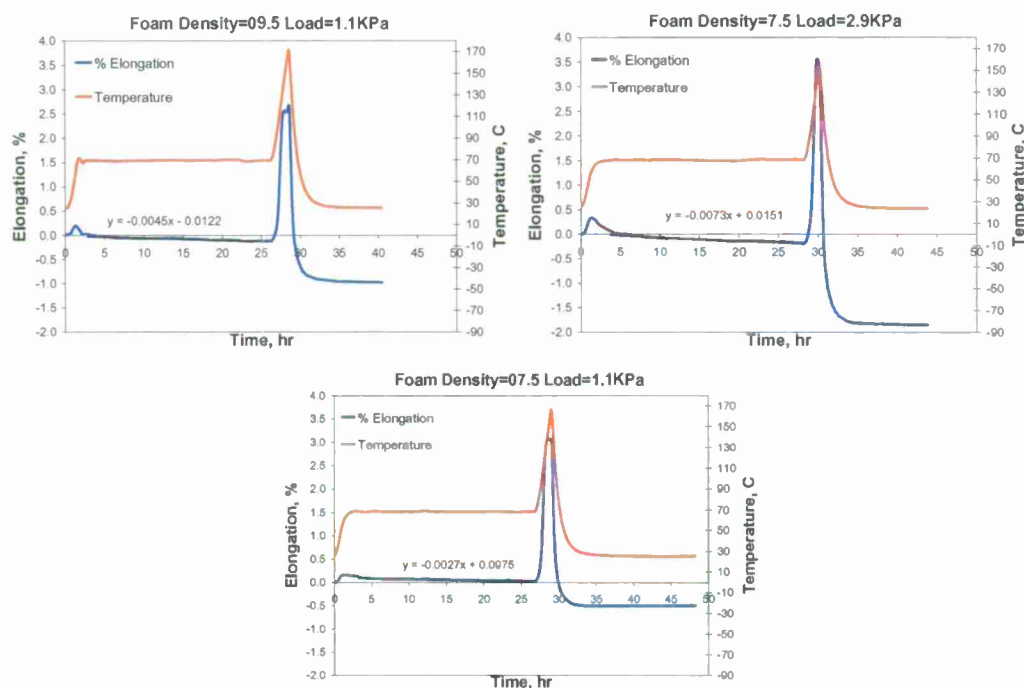


Figure 9-14 Expansion and heating profiles for samples held at an intermediate temperature.

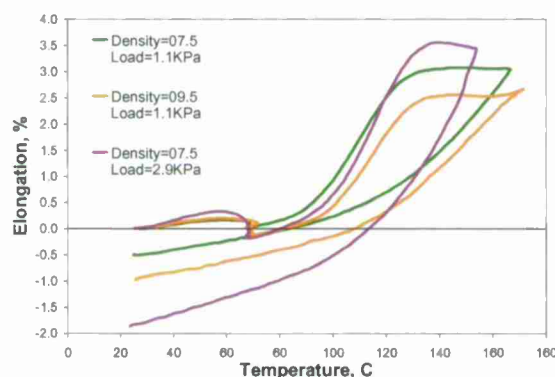


Figure 9-15 Thermal expansion curves for samples held at an intermediate temperature.

For a final test, a foam sample of 9.5 lbs /ft³ under minimal pressure was heated using a stepped heating profile. This heating profile was set to increase and hold the oil temperature in approximately 20°C increments. The time between initiating each temperature increase was five hours, with the resulting holding time varying based on how quickly the set temperature was reached. When the foam was held at 43°C no change in length was noticed over 2.5 hours (Figure 9-16.). Slow rates of contraction were noticed during holds at higher temperatures below 90°C. When the hold temperatures reached values where the foam's coefficient of thermal expansion increased the rate of contraction also increased. Upon holding at a maximum temperature of 161°C and cooling back to room temperature the length of the foam had shrunk to 97.4% of the initial length (Figure 9-17.).

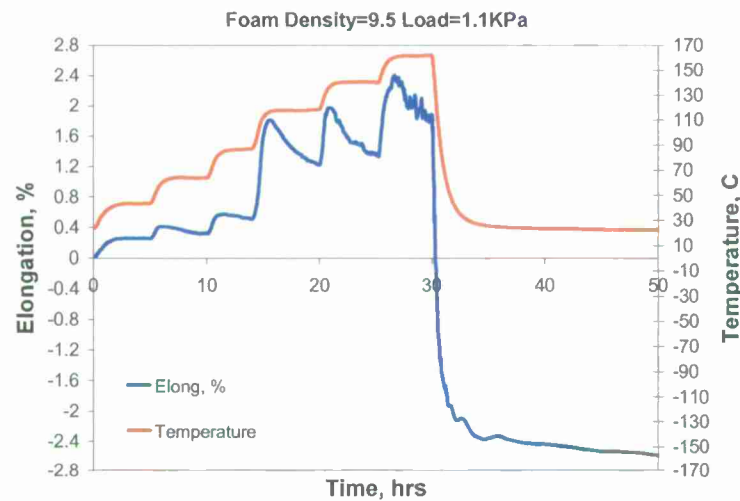


Figure 9-16 Expansion and heating profile of foam experiencing a stepped heating profile.

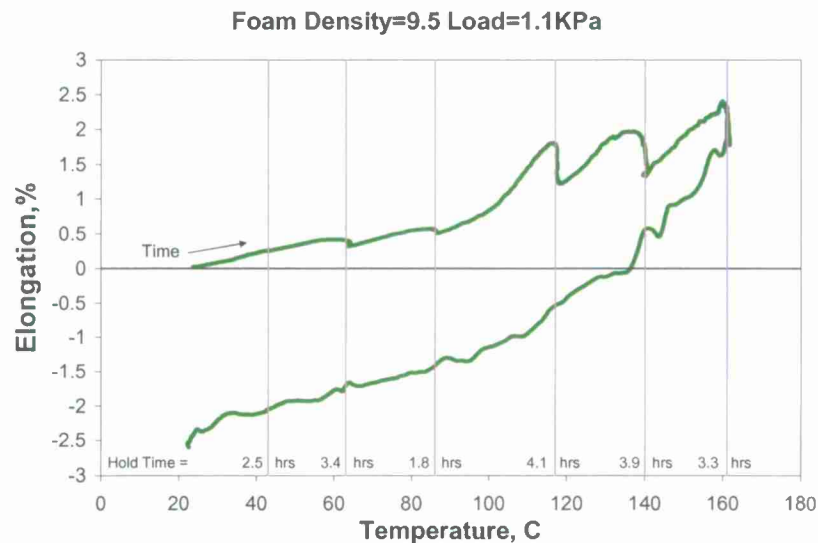


Figure 9-17 Thermal expansion curve of foam experiencing multiple holding temperatures.

Though holding the foam at a temperature below its relaxation or decomposing temperature causes it to temporarily contract, it will have no positive results when heating increases again. Based on the results when applying 5.9 KPa pressure on the foam samples during testing, it can be inferred that the maximum pressure the foam will exert on a ceramic mold during firing is slightly higher than 5.9 KPa if the shell has zero deformation.

Foam modulus. The elastic modulus of the foam is a needed for accurate simulation of the pattern removal. Compression testing of the foam at several densities and temperatures was done to determine the elastic modulus. The foam was heated in an oil bath and the temperature of the bath, as well as of the inside of the foam was measured to achieve a uniform temperature distribution. All tests were run to maximum 120 MPa pressure and

25, 60, and 100°C. Results shown in Figure 9-18 indicate that the modulus decreases with increasing temperature.

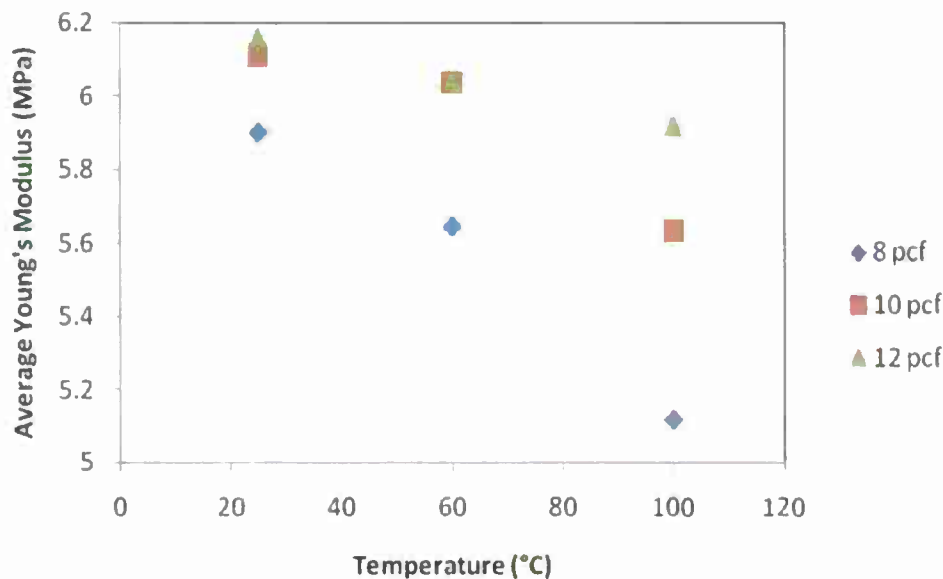


Figure 9-18 Average Young's modulus for varying temperature foam samples.

Results/Key Findings: Year 2:

Task 12. Model refinement and parametric studies of high density foam pattern removal

Bullet items:

- The effect of shell thickness on the ceramic shell behavior during FOPAT removal process has been studied using 3D thermo-mechanical coupled finite element model and simulation results are presented

Results

The developed 3D thermo-mechanical coupled finite element model has been used to study the effect of shell thickness on ceramic shell behavior during pattern removal process. Three shell thicknesses namely, 3.82 mm (thin), 6.4 mm (medium) and 9.7 mm (thick) have been investigated. Flash heating at temperature 600°C is used for simulation. Material properties of ceramic shell and FOPAT pattern are listed in Table 9-5. Failure strength of three types of shell is assumed to be 7.2 MPa. Figures 9-19 and 9-20 show the stress distribution of ceramic shell when foam temperature reaches 155°C for thin shell and thick shell respectively. When the thickness of shell changes, the positions of maximum value of principal stress will change. However, the most vulnerable positions of shell are the internal corners of the pocket. Table 9-6 shows the simulation results for ceramic shell with different thicknesses. If the shell thickness increases, the stress of ceramic shell will decrease accordingly. The thick shell does not fail while other two shells fail. However, thick shell requires longer time to reach temperature 155°C.

Table 9-5 Material properties of ceramic shell and foam pattern

Type	Ceramic shell	Foam pattern
Density	1800 kg/m ³	170 kg/m ³
Elastic modulus	2000 MPa	53 MPa (<80°C) 1 MPa (>155°C)
Poisson's ratio	0.24	0
Specific heat	650 J/kg	1300 J/kg
Thermal conductivity	1.0 W/m/K	0.06 W/m/K
Coefficient of thermal expansion	$2 \times 10^{-6} \text{ K}^{-1}$	$80 \times 10^{-6} \text{ K}^{-1}$ (<80°C) $400 \times 10^{-6} \text{ K}^{-1}$ (>100°C)
Foam decomposition temperature	N/A	155 °C

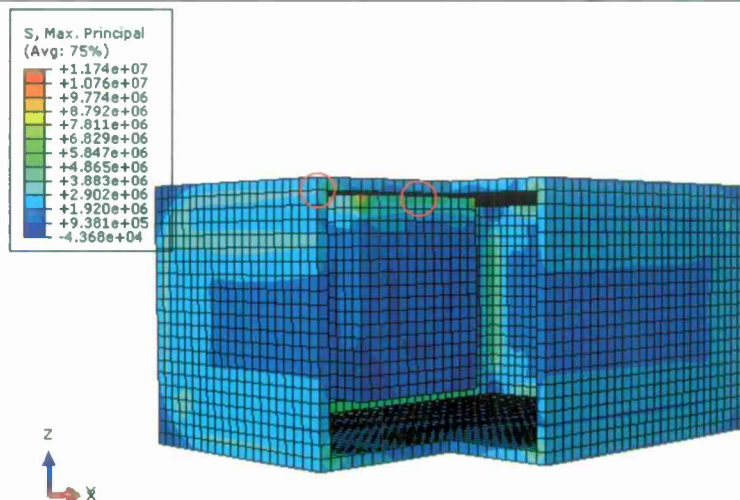


Figure 9-19 Stress distribution of thin ceramic shell (thickness: 3.82mm, cut view, time=47.98s, position of max stress denoted by red circle).

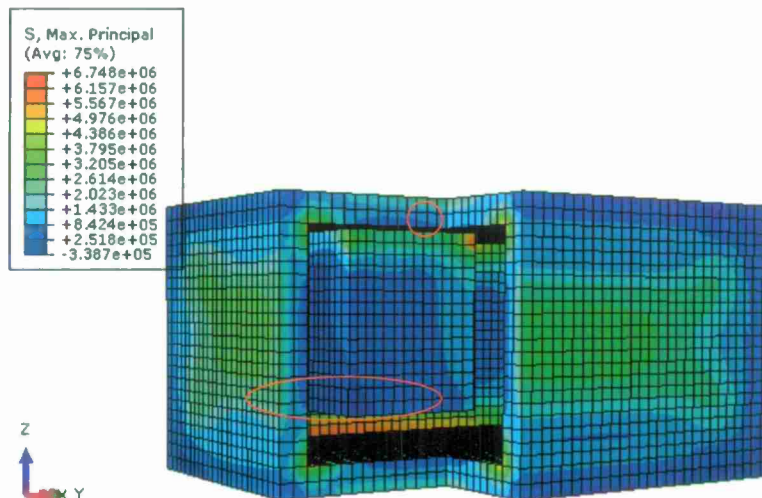


Figure 9-20 Stress distribution of thick ceramic shell (thickness: 9.7mm, cut view, time=117.8s, position of max stress denoted by red circle).

Table 9-6 Simulation results (failure strength=7.2 MPa)

Case No.	Shell thickness, mm	Time, s	Maximum principal stress, MPa	Middle principal stress, MPa	Foam temperature, °C	Fail
1	3.82	47.98	11.74	3.438	155	Yes
2	6.4	76.31	8.164	3.052	155	Yes
3	9.7	117.8	6.748	2.915	155	No

Task 13. Foam aging data

Bullet items:

- The effect of foam aging on the pattern properties and removal process in investment casting has been investigated

Results

Figure 9-21 shows the experimental foam degradation properties considered in simulation model. Above a certain temperature, the foam modulus decreases steadily until the foam decomposes. Figure 9-22 describes the thermal expansion coefficient variation of aged and un-aged foam patterns through temperature line. In simulation cases, aging effect is reflected by reduced thermal expansion coefficient below certain temperature for the foam model.

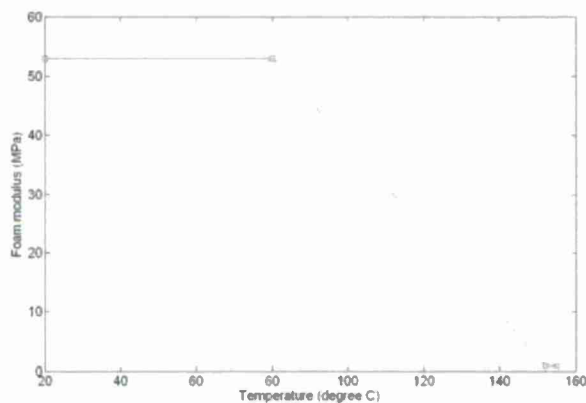


Figure 9-21 Foam degradation regarding modulus versus temperature.

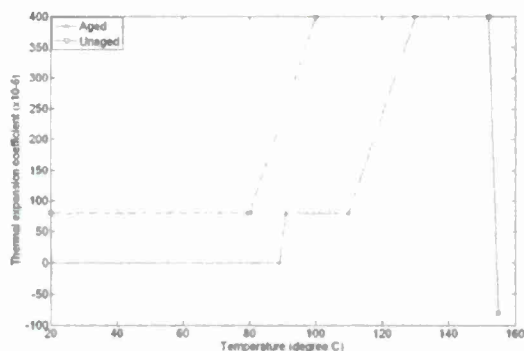


Figure 9-22 Thermal expansion coefficient of aged and un-aged foam.

Foam aging effect: simulation results. The thermal-displacement coupled finite element model which has been developed was used to study the effect of foam aging on ceramic shell behavior during pattern removal process. Table 9-7 lists the thermal and mechanical properties of the ceramic shell and foam pattern. Four simulation cases with respect to flash heating were investigated. Two types of shell thicknesses and accordingly two failure strengths were used in simulation. All four simulation cases use the same foam dimensions, 2.5 inch x 2.5 inch x 2 inches (6.35mm×6.35mm×50.8mm) with sharp corners. Table 9-8 lists the simulation cases in terms of shell thickness, failure strength and aging process. Simulation results are listed in Table 9-9. Figure 9-22 shows the stress distribution of ceramic shell for case 3 when foam temperature reaches 155°C, and critical regions named A, B and C are identified in the figure. Figure 9-23 and Figure 9-24 show temperature and maximum principal stress as a function of time in critical locations of ceramic shell for both aged and un-aged cases. From the results, it can be seen that the aging effect plays a vital role on reducing the chance of ceramic shell cracking.

Table 9-7 Material properties of ceramic shell and foam pattern.

Type	Ceramic shell	Foam pattern
Density, kg/m ³	1800	170
Elastic modulus, MPa	2000	See Fig. 20
Poisson's ratio	0.24	0
Specific heat, J/kg	650	1300
Thermal conductivity, W/m/K	1.0	0.06
Coefficient of thermal expansion, K ⁻¹	2×10 ⁻⁶	See Fig. 21
Foam decomposition temperature, °C	N/A	155

Table 9-8 Simulation cases.

Case	Shell Thickness, mm	Failure Strength, MPa	Aging process
1	3.8	4.4	No aging
2	3.8	4.4	100 °C / 24 hours
3	6.4	7.2	No aging
4	6.4	7.2	100 °C / 24 hours

Table 9-9 Simulation results.

Case No.	Maximum principal stress, MPa	Middle principal stress, MPa	Maximum principal strain, x10 ⁻³	Foam temperature, °C	Fail
1	3.48	1.09	4.45	105	Yes
2	3.55	1.43	1.83	155	No
3	6.66	2.64	3.13	155	No
4	3.16	1.23	1.69	155	No

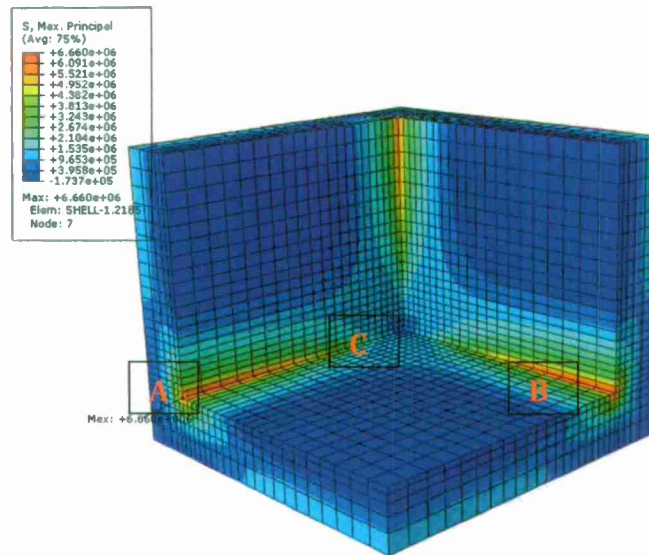


Figure 9-22 Stress distribution in ceramic shell (case 3).

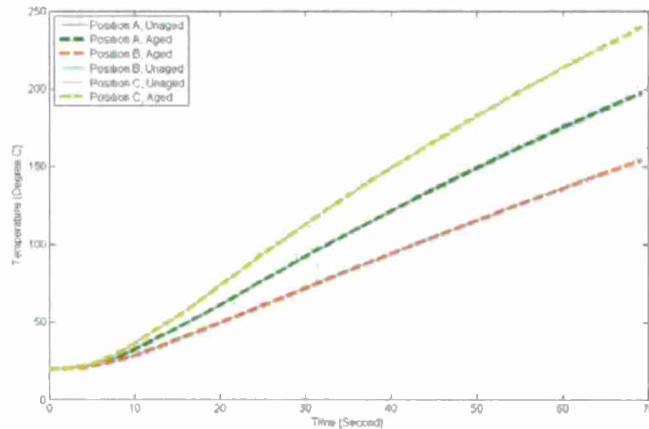


Figure 9-23 Temperature development through time in different locations (cases 3 and 4).

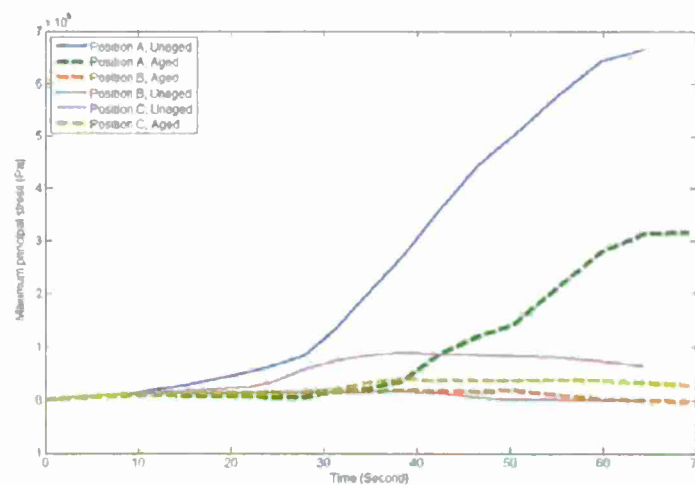


Figure 9-24 Maximum principal stress development through time in different locations (cases 3 & 4).

Task 14. Confirmation tests of pattern removal based on modeling

Bullet items:

- Coupled thermal mechanical model for investment shell tree during foam pattern removal was updated based on experimental trials and materials data
- Confirmations trial using laboratory-produced shells were done and supported modeling predictions

Results:

Shell cracking tests: The cracking tests to date are presented below which will be compared to modeling results for refinement of the model where the variables are:

- Corner radiuses (*R*) or sharp (*S*).
- Shell thickness: light medium or heavy
 - a. light (*L*): 1 primary, 2 backup and 1 seal coat
 - b. medium (*M*): 1 primary, 3 backup and 1 seal coat
 - c. heavy (*H*): 1 primary, 4 backup and 1 seal coat
- Firing regimes: Continuous heating till 600 C with 3 C/min heating rate and flash firing is done at 600 C. Initial furnace temperature is 20 C in both the cases.

The firing test results are shown in Table 9-10 and examples of crack locations are illustrated in Figure 9-25.

Table 9-10 Pattern removal test results.

Type of Shell	Firing method	Cracking	Crack Location
NS	Flash fire	Yes	2 side corners.
NR	Flash fire	Yes	Along the cup
NR	Continuous heating	Yes	All corners except cup
LS	Flash fire	Yes	Along all corners but not in the cup
HS	Flash fire	Yes	Along bottom corners but not in the cup
HR	Flash fire	Yes	Along bottom corners but not in the cup

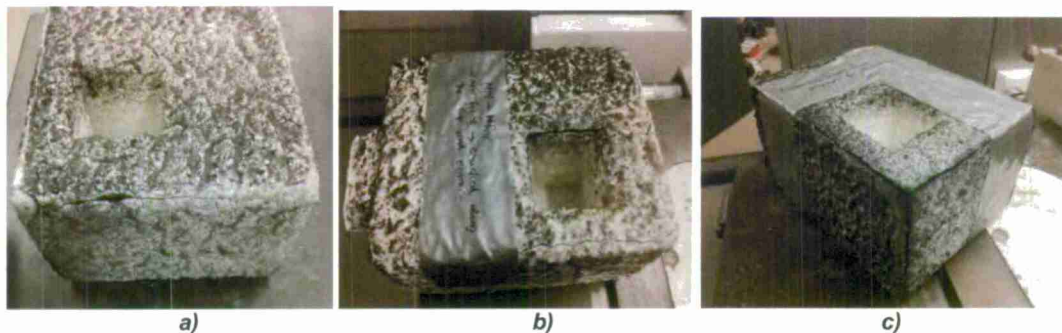


Figure 9-25 Shell cracking: a) along the corners of sharp cornered normal thickness flash fired shell, b) along the cup of a radius cornered normal thickness shell, and c) along the corners of sharp cornered light thickness shell.

Task 15. Shelling and pattern removal tests at Conbraco

Bullets:

- Sets of shelled patterns were obtained from both Conbraco and Mercury Marine for developing the data base input for the modeling of industrial trials and lab trials with industrial shells

Results:

Figure 9-26 shows the dimensions of the pattern: Two types of patterns are used namely sharp cornered and 5mm radius cornered.

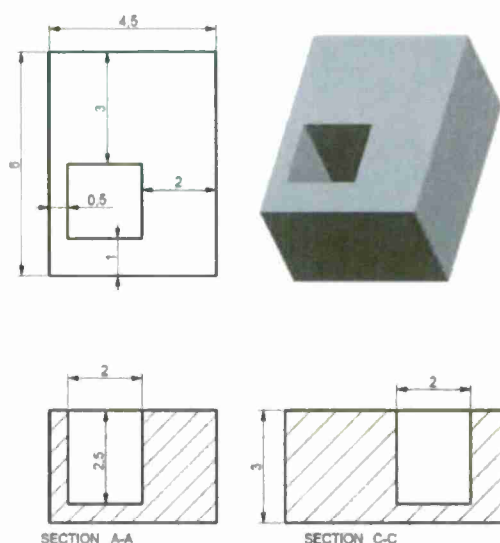


Figure 9-26 Fopat complex object test pattern

The results of modeling and laboratory pattern removal from industrially produced mold shells are compared in Tables 9-10 and Table 9-11. The parameters varied in this experiment were heating method (gradual heating compared to flash firing), the effect of pattern radius and the effect of shell thickness.

Table 9-10 Comparison of modeling and experimental results for Conbraco.

Thickness, mm	Sharp	Firing regime	Shell fail (Exp)	Location	Shell fail (Modeling)
3.8 ± 0.2	X	Flash firing	YES	one edge adjacent to cup & in cup	YES
	X	Continuous	YES	All edges	YES
	X	Aging and FF	NO	-	NO
6.8 ± 0.3	X	Flash firing	YES	one edge adjacent to cup	YES
	X	Continuous	YES	Bottom and side edges	YES
	X	Aging and FF	NO	-	NO
9.9 ± 0.3	X	Flash firing	NO	-	NO
	X	Continuous	NO	-	NO
	X	Aging and FF	NO	-	NO

Table 9-11 Comparison of modeling and experimental results for Mercury Marine.

Thickness, mm	Sharp	Firing regime	Shell fail	Location	Shell fail (Modeling)
4.4 ± 0.2	X	Flash firing	YES	All edges except bottom edges.	
	X	Continuous	YES	Top and bottom edges.	
	X	Aging and FF	YES	One bottom edge	YES
6.7 ± 0.3	X	Flash firing	YES	All edges	
	X	Continuous	YES	All edges	
	X	Aging and FF	NO	-	
8.2 ± 0.3	X	Flash firing	YES	Bottom edges	
	X	Continuous	YES	All edges	
	X	Aging and FF	NO	-	NO

Task 17. Properties measurements of industrial shells

Bullets:

- Property measurements of industrial shells were done and used for input to modeling
- The property data was used in FEM modeling to predict the effect of technological parameters on shell cracking.

Results:

Thickness, strength and porosity results are shown in Table 9-12 – Table 9-14. This data will be used in the FEM modeling of the pattern removal process for the industrial shells.

Table 9-12 Thickness of the industrial shells.

Producer	Light, mm	Normal, mm	Heavy, mm
Conbraco	3.82 ± 0.2	6.70 ± 0.2	9.7 ± 0.2
Mercury Marine	4.4 ± 0.2	6.60 ± 0.2	8.2 ± 0.2

Table 9-13 MOR (strength) test results

	Green MOR, MPa	Fired MOR (fired at 850°C, 1 hour), MPa
Conbraco	3.51	5.17
Mercury Marine	2.55	3.94

Table 9-14 Density and porosity of the shells.

Shells	Porosity, %	Density, g/cm ³
Conbraco	28.5±0.2	1.95
Mercury Marine	30.2±0.2	1.65

Task 16 – Simulation of Industrial Trials

Bullet

- This was done out of task sequence numbering to use the data from Task 17. This modeling work was done in advance of the industrial trial at Conbraco. More cases were modeled than actually used in industrial trials to identify the critical parameters for the industrial confirmation trial.

The simulation results for all industrial trial cases were reported using the extended 3D thermo-mechanical coupled finite element model. The extended 3D thermo-mechanical coupled finite element model is used to evaluate industrial trial shell behavior during FOPAT removal process. The model employs the most recent FOPAT material properties used for the trial. The mechanical and thermal properties of the industrial shell from Conbraco were measured and incorporated into the model. Two types of FOPAT with sharp corner and with round corner have been evaluated as shown in Figure 9-27. Aging effect was introduced into the model to study the effect from aging of FOPAT after shelling on the stress in shell. Three shell thicknesses (different number of layers) in terms of thin, medium and thick with different modulus of rupture (MOR) strengths were studied as shown in Table 9-15. The simulation of FOPAT removal process was conducted at three temperature levels (1200°F, 1400°F and 1600°F).

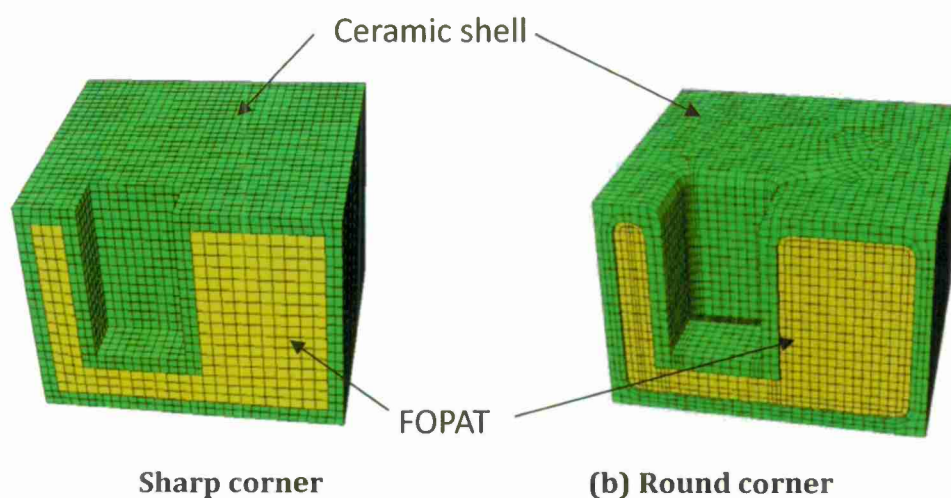


Figure 9-27 Finite element model of shell and FOPAT with complicated geometry.

Table 9-15 Three types of shell from Conbraco.

Shell type	Thin	Medium	Thick
Thickness, mm	3.8	6.8	9.9
Failure strength, MPa	3.9	4.7	4.2

The detailed simulation results for each industrial trial case are shown in Table 9-2 (shell with sharp corner) and Table 9-3 (shell with round corner). For thicker shell, less strain and stress are observed during FOPAT removal process. A similar phenomenon is observed for shell with round corner or aged FOPAT. The increase of temperature of flash firing seems not contribute in terms of reduction of shell stress and prevention of shell cracking, although less time is required to remove FOPAT.

Table 9-16 Simulation results for the shell with sharp corner.

Thickness, mm	Flash firing temperature, F	FOPAT aging	Time, s	Maximum principal stress, MPa	Middle principal stress, MPa	Maximum principal strain in shell, $\times 10^{-3}$	Foam temperature, °C	Fail
3.8 ± 0.2	1200	No	46	5.123	1.341	3.939	139	Yes
		Yes	51	2.682	0.5341	1.465	155	No
	1400	No	37	3.327	1.312	4.14	143	Yes

6.8 ± 0.3	1600	Yes	40	2.906	1.044	1.463	155	No
		No	29	4.841	1.506	3.827	144	Yes
		Yes	31	2.927	1.098	1.499	155	No
	1200	No	91	3.436	1.146	3.002	138	Yes
		Yes	98	1.744	0.916	1.555	155	No
		No	72	3.876	1.922	2.802	139	Yes
	1400	Yes	77	1.545	0.8463	1.411	155	No
		No	59	3.897	2.026	2.863	142	Yes
		Yes	62	1.511	0.5451	1.367	155	No
	9.9 ± 0.3	No	168	2.508	1.345	2.055	155	No
		Yes	169	1.865	0.9628	1.59	155	No
		No	135	2.951	1.506	2.252	155	No
		Yes	135	2.091	1.074	1.703	155	No
		No	111	3.314	1.637	2.425	155	No
		Yes	109	1.848	1.057	1.624	155	No

Table 9-17 Simulation results for the shell with round corner.

Thickness, mm	Flash firing temperature, F	FOPAT aging	Time, s	Maximum principal stress, MPa	Middle principal stress, MPa	Maximum principal strain in shell, x10 ⁻³	Foam temperature, °C	Fail
3.8 ± 0.2	1200	No	51	3.631	0.9312	2.744	155	No
		Yes	51	2.642	0.9977	2.08	155	No
	1400	No	37	3.77	0.923	2.8	155	No
		Yes	37	1.94	0.802	1.572	155	No
	1600	No	28	3.698	0.8519	2.724	155	No
		Yes	28	1.35	0.6141	1.215	155	No
6.8 ± 0.3	1200	No	97	2.651	0.5796	2.036	155	No
		Yes	97	1.945	0.6587	1.569	155	No
	1400	No	77	2.794	0.659	2.121	155	No
		Yes	77	2.063	0.7697	1.637	155	No
	1600	No	63	3.178	1.162	2.357	155	No
		Yes	63	2.236	0.9136	1.734	155	No
	1200	No	177	2.195	0.5161	1.762	155	No
		Yes	172	1.572	0.487	1.342	155	No
9.9 ± 0.3	1400	No	138	2.119	0.5912	1.688	155	No
		Yes	127	1.69	0.5149	1.371	155	No
	1600	No	108	2.256	0.7193	1.731	155	No
		Yes	108	1.83	0.6333	1.522	155	No

Task 18 is part of the transition to industry and will be covered under that section.

Task 19. Foam decomposition chemistry

Bullets:

- The chemistry of industrial pattern decomposition products was experimentally verified
- The volume of HCN during polyurethane foam pattern removal was measured under various conditions

- Flash firing with excess air and increased exposure time of the combustion product to elevated temperature would drive HCN levels down to below detectable limits.

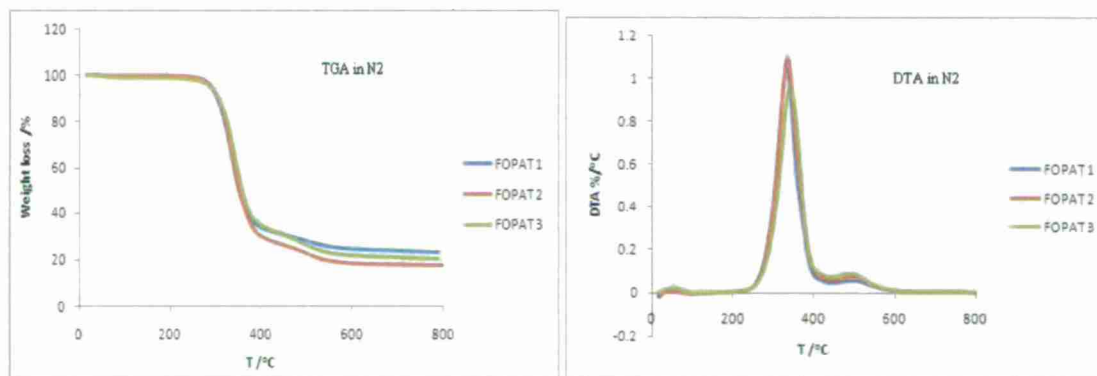
Results:

These studies were necessary to insure Environmental Health and Safety (EHS) compliance. Based on elementary analysis, there are about 64% carbon and 6% nitrogen for FOPAT patterns of the three densities being studied: 7.5pcf (FOPAT 1), 9.5pcf (FOPAT2) and 10.5pcf (FOPAT 3). The ash contents of FOPAT patterns were also determined to be about 0.01% at 900°C after 7h (Table 9-18).

Table 9-18 Elemental chemical composition of FOPAT (weight %).

Material	C	H	N
FOPAT 1	64.4	6.3	6.3
FOPAT 2	64.4	6.4	6.2
FOPAT 3	64.3	6.8	6.1
FOPAT Ash	0.1	0	0

The thermal decomposition of foam patterns in N_2 and air were studied. In air, FOPATs decomposed completely at 680°C, but still had about 20% residue remaining at 800°C in N_2 . In air, we noted that degradation rate increased with the decreasing FOPAT density. This suggests a decrease of pattern removal time with the increasing density of foam pattern. The decomposition products play an important role during casting process. Because it will affect the rate of removal of products (Figure 9-28) which subsequently influence the casting quality and some hazardous gas such as HCN can be generated when polyurethane is used as foam pattern (Table 9-19, Table 9-20). Consequently, it is necessary in manufacturing to increase the gaseous fraction in the decomposition products and decrease the amount of hazardous substances. Some techniques, such as oxygen addition, as suggested by Buycastings.com, and higher temperature during the flash firing process may be helpful to achieve those ends.



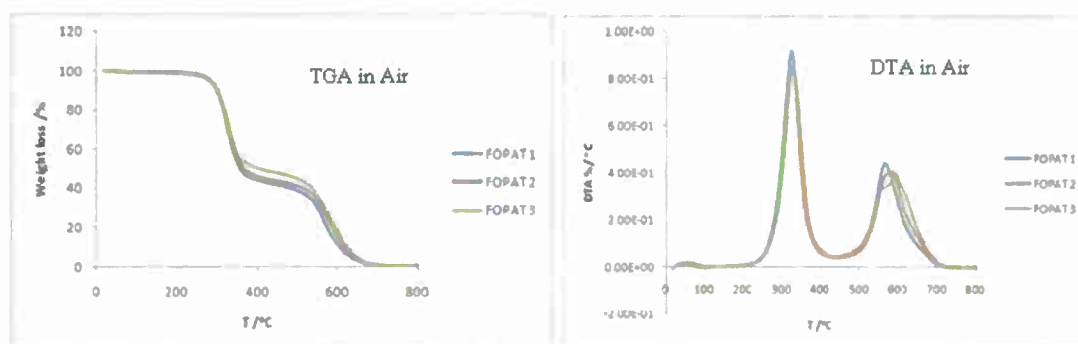


Figure 9-28 Effect of density of FOPAT on degradation in N2 and air.

Table 9-19 Product distribution of Polyurethane (FOPAT)pyrolysis at 800oC(no oxygen).

Gas Fraction		Liquid Fraction		Solid Fraction	
CO	34%	Benzene	4.5%	carbon coke	5%
CO ₂	1%	Toluene	0.6%	-	-
Methane	16%	Naphthalene	2%	-	-
Ethene	6%	Tar	8%	-	-
HCN	4.2%	Water	4%	-	-
-	-	Other aromatics	3%	-	-

Table 9-20 Product distribution of Polyurethane (FOPAT) pyrolysis at 850oC (no oxygen)

Gas Fraction		Liquid Fraction		Solid Fraction	
CO	26%	Benzene	7%	carbon coke	1%
CO ₂	17%	Toluene	1%	-	-
Methane	12.5%	Naphthalene	4%	-	-
Ethene	3%	Tar	11%	-	-
-	-	Water	1.7%	-	-
-	-	Other aromatics	5%	-	-

The generations of HCN from the decomposition of FOPAT pattern at different conditions were studied. It demonstrates that if the products stay in hot zone for a longer time, less HCN was produced. When the sample drawing method is 0.5h without vacuum pump and following by 0.5h pump, no any significant HCN was detected for any types of FOPAT samples. The HCN content was listed in the report at different conditions. The main factors which affect the HCN generation were also discussed in this report. It showed HCN level will increase when the decomposition temperature increase and increasing the oxidant/fuel ratio decreases HCN generation after reaching a maximum value. If the products stay in a hot zone for a longer time, less HCN is generated.

The polyurethane materials such as FOPAT pattern are known to produce a significant amount of toxic hydrogen cyanide (HCN) when they are thermally degraded in air. In order to assess the level of HCN generated from the FOPAT patterns during the firing in casting process, a laboratory experiment was performed (Table 9-21).

Table 9-21 Level of hydrogen cyanide detected (750oC).

	FOPAT	Sample Collection	HCN% (weight)	FOPAT sample, g in 100m ³ area reaching NOISH limits
Flash Firing (tube furnace)	8pcf without shell, 2g	0.5h non-pump + 0.5h pump	Non-detectable	-
Flash Firing (tube furnace)	10pcf with 5 shell layers, 5g	0.5h non-pump + 0.5h pump	Non-detectable	-
Flash Firing (tube furnace)	10pcf with 3 shell layers, 5g	0.5h non-pump + 0.5h pump	Non-detectable	-
Flash Firing (tube furnace)	10pcf with 3 shell layers, 5g	1h pump, 320mL/min (pump rate)	0.0057	9070g (REL) 96500g (IDLH)
Continuous Heating (muffle furnace)	8pcf with shell, 10g	1h pump, 160mL/min (pump rate)	0.0342	1511g (REL) 16100g (IDLH)

Note: NIOSH (National Institute for Occupational Safety and Health) Exposure Limits:

REL (Recommended exposure limits): 5mg/m³ or 4.7ppm in air

IDLH (Immediately dangerous to life or health): 55mg/m³ or 50ppm in air

At flash firing condition, both FOPAT patterns with and without shell produce negligible HCN if drawing sample did not use pump at the first half an hour. However if the pump was used from the beginning of the decomposition, certain HCN level was detected by the titration method. In Table 9-22 it is shown that 0.0057% (weight of FOPAT pattern) HCN was generated for FOPAT 10pcf with 3 layers. In this case, in working area of 100m³, 9070g FOPAT 10pcf would produce HCN which is harmful for human's skin and 96500g will be dangerous for human's life. For continuous heating, the decomposition experiences heating from room temperature to high temperature; at low temperature (200-500°C), it showed more HCN may be produced This demonstrates that if the products stay in the hot zone for a longer time, the HCN will decompose thus resulting less HCN.

Collaborative Activities/Transition into Industry:

Task 18 was an industrial trial demonstration of the model. Additionally results of this program were presented at AFS 4L investment casting committee meetings to disseminate results to industry. The universal die set is in the possession of buycastings.com for use by any foundry wishing to buy test patterns.

Task 18 -- Industrial trial results report

Objective: Industrial testing of shells for shell cracking based on the simulated model at three different temperatures provided by Conbraco involving two types of Polyurethane foam patterns of complicated geometry.

Background: Polyurethane foam patterns with complicated geometry (having deep internal pockets), which are sensitive to crack formation are sent to the industrial Conbraco.

- Requested industrial Conbraco to shell three different shell thicknesses on two types of patterns. Specifically sharp corner (shown in Table 9-22) and 5mm radius corner (shown in Table 9-23).
- The three different shell thicknesses were considered in simulation consisting of normal thickness, heavy (+2 layers than normal) and light thickness (-2 layers than normal). However the key test of model sensitivity in the results seemed to lie in the normal shell thickness range. Therefore in the interest of economical use of industrial trial facilities, the normal shell thickness results were the focus of the industrial burnout experiments.
- Two firing regimes were to be employed: specifically flash firing (at 1200, 1400 and 1600F) and Aging (at 212F for 24 hrs) and flash firing (1200, 1400 and 1600 F).

Table 9-22 Simulation and Experimental Results of Industrial Conbraco – Sharp corner

Thickness (mm)	Firing regime	Foam Aging	Time (s)	Max principal stress (MPa)	Mid Principal stress (MPa)	Max principal strain in shell (X10 ⁻³)	Max plastic principal strain in shell (X10 ⁻³)	Shell Fail (Simulation)	Shell fail (Industrial experiment)
6.8 ± 0.3 (Normal shell thickness)	FF (1200F)	No	97.17	2.651	0.5796	2.036	0	No	No
		Yes	97.17	1.945	0.6587	1.569	0	No	No
	FF (1400F)	No	77.3	2.794	0.659	2.121	0	No	*
		Yes	77.3	2.063	0.7697	1.637	0	No	No
	FF (1600F)	No	62.96	3.178	1.162	2.357	0	No	No
		Yes	62.96	2.236	0.9136	1.734	0	No	No

Table 23: Simulation and Experimental Results of Industrial Conbraco – Round corner

Thickness (mm)	Firing regime	Foam Aging	Time (s)	Max principal stress (MPa)	Mid Principal stress (MPa)	Max principal strain in shell (X10 ⁻³)	Max plastic principal strain in shell (X10 ⁻³)	Shell Fail (Simulation)	Shell fail (Industrial experiment)
6.8 ± 0.3 (Normal shell thickness)	FF (1200F)	No	90.5	3.436	1.146	3.002	0.3178	Yes	Yes
		Yes	97.65	1.744	0.916	1.555	0	No	No
	FF (1400F)	No	71.98	3.876	1.922	2.802	0.3929	Yes	Yes
		Yes	77.05	1.545	0.8463	1.411	0	No	No
	FF (1600F)	No	59.37	3.897	2.026	2.863	0.398	Yes	Yes
		Yes	61.99	1.511	0.5451	1.367	0	No	No

*- Shell breakage due to human error

Observations and discussion:

- The experiment and simulation results match very well for both the geometries and firing regimes.
- It has been observed that no shell (even those of light thickness) of 5mm radius corner fails in simulation and experiment in both the firing regimes. This may be due to the fact that the effect of the 5 mm radius corner is reflected on the principal stress as well as the principal strain. The shell with radius corner has less stress than the one with sharp corner in terms of maximum principal stress, middle principal stress, and the strain is less as well.

- For the shells with sharp corner, only the shells which were aged did not crack. This can be seen in the given Figure 9-29 below. Also is of importance is the two fold (approx.) reduction in the maximum principal stress and strain when the shell is aged (from Table 9-22). Therefore as it is evident from the simulation and experimental results, aging effectively prevents shell cracking.
- It is also found from experimental results that mold penetration in casting after pouring was more in the case of non-aged shells when compared to aged ones.

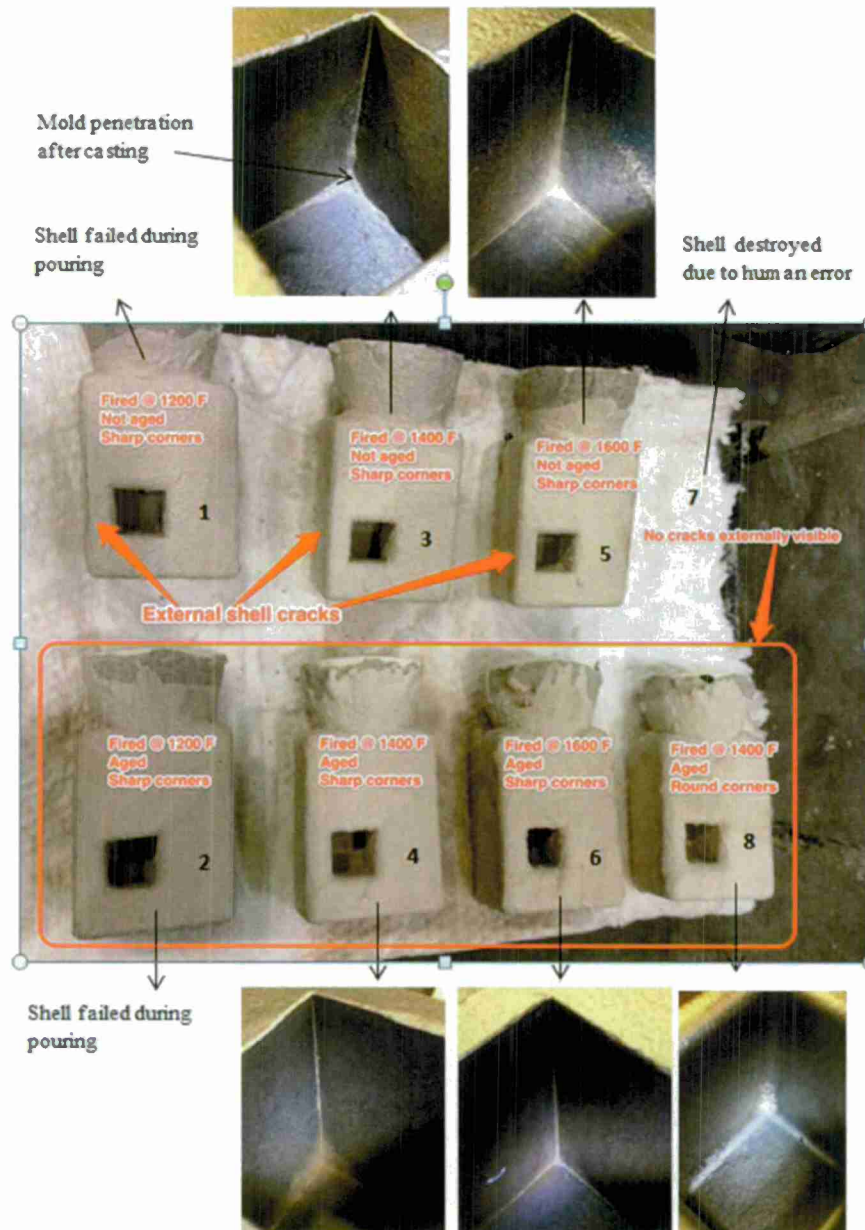


Figure 9-29 Figure showing the temperatures of testing, cracked and non-cracked shells and the extent of mold penetration at Conbraco

Further observations:

Shell #1 cracked during firing. It was patched prior to pouring. During pouring the Shell failed completely.

Shell #2 showed no signs of cracks after firing. However during pouring the Shell failed completely.

Shell #3 cracked during firing. The mold was patched so it could be poured. In the pocket some mold penetration can be seen in the corners.

Shell #4 No cracking was observed on this mold. The casting had slight mold penetration in the corners of the pocket but much less than shell #3.

Shell #5 cracked during firing. Shell was patched before pouring. The shell also revealed a shell crack on the back after casting. The pocket corners also showed mold penetration.

Shell #6 (1600F fire, aged): No cracks observed from firing. Pocket corners show slight penetration but less than mold #5.

Shell #7 is scrapped prior to testing (human error)

Shell #8 No cracking was observed. Very little penetration is observed.

Conclusions from industrial trial:

Aging the shell prior to flash firing not only prevented shell cracking but also ensured that:

- No patching is required after firing.
- Souder casting as a result of much less mold penetration
- Aging plus flash firing allows meeting the metric of zero shell cracking defects

Conclusions and Recommendations

Conclusions:

- Developed a three dimensional thermo-mechanical coupled finite element model which was used to predict ceramic shell behavior during pattern removal process by thermal decomposition of the foam.
- A revised edge test model was developed under the High Performance Steels program, but it was applied to shells produced under this program as well. It was found that the model reported in the literature contained a significant error and did not include the edge curvature effects
- Mechanical and thermal property data was developed for the FOPAT Material.
- The model was confirmed with laboratory trials and an industrial confirmation trial.

Recommendations include:

1. Aging the pattern and shell assembly after the shell build at 100C for 24 hours
2. Flash firing at 1600F with excess air injection for pattern removal
3. Use of rounded corners of 5 mm radius at entrances to internal pockets

Using these recommendations we were able to achieve the metric of zero shell cracking including the edges of internal pocket configurations in the pattern.

Publications

1. Effects of Complex Geometry, Shell Thickness and Firing Regimes on Shell Cracking in Industrial Investment Casting Shells during Rigid Polymer Pattern Removal, S. Komaragiri, H. Li, S.N. Lekakh, K. Chandrashekhara, V.L. Richards. (Submitted for AFS Casting Congress 2013)
2. Foam Pattern Aging and its Effect on Crack Formation in Investment Casting Ceramic Shells, W.A. Everhart, S.N. Lekakh, V.L. Richards and J.D. Smith, H. Li and K. Chandrashekhara, H. Zhao and P.S. Nam, AFS Casting Congress 2012, paper 12-025
3. Characterization of Low Density Polymer Patterns for Large Steel Investment Casting, H. Zhao, M. Xu, H. Li, W. Everhart, S. Lekakh, V. L. Richards, K. Chandrashekhara³ and P. Nam, Investment Casting Institute 58th technical Conference and equipment exposition, October 2011.
4. Prevention of Crack Formation in Investment Casting Ceramic Shells by Foam Pattern Aging, W.A. Everhart, S.N. Lekakh, V.L. Richards and J.D. Smith, H. Li and K. Chandrashekhara, H. Zhao, International Journal of Metal Casting, accepted for publication.

***10. Steel Founders' Society of America (SFSA) Final Report: Principal Investigator
Malcolm Blair, SFSA***

During the period of performance SFSA provided guidance and facilitated a liaison between industry and the researchers in the SWC program. This liaison consisted of communications with the researchers on the day-to-day management issues such as the availability of materials from foundries, candidates for industrial trials, implementation of findings, and guidance to maintain focus for industry. The findings of the work were also distributed to other industry groups such as the American Society for nondestructive Testing (ASNT) and American Petroleum Institute (API) who have a keen interest in the visual inspection work carried out by Iowa State.

The industry involvement in developing guidance and awareness of the progress in these projects was essentially through the SFSA research committees, meetings throughout the USA, SFSA Board of Directors, and national meetings. The research committees and national meetings provided industry with direct access to the researchers to ensure industry input and relevance to ensure transition of results.

Typically there are six meetings through the USA that provide the opportunity for SFSA to give updates on progress of the work. The national meetings consist of one meeting in the middle of the year and a national conference at the end of the year. It is estimated that approximately 400 industry employees will attend these meetings each year.

Over the period of the SWC contract, SFSA has conducted the following efforts to ensure SWC technology transition into industry:

- Carbon and Low Alloy Research Review meeting, Schiller Park, IL, July 14-15, 2010. All Researchers operating in the Carbon and Low Alloy area presented information on the progress of their work to an open meeting of SFSA members. The members provided feedback and guidance.
- Eastern Division Technical & Operating meeting, Pittsburgh, PA, August 25, 2012. Update and discussion with technical and operating personnel of SFSA member foundries on the status and progress of SWC projects.
- SFSA Annual Meeting, Barr Harbor, ME, September 14, 2010. Update and discussion with senior executives and owners of SFSA member foundries on the status and progress of SWC projects.
- Joint meeting of Carbon and Low Alloy and High Alloy Research Committees, Ames, IA October 14, 2010. Update and discussion with research committees on the status and progress of SWC projects.
- National Technical and Operating Conference, Chicago, IL, December 8-11, 2010. Presentations and discussion with on the status of SWC projects. More than 200 technical and operating personnel of SFSA member foundries present at the conference.
- SFSA Board meeting, January 15, 2011. The status of the ISU Visual Inspection work was discussed at great length. Board members were very interested in the current findings related to the qualities of operators carrying out visual inspection.

- SFSA Safety/HR meeting, February 23, 2011. Presentation on Visual Inspection selection of operator issues and working conditions for visual inspection. Richard Stone of ISU made the presentation. There was great interest from the HR attendees as to how they might use selection procedures for visual inspectors and training issues to improve visual inspector performance.
- March 8-9, 2011. Discussions at ISU with Richard Stone and Frank Peters on the use of a screening test to select personnel with an aptitude for visual inspection.
- Meeting of SFSA High Alloy Research Committee on March 16, 2011 at Penn State to discuss the results and next steps in the High Strength Steels work with Bob Voigt. A number of foundries volunteered to produce test material.
- Discussion with John Griffin of UAB on April 6, 2011 regarding the testing program.
- Meeting with Chris Thimes, Benet and John Griffin, UAB on April 7, 2011 to discuss the scope of the program and the testing protocol
- Discussions at the SFSA Board of Directors on May 25, 2011 regarding progress on the SWC research progress.
- Carbon and Low Alloy Research Review meeting, Chicago, IL, July 12-13, 2011. All of the researchers presented updates on their projects. Approximately 45 industry representatives and researchers attended the meeting.
- Southern Division met on July 20-21, 2011 in Muskogee, OK where the research projects were discussed with industry.
- Safety/HR meeting on August 9-10, 2011 in Spokane discussed the use of MFFT in Visual Inspector testing.
- Eastern Division met in Bay City, MI on August 17-18 2011 where the research projects were discussed with industry.
- Meeting of Carbon and Low Alloy Research Committee on October 13, 2011 at ISU, Ames, IA. Received an update and demonstration of the Visual Inspection project by Frank Peters and Richard Stone. The committee could see applications in other areas of visual inspection, e.g. magnetic particle inspection.
- Conference call with ATI/PSU on October 31, 2011 to discuss plans to obtain material from member foundries for PSU.
- SFSA T&O conference, Chicago, IL, December 7-10, 2011. A practical demonstration of the MFFT was given to over 60 attendees to determine their aptitude for visual inspection. Updates from ISU, UAB, and Penn State. More than 200 attendees from industry and universities.
- Southern Division T&O meeting in Longview, TX, March 13-14, 2012. The research projects were discussed.
- Visit to ISU, Ames, IA, on March 27-28 2012 to review and discuss the Visual Inspection work.
- January 9 and February 7, 2012. Presentations on visual inspection were made at meetings of ASNT (Chicago, IL) and at MS&T (Rolla, MO).

- Eastern Division T&O, May 23-24, 2012. Presentation on all SFSA SWC projects (SFSA, ISU, UAB and PSU) to members.
- SFSA Board of Directors meeting, June 12-13, 2012. The status and findings of the SWC program was discussed.
- Meeting of Western Division T&O, Berkeley, CA, July 12-13, 2012.
- Carbon and Low Alloy Research Review, Chicago, IL, July 17-18, 2012. All of the researchers presented updates on their projects. More than 30 industry and research attendees
- Training Meeting, Spokane, WA, August 14-15, 2012. Presentation on lessons learned and the implementation of the findings from work on SWC projects. Approximately 25 attendees were present.
- Meetings of SFSA Executive Committee and Board of Directors, September 8-9, 2012. The results of the SWC work were discussed.

Throughout the course of the SWC program monthly and quarterly reports from researchers were circulated to the SFSA research committees for their information and comment. SFSA also participated in bi-monthly Technical Advisory Committee (TAC) meetings to review and discuss the progress of the program.

11. American Foundry Society (AFS) Final Report: Principal Investigator Thomas Prucha, AFS

Under the SWC program, AFS has worked to link their SWC-sponsored research with the metalcasting industry and Benet/DoD in order to maximize the impact of the resulting SWC technology developments. AFS has leveraged their knowledge, expertise, and membership to monitor project progress and promote the transition of the technology developed under SWC into industry. This knowledge transfer will maximize the return on investment made by both government and industry, expand and deepen existing industrial partnerships, and result in higher strength, lower cost castings for Benet and DoD. The emerging SWC metalcasting technology will be applied to known problematic cast parts that might lack sources of supply, involve redesign requirements or revising product, process, or test specifications. AFS also participated in bi-monthly Technical Advisory Committee (TAC) meetings.

Specifically, AFS has conducted the following efforts to ensure the successful transition of SWC technology into industry:

- AFS published quarterly SWC Update Summary Reports for the International Journal of Metalcasting (IJMC), which it published on a quarterly basis
- Weekly SWC Conference Calls with SWC researchers
- AFS Wisconsin Regional Meeting, April 21, 2010
- AFS Research Board meeting, June 14, 2010, Schaumburg, IL
- AFS Division Council meeting, June 15, 2010, Schaumburg, IL
- 2011 Metalcasting Congress, Schaumburg, IL, April 5-8, 2011 (including individual project reviews)
- 2011 AFS Casting Congress Panel Report (11-165) Visual Inspection Research Report, April 6, at the 3:45pm Engineering Session, including:
 - Frank Peters – ISU
 - Ted Shorn – Enkei
 - Nick Fox – Galesburg Casting
- AFS Research Board, June 14, 2011, Schaumburg, IL
- AFS Division Council, June 15, 2011, Schaumburg, IL
- AFS Aluminum Division (Div. 2), June 16, 2011, Schaumburg, IL
- AFS Energy Conference, June 28-29, 2010, Schaumburg, IL
- SWC status update in V.P. Report for AFS Board meeting, Schaumburg, IL, August 17, 2011
- AFS Research Board meeting, Schaumburg, IL, August 23, 2011
- AFS Aluminum Division meeting, Schaumburg, IL, September 15, 2011
- AFS Cast Iron Research Committee meeting, Schaumburg, IL, September 22, 2011
- AFS Division Council, November 15, 2011, Schaumburg, IL
- AFS Research Board, November 16, 2011, Schaumburg, IL

- UAB Project review at Div. 2 Aluminum meeting, Schaumburg, IL, January 26, 2012
- SWC status update in V.P. Report for AFS Board meeting, Schaumburg, IL, January 28-29, 2012
- AFS Research Board meeting, February 7, 2012
- MS&T Project review, 4L Investment Casting Research meeting, MS&T, Rolla, MO, February 9, 2012
- 2012 Metalcasting Congress, Columbus, OH, April 17-20, 2012 (including individual project reviews)
- Reviewed SWC papers for presentation at 117th Casting Congress and CastExpo'13, St. Louis, MO, April 6-9, 2013

12. North American Die Casting Association (NADCA) Final Report: Principal Investigator Steve Udvardy, NADCA

Transfer of technological information and results from this project were provided by various means in order to transition the technology into the public domain. Monthly and quarterly reports were provided throughout the project. Presentations to the NADCA R&D Committee transferred information to the committee members. The R&D Committee, which meets three times per year, also assisted in monitored and providing oversight to the project. Similarly, presentations were provided during the semi-annual Worcester Polytechnic Institute's Advanced Casting Research Center Consortium meetings, transferring information to the consortium members. Two annual progress presentations were also provided for Benet Laboratories personnel. Information on this project was also presented during various NADCA Chapter presentations and visit to die casting companies around the country as well as during select NADCA courses, such as Introduction to Die Casting and Die Casting Defects.

A description of the project was encompassed in two articles on the NADCA R&D Strategic Plan and Roadmap which were published in the July 2011 and July 2012 issues of the Die Casting Engineer Magazine and also posted on the NADCA website. In addition, a 2012 NADCA Congress Transactions paper was published and presented at the 2012 Die Casting Congress & Exposition which was held October 8-10, 2012 at the Indiana Convention Center in Indianapolis, Indiana.

Details of the technology transfer efforts are included in the list below.

- An overview of the High Performance Nano-Composite Materials project was presented at a kick-off meeting that was held at Benet Laboratories on April 29, 2010.
- An update presentation of this work was provided at the NADCA R&D Committee meeting on October 14, 2010.
- A NADCA R&D Program presentation including information on this project was provided for the NADCA Chapter 39 in Southwestern Michigan on October 14 and for NADCA Chapter 9 in Central New York on October 27, 2010.
- A NADCA R&D Program presentation including information on this project was provided for the NADCA Chapter 30 in Los Angeles on November 10, 2010.
- A NADCA Update presentation, including the R&D Program and this project, was provided for the NADCA Chapter 29 in Lewisburg, TN on January 26, 2011.
- Information on this project was provided during a presentation for NADCA Chapter 16 in Minneapolis, MN on February 9, 2011 and NADCA Chapter 5 in Chicago, IL on February 10, 2011.
- Information on this project was provided on March 23, 2011 at the NADCA Executive Conference which was held in Tucson, Arizona.
- Information on nano-composites was presented at the NADCA Plant Management Conference which was held in Cleveland, Ohio on May 18-20, 2011.

- Updates on the GLN and IDP work were provided during project reviews at WPI on May 25, 2011.
- A project update was provided at the JDMTP Review at Benet on June 7, 2011.
- Presentations on the project were provided at the NADCA Technical Committee meetings held at Mercury Marine on June 15 and 16, 2011.
- Information on nano-composites was given during a NADCA course presented to NADCA Chapter 17 on June 2, 2011 in Sikeston, MO.
- An overview of the NADCA R&D Strategic Plan and Roadmap, citing this project, was published in the July 2011 issue of Die Casting Engineer Magazine.
- A NADCA research and technology presentation, containing information from this project, was presented at a NADCA Chapter 3 meeting on September 29, 2011.
- Information on the nano-composite development was presented during the NADCA Technical Committee meetings on October 13 and 14, 2011 at NADCA Headquarters.
- Nano-composite development information was providing during a die casting course that was presented on November 4, 2011 for NADCA Chapter 3 in Grand Rapids, Michigan.
- Update presentations were made during the Worcester Polytechnic Institute casting consortium meeting on December 7, 2011.
- AN update on the nano-composite development was providing during a visit to the NADCA St. Louis, Missouri Chapter 17 on January 17, 2012.
- An update presentation on this project was provided to the NADCA R&D committee on February 9, 2012 at NADCA headquarters and an update was providing during a visit to the NADCA Chapter 3 on February 16, 2012 in Grand Rapids, Michigan.
- Information on this project was provided during a presentation at a NADCA Chapter 10 event on May, 2012 in Toronto, Canada.
- An Update on the nano-composite development was presented during the Worcester Polytechnic Institute casting consortium meeting on June 6, 2012 and the NADCA Technical Committee meetings June 13 and 14, 2012, at Twin City Die Castings Company in Minneapolis, MN.
- An article on the 2013 NADCA R&D Strategic Plan and Roadmap, citing this project, was published in the July 2012 issue of Die Casting Engineer Magazine.
- A presentation on this project was provided at the AMC Review which was held on Milwaukee on July 24 and 25, 2012.
- Nano-composite materials and this project was mentioned during a NADCA Introduction to Die Casting course that was presented at Madison Precision Products in Madison, Indiana on August 22 and 23, 2012.
- A paper containing information about this project was completed for the NADCA Die Casting Congress. The paper is entitled "Development of High Performance Nano-Composite Materials" and was presented at the Congress on October 8, 2012 at the Indiana Convention Center in Indianapolis.

